CELLULAR AND EXTRACELLULAR DETERMINANTS OF 3D CANCER CELL INVASION

A Dissertation

Presented to the Faculty of the Graduate School

of Cornell University

In Partial Fulfillment of the Requirements for the Degree of

Doctor of Philosophy

by

Shawn Patrick Carey

August 2015

EXPLORING CELLULAR AND EXTRACELLULAR DETERMINANTS OF 3D CANCER CELL INVASION

Shawn Patrick Carey, Ph.D.

Cornell University 2015

Breast cancer metastasis is a stepwise process during which cells dissociate from the primary tumor and migrate through extracellular matrix (ECM) and tissue barriers to spread to secondary sites. Metastasis is initiated when tumor cells acquire a motile phenotype and invade into the stromal ECM surrounding the tumor, which is heterogeneous and contains three-dimensional (3D) structural features including a diversity of fiber and pore microarchitectures, varying degrees of matrix alignment, and track-like structures. Notably, it is largely unknown whether, or how, these physical cues integrate with intracellular signaling to affect the behavior of invading cells. Furthermore, intratumor heterogeneity and cellular plasticity result in diverse and evolving invasive phenotypes whose molecular mechanisms are not well understood. Thus, despite the clinical importance of understanding and identifying invasive progression, the cellular and extracellular determinants that enable the invasive cancer cell phenotype remain unclear.

Here, we study the process of 3D cancer cell migration within biologically inspired *in vitro* models that mimic key aspects of the *in vivo* interstitial stroma and demonstrate

that the structure of a cell's local ECM regulates its invasive behavior. We show that 3D ECM microarchitecture controls the acquisition of cell motility by directing subcellular protrusion dynamics. By inducing adhesion signaling-dependent anisotropy of these cellular morphodynamics, aligned matrix guides and accelerates 3D cell spreading and migration. Furthermore, we find that physiological ECM-free microtracks provide additional pro-invasive cues that substantially reduce the mechanistic burden of 3D cell migration.

We further observe in an *in vitro* model of intratumor heterogeneity that malignant "leader" cells create invasion-enabling microtracks within 3D ECM that can induce invasion of otherwise non-invasive "follower" cells. Through further studies, we determine that invasive fitness, which can be heterogeneous across a cell population, is an intrinsic and heritable cell trait. We exploit this finding to establish invasive and non-invasive cancer cell subpopulations, which we subsequently use to identify characteristic molecular and phenotypic attributes of invasive and non-invasive cells. Finally, we explore a potential consequence of "follow-the-leader" invasion and demonstrate that exposure to a stroma-like collagen-rich microenvironment induces mesenchymal gene expression and an invasive phenotype in non-invasive, non-transformed mammary epithelial cells.

Together, our findings demonstrate that invasiveness is coordinately determined by a cell's intrinsic 3D migration propensity as well as its local 3D extracellular matrix, both of which can be heterogeneous across a given tumor-stroma microenvironment.

Despite the inevitable complexity that arises from this heterogeneity, these findings contribute to our understanding of invasion-enabling extracellular features as well as the context-dependent molecular mechanisms by which cells to respond to such features during 3D cancer cell invasion.

BIOGRAPHICAL SKETCH

Shawn Patrick Carey was born in New Britain, Connecticut on May 19, 1987 as the second of three sons to Kevin and Rosanne Carey. He grew up in Southington, Connecticut, with his brothers, Ryan and Brendan, with whom he shared interests in music and science. Shawn graduated from Southington High School in 2005 and attended Worcester Polytechnic Institute as a Charles O. Thompson Scholar and Dean's Scholar. He graduated with High Distinction in May 2009 with a B.S. in Biomedical Engineering and minors in Material Science and Cell Biology and was presented the Salisbury Award. In August 2009, Shawn entered the Ph.D. program in Biomedical Engineering at Cornell University and joined the lab of Dr. Cynthia Reinhart-King, where he studied the cellular mechanisms and extracellular matrix factors that regulate tumor cell migration and invasion. He was awarded a GAANN Fellowship in 2009, as well as an HHMI Med-into-Grad Fellowship and a National Science Foundation Graduate Research Fellowship in 2010, and he received an M.S. in Biomedical Engineering in 2013. Outside of research, Shawn is involved in service to the field of Biomedical Engineering at the local and national levels, and has served as the Student Representative to the National Biomedical Engineering Society Board of Directors and the National Student Treasurer of Alpha Eta Mu Beta, the Biomedical Engineering Honor Society. In his free time, Shawn likes to spend time cooking and enjoying music and life with his wife, Teri, and son, PJ.

For my friends and family

ACKNOWLEDGMENTS

I have been very fortunate throughout my life to enjoy the support of many people, without whom this work would not have been possible.

I would first like to thank my advisor Dr. Cynthia Reinhart-King for many fantastic years of mentorship. Cindy entrusted me to direct my own research from day one, allowing me to make mistakes (and learn from them) while exploring countless project directions, all the while maintaining a seemingly always open door and an endless willingness to discuss science and life. Regardless of whether she knew it or not (she knows now), this experience taught me how to effectively formulate and address questions in research, gave me a tremendous amount of confidence, and strengthened me as a scientist and a mentor. I admire the patience and trust she showed when I notoriously refrained from showing her results until the “big reveals”, as well as her understanding of when to step in to refocus or redirect a project. I am deeply grateful for her mentorship and I will always appreciate the scientific, professional, and personal wisdom Cindy has shared with me.

I would also like to acknowledge and thank my dissertation committee members, Dr. Anthony Bretscher and Dr. Warren Zipfel, for their support and supervision of my research.

In a variety of ways, the members of the Reinhart-King (CRK) Lab have played a major role in my time at Cornell and the building of this dissertation, and it has been my privilege to work with them. I would like to first acknowledge my graduate student predecessors Joe Califano, John Huynh, Casey Kraning-Rush, and Brooke Mason for welcoming me, teaching me the ways of the CRK lab, and providing many years of fantastic collaboration and friendship. Thanks to my lab contemporaries, Jon Charest and Courtney Faber (and Brad), as well as Dr. Francois Bordeleau, Marsha Lampi, Julie Kohn, Joe Miller, Aniqua Rahman, Danielle LaValley, Lauren Hapach, Jacob VanderBurgh, and all other members of the CRK lab for collaboration and friendship over the years.

I am especially grateful for and indebted to the members of the CRK lab I was fortunate to mentor: Karen Martin, Zach Goldblatt, and Allie Braun made tremendous contributions to this work, and it was truly a pleasure to watch each of them grow into superb scientists over the years we worked together.

I would also like to acknowledge the colleagues with whom I have had the opportunity to formally collaborate. Thank you to Dr. Sandra Shin, Dr. Timothy D'Alfonso, Dr. Rebecca Williams, and Dr. Betsy Romero for graciously providing their time, resources, and expertise.

I gratefully acknowledge the funding that has supported this work, including a U.S. Department of Education Graduate Assistantship in Areas of National Need

(GAANN) Fellowship, a National Science Foundation Graduate Research Fellowship, a Douglas Family Fellowship, and a Howard Hughes Medical Institute Med-into-Grad Fellowship.

My path in Biomedical Engineering began at Worcester Polytechnic Institute, and I am grateful to my undergraduate research advisor Dr. George Pins and my supervising graduate student Dr. Kevin Cornwell for instilling in me a passion for BME research. Thanks also to Dr. Kris Billiar, Dr. Glenn Gaudette, and Dr. Marsha Rolle for phenomenal teaching and mentoring that began at WPI and continues to this day.

I am particularly thankful for the friendship and support of my fellow graduate classmates, Jen Richards, Katie Melville (and Alex), Jenny Puetzer, Jon Charest, and Mitch Cooper. From class assignments that turned into outlining wacky projects that somehow combined all of our unique research interests, to Thursday night dinners, to just unwinding with friends, I have truly enjoyed the time we have spent together and sincerely appreciate the advice, support, relaxation, and fun that came along with it.

Finally, I am indebted to my family for their inspiration, encouragement, and unconditional love. Thanks to my parents, Kevin and Rosanne, and my brothers, Ryan and Brendan, for instilling in me a passion for learning and problem solving, and providing support in all forms throughout my education and life. There are not words to express the extent of my gratitude for my wife, Teri. In addition to providing me with loving and supportive in-laws, she has sacrificed so much in her life and career

for our family and has masterfully handled the better part of the parenting load, especially over the past 6 months. Her positivity and love are endless, and I could not imagine a better partner with whom to journey through the rest of life. Finally, thank you to my son, PJ, who I hope will read this someday and know that his curiosity, enthusiasm, and energy have served as the ultimate inspiration for me in writing this – in his words – “my story”.

TABLE OF CONTENTS

Biographical Sketch iii
Dedication iv
Acknowledgments v
Table of Contents ix
List of Figures xi

Chapter 1 Introduction 1

Chapter 2 Biophysical Control of Invasive Tumor Cell Behavior by Extracellular Matrix Microarchitecture

2.1 Abstract 23
2.2 Introduction 24
2.3 Materials and Methods 28
2.4 Results 33
2.5 Discussion 43

Chapter 3 Mechanisms of 3D Cancer Cell Migration Guidance by Local ECM Alignment

3.1 Abstract 50
3.2 Introduction 51
3.3 Materials and Methods 52
3.4 Results 57
3.5 Discussion 76

Chapter 4 Comparative Mechanisms of Cancer Cell Migration Through 3D Matrix and Physiological Microtracks

4.1 Abstract 85
4.2 Introduction 86
4.3 Materials and Methods 89
4.4 Results 96
4.5 Discussion 111

Chapter 5 Leading Malignant Cells Initiate Collective Epithelial Cell Invasion in a 3D Heterotypic Tumor Spheroid Model

5.1 Abstract 121
5.2 Introduction 122
5.3 Materials and Methods 126
5.4 Results 131
5.5 Discussion 146

Chapter 6 Sorting Out Tumor Cell Heterogeneity: Phenotypic Isolation of Differentially Invasive MDA-MB-231 Subpopulations

6.1 Abstract 160

6.2 Introduction 161
6.3 Materials and Methods 163
6.4 Results 169
6.5 Discussion 182

Chapter 7 Induction of a Mechanosensitive Invasive Epithelial Phenotype by 3D Collagen Matrix

7.1 Abstract 191
7.2 Introduction 192
7.3 Materials and Methods 194
7.4 Results 198
7.5 Discussion 211

Chapter 8 Conclusions and Future Directions

8.1 Conclusions 222
8.2 Future Directions 228

Appendix A Epithelial and malignant breast cell culture 237
Appendix B Type I collagen isolation and purification 241
Appendix C 3D collagen matrix alignment 243
Appendix D Multicellular spheroids 247
Appendix E siRNA transfection of MCF-10A and MDA-MB-231 cells 251
Appendix F Extraction of mRNA from 3D matrix samples 253
Appendix G Immunofluorescence of 3D samples 255
Appendix H Phenotypic cell sorting 257

References 260

LIST OF FIGURES

Chapter 2

Figure 2.1. Confocal reflectance microscopy reveals differential collagen gel microarchitecture in response to media formulation and gel thickness. 34
Figure 2.2. Quantitative analysis of collagen gel microarchitecture with image autocorrelation analysis. 35
Figure 2.3. Sensitivity of collagen gel microarchitectural features to media formulation and gel thickness. 36
Figure 2.4. Collagen gels for cell behavior studies. 38
Figure 2.5. Collagen gel microarchitecture impacts cell morphology. 40
Figure 2.6. Influence of collagen gel microarchitecture on cell migration and proliferation. 42

Chapter 3

Figure 3.1. Extracellular matrix alignment *in vivo* and *in vitro*. 58
Figure 3.2. Morphodynamics of early 3D cell spreading and migration initiation. 60
Figure 3.3. Protrusion formation rate during 3D migration. 62
Figure 3.4. Cell-matrix interactions during early matrix probing. 63
Figure 3.5. *In vitro* alignment of 3D collagen matrix. 64
Figure 3.6. Guidance of 3D cell spreading by extracellular matrix alignment. 66
Figure 3.7. Spatial guidance of early protrusion dynamics by extracellular matrix alignment. 68
Figure 3.8. Guidance of 3D cell migration by extracellular matrix alignment. 70
Figure 3.9. Guidance of 3D protrusion and adhesion formation by matrix structure. . 71
Figure 3.10. Regulation of 3D matrix alignment-induced protrusion anisotropy. 73
Figure 3.11. Regulation of 3D matrix alignment-induced morphology anisotropy. 74
Figure 3.12. Regulation of 3D matrix alignment-induced migration anisotropy. 75

Chapter 4

Figure 4.1. Channel-like gaps in stromal extracellular matrix and microfabricated collagen tracks. 98
Figure 4.2. Density-dependent cell migration through 3D collagen matrix and microtracks. 100
Figure 4.3. Effect of β1 integrin function blocking on cell migration. 101
Figure 4.4. Regulation of elongated microtrack migration by β1 integrin. 102
Figure 4.5. Role of cell contractility and traction forces in microtrack migration. 104
Figure 4.6. Role of MLC phosphorylation in regulating cell behaviors. 107
Figure 4.7. Requirement for microtubule dynamics during migration through physiological ECM. 109
Figure 4.8. Requirement for actin cytoskeleton dynamics during migration through physiological ECM. 110

Chapter 5

Figure 5.1. Multicellular spheroid compaction. 132
Figure 5.2. Cell organization within heterotypic co-culture spheroids. 133
Figure 5.3. Three-dimensional multicellular tumor spheroid invasion. 135
Figure 5.4. Leader-follower behavior in invasive strands. 136
Figure 5.5. Matrix reorganization associated with malignant cell invasion. 138
Figure 5.6. Intercellular interactions during co-invasion. 140
Figure 5.7. Effects of proteolysis and cell contractility on matrix reorganization during invasion 142
Figure 5.8. Role of proteolysis and cell contractility in induced collective epithelial cell invasion. 143
Figure 5.9. Effects of MMP and ROCK inhibition on co-culture and malignant spheroid invasion. 145

Chapter 6

Figure 6.1. Heterogeneity and heritability of 3D migration in parental MDA-MB-231 cells. 170
Figure 6.2. Phenotypic cell sorting to purify differentially invasive MDA-MB-231 subpopulations. 171
Figure 6.3. 3D matrix migration of purified MDA-MB-231 subpopulations. 173
Figure 6.4. 3D morphodynamics of purified subpopulations. 174
Figure 6.5. 3D collagen microtrack migration of purified subpopulations. 176
Figure 6.6. Differential cell morphology of purified subpopulations. 177
Figure 6.7. Differential adhesion signaling of purified subpopulations. 178
Figure 6.8. 2D protrusion and Src-dependent membrane dynamics. 180
Figure 6.9. Cell contractility and ROCK-dependent matrix remodeling. 182

Chapter 7

Figure 7.1. 3D matrix-induced epithelial cell phenotypes. 199
Figure 7.2. 3D matrix-dependent gene expression. 201
Figure 7.3. Regulation of invasive epithelial phenotype by matrix-induced MT1-MMP. 203
Figure 7.4. Matrix pore size-dependent epithelial cell migration and invasion. 205
Figure 7.5. Molecular regulation of the invasive epithelial phenotype. 207
Figure 7.6. Role of cell and matrix mechanics in regulating invasive epithelial phenotype. 208
Figure 7.7. Mechanosensitivity of the invasive epithelial phenotype. 210

Chapter 8

Figure 8.1. Adhesion signaling and Rho GTPases in 3D cell spreading. 230

Figure 8.2. Autologous mechanotaxis. 232
Figure 8.3. Differential gene expression in MDA^{INV} and MDA^{NON} cells. 233
Figure 8.4. Anticipated results of matrix-induced gene expression studies. 235

CHAPTER 1

INTRODUCTION

Portions of this chapter were published in *Critical Reviews in Oncology/Hematology* [1] and *Cellular and Biomolecular Mechanics and Mechanobiology* [2].

Cancer metastasis, which accounts for 90% of human cancer deaths, requires stepwise dissociation from the primary tumor, dissemination across matrix and tissue barriers, and colonization and growth of cancer cells within distant tissues [3]. As one of the earliest steps of metastasis, local tissue invasion represents a critical transition from local deregulated cell growth to potentially lethal disease. Cancer invasion is an adaptive, inherently biophysical process that requires cells to adeptly coordinate adhesion, motility, mechanobiological, and proteolytic cellular machinery to overcome barriers in the microenvironment [4–6]. Clinically, the histopathological identification and characterization of tumor invasion is a key component of carcinoma staging, and as such, the extent and nature of invasion largely determine management strategy [1]. Thus, the invasive potential of tumor cells is of particular biological and clinical relevance, and definition of cellular and extracellular determinants of the invasive cancer cell phenotype remains a major goal. While tissue invasion and metastasis correlate with high mortality in all types of cancer, this dissertation focuses on breast cancer.

The mammary epithelial microenvironment in health and malignancy: a clinical perspective

The mammary gland is a highly organized tissue consisting of cellular and noncellular components that exhibit an intimate tie between structure and function. As in all epithelial tissues, a continuous basement membrane primarily consisting of the extracellular matrix (ECM) molecules laminin and type IV collagen coats the basal surface of ducts and lobules in healthy breast tissue [7], forming a dense meshwork that is maintained by both epithelial cells and stromal fibroblasts [8] and prevents epithelial cells from entering the interstitial stroma [9, 10]. Underlying the basement membrane is the type I collagen-rich stroma, which is a complex three-dimensional mixture of cells and connective tissue that can be highly heterogeneous in cellular and ECM composition and organization [11–13].

Malignancy of the breast epithelium is associated with many changes in tissue architecture, cytology (the basic anatomy of a cell), and the stroma [14, 15]. Invasive carcinomas of the breast, which can originate from either the ducts or lobules of the luminal epithelium, generally present clinically as cells exhibiting malignant cytoarchitectural features and infiltrating the stromal compartment either singly or organized into tubules. The migration of epithelial/carcinoma cells into the stromal compartment during invasion exposes cells to a microenvironment that is vastly different from that of the epithelial compartment, and critically, allows invading cells to access blood and lymphatic vessels through which they metastasize to secondary sites [9, 13, 16]. Of note, molecular studies of invasive tumor cells and their non-

invasive malignant counterparts have not been able to reveal gene signatures predictive of or even consistently associated with invasive progression [17, 18]. Thus, while the clinical importance and risk of cancer invasion are universally appreciated, our mechanistic understanding of how invasion is initiated and sustained in breast carcinoma cells remains limited.

Many of the most dramatic and clinically useful changes that occur during tumor invasion affect elements of the tumor microenvironment rather than invading cells themselves. The most significant of these changes is the loss of the myoepithelium and epithelial basement membrane [9, 19–21]. The absence of both of these components serves as a critical diagnostic marker of invasive carcinoma, allowing pathologists to distinguish between invasive carcinoma and carcinoma *in situ* [22], which refers to a non-invasive carcinoma that does not disrupt the epithelial basement membrane to infiltrate the surrounding stroma. Interestingly, the loss of basement membrane can arise from both downregulation of ECM synthesis and proteolytic degradation of the ECM barrier [23, 24] and despite extensive cell and ECM dynamics during physiological tissue remodeling, hyperplastic disorders, and carcinoma *in situ*, only during invasive migration do epithelial/carcinoma cells breach the basement membrane and pass into the stromal compartment [9, 25].

Recently, the tumor stroma, which is biochemically and biophysically heterogeneous and dynamic, has gained increasing attention for its role in cancer progression, and more specifically, tumor cell invasion [17, 26–28]. Invasive carcinoma has a firm

texture and an infiltrative appearance due to the development of a fibrocollagenous stroma around the tumor, termed desmoplasia [29]. Since carcinoma *in situ* lacks a desmoplastic response, there is great interest in determining whether desmoplasia is induced by malignant tumor cell invasion or is itself a precursor to and initiator of tumor invasion [30–32]. Notably, stromal desmoplasia is associated with increased myofibroblast composition and enhanced deposition of fibrin, fibronectin, and type I collagen ECM, all of which are important for invasive cancer progression [12]. Myofibroblasts persistently reside in the tumor stroma, but not in benign breast tissue [33], and are thought to contribute to tumor cell invasion in a number of ways including through the production and degradation of ECM [34] and the generation of contractile forces that result in ECM remodeling [33, 35]. Thus, myofibroblast-mediated ECM remodeling contributes in part to the stromal heterogeneity observed in invasive breast carcinoma, with loose and dense ECM associated with active, ECM-secreting fibroblasts and contractile mature myofibroblasts, respectively [33].

As demonstrated by recent advances in intravital microscopy and imaging of the tumor microenvironment [36–38], further physical diversity of the malignant stroma arises from anisotropic ECM features such as aligned matrix fibers [27, 39] as well as track-like structures including tissue interfaces, clefts between discrete ECM components, proteolysis-derived matrix channels, and coordinated networks of ECM pores [37, 40–42]. Together, these features provide a diversity of physical structures through which carcinoma cells can negotiate during invasion within the stromal ECM. Since the extracellular matrix that comprises the interstitial stroma can simultaneously

serve roles as adhesion substrate, force transducer, guidance cue, and steric barrier for cells within it [13], such cell-scale structural properties of the stromal ECM are likely of critical importance to invasive migration.

Nonetheless, despite a growing awareness of these characteristic ECM signatures of invasive tumor progression (e.g., compromised basement membrane, modification of tumor stroma), our understanding of the effects of these "ECM biomarkers" is minimal. At best, this knowledge is generally limited to whether or not an ECM biomarker is predictive of metastasis and how it correlates with patient prognosis and survival. This level of understanding is certainly important clinically, where such prognostic indicators can help direct management strategy [1, 20, 39]. However, defining the mechanisms by which tumor cells detect, integrate, and ultimately respond to such ECM cues during invasive migration will be necessary to design therapeutic strategies to block this critical aspect of tumor progression. Thus, it remains to be determined: 1) to what extent the stromal ECM mediates the invasive phenotype, and 2) the mechanisms by which this regulation occurs. To appropriately define the cellular mechanisms and extracellular matrix determinants of the invasive phenotype, analysis of actively invading tumor cells in suitable *in vitro* and *in vivo* model systems is required.

Tumor cell invasion: a mechanobiology perspective

Although it is detected clinically as a static histopathological observation, tumor cell invasion is a dynamic, inherently biophysical process that involves physical changes at

the cell and tissue scales, extracellular matrix remodeling, and directed locomotion of malignant cells through complex three-dimensional ECM [9, 43, 44]. Analysis of cell migration on 2D substrates has shown that cells must orchestrate several fundamental cellular mechanisms including cell-matrix adhesion and protrusive/contractile cytoskeleton dynamics to achieve "shape change with a bias" [2, 45]. Critically, properties of the 2D migration substrate including composition, stiffness, and ligand density are detected by cells and can dramatically influence migration [44]. To achieve movement in 3D microenvironments, mesenchymal cells (e.g., fibroblasts, cancer cells) must coordinate cell-matrix adhesion and cytoskeleton dynamics as in 2D, but the 3D ECM contains additional biophysical and biochemical complexity, including intricate topographical, architectural, and mechanical cues, that can directly affect cell motility as well as determine the mechanistic burden of migration [44, 46, 47]. Critically, many of the features that influence 3D motility are analogous to those observed in the invasive tumor stroma, so understanding the regulatory effects of 3D matrix features on cell migration is of utmost importance.

While advances in intravital microscopy have enabled the study of 3D cell motility *in vivo* [48–51] the majority of our mechanistic understanding of 3D cell migration has come from the study of cell migration using 3D reconstituted type I collagen and cell-derived matrices. Whereas cell-derived ECM provide biochemical and biophysical complexity resembling *in vivo* matrix environments [52, 53], reconstituted matrix models provide the ability to experimentally tune structural, mechanical, and chemical ECM properties [41, 42, 47, 54–57]. Thus, systematic analyses of migration within

defined 3D matrices have begun to define the role of 3D ECM composition [58], microarchitecture [41, 47, 55, 59, 60], topography [56], and stiffness [57] in regulating 3D cancer cell migration. Still, the study of 3D microenvironmental context-specific migration mechanisms remains in its infancy [44].

The ultimate goal of studying 3D tumor cell migration is to sufficiently understand how and why cancer cells invade such that therapeutic strategies specifically targeting key enabling molecular, cellular, and extracellular processing during invasive progression can be developed. To date, the study of cancer cell migration in various contexts (2D, 3D, *in vivo*) has revealed a wealth of information with regard to the basic biophysical mechanisms that together define the "invasive phenotype" [1]. Effective negotiation of stromal 3D ECM broadly requires coordination of adhesion, protrusion, and contractility mechanisms as in 2D migration, as well as matrix remodeling and more advanced decision-making unique to 3D microenvironments. Thus, in the following sections, we present the "invasive phenotype" as the integration of biophysical behaviors that are determined by interconnected molecular and mechanical networks that participate in the regulation of mechanotransduction, cytoskeletal dynamics, cell adhesions, and thus, cell shape, mechanics, and migration. Where they have been identified, we describe context-specific behaviors and mechanisms including the effects of ECM stiffness and structure, but as indicated above, this knowledge generally remains limited.

Initiation of invasion

While the molecular mechanisms that initiate invasion are complex [61], it is clear that neoplastic epithelial cells must undergo changes in their adhesion status, morphology, and motility to invade the tumor stroma. Though these changes together resemble a conversion to a classical mesenchymal phenotype, the involvement of epithelial-mesenchymal transition (EMT) in cancer progression is controversial [62–64] because a complete plastic transition from epithelial to mesenchymal phenotypes is rarely observed clinically. Recently, an emergent perspective suggests that the phenotypic flexibility observed in malignant epithelial cells should not be attributed to EMT as if it were a single conserved process, but rather, that the many biological intermediaries should be considered as grades of "EMT-like" behavior [65–67]. Thus, because malignant cells are able to transiently exhibit select attributes along a spectrum between the epithelial and mesenchymal phenotypes, they can be considered *metastable* [66]. Indeed, this proposition supports the hypothesis that the mode of tumor cell invasion can be "tuned" through intra- and extracellular regulation of cell adhesions, protrusions, and tractions [68, 69]. In recent work, Nelson et al. identified a link between cellular mechanobiology and this epithelial-mesenchymal spectrum, showing that cell spreading positively affects epithelial cells' sensitivity to the classic EMT-inducing factors MMP3 and Rac1b [70]. A continuation of this work using engineered culture systems, traction force microscopy, and finite element modeling demonstrated that intercellular mechanical tension in multicellular tissue analogs generates gradients of mechanical stress and that regions exposed to the highest endogenous mechanical stresses are most likely to acquire mesenchymal attributes

[71]. Since selective loss of basement membrane at the invasive front is associated with acquisition of a more mesenchymal phenotype at the molecular level [23], the relationship among cell morphology and mechanics, basement membrane degradation, and the mesenchymal phenotype remains an intriguing area of research. While a universal initiator of tumor invasion has not been defined, there is mounting evidence that cell mechanics, through cell adhesions, cell and tissue morphology, and both endogenous and exogenous stresses, plays a role in driving this first step in the metastasis process [61].

Breaching the basement membrane

The epithelial basement membrane is important for maintaining epithelial polarity and differentiation [72], and thus, epithelial tissue homeostasis and structure. The ability of neoplastic cells to proteolytically degrade the basement membrane has long been considered an indicator of metastatic potential [19, 73], and there is evidence that synthesis of basement membrane components by epithelial cells is critical for its integrity and function [23, 72]. These findings, as well as the aforementioned clinical importance of basement membrane histopathology as a prognostic indicator of invasion, have motivated a number of studies examining the mechanistic role of basement membrane degradation in tumor invasion. Thus, it is now accepted that invading tumor cells proteolytically degrade the underlying extracellular matrix through specialized actin-rich protrusive structures known as invadopodia [74]. *In vitro* studies, in which invadopodia are induced by plating cells on top of extracellular matrix gels, as well as *in vivo* analysis of tumor cell invasion have demonstrated that

invadopodia formation and ECM degradation are important in tumor cell invasion [75, 76]. The molecular composition, structure, and regulation of invadopodia are therefore of great interest [50, 77–79]. Of particular interest is the presence of adhesion, signaling, cytoskeleton, and cell contractility molecules that together impart a mechanosensing capability in invadopodia. Notably, Alexander et al. demonstrated that increased stiffness of the underlying ECM substrate up-regulates invadopodia number and activity through the signaling molecules FAK and p130Cas [80]. Interestingly, the biophysical relationship between extracellular matrix stiffness and the invasive capacity of tumor cells is reminiscent of the clinical observation of fibrocollagenous stromal ECM surrounding invasive carcinomas. Accordingly, there is considerable support for a mechanistic tie between stromal density and invasive progression [81–83].

Cell protrusions

While invadopodia are critical for the initial breach of the basement membrane and exposure to stromal ECM, it is the maturation of these structures into larger protrusive extensions that enables invasion into the surrounding stroma [84]. By analyzing the growth rate, orientation, and lifetime of tumor cell protrusions and comparing them to the speed of cell migration, Fraley et al. showed that tumor cell migration is in part driven by the frequent extension of exploratory membrane protrusions [85]. As in invadopodia, the development of such invasive pseudopodia depends heavily upon proteolytic degradation and the microtubule and actin cytoskeletons [86–88]. Advances in molecular and imaging technologies have contributed to a detailed

understanding of how networks of Rho GTPases regulate the actin cytoskeleton [89], and these insights have been applied to the study of tumor invasion both *in vitro* and *in vivo* [90, 91]. Of the many known regulatory cascades, the largely antagonistic Rac1/WAVE2/Arp2/3 and RhoA/ROCK pathways, which generally control protrusive and contractile cell processes, respectively, are particularly relevant to the invasive phenotype [92]. Rac1-mediated signaling, along with effectors of Cdc42 [93] and R-Ras [94], contributes to an elongated, motile phenotype through the induction of membrane protrusions as well as the repression of actomyosin contractility, which, unchecked, tends to revert cells to an amoeboid, or rounded, phenotype [95–97]. Interestingly, the exogenous repression of pseudopod-specific proteins in several metastatic human cancer cell lines reverted these cells to a more epithelial phenotype and inhibited cell invasion [98], demonstrating the dynamic interchange between molecular regulators and effectors of pseudopodia and supporting the finding by Nelson et al. that changes in tumor cell morphology may be coupled with intermediary phenotypes along the epithelial-mesenchymal spectrum.

Cell-matrix adhesions

As cells generate invasive protrusions into the surrounding ECM, they develop integrin-based adhesions along the cell body, stimulating RhoA/ROCK activity, which causes actomyosin contractility and locally suppresses Rac-based actin polymerization and cell protrusion [99]. Integrin activation via attachment to extracellular matrix ligands is part of a bidirectional signaling network between the ECM and the cytoskeleton that drives mechanotransduction, molecular switching, and signal

transduction, and plays a critical role in cancer progression [100, 101]. The contribution of integrin signaling to tumor invasion regulation is mediated through receptor tyrosine kinases such as focal adhesion kinase (FAK) and its many effectors, which control, among other things, the orchestration of motility machinery, cell-cell and cell-matrix adhesion modulation, gene transcription, and ECM degradation enzymes [2, 4, 101, 102].

Recently, an *in vitro* tumor migration model was used to show that the "tactile" ability of tumor cells is achieved through orchestration of cell protrusions, adhesions, and cytoskeletal contractility [85]. The authors suggested that the ability of cells to negotiate through their fibrillar three-dimensional microenvironment is dependent on 1) the extension of protrusive processes into the matrix, 2) the generation of short-lived adhesions and localized contractile cell forces to "feel" the physical and biochemical properties of the ECM, and finally, as determined through this assessment of the microenvironment, 3) the selection of a suitable direction in which to further engage the ECM and spread [85]. This study demonstrated the critical ability of integrins and their downstream effectors to act as intermediary regulators between the Rac and Rho pathways and contribute to both the protrusive/contractile, and thus, migratory behavior of tumor cells [99].

Several recent mechanobiological studies have revealed a strong relationship among the biophysical properties of the extracellular matrix, deregulated integrin signaling, and cancer progression. Increased expression and activation of β1-integrin-dependent

signaling regulators contribute to a number of cancers [102], and the β1-integrin subunit itself is required for tumorigenesis in a mouse breast cancer model [103]. One proposed mechanism for this observation is that, in addition to regulating Rac and Rho activity [99], abnormal integrin/receptor-tyrosine-kinase signaling induces loss of cell-cell adhesions, which normally have a role in maintaining tissue organization and structure [104]. Indeed, ECM stiffness-dependent over-activation of FAK and extracellular-signal-regulated kinase (ERK) has been shown to lead to deregulation of *in vitro* mammary tissue structure analogs through destabilization of cell-cell adhesions and enhanced cell contractility [81]. Additionally, high-density (stiff) collagen gels can induce an invasive phenotype through a FAK/ERK mechanotransduction network, with ERK acting to regulate transcriptional responses as well as cell contractility [105]. Finally, stiffening of the tumor stroma via crosslinking enhances tumor invasion through amplification of integrin and phosphoinositide 3-kinase (PI3K) signaling both *in vivo* and *in vitro* [106]. Together, these results present compelling evidence that maintenance of breast tissue structure is highly dependent on cellular adhesion homeostasis and that the mechanosensing role of cell-matrix adhesions and their downstream effectors can contribute to the physical disruption of mammary epithelium in an ECM-dependent manner.

Cell contractility

Cell contractility occurs when the motor protein myosin II forms oligomeric complexes that engage two overlapping actin filaments, translating them in anti-parallel directions and generating cytoskeletal tension [107]. The phosphorylation of

the myosin light chain (MLC) signifies a key controlling step in this process and involves a number of regulators, most notably, the Rho-associated kinase (ROCK) and myosin light chain kinase (MLCK) [108]. The kinase activity of ROCK is enabled by binding the active form of either of the small GTPases RhoA or RhoC and is responsible for directly phosphorylating MLC [109] and deactivating the negative regulator of MLC, myosin light chain phosphatase [109, 110]. Notably, RhoA and RhoC are generally over-expressed in tumors and play a number of critical, but distinct [111], roles in tumor progression [112, 113]. MLC-dependent contractility can also be mediated through MLCK activation by the mitogen-activated protein kinase (MAPK)/ERK linkage, which is downstream of adhesion- and growth-factor-dependent signaling through FAK/Src [114]. This FAK/ERK/MLCK pathway was shown to promote cell motility *in vitro* [115] through enhanced adhesion turnover [123]. Provenzano et al. recently showed that the FAK/ERK/contractility network enables an ECM density-dependent protrusive and invasive phenotype in cultured breast cells [105]. Importantly, both the FAK/ERK/MLCK-contractility [117] and Rho/ROCK-contractility [118] pathways have been shown to be part of bidirectional mechanotransduction circuits, and it has been suggested that deregulation of these positive feedback circuits can contribute to tumorigenesis and tumor invasion [81, 119]. Since malignancy-induced changes in the mechanics of the breast stroma are widely appreciated [14, 83], cellular mechanobiology is a major determinant in the process of tumor invasion.

Mechanosensing, which has been introduced above in the context of other invasive cell behaviors, is a cell's ability to sense and respond to the mechanical properties of its microenvironment. Through its biochemical linkage with, and dependence upon, cell adhesions, the cytoskeleton, and Rho GTPases, cell contractility plays a central role in coupling both the "sensing" and "responding" mechanisms [120, 121]. Stiffness, which is the resistance of a material to deform under application of an external load, is of intense interest in tumor mechanobiology, and a great deal of work has been done to determine how cells use mechanotransduction to modify their phenotype in response to properties of the ECM such as stiffness [122–127].

In addition to its role in mechanotransduction, MLC-based cell contractility is involved in a number of molecular tumor cell functions including regulation of proliferation [128] and differentiation [122] as well as many more classically mechanical cell functions such as cell morphology determination and traction generation [129]. The mechanical outcome of cell contractility depends on where and when it is generated as well as the combined states of the Rho GTPase family of cytoskeletal regulators [89]. Generally, cytoskeleton dynamics are responsible for establishing and supporting cell morphology, which largely determines physical cell function [130, 131]. Of particular interest to the mechanobiological study of tumor cell invasion is contractility in the cell cortex, which is a complex cytoskeleton-enriched structure on the inner surface of the cell membrane that plays a critical role in cell morphology determination [132]. ECM stiffness-dependent Rho-based contractility in the cortical actin network has been shown to inhibit cell protrusions, and local

depletion of this myosin II activity sufficiently destabilizes the stressed cortical cytoskeleton network to launch pseudopodia [133]. These findings demonstrate that cell contractility machinery can play a permissive role in enabling Rac- and Cdc42-mediated protrusions, and indeed, it has been suggested that actin-myosin contractility exhibits a dominant effect on cell morphology and migration in three-dimensional environments [95, 96, 134, 135].

When cells transfer cytoskeletal contraction to the extracellular matrix through integrins, forces known as cell traction forces are produced. Recently, there has been increasing interest in characterizing the molecular and extracellular regulators of these traction forces and factors such as substrate mechanics, cell adhesion, and traction-dependent ECM deposition are increasingly well understood for cells on planar substrates [124, 136–139]. However, the regulation and outcome of cell traction forces in the three-dimensional microenvironment of *in vitro* model systems and *in vivo* tissues are more obscure because of their spatial complexity and dimensionality [85, 86, 129, 140, 141]. Nonetheless, it is clear that tumor cells generate such myosin-dependent traction forces both *in vitro* and *in vivo* to modify cell-matrix adhesions and probe their mechanical environment as previously discussed, as well as to deform and remodel the extracellular matrix and translate the cell body during migration [97]. Cell-induced extracellular matrix reorganization is functionally important for tumor cells and occurs when cells repeatedly “gather” extracellular matrix towards the cell body via Rho/ROCK-based myosin contractility [142]. Notably, such cellular contractility has been shown to cause radial realignment of ECM adjacent to *in vitro*

tumor models, enabling a phenomenon known as *contact guidance*, whereby cells preferentially migrate through aligned regions of the ECM [56, 143, 144]. This cell-induced alignment closely resembles the stromal ECM remodeling seen in invasive tumors *in vivo* [27, 39], and microscopically pre-aligned collagen gels support Rho/ROCK-independent tumor cell invasion [56]. In addition to inducing extracellular matrix reorganization, cell tractions can enable translation of the cell body through the 3D ECM [134, 145]. Importantly, these propulsive traction forces are spatially, temporally, and functionally distinct from the traction forces that regulate matrix probing and remodeling [146]. A cell chooses among the distinct outcomes of cell traction forces in a context-dependent manner and, while it remains poorly understood, mechanobiology models and the ability to quantitatively assess physical cell behavior have improved understanding of this selection process.

Cell mechanics and deformability

There is considerable interest in understanding how the biomechanical state of tumor cells influences, and is influenced by, invasion [147]. The molecular basis, assessment, and implications of whole-cell biomechanical properties such as deformability and viscosity are of particular relevance to tumor cell invasion and are ultimately controlled by cell contractility and cytoskeleton dynamics [147, 148]. The cytoskeleton is organized into diverse and intricate networks of molecules that exhibit elegant form-function relationships and allow them to participate in sensing, resisting, and responding to internal and external mechanical forces [148–150]. The adaptability and dynamics of these networks allows cells to mechanically respond to the

mechanical, structural, and biochemical properties of the ECM [121, 128, 130, 151] and many methods have been developed to probe the subcellular and whole-cell mechanical reaction to both intracellular and extracellular factors [61, 147]. These analyses have shown that cell stiffness decreases with metastatic potential [152], and experiments with live human cells demonstrated that metastatic cancer cells are considerably less stiff than their normal epithelial counterparts [153]. Interestingly, the finding that tumor cell stiffness and metastatic potential are inversely related has been reported in a number of epithelial cancer models [154–157].

Work by Peter Friedl and coauthors indicates that this observation has consequences for invasive migration as cell contractility and deformability enable cells to use various modes of migration as they encounter steric obstructions in the extracellular matrix. For example, if the fibrillar three-dimensional ECM contains architectural features that restrict cell migration, the tumor cell is forced to either degrade ECM using contact-mediated pericellular proteolysis or squeeze through these features [47, 158]. Thus, cells use cytoskeletal contractility machinery to deform the cell body sufficiently to negotiate restrictive ECM [47, 159–161]. Notably, the cell nucleus, which is larger and stiffer than other organelles, can prevent a cell from successfully migrating through regions with particularly small pores or deformation-resistant extracellular matrix [47, 158]. Alternatively, sufficiently large ECM pores and matrix-free gaps in 3D interstitial ECM enable protease-independent migration [60, 162]. Therefore, there is interest in measuring the mechanical properties of the cell nucleus [163] and determining its role in invasive tumor cell migration [164].

Context-dependent integration of biophysical invasive behaviors

Invasive tumor migration requires coordination of the above described "invasive phenotype" functions, including initiation of invasion, breaching the basement membrane, generation of cell protrusions, cell-matrix adhesion dynamics and signaling, and the generation and application of cell contractility. By sequentially employing the *pushing*, *sticking*, *pulling*, and *squeezing* actions described above, tumor cells, acting either alone or in collaboration with one another, are able to invade and negotiate through the stromal extracellular matrix. Importantly, tumor cells apply these behaviors to varying degrees in a cell- and context-dependent manner, which results in diverse and dynamic migration phenotypes [68, 69]. As discussed, the invasive tumor stroma can contain ECM that exhibits diverse structural features and mechanical properties [27, 33, 106] that are presumed to provide extracellular control over tumor invasion *in vivo* [69]. Although the ECM influences proteolysis, cell-cell, and cell-matrix adhesions, as well as Rho GTPase-mediated cell mechanobiology [44, 95, 134, 165–167], the specific mechanisms by which 3D ECM cues integrate with intracellular signaling to co-regulate the invasive phenotype require further investigation.

Dissertation organization

The goals of this dissertation are to identify determinants of tumor cell invasiveness and define context-specific cellular mechanisms of invasion. To pursue this goal, our general approach is to study the process of 3D cell migration within rationally

designed 3D models that recapitulate extracellular and cellular elements of the tumor microenvironment hypothesized to influence invasive progression.

In Chapter 2, we begin to explore the role of stromal ECM microarchitecture in regulating the invasive phenotype of breast carcinoma cells. By tuning 3D collagen matrix structure independently of gel density, we show that cell-scale ECM microarchitecture trumps bulk-scale ECM density in regulating 3D cancer cell morphology and migration.

Having shown that ECM structure is a potent regulator of cell migration, we next set out to define the mechanisms by which a cell's local ECM microenvironment directs its 3D migration. Motivated by the prevalence of locally aligned 3D ECM within *in vivo* and *in vitro* tumor cell microenvironments, we study the cellular response to aligned structural ECM cues in Chapter 3. We present 3D cell spreading as an effective reductionist model of 3D cell migration, showing that extracellular matrix structure directs the transition from 3D matrix probing to 3D migration by locally controlling protrusion dynamics. Additionally, we find that matrix alignment induces FAK and Rac-dependent anisotropy of cell protrusions and spreading that accelerates and increases the efficiency of 3D cell migration, providing insight into mechanisms of contact guidance-mediated migration at the invasive front.

In Chapter 4, we examine the cellular mechanisms that enable cell migration within physiological collagen microtracks that mimic cell-scale channel-like gaps in native

mammary stroma. By comparing cell migration in 3D collagen matrix and microtracks, we demonstrate that 3D cancer cell migration mechanisms are context-specific and show that preformed paths of least resistance within the ECM considerably reduce the mechanistic threshold for cancer cell migration.

To explore the hypothesis that distinct tumor subpopulations may cooperate during invasion, we develop and study a heterotypic multicellular spheroid invasion model in Chapter 5. We demonstrate that malignant cells can act as leader cells to induce the 3D invasion of otherwise non-invasive follower cells. Additionally, we show that this follow-the-leader behavior is associated with and requires proteolytic and cell contractility-mediated matrix remodeling by leader cells.

In Chapter 6, we further explore themes of intratumor heterogeneity. We first develop a phenotypic cell sorting technique designed to purify cells based on their invasive fitness, and show that a parental breast cancer cell line contains distinct subpopulations of invasive and non-invasive cells. We demonstrate that these subpopulations show heritable, cell-intrinsic collagen-invasive and 3D migration behavior, and exploit these subpopulations to define molecular and phenotypic characteristics of invasive (and non-invasive) carcinoma cells.

In Chapter 7, we build off of our finding that malignant leader cells can induce invasive migration of otherwise non-invasive epithelial cells by studying the molecular and phenotypic response of non-transformed mammary epithelial cells to

stromal-like 3D collagen matrix. We demonstrate that exposure to collagen promotes mesenchymal gene expression and a mechanosensitive invasive epithelial phenotype. Additionally, we show that 3D collagen-dependent upregulation of MT1-MMP is required for invasive epithelial behavior, which also requires signaling through Src, PI3K, and Rac.

Chapter 8 includes conclusions and future directions of the work presented herein.

CHAPTER 2

BIOPHYSICAL CONTROL OF INVASIVE TUMOR CELL BEHAVIOR BY EXTRACELLULAR MATRIX MICROARCHITECTURE

This chapter was published in *Biomaterials* [55].

2.1 Abstract

Fibrillar collagen gels, which are used extensively in vitro to study tumor-microenvironment interactions, are composed of a cell-instructive network of interconnected fibers and pores whose organization is sensitive to polymerization conditions such as bulk concentration, pH, and temperature. Using confocal reflectance microscopy and image autocorrelation analysis to quantitatively assess gel microarchitecture, we show that additional polymerization parameters including culture media formulation and gel thickness significantly affect the dimensions and organization of fibers and pores in collagen gels. These findings enabled the development of a three-dimensional culture system in which cell-scale gel microarchitecture was decoupled from bulk gel collagen concentration. Interestingly, morphology and migration characteristics of embedded MDA-MB-231 cells were sensitive to gel microarchitecture independently of collagen gel concentration. Cells adopted a polarized, motile phenotype in gels with larger fibers and pores and a rounded or stellate, less motile phenotype in gels with small fibers and pores regardless of bulk gel density. Conversely, cell proliferation was sensitive to gel

concentration but not microarchitecture. These results indicate that cell-scale gel microarchitecture trumps bulk-scale gel density in controlling specific cell behaviors, underscoring the biophysical role of gel microarchitecture in influencing cell behavior.

2.2 Introduction

The tumor microenvironment exhibits intricate control over cancer progression by affecting the behavior of tumor cells both within the tumor mass as well as those that have invaded the surrounding stroma [1, 28]. A critical component of this microenvironment is the extracellular matrix (ECM), which is a complex and dynamic biopolymer network that provides tumor cells with integrated biophysical and biochemical cues that influence cell survival and differentiation signaling [105], cell-cell interactions, cell mechanics, tissue homeostasis [81, 168, 169], and ultimately, clinical outcome [170, 171]. Recently, there has been increasing interest in decoupling physical and chemical microenvironmental stimuli to determine their relative roles in cancer progression, and *in vitro* model systems of the tumor microenvironment have emerged as useful tools to study extracellular regulation of tumor cell behavior. While it is now widely accepted that physical ECM properties such as matrix stiffness are critical regulators of cell biology in two-dimensional (2D) *in vitro* environments [119–121, 172], the tumor microenvironment exhibits three-dimensional (3D) complexity and physical cell-scale features that obscure the distinction between biochemical and physical regulators of cell behavior [69, 173, 174]. Therefore, to fully appreciate how the ECM physically contributes to cancer progression, it will be critical to study tumor

cell behavior in biophysically and biochemicallydefined 3D *in vitro* model systems that recapitulate the *in vivo* microenvironment.

Extracellular matrix is a heterogeneous, fibrous biopolymer network with tissue-specific molecular composition, organization, and function [42, 173]. Notably, unlike ECM in 2D experimental systems, ECM in interstitial tissues exhibits three-dimensional cell-scale *microarchitecture* that is dependent primarily upon the dimensions and arrangement of the type I collagen structural fibers that comprise the matrix [175]. These collagen fibers can serve as adhesion substrates, steric barriers, and tracks, making them potent extracellular determinants of biophysical cell behavior [56, 140, 160, 176, 177]. Additionally, this collagen fiber network serves as both a transducer of exogenous forces and a source of endogenous micro-scale mechanical properties [178–180], and there is a growing body of experimental and theoretical work investigating the relationship among microarchitecture-derived cell-scale matrix mechanics, cellular biomechanics, and bulk mechanical properties [181–184]. Thus, since matrix microarchitecture is one of the most influential physically instructive components of the ECM, it is an ideal candidate for *in vitro* studies of biophysical regulation of cell behavior.

A number of strategies have been employed to study biophysical cell behavior as a function of matrix microarchitecture. Generally, cells are seeded within 3D matrices composed of various biomaterials including type I collagen, fibrin, basement membrane extract, or cell-derived matrix [185, 186] and the ECM and cells are

visualized with confocal or multiphoton microscopy [42]. Several groups have controlled 3D matrix microarchitecture and mechanical properties in these systems by tuning the density of collagen I or Matrigel, consistently finding that increased polymer concentrations yield gels with higher moduli, decreased pore size, and increased steric barriers. Interestingly, these studies have shown that cell mechanobiology and matrix remodeling [187, 188], morphogenesis [81, 105], and cell migration [57, 189, 190] are dependent upon these steric and mechanical properties of the 3D ECM as controlled by bulk gel concentration. To more accurately recapitulate tissue-specific ECMs, several researchers have monitored cell behavior in composite ECMs created by supplementing collagen scaffolds with additional ECM proteins such as fibronectin and laminin [57, 176], glycosaminoglycans (GAGs) such as hyaluronan and chondroitin sulfate [191], and the polysaccharide agarose [192]. While all of the above strategies changed the matrix microarchitecture and biophysical properties, these modifications also significantly altered the biochemical composition and bioactivity of the scaffolds, preventing the complete decoupling of physical and chemical microenvironmental stimuli.

To isolate ECM biophysics and biochemistry, several groups have developed strategies to tune the microarchitecture of pure type I collagen gels independently of bulk gel density and chemical modification. Collagen gel polymerization is initiated *in vitro* by raising an acidic solution of collagen to neutral pH, which causes soluble collagen to condense and crosslink laterally into fibrils that subsequently elongate to form an entangled meshwork of fibers. Fiber density, and thus, matrix

microarchitecture, depend upon the rate of this fibril self-assembly, which is influenced by parameters such as pH, temperature, and ionic strength [42, 173]. Importantly, collagen assembly is rapid at low or very high ionic strength [193], high pH [179], and high temperature conditions [181, 194], yielding gels with small pores and high fiber density. Conversely, assembly is slower under moderate ionic strength, low pH, and low temperature conditions, resulting in gels with relatively larger pores and sparse, but larger fibers. Recently, Yang et al. assessed glioma cell behavior within pure collagen gels polymerized at high (small pores) and low (large pores) temperatures, and found that pore size positively regulated invasive migration [194]. While such studies have begun to characterize exclusively biophysical determinants of cell behavior, the precise roles of matrix microarchitecture are not yet fully understood.

In this study, two critical parameters – gel thickness and media type – were explored as polymerization parameters used to alter gel microarchitecture independently of gel concentration, pH, temperature, and ionic strength. Gel microarchitecture was assessed with confocal reflectance microscopy (CRM) and quantified with spatial autocorrelation methods. Findings from acellular experiments were exploited to create a culture system that was used to probe the relative influences of cell-scale gel microarchitecture and bulk gel concentration on the migratory, morphological, proliferative, and ECM remodeling behavior of embedded MDA-MB-231 highly metastatic breast adenocarcinoma cells.

2.3 Materials and Methods

Cell culture

GFP-expressing MDA-MB-231 highly metastatic breast adenocarcinoma cells (Cell BioLabs, San Diego, CA) were cultured at 37°C and 5% CO_2 in Dulbecco's Modified Eagle Medium (DMEM; Invitrogen, Carlsbad, CA) supplemented with 2 mM L-glutamine, 10% Fetal Bovine Serum (Atlanta Biologicals, Norcross, GA), 0.1mM MEM Non-Essential Amino Acids, and 1% penicillin-streptomycin (Invitrogen).

Collagen gel preparation

Type I collagen was extracted from rat tail tendons (Pel-Freez Biologicals, Rogers, AR) via acid-solubilization, purified via centrifugation and lyophilization, and reconstituted in 0.1% acetic acid at 10 mg/ml. For acellular gel microarchitecture experiments, 10 mg/ml stock collagen solution was diluted to the desired final concentration by gently mixing with culture media or PBS on ice and neutralized to pH 7.0 with 1N NaOH. Gel solution was seeded into glass-bottom 24-well plates (MatTek, Ashland, MA). To determine the effects of media formulation on collagen gel microarchitecture, several base media types were used to dilute collagen: Dulbecco's Modified Eagle Medium (DMEM), Minimum Essential Medium (MEM), RPMI, Medium 199 (M199), and PBS (Invitrogen). To control gel thickness, either 250 µL or 1000 µL of neutralized gel solution was pipetted onto the glass bottom of 24-well plate. These volumes resulted in 'thin gels' (~1.5 mm thickness) and 'thick gels' (~5.3 mm thickness), respectively. Gels were incubated at 37°C for 60 minutes

for collagen polymerization after which they were overlaid with additional pre-warmed culture media or PBS.

To mitigate the biochemical effects of media composition on cell behavior, all cell experiments were performed in collagen gels made with complete DMEM as described above. After stock collagen solution was diluted to either 1.5 mg/ml or 3.0 mg/ml with ice-cold DMEM, the solution was neutralized with sodium hydroxide and a small volume (<5% total gel volume) of MDA-MB-231/GFP cell suspension was added such that gels would contain 5×10^4 cells/mL. As in acellular experiments, gel solutions were seeded into glass-bottom 24-well plates in 250 µL and 1000 µL volumes for 'thin gels' and 'thick gels', respectively. Gels were incubated at 37°C for 60 minutes for collagen polymerization after which they were overlaid with pre-warmed complete DMEM and cultured for 24 hours prior to time-lapse imaging and 48 hours prior to morphology measurements.

Quantitative characterization of collagen microarchitecture

Collagen gel microarchitecture was assessed with a Zeiss LSM700 confocal microscope on a Zeiss AxioObserver Z1 inverted stand equipped with a long working distance water-immersion C-Apochromat 40×/1.1 NA Zeiss objective and operated by ZEN software (v. 2010, Carl Zeiss MicroImaging GmbH, Jena, Germany). For confocal reflectance microscopy, a solid state 405 nm laser illuminated the gel and backscattered light from collagen fibers was captured through a 32-µm pinhole, giving 1-µm thick confocal slices. Pixel dwell time was 2.55 µs and four scans were averaged

per image. All gel microarchitecture imaging was performed near the gel center approximately 200 μm above the glass with imaging parameters kept consistent to enable quantitative comparison of gel microarchitecture across treatments.

The dimensions of collagen gel fibers and pores were quantified from CRM images using ImageJ (v. 1.43u, National Institute of Health, Bethesda, MD). Briefly, ImageJ's grid feature was used to overlay horizontal lines spaced 15 μm apart over CRM images. The line-drawing feature was used to measure the length of all collagen fibers that intersected these horizontal guide lines ($n \geq 300$ fibers / image). Pore diameter was measured as the horizontal distance between fibers intersecting the guide lines ($n \geq 200$ pores / image). The single-image distributions and averages of fiber length (L_{Fiber}) and pore diameter (D_{Pore}) were analyzed for $n = 4$ images per gel condition from two independent experiments.

Two-dimensional spatial autocorrelations were used to automatically analyze CRM images of acellular collagen gels. This technique has been used to analyze alignment of image features [195], as well as to describe the characteristic dimensions of image features in relatively isotropic images [179, 196], making it ideal for quantifying the microarchitecture of the gels in this study, which consist of randomly aligned fibers. A custom-written algorithm was used in the IDL data analysis environment (Exelis Visual Information Solutions, Boulder, CO) to calculate the two-dimensional autocorrelation function (ACF) of mean-normalized CRM images of collagen gels:

$$ACF(\alpha,\beta) = \frac{(1/MN)\sum_{x=1}^{M}\sum_{y=1}^{N} i(x,y)i(x+\alpha,y+\beta)}{\left[(1/MN)\sum_{x=1}^{M}\sum_{y=1}^{N} i(x,y)\right]^2} - 1,$$

where *i(x,y)* is the function representing an M × N pixel image, and α and β are the tessellation coordinates along the x and y axes, respectively. The resulting ACFs were fit to Gaussian surfaces and the $1/e^2$ half-width was defined as ω_{ACF}. Mean ω_{ACF} was interpreted as the characteristic collagen fiber dimension for n = 4 images per acellular gel condition from two independent experiments.

Analysis of cell behavior

Tumor cell behavior within thin and thick 1.5 mg/ml and 3.0 mg/ml gels collagen gels was monitored by time-lapse confocal fluorescence imaging with a Yokogawa CSU-X1 spinning disk confocal on a Zeiss AxioObserver Z1 inverted stand that was equipped with a Plan-Apochromat 10×/0.45 NA Ph1 Zeiss objective, Hamamatsu ORCA-ER camera, and a temperature-, humidity-, and CO_2-controlled microscope incubation chamber. Cells were imaged at 15-minute intervals for 20 hours using AxioVision software (v. 4.8, Carl Zeiss MicroImaging GmbH, Jena, Germany). At each time point, 11 sequential focal planes were acquired in 10-μm z-steps at 5-10 positions near the gel center approximately 200 μm above the glass. Projected z-stacks were used for assessment of cell morphology, migration, and mitosis, with 5-15 isolated cells distinguishable per field of view. Cell morphology was examined from z-projections acquired 48 h after cells were seeded in collagen gels. Using ImageJ, isolated cells were outlined and the cell morphology parameters circularity and aspect ratio were measured for n ≥ 75 cells per condition from three independent

experiments. Circularity describes the roundness of a cell, and is defined as ($4\pi \times$ Area / Perimeter^2). Aspect ratio describes a cell's elongation, and is defined as (Major axis / Minor axis) of the best-fit ellipse for a cell.

For cell motility analysis, four-dimensional confocal fluorescence datasets were projected in both the time- and z-dimensions to create 2D fluorescence images that represented cells' entire migration history through the 20 h experiment. Cell motility index was measured as the ratio of a cell's time-projected area to its initial area for $n \geq 30$ cells per condition from three independent experiments. To account for a variety of motile phenotypes, all cells in the field of view were analyzed as long as they did not interact with other cells or divide during the experiment. To control and account for cell division, complete culture media was replaced immediately prior to time-lapse experiments and cell proliferation rate was quantified from time-lapse videos as the ratio of cell divisions to the initial number of cells in the field of view for $n \geq 15$ fields of view per condition from three independent experiments.

Statistical analysis

Data was compared by two-way analysis of variance (ANOVA) with post-hoc Tukey HSD tests using JMP Pro software (v. 9.0.2, SAS Institute, Cary, NC). Collagen gel microarchitecture measurements including fiber length, pore diameter, and ωACF were compared across five media formulations and two gel thicknesses for Figure 2.3 and across two collagen concentrations and two gel thicknesses for Figure 2.4. Cell behavior parameters including circularity, aspect ratio, motility index, and cell mitosis

were compared across two collagen concentrations and two gel thicknesses. All data is reported as mean ± SEM; statistical significance was considered with $p < 0.05$.

2.4 Results

Confocal reflectance microscopy of thickness- and media-type dependent collagen gel microarchitecture

Collagen gels are comprised of interconnected networks of micron-scale fibers and pores whose properties are largely determined during gel polymerization. Since fibers reflect focused laser light due to refractive index mismatch at interfaces between fibers and aqueous pores, confocal reflectance microscopy (CRM) is useful for nondestructively visualizing the microarchitecture of collagen gels. Here, CRM was used to probe this microarchitecture in 1.5 mg/ml collagen gels made with different media types and in two thicknesses. CRM images showed qualitatively dissimilar fiber and pore organization between thin and thick gels (Figure 2.1; top and bottom, respectively). Generally, thin gels consisted of a tight meshwork of short fibers while thick gels contained larger and more irregular pores as well as longer and more bundled fibers as compared to their thin counterparts for all media formulations studied. While thin gels appeared more homogeneous and showed little variation among media formulations, thick gels were highly heterogeneous and showed increased variance among media types.

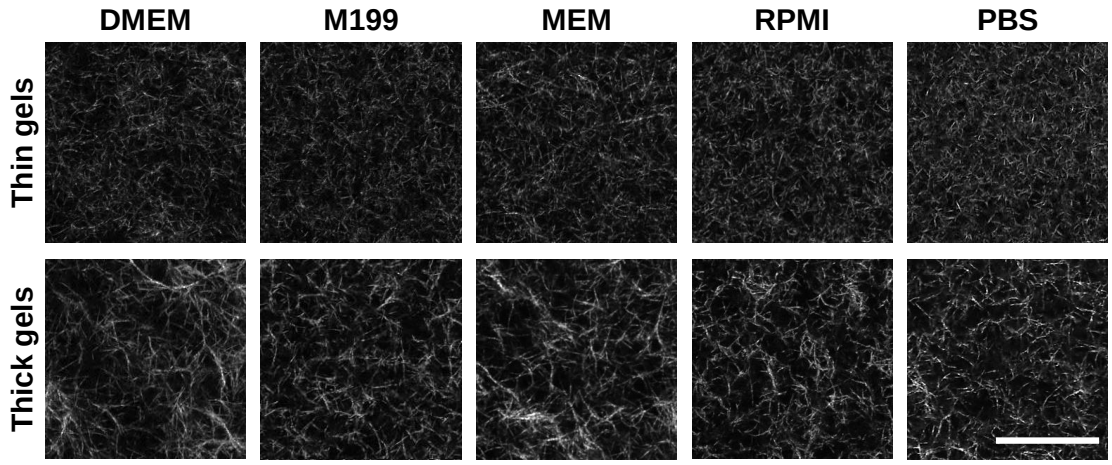

Figure 2.1. Confocal reflectance microscopy reveals differential collagen gel microarchitecture in response to media formulation and gel thickness. Confocal reflectance images (40×, 2× zoom) of 1.5 mg/ml collagen gels made with different media formulations and in two thicknesses. All gels were polymerized at 37°C in a glass-bottom 24-well plate. "Thin" gels (top) were made with 250 µL of gel solution and were ~1.5 mm thick; "thick" gels (bottom) were made with 1000 µL of gel solution and were ~5.3 mm thick. Each image is a 1-µm thick slice taken 200 µm into collagen gel. Scale bar: 50 µm.

Quantitative assessment of collagen gel microarchitecture

To quantitatively compare ECM microarchitecture across treatment groups, CRM images of collagen gels were analyzed by measurement of fiber and pore dimensions as well as by automated spatial autocorrelation for thin (top) and thick (bottom) 1.5 mg/ml gels made with MEM (Figure 2.2A). These images were used to calculate 2D autocorrelation functions (Figure 2.2B). Since the ACF can be approximated by a 2D Gaussian surface, the $1/e^2$ radius was extracted and is shown as the red outline in Figure 2.2B. The mean $1/e^2$ radii, or the mean ω_{ACF} lengths, were 2.0 µm and 5.8 µm for the thin and thick gels, respectively. Collagen fiber lengths and pore diameters were calculated for thin and thick gels (Figure 2.2C). Mean fiber length, L_{Fiber}, was 4.6

μm and 8.6 μm and mean pore diameter, D_{Pore}, was 2.6 μm and 4.0 μm for the thin and thick gels in Figure 2.2A, respectively.

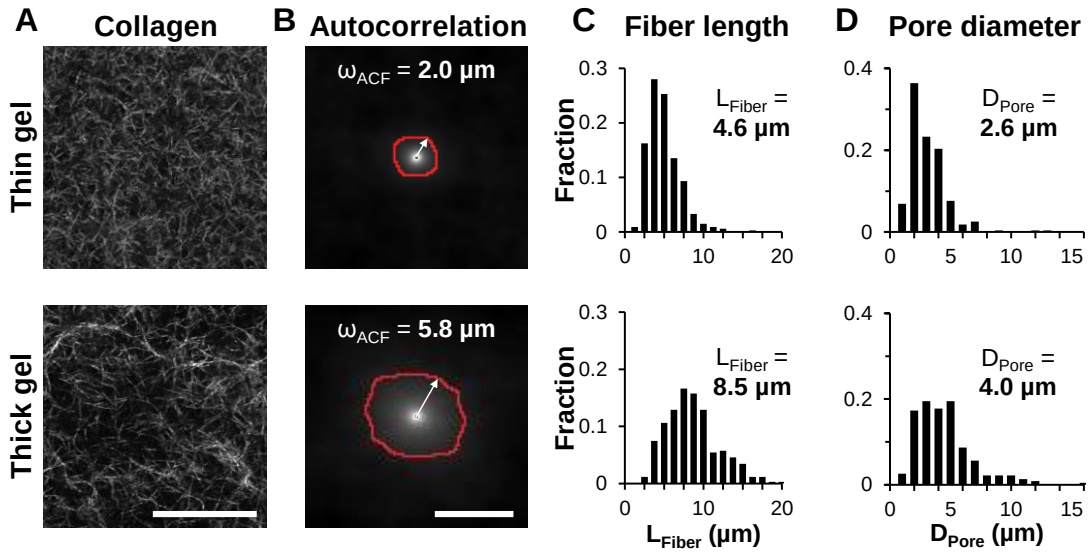

Figure 2.2. Quantitative analysis of collagen gel microarchitecture with image autocorrelation analysis. (A) Representative confocal reflectance images of thin (top) and thick (bottom) collagen gels made with MEM. Scale bar: 50 μm. **(B)** Autocorrelation functions (from Equation 1) of the confocal reflectance images in A. Red outlines represent the $1/e^2$ radii, or ωACF characteristic lengths, whose means were 2.0 μm and 5.8 μm for the thin and thick gels, respectively. Scale bar: 10 μm. **(C)** Distributions of collagen fiber lengths in A, whose means were 4.6 μm and 8.5 μm for the thin and thick gels, respectively (>300 fibers measured per image). **(D)** Distributions of pore diameters in A, whose means were 2.6 μm and 4.0 μm for the thin and thick gels, respectively (>200 pores measured per image).

To determine the effects of media formulation and gel thickness on collagen gel microarchitecture, the analyses illustrated in Figure 2.2B-D were applied to CRM images of collagen gels for each condition and mean L_{Fiber}, and D_{Pore}, and ω_{ACF} were averaged for n = 4 gels per condition from two independent experiments. Increased gel thickness induced an approximately two-fold increase in mean collagen fiber length across all media types (Figure 2.3A). Average pore diameters were approximately 50% larger in thick gels than in thin gels for all media types (Figure 3B). Similarly,

the ω_{ACF} characteristic lengths calculated from automated autocorrelation analysis were larger in thick gels than in thin gels for all media types (Figure 3C). For each parameter, a statistically significant difference was observed between media-matched thin and thick gels by two-way ANOVA.

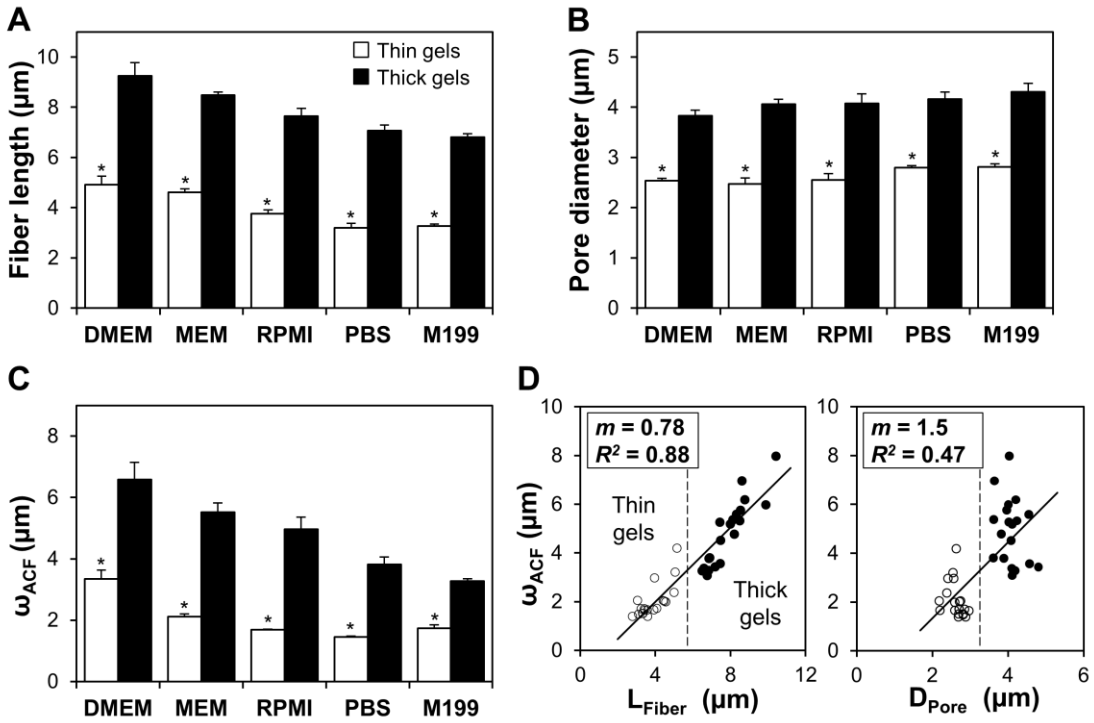

Figure 2.3. Sensitivity of collagen gel microarchitectural features to media formulation and gel thickness. (A) Mean collagen fiber lengths and **(B)** pore diameters for thin (open bars) and thick (filled bars) collagen gels made with different media formulations. **(C)** Mean ω_{ACF} characteristic lengths ($1/e^2$ radii from autocorrelation function) for thin (open bars) and thick (filled bars) collagen gels made with different media formulations; n = 4 images from two gels per condition; * indicates statistically significant difference between thin and thick media-matched gels. **(D)** Comparison of each image's mean fiber length (L_{Fiber}, left) and mean pore diameter (D_{pore}, right) with its mean ω_{ACF} characteristic length; dashed vertical lines graphically differentiate thin gels (open circles) from thick gels (filled circles); slopes and R_2 values for best-fit lines are provided.

While gel thickness significantly affected each of the three measured collagen gel microarchitecture parameters, media type alone did not induce any statistically significant change in pore diameter within thickness groups (Figure 2.3B; statistics not shown in figure). However, both fiber length (Figure 2.3A) and autocorrelation characteristic length (Figure 2.3C) were sensitive to gel thickness as well as media type. For example, within the thick gel group, there was a statistically significant difference in mean fiber length and ω_{ACF} between gels made with DMEM and gels made with RPMI, M199, and PBS for thin and thick gels (statistics not shown).

Mean ω_{ACF} characteristic length correlated well with mean fiber length for all conditions when assessed on a per-image basis ($R^2 = 0.88$) as both ω_{ACF} and fiber length showed comparable ranges of values for all gel images analyzed. However, ω_{ACF} correlated less strongly with pore diameter ($R^2 = 0.47$) as the latter exhibited a biphasic thickness-dependent, media type-independent response (Figure 2.3D). However, correlation analysis could be used to differentiate gels by thickness, with gels clustered on the left (thin gels) and right (thick gels) of the dashed vertical lines (Figure 2.3D).

Behavior of tumor cells within collagen gels

To investigate the effect of collagen gel microarchitecture on tumor cell behavior, GFP-expressing MDA-MB-231 cells were sparsely seeded into collagen gels and were monitored by confocal microscopy. To control for biochemical effects of media composition on cell behavior, only gels made with complete DMEM were used. To

mitigate non-microarchitecture-related effects of gel thickness and probe the relationship between collagen gel concentration and microstructure, thin and thick 1.5 mg/ml gels as well as thin and thick high concentration 3.0 mg/ml gels were used. Confocal reflectance microscopy of cell-free areas of gels showed that both thin and thick 3.0 mg/ml gels resemble thin 1.5 mg/ml gels, with short collagen fibers organized into tight lattices, while thick 1.5 mg/ml gels contain larger pores and longer fibers (Figure 2.4A; pore structures are highlighted with yellow dashed lines). Statistically significant increases in mean L_{Fiber}, and D_{Pore}, and ω_{ACF} were observed for thick 1.5 mg/ml gels compared to all other gel conditions by two-way ANOVA (Figure 2.4B).

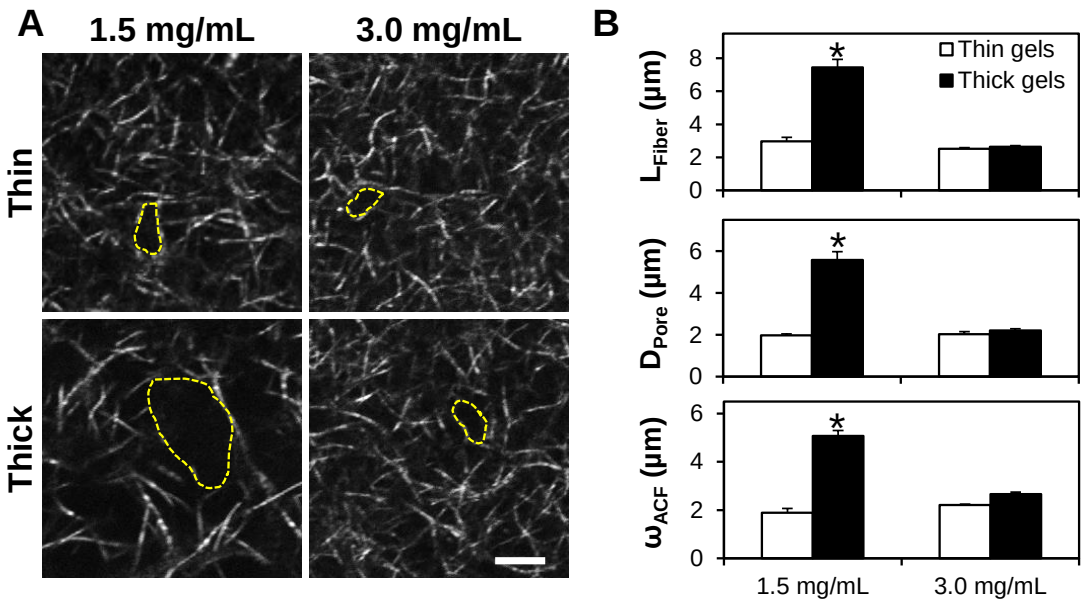

Figure 2.4. Collagen gels for cell behavior studies. (A) High-power (40×, 3× zoom) confocal reflectance images of 1.5 mg/ml (left) and 3.0 mg/ml (right) collagen gels polymerized in thin (top) and thick (bottom) volumes. Representative pores are highlighted (dashed yellow line). **(B)** Microarchitectural features were calculated as previously shown for thin (open bars) and thick (filled bars) gels; n = 4 images from two gels per condition; * indicates statistically significant difference between thick 1.5 mg/ml gels and all other conditions. Scale bar: 5 µm.

Cell morphology

Because gel microarchitecture was consistent between thin and thick 3.0 mg/ml gels, these gels were used as controls for macro-scale effects of gel thickness such as nutrient availability and diffusion. Thus, using these gels together with thin and thick 1.5 mg/ml gels, cell behavior in response to micro-scale physical ECM traits could be studied in relative isolation. MDA-MB-231/GFP cells were cultured within collagen gels for 48 h. To capture population diversity in cell morphology, all single cells were analyzed in each z-projected field of view for each gel condition. Circularity describes the roundness of a cell and ranged from 0 to 1, with 1 denoting cells with rounded morphologies. Aspect ratio describes the elongation of a cell and was larger than 1, with increasing values denoting cells with increasingly polarized morphologies. These parameters were used together to describe the observed cell morphologies, which were distributed between two general morphology categories: 1) rounded, with high circularity and low aspect ratio (Figure 2.5A; panels iii-iv), and 2) bipolar (elongated), with low circularity and high aspect ratio (Figure 2.5A; panels i-ii). The distributions of cell morphologies observed in thin 1.5 mg/ml gels, thin 3.0 mg/ml gels, and thick 3.0 mg/ml gels were similar (Figure 2.5). Additionally, cells embedded within these gels exhibited similar mean circularities and aspect ratios since no statistically significant differences among treatment groups were detected for either metric by two-way ANOVA (Figure 2.5B,C; insets). These generally low aspect ratios and mid-to-high circularities are consistent with rounded to multipolar morphologies (Figure 2.5A; panels iii-iv). In contrast, cells in thick 1.5 mg/ml gels showed low circularities

and an approximately two-fold enhancement in aspect ratio (Figure 2.5B), consistent with increased bipolar cell spreading (Figure 2.5A; panels i-ii).

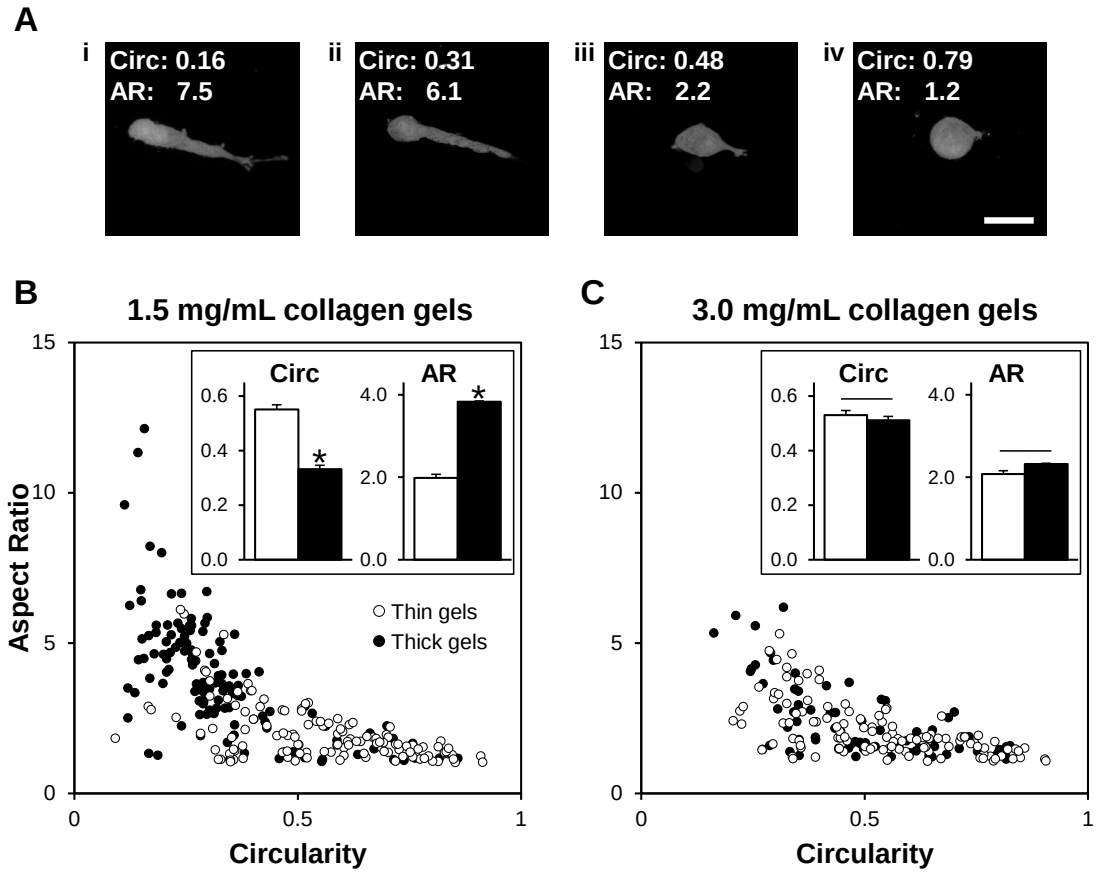

Figure 2.5. Collagen gel microarchitecture impacts cell morphology. (A) Representative z-projected images of embedded MDA-MB-231/GFP cells demonstrate bipolar (i-ii) and rounded (iii-iv) morphologies. Scale bar: 25 μm. Morphologies of MDA-MB-231/GFP cells were determined by analyzing the circularity (x-axis) and aspect ratio (y-axis) of cells embedded in **(B)** 1.5 mg/ml and **(C)** 3.0 mg/ml gels; each data point represents a single cell. Circularity ($4\pi \times$ area / perimeter^2) describes the roundness of a cell and can range from 0 to 1, with 1 denoting circular cells; aspect ratio (major axis / minor axis) describes the elongation of a cell and is larger than 1, with increasing values denoting increasingly polarized morphology. Insets: Mean morphological parameters for each concentration and gel thickness condition; $n \geq 75$ cells per condition from three separate experiments; * indicates statistically significant difference between thick 1.5 mg/ml gels and all other conditions.

Mean circularity and aspect ratio for cells in these gels were significantly different from morphology parameters of cells in all other gel conditions (Figure 2.5B,C; insets). Notably, because of the relationship between aspect ratio and circularity, it was impossible for a cell to have both high aspect ratio and high circularity, resulting in the given distributions of morphologies (Figure 2.5).

Cell motility

Since cell morphology and migration are closely interrelated biophysical cell behaviors, spontaneous random migration of cells embedded within collagen gels was monitored for 20 hours with time-lapse confocal microscopy. Representative confocal z-projections of an isolated MDA-MB-231/GFP cell migrating through collagen extracellular matrix at 0 h, 5 h, 10 h, and 20 h show that motile cell behavior consists of both random cell protrusions and cell body translation, both of which contribute to the 20-hour fluorescent "trail" of a migrating cell (Figure 2.6A). Motility index was calculated as the ratio of a cell's time- and z-projected area, A_{Sum}, (Figure 2.6A; bottom panel) to its initial area, A_i (Figure 2.6A; top panel). Cells in thin 1.5 mg/ml gels and thin and thick 3.0 mg/ml gels extended many protrusions (data not shown), but they did not exhibit substantial cell body translation, resulting in relatively low motility indices (Figure 2.6B; no statistically significant differences among treatment groups). Conversely, cells in thick 1.5 mg/ml gels were both protrusive and highly motile, which contributed to a statistically significant two-fold increase in motility index for cells in these gels over the other three gel conditions (Figure 2.6B). To ensure that gel microarchitecture-dependent differences in cell migration were

independent of cell proliferation, only isolated cells that did not divide during the 20-hour analysis were analyzed.

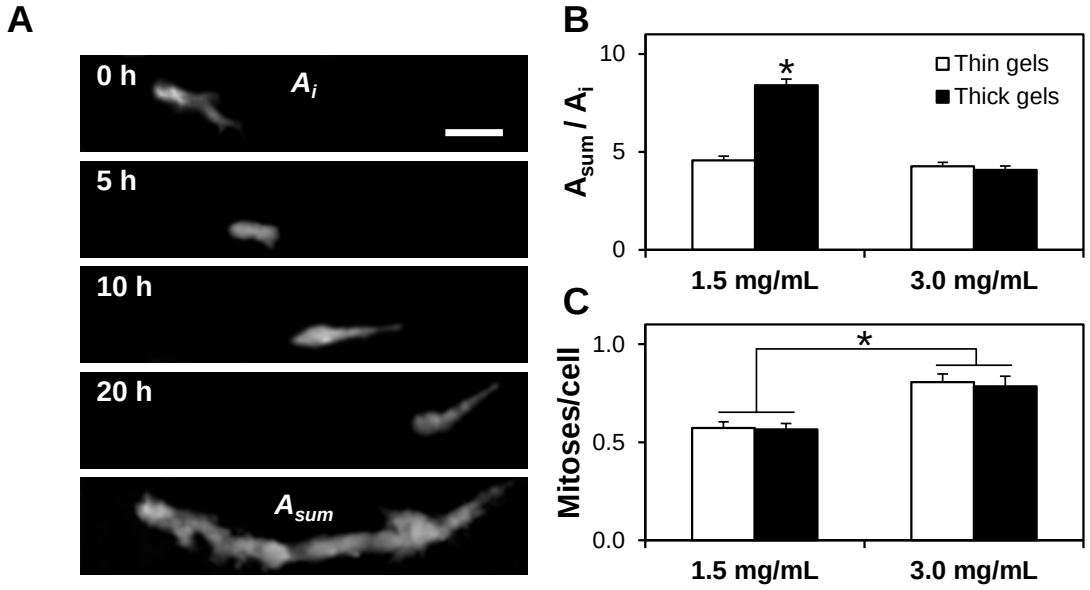

Figure 2.6. Influence of collagen gel microarchitecture on cell migration and proliferation. (A) Representative time-series of a MDA-MB-231/GFP cell migrating through a thick 1.5 mg/ml 3D collagen gel. Time points (0 – 20 h) are projections of confocal z-stacks; the final panel is the time-projection of all z-stacks, representing the migration history of the cell. Scale bar: 50 μm. **(B)** Migration index was calculated as the ratio of a cell's time-projected area to its initial area (A_{sum}/A_i) for cells randomly migrating within thin (open bars) and thick (filled bars) 1.5 mg/ml and 3.0 mg/ml gels; $n \geq 30$ cells per condition; * indicates statistically significant difference between thick 1.5 mg/ml gels and all other conditions. **(C)** Cell proliferation was assessed from time-lapse videos of cells embedded within thin (open bars) and thick (filled bars) 1.5 mg/ml and 3.0 mg/ml gels; $n \geq 15$ fields of view per condition; * indicates statistically significant difference between 1.5 mg/ml and 3.0 mg/ml collagen gels.

Cell proliferation

To further characterize the effect of 3D collagen gel microarchitecture on cell behavior, cell proliferation rate was quantified from time-lapse datasets. While gel thickness did not affect the frequency of cell division, gel concentration induced a statistically significant difference in cell proliferation rate, with 3.0 mg/ml gels

showing an approximately 50% increase in cell proliferation frequency over 1.5 mg/ml gels (Figure 2.6C).

2.5 Discussion

Collagen I hydrogels are widely used as *in vitro* ECM models to study tumor cell behavior in three-dimensional microenvironments because they possess biophysical and biochemical properties that can be tuned to match those of the interstitial tissues into which tumor cells invade [42]. Recently, there has been intense interest in determining how ECM properties such as stiffness, fiber alignment, and porosity regulate cell phenotype and can influence invasive tumor behavior [27, 57, 81, 82, 105, 106, 158, 190, 191]. However, despite these physical properties being tied to matrix microarchitecture [42, 179, 180, 183], it remains to be determined how ECM microarchitecture alone can impact tumor cell biology. Here, collagen matrix structure was controlled independently of gel concentration by modulating gel thickness. Notably, preliminary studies with metastatic breast cancer cells show that tumor cell behaviors including morphology and migration can be regulated in a strictly microarchitecture-dependent manner.

Collagen gel microarchitecture is sensitive to gel thickness and media composition

In this study, low concentration 1.5 mg/ml collagen gels exhibited gel thickness-dependent differences in microarchitecture: thin gels (~1.5 mm thickness) were composed of tight networks of short, regular fibers while thick gels (~5.3 mm

thickness) contained looser, more irregular networks consisting of longer and more substantially bundled fibers. Quantitative image analysis showed that both thin and thick gels contained collagen fibers between 0 – 10 μm in length and pores between 0 – 5 μm in diameter, but only thick gels contained fibers and pores with dimensions exceeding these ranges, resulting in statistically significant differences in mean fiber length, pore diameter, and, thus, the ω_{ACF} characteristic length between thin and thick media type-matched gel replicates. Notably, the results of this study were consistent with previous reports showing that the rate of collagen fibril self-assembly and thus, fiber dimensions and organization, can be influenced by polymerization temperature [181, 194] and/or treatment with pepsin, which removes cross-link mediating telopeptides [42]. As expected, thin collagen gels exhibited fiber and pore structures similar to those of gels rapidly polymerized at 37°C, while thick gels contained structural features analogous to gels polymerized slowly at 4-24°C [181]. Indeed, once 4°C gel solution was transferred to the culture plate and moved to 37°C, thin gels polymerized faster than thick gels (data not shown), presumably due to limited heat transfer in thick gels. The rapid increase in solution temperature in thin gels caused collagen monomers to quickly assemble, resulting in many polymer nucleation sites and thus, small pores and short fibers. Conversely, the relatively slow increase in collagen solution temperature in thick gels caused an impeded assembly phase, resulting in greater interfibrillar spacing, longer and thicker fibers, and increased heterogeneity.

While media type alone elicited statistically significant differences in fiber length and ω_{ACF} among some gel formulations (DMEM versus RPMI, M199, and PBS, for example), it did not significantly affect pore diameter within thickness groups (statistics among media types not shown in Figure 2.3 for clarity). These results suggest that the temperature-dependent effects of gel thickness largely determine interfibrillar spacing and gel porosity, and that media composition, through ionic strength and/or the presence of other compounds during gelation [193], can affect fiber dimensions following assembly initiation. Given the variability in collagen fiber dimensions and ω_{ACF} among gels made with different base media types, these results demonstrate how sensitive the micro-scale structural features of collagen matrices are to polymerization conditions, and highlight the importance of monitoring gel microarchitecture in 3D ECM model systems.

Previously, Raub et al. demonstrated the utility of two-dimensional spatial image correlation spectroscopy for measuring the characteristic dimensions of isotropic distributions of collagen fibers and matrix pores [179]. The authors modulated polymerization pH to tune gel microarchitecture and found that the image autocorrelation length parameter could be used to differentiate among matrix structures. In this study, mean ω_{ACF} showed a strong dependence on gel thickness, with thick gels exhibiting an approximately two-fold increase in characteristic length over their thin counterparts. Since ω_{ACF} is based upon image feature dimensions, it was expected that each image's ω_{ACF} would scale with its mean fiber length. The relatively poor correlation between ω_{ACF} and pore diameter was also expected since

pore size showed little dependence upon media type. These results support image correlation spectroscopy as an effective technique by which to automatically probe gel microarchitecture and differentiate between gel thickness-dependent matrix structure. Notably, the relatively small variability in mean fiber, pore, and ω_{ACF} measurements within treatment groups suggests that these metrics together comprise a suitable microarchitectural analysis scheme that could be employed to ensure gel consistency and validate experimental design of 3D collagen microenvironments for *in vitro* studies.

The finding that 3.0 mg/ml gels did not exhibit thickness-dependent microarchitecture is supported by previous work showing that higher concentration collagen gels polymerize more rapidly due to increased monomer availability [184]. The polymerization of high concentration gels was apparently insensitive to the subtle temperature differences in the gel thickness model, making thick and thin 3.0 mg/ml gels effective controls for non-microarchitecture related effects of gel thickness such as diffusion. Notably, the structural resemblance of thin and thick 3.0 mg/ml gels to thin 1.5 mg/ml gels – small pores and small, regular fibers – allowed gel microarchitecture to be decoupled from bulk gel concentration in cell experiments such that *only* thick 1.5 mg/ml gels contained pores larger than 5 μm in diameter and long, sparse fibers.

Microarchitectural control of tumor cell behavior

Recently, the role of the three-dimensional physical microenvironment in influencing cell behaviors such as adhesion, morphology, matrix remodeling, and migration has become a topic of intense interest as molecular mechanisms of 3D mechanotransduction – and 3D cell behavior in general – are increasingly understood [42, 52, 129, 173]. Biophysical regulation of cell behavior has garnered particular interest in the cancer mechanobiology community due to tumor-associated changes in ECM structure and mechanics [27, 42, 106]. In this study, matrix microarchitecture was controlled independently of bulk gel concentration using a novel model system to investigate how this critical, yet understudied, ECM parameter can impact the behavior of embedded metastatic MDA-MB-231/GFP cells. Quantitative morphology analysis showed that thick 1.5 mg/ml gels (loose matrices) were substantially more permissive to bipolar cell spreading than thin 1.5 mg/ml gels and all 3.0 mg/ml gels (dense matrices). These findings are consistent with previous work with fibroblasts showing that cells within low concentration collagen gels exhibit more elongated morphologies than those within high concentration gels [187]. Notably, while all gels in this study contained cells with rounded and multipolar morphologies, only loosely networked gels contained an additional subpopulation of polarized cells. These results suggest that structural properties of 3D ECM such as fiber and pore size can selectively facilitate bipolar, uniaxial cell spreading, which may enable other biophysical cell behaviors that are closely linked to morphology, such as migration [2, 91, 143].

Time-lapse microscopy revealed that the random migration of MDA-MB-231/GFP cells within collagen gels was sensitive to gel microarchitecture, with loose ECM (thick 1.5 mg/ml gels) more permissive to migration than dense ECM. While this study is the first to demonstrate that collagen gel thickness-dependent matrix microarchitecture can regulate cell migration, these findings are consistent with previous reports that cell migration is more efficient within gels with larger pores [158, 176, 191, 194]. In the present study, all gels contained pores that were 1-5 μm in diameter, but enhanced cell migration was observed only in thick 1.5 mg/ml gels, which contained pores with diameters greater than 5 μm. This apparent pore size threshold may be linked to nuclear deformability since pores larger than 5 μm would provide minimal steric resistance to the cell nucleus, which can be 5-15 μm in diameter in 3D microenvironments [164]. Interestingly, while cells in small-pore gels exhibited limited cell body translation, these cells continuously extended and retracted random pseudopodial protrusions (data not shown), suggesting that, even in a biophysically restrictive 3D matrix, cells were still actively probing their microenvironment [85]. Together, these results imply that collagen gel thickness-dependent matrix microarchitecture regulates the three-dimensional migration of MDA-MB-231 cells through steric hindrance at matrix pores. Further analysis of behaviors such as matrix adhesion [105, 187], remodeling [129, 187, 188], and degradation [158, 197], all of which are sensitive to bulk matrix density, may provide additional insight into specific molecular mechanisms underlying the microarchitecture-dependent cell behaviors reported here.

A critical finding of this study is that bulk gel density does not necessarily reflect the cell-scale matrix density that cells perceive. By modulating gel thickness, it is possible to create low-density collagen gels that physically resemble high-density gels at the cellular scale. Interestingly, while microscale gel structure significantly affected cell morphology and migration regardless of gel concentration, cell proliferation was concentration-dependent, with cells cultured in 3.0 mg/ml gels exhibiting a significant increase in proliferation rate over those cultured in 1.5 mg/ml gels. Consistent with this finding, it has been shown that increased matrix density enhances proliferation in 3D due to an increase in matrix stiffness that accompanies increased density [105]. Such results suggest that the model system described herein could be used to study the complex relationship among matrix microarchitecture, matrix mechanics, and their associated matrix biochemistry to better understand coordinated physicochemical cell signaling by the extracellular matrix.

CHAPTER 3

MECHANISMS OF 3D CANCER CELL MIGRATION GUIDANCE BY LOCAL ECM ALIGNMENT

Portions of the data in this chapter were contributed by Karen Martin and Zachary Goldblatt.

3.1 Abstract

Cell migration in 3D microenvironments is sensitive to extracellular matrix properties including fibrillar microarchitecture, but the mechanisms that regulate migration guidance by 3D matrix features remain unclear. To examine the mechanisms underlying the cell migration response to 3D matrix alignment, we utilized early 3D cell spreading as a reductionist model for the complex process of 3D cell migration. We found that ECM alignment induced spatial anisotropy of matrix probing by promoting protrusion frequency, persistence, and lengthening along the axis of matrix alignment and suppressing protrusion dynamics orthogonal to alignment. This preference for on-axis behaviors continued throughout cell spreading and migration within aligned 3D matrix. Ultimately, cells within aligned ECM exhibited accelerated elongation, front-rear polarization, and migration relative to cells in random ECM, indicating that coordination of cues from the ECM promotes migration efficiency. Inhibition of FAK and Rac1 signaling abolished matrix alignment-induced behavioral

anisotropy, implicating adhesive and protrusive signaling as key mediators of cell migration guidance by 3D matrix structure.

3.2 Introduction

Cell migration through 3D ECM is a fundamental feature of many physiological and pathological processes including development, wound healing, and tumor cell invasion. Efficient motility depends on precise coordination of cell protrusion, adhesion, and contractility mechanisms, which are largely governed by intracellular signaling networks [198]. However, 3D migration is also sensitive to local extracellular cues, which can integrate with established intracellular signaling to influence migration mode and efficiency [69] and impart migration directionality by inducing cell polarity [143]. Such extracellular guidance of cell migration in 3D environments can be attributed to soluble factors that induce chemotaxis [198, 199] as well as physical ECM cues including interfacial boundaries [200], gradients of adhesive ligands [201] and matrix stiffness [202], and local matrix alignment [56, 203]. Notably, tumor progression is associated with biochemical, mechanical, and structural changes in the stromal ECM that are presumed to impact invasive cancer cell migration [13, 39, 40, 204], and understanding the mechanisms by which these changes affect tumor cell behavior is critical.

ECM linearization and alignment resulting from cell traction force generation [56, 129, 205] can drive several processes including epithelial tissue branching [206] and disruption [207] and invasive migration into the stroma [27, 144, 208, 209]. Since the

stromal matrix surrounding tumors is highly linearized as compared to the ECM of normal epithelial tissue [27, 106], understanding the molecular and cellular mechanisms by which cancer cells detect and respond to locally aligned matrix could inform therapeutic strategies to target stromal invasion. While the effects of 3D matrix alignment and contact guidance on cell morphology and migration have been appreciated for some time [160, 203, 209–211], our mechanistic understanding of these cellular responses to matrix alignment remains limited.

In this study, we introduced early 3D cell spreading as a reductionist model for deciphering the role of the ECM in regulating 3D cell migration. By examining the morphodynamics of early 3D cell spreading in random and aligned 3D collagen matrix, we defined the subcellular behaviors that mediate 3D contact guidance. We found that matrix alignment accelerates and spatially directs spreading, cell polarization, and migration by promoting "on-axis" and suppressing "off-axis" protrusion and cell body displacement. Through pharmacological screening of cell motility regulators, we found that this matrix alignment-induced behavioral anisotropy was dependent on focal adhesion kinase (FAK) and Rac1 signaling.

3.3 Materials and Methods

Cell culture and reagents

MDA-MB-231 breast adenocarcinoma cells (HTB-26; ATCC, Rockville, MD) were maintained in DMEM (Life Technologies, Grand Island, NY) supplemented with 10% FBS (Atlanta Biologicals, Flowery Branch, GA), 100 U/ml penicillin, and 100 µg/ml

streptomycin (Life Technologies). GFP-expressing MDA-MB-231 (AKR-201; Cell Biolabs, San Diego, CA) were maintained in complete MDA-MB-231 medium as described above supplemented with 0.1 mM MEM nonessential amino acids (Life Technologies). MDA-MB-231 cells were transiently transfected with GFP-Lifeact as previously described [41]. All cell culture and time-lapse imaging was performed at 37°C and 5% CO_2.

The following reagents were used for fluorescent imaging: polyclonal anti-pFAK^{Y397} (3283; Cell Signaling Technology, Danvers, MA); Alexa Fluor 568-conjugated anti-rabbit (A-11036, Life Technologies); Alexa Fluor 488-conjugated phalloidin (Life Technologies). The Rac1 inhibitor NSC23766 (50 μM; Santa Cruz Biotechnology, Santa Cruz, CA), FAK inhibitor PF573228 (5 μM; Santa Cruz Biotechnology), Src kinase inhibitor PP1 (10 μM; Sigma-Aldrich, St. Louis, MO), PI3K inhibitor LY294002 (20 μM; EMD Millipore, Billerica, MA), and β1 integrin blocking antibody 4B4 (10 μg/ml; Beckman Coulter, Brea, CA) were used as described below.

In vivo and in vitro invasion assays

A murine mammary cancer model was used as previously described [41, 212]. Mice were maintained according to Cornell University Animal Care guidelines, and methods were approved by the Cornell Institutional Animal Care and Use Committee (protocol 2009-0101; R.M. Williams). Briefly, GFP-expressing MDA-MB-231 cells were injected into the cleared mammary fat pad and allowed to form orthotopic tumors for 3 weeks, at which point tumors and the surrounding stroma were excised and the

tumor-stroma interface was imaged *ex vivo* as described below. The multicellular spheroid collagen invasion assay was performed using GFP-expressing MDA-MB-231 cells as described [144].

Characterization of cell morphodynamics and migration from time-lapse imaging

Cells were seeded within 1.5 mg/ml collagen matrices prepared from acid-solubilized type I rat tail tendon collagen as previously described [41]. Following polymerization, matrices were overlaid with culture medium and immediately transferred to temperature-, humidity-, and CO_2-controlled microscope incubation chambers for time-lapse studies. For inhibitor studies, cells were pretreated with inhibitors in suspension for 30 min prior to collagen seeding and polymerized matrices were overlaid with culture medium supplemented with appropriate inhibitors. Time-lapse, phase contrast imaging was performed using a Zeiss Axio Observer Z1 inverted microscope using a Plan-Apochromat 10×/0.45 NA or a Plan-Neofluar 20×/0.4 NA equipped with a Hamamatsu ORCA-ER camera and AxioVision software (version 4.8, Carl Zeiss Microscopy). All images were acquired > 200 μm above the bottom surface of 3D matrices. All image analysis was performed using ImageJ (version 1.49b, National Institutes of Health, Bethesda, MD).

For detection of subcellular protrusion dynamics, images were acquired at 2-min intervals starting immediately after matrix polymerization. Protrusion angle (from cell body surface into surrounding matrix), length, and lifetime were recorded for all protrusions generated by a cell. For quantification of protrusion dynamics during early

spreading, protrusions were monitored for 3-4 h or until the cell extended a major polarizing protrusion. Cell morphodynamics were analyzed by manually tracing cell contours from time-lapse image series. Aspect ratio and circularity were jointly used to describe cell morphology [55], and cell elongation angle was defined by the angle of an elongated cell's major axis. Cell body positions were manually tracked from time-lapse image series to measure stepwise cell body movement speeds and angles. A cell was considered motile if it displaced at least one cell diameter (~ 15 μm) during a 2-h period, and 'motile fraction' was defined as the ratio of motile cells to total cells. Single cell stepwise migration speed and orientation were measured between 8-24 h after collagen seeding.

Collagen matrix alignment

Collagen matrix was aligned using magnetic field-induced flow of magnetic beads during matrix polymerization [56, 213]. Paramagnetic polystyrene beads (PM-20-10; Spherotech, Lake Forest, IL) were incorporated into cell-containing collagen solution at 1% (v/v). This solution was loaded into one well of a custom cell culture device consisting of polydimethylsiloxane (PDMS) walls bonded to coverglass on the bottom and ends. The opposing well was filled with cell-containing collagen solution without beads to serve as a matched random matrix control. The device was positioned adjacent to a neodymium magnet (BZX0Y0X0-N52; K&J Magnetics, Pipersville, PA) with surface field strength > 4kG and matrices were polymerized at room temperature for 30 min before being overlaid with culture medium.

Confocal imaging of cells and extracellular matrix

Confocal fluorescence and reflectance imaging of *ex vivo* and *in vitro* matrix-embedded cells was performed using a Zeiss LSM700 confocal microscope operated by ZEN software (version 2010, Carl Zeiss) and equipped with a C-Apochromat 40×/1.1 NA long working distance water immersion lens. Time-lapse confocal imaging of Lifeact-GFP-transfected MDA-MB-231 cells was performed 30-60 minutes after matrix polymerization to allow for sample stabilization. Following the indicated length of culture, aligned matrix samples were fixed with 3.7% formaldehyde, rinsed, blocked, and stained with anti-pFAK^{Y397} antibody for immunofluorescence imaging. Lifeact-GFP and fluorescent adhesion images are maximum intensity projections of three sequential ~1 μm thick confocal slices at the cell middle. Cell morphologies 24 h after seeding were determined from 10 × magnification maximum intensity confocal projections of fixed phalloidin-labelled samples. Extracellular matrix alignment was quantified from confocal reflectance images of mammary stroma or *in vitro* collagen matrix using the ImageJ plugin OrientationJ as previously described [144]. Briefly, single confocal slices (~1 μm thickness) were analyzed using a 0.6-μm Gaussian window to create distributions of pixel orientation. Pixel orientation relative to horizontal was used to pseudocolor matrix images. For all angle-dependent measurements, 0° reference was set to collagen alignment axis for aligned matrix and set arbitrarily for random matrix.

Statistical analysis

All numerical data are from n = 3 independent experiments and are presented as individual measurements, mean ± SEM, or box-and-whisker plots, where boxes represent medians and $25^{th}/75^{th}$ percentile and bars indicate the 5^{th} and 95^{th} percentiles. Means were compared by one-way analysis of variance (ANOVA) with a post hoc Tukey's HSD test using JMP (version 10; SAS Institute, Cary, NC). Cell migration speeds were compared using a nonparametric Wilcoxon test. Angle-dependent measurements including protrusion dynamics, cell elongation distributions, angular displacement distributions, and stepwise cell migration speeds were compared using linear regression analysis in JMP; goodness of fit (R^2), slope, and significance are reported.

3.4 Results

Cancer cells encounter aligned 3D extracellular matrix in vivo and in vitro

During the process of cancer invasion and metastasis, tumor cells pass through diverse ECM microenvironments that can provide a variety of biochemical, mechanical, and structural cues that affect cell migration. In particular, the stromal ECM surrounding tumors can show linearization and fiber alignment that is associated with enhanced invasion [27]. Here, using an orthotopic mammary tumor model, we found that invasive cells can detach from the primary tumor and migrate into regions of highly organized stromal ECM (Figure 3.1A). Analysis of stromal matrix orientation demonstrated that matrix fibers surrounding invading cells were preferentially aligned

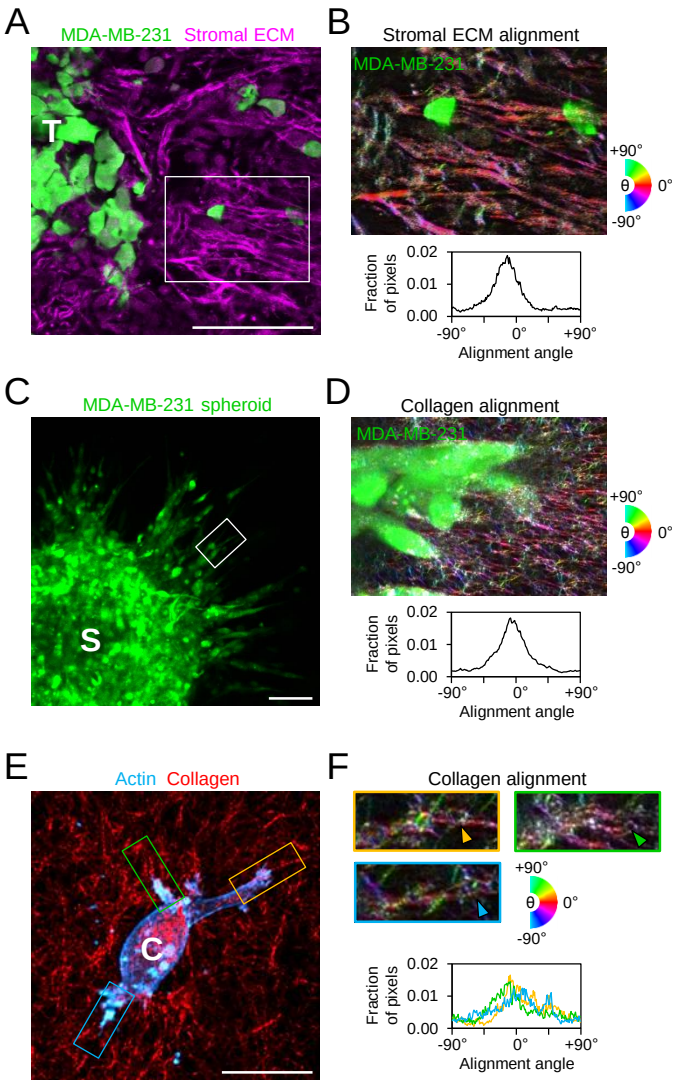

Figure 3.1. Extracellular matrix alignment *in vivo* and *in vitro*. (A) *Ex situ* confocal image of tumor-stroma interface following 3 weeks of orthotopic mammary tumor growth and invasion. GFP-labeled MDA-MB-231 cells (green) invading from the tumor ('T') into the surrounding stromal extracellular matrix (magenta). Scale bar: 100 μm. **(B)** Alignment-pseudocolored image and orientation analysis of stromal ECM indicated in A. Colors correspond to alignment relative to horizontal. **(C)** Fluorescently labeled MDA-MB-231 cells (green) invading from a multicellular spheroid ('S') into the surrounding collagen matrix. Scale bar: 100 μm. **(D)** Alignment-pseudocolored image and orientation analysis of collagen matrix surrounding an invasive strand of cells such as that indicated in C. **(E)** Maximum intensity projection of an isolated MDA-MB-231 cell ('C') following 24 h of spreading in 3D collagen matrix (red). Yellow, green, and blue regions highlight major cell protrusions. Scale bar: 20 μm. **(F)** Alignment-pseudocolored images and orientation analysis of plane of interest for regions indicated in E. Arrowheads indicate protrusion-aligned collagen fibers.

orthogonal to the tumor-stroma interface (Figure 3.1B). Furthermore, in an *in vitro* multicellular spheroid model of tumor invasion, cancer cells migrate outward in radially oriented strands of cells (Figure 3.1C) that associate with aligned type I collagen matrix (Figure 3.1D) [144]. Finally, analysis of single cells following spreading within 3D collagen matrix (Figure 3.1E) revealed an association of major cell projections with locally aligned matrix (Figure 3.1F; arrowheads). Since alignment of 3D matrix provides cells with coordinated linear structural cues at the tumor-stroma interface *in vivo* as well as *in vitro*, we aimed to determine how local matrix alignment affects 3D cancer cell migration behavior.

Migrating cells exchange frequent protrusion formation during spreading for cell elongation, polarization, and displacement

Tunable 3D *in vitro* culture models have become valuable tools for defining the mechanisms by which matrix structure guides cell migration [47, 55, 214]. However, since cells constantly interact with their surrounding ECM during 3D migration and engage in dynamic ECM remodeling, the effects of initial matrix structure and cell-modified matrix structure are difficult to decouple. Therefore, traditional 3D migration assays and metrics may not be able to rigorously uncover matrix guidance mechanisms since both the cells and surrounding matrix itself are in constant flux. To overcome this, we used initial 3D cell spreading, where cells are seeded into naïve 3D matrix and their immediate response is examined, as a reductionist experimental model to study extracellular guidance of 3D migration. A similar strategy of studying

cell spreading has proven effective for defining cellular and molecular mechanisms of 2D migration [215, 216], but this strategy has not been translated to 3D.

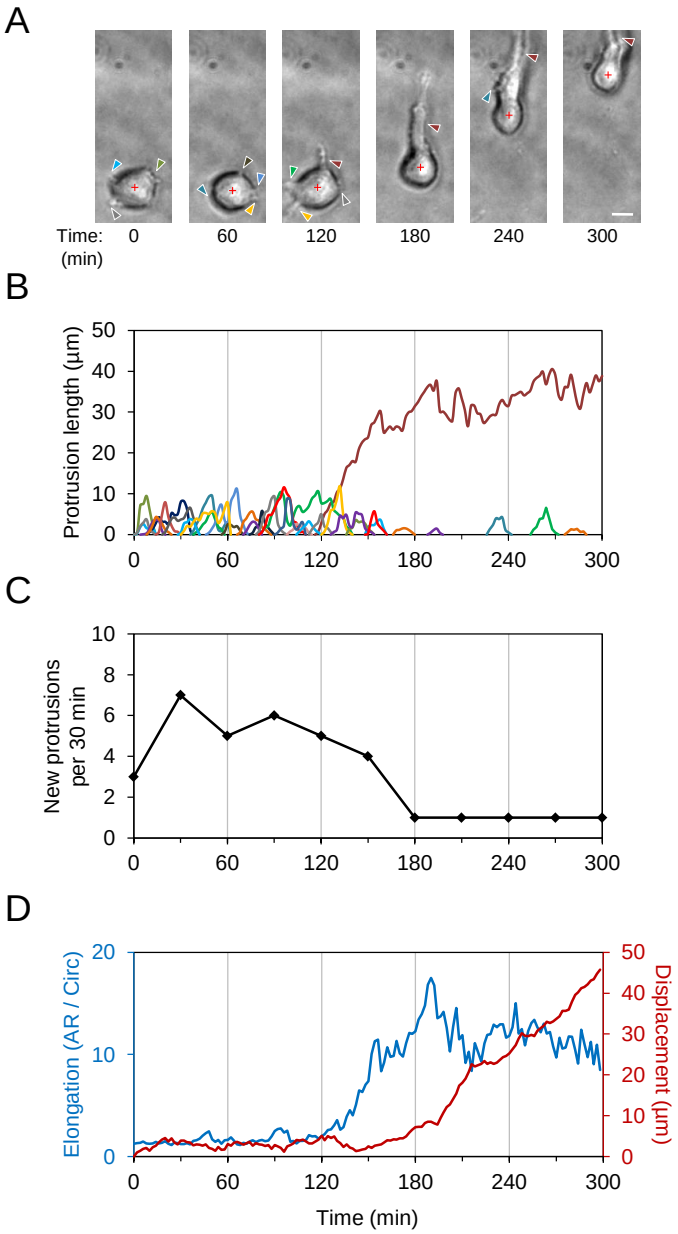

Figure 3.2. Morphodynamics of early 3D cell spreading and migration initiation. **(A)** Time-lapse image series of MDA-MB-231 cell spreading in three-dimensional 1.5 mg/ml collagen matrix immediately following matrix polymerization. Arrowheads indicate cell protrusions. Red crosses denote cell body centroid. Scale bar: 10 µm. **(B)** Traces of individual matrix-probing protrusions generated by the cell shown in A. **(C)** Rate of new protrusion formation by cell shown in A. **(D)** Cell elongation (aspect ratio / circularity) and net cell body displacement of cell shown in A.

To validate this approach, we first investigated the integrated processes of cell spreading and migration within 3D ECM by seeding cells within fibrillar type I collagen matrix and immediately monitoring their behavior using high temporal resolution time-lapse microscopy. We used the malignant MDA-MB-231 breast cancer cell line throughout this study as a model for mesenchymal migration. Simultaneous analysis of cell morphology, protrusion dynamics, and cell body movement revealed the subcellular coordination associated with spreading and the initiation of 3D migration (Figure 3.2A-D). Immediately following collagen ECM polymerization, cells generated matrix-probing protrusions that extended into the pericellular space (Figure 3.2A; arrowheads). These pseudopodial protrusions were 2-10 μm in length and persisted for 10-30 min before being retracted (Figure 3.2B). Notably, once the cell effectively chose a direction by extending a major, long-lived protrusion (Figure 3.2B; dark red protrusion trace) and polarizing to define a front-rear axis, it substantially changed its phenotype, resulting in a significant reduction in new protrusion formation (Figure 3.2C), increased cell elongation, and migration initiation (Figure 3.2D; blue and red traces, respectively). Notably, while the cell in Figure 3.2A-D made the transition from matrix probing to motility 120-180 min after seeding, the timing and efficiency of cells' transition between these two states varied widely across cells. Nonetheless, the ability to switch off new protrusion formation was uniquely characteristic of efficient 3D migrators (Figure 3.3A), and high migration speeds were associated with low new protrusion formation rates (Figure 3.3B). Together, these data demonstrate that the highly coordinated stepwise process of 3D cell spreading is closely related to 3D cell migration and suggest that analysis of

a cell's morphodynamics during spreading could provide insight into migration behavior.

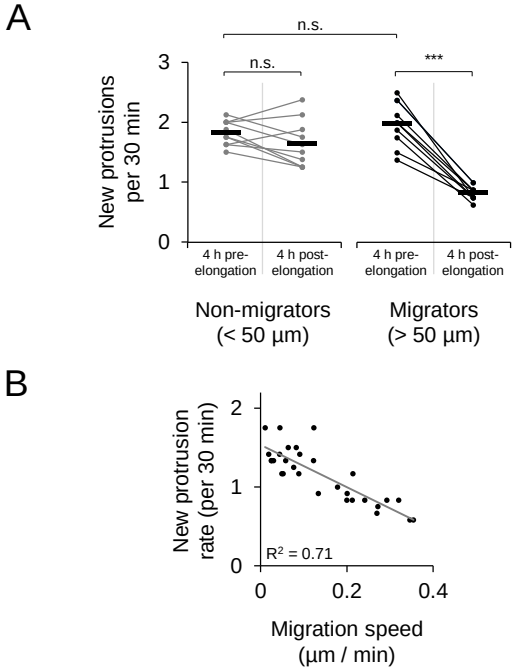

Figure 3.3. Protrusion formation rate during 3D migration. (A) New protrusion formation rate for individual cells before and after cell elongation event (aspect ratio / circularity > 5). Each cell's measurements are connected by a line to highlight change before and after elongation. Horizontal bars indicate mean protrusion formation rates. "Migrators" are cells that eventually displaced at least 50 µm. ***, $P < 0.0001$. n.s., not significant. (F) Linear correlation between new protrusion formation rate and net cell migration speed. Each data point represents an individual cell measured 12 h after seeding in collagen.

Matrix-probing filopodia engage fibrillar collagen during early 3D cell spreading

We previously reported that the transition from matrix probing to motility in 3D collagen is sensitive to ECM density and structure [41, 55], suggesting that cell-matrix interactions underlie this critical transition. To determine whether the process of 3D cell spreading is indiscriminate and spatially random or directed by the ECM, we used time-lapse confocal microscopy to simultaneously monitor collagen matrix structure

and the behavior of embedded Lifeact-GFP-transfected MDA-MB-231 cells. Spreading cells initially generated filopodia-like, actin-containing protrusive structures that extended into the pores and along the fibers of the surrounding collagen matrix. When these dynamic structures emerged within ECM pores, they were generally less than 5 µm in length and persisted for several minutes before buckling or retracting back into the cell cortex (Figure 3.4A; red boxes). Notably, when filopodial protrusions emerged near radially aligned collagen fibers adjacent to the cell (Figure 3.4B; black arrowhead), they persisted and developed into larger protrusive structures that extended along the initial matrix alignment. These findings suggest that fibrillar matrix structure locally guides 3D cell spreading by promoting the development of matrix-probing protrusions into larger pseudopodial protrusions.

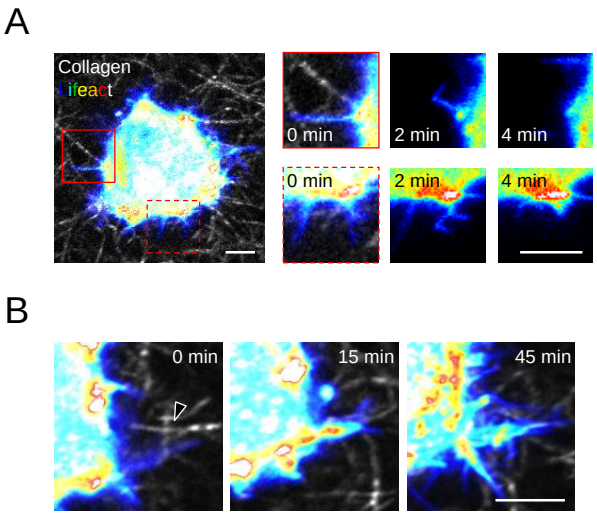

Figure 3.4. Cell-matrix interactions during early matrix probing. (A) Lifeact-GFP-transfected MDA-MB-231 cell spreading in collagen matrix immediately after polymerization. Insets highlight dynamics of transient protrusions. **(B)** Extension and maintenance of actin-rich protrusion along radially aligned matrix at the cell periphery (arrowhead) that supports protrusion persistence. Scale bars: 5 µm.

Local ECM alignment accelerates and directs cell elongation, polarization, and the transition from matrix probing to migration

Having established 3D cell spreading as an effective simplified model of cell migration and demonstrating the involvement of local ECM structure in this process, we next sought to define and systematically analyze the mechanisms by which cells detect and respond to ECM alignment. To do so, we seeded cells within an aligned collagen matrix by preparing collagen solution to include metal beads that were pulled through the solution by a magnet during matrix polymerization, aligning collagen fibers as they formed (Figure 3.5A). Collagen fibers in aligned matrix showed significant linear organization whereas those in random matrix showed no orientation bias (Figure 3.5B,C). For reference, the axis of fiber alignment was considered 0° throughout this study.

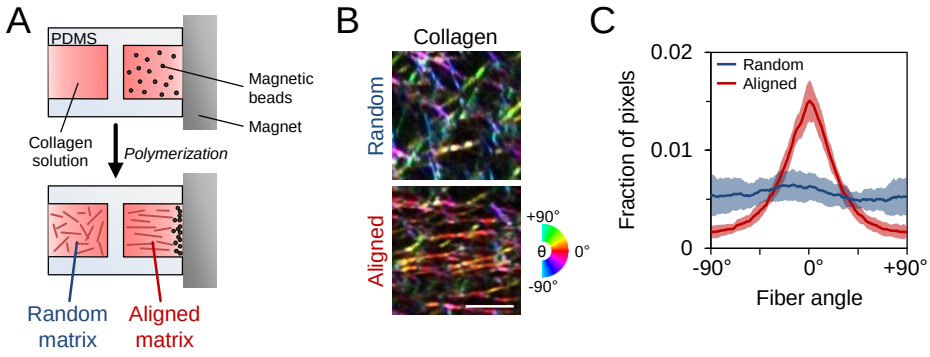

Figure 3.5. *In vitro* alignment of 3D collagen matrix. (A) Schematic of custom glass-bottomed cell culture device used to align collagen matrix. **(B)** Confocal reflectance images of random and aligned collagen matrix. Images were pseudocolored such that fiber hue corresponds to alignment relative to horizontal. Scale bar: 5 μm. **(C)** Quantification of collagen fiber alignment. Data are represented as mean ± SD for 10 images (160 μm × 160 μm).

To determine how matrix alignment regulates early 3D cell spreading, we used time-lapse imaging to compare the behavior of MDA-MB-231 cells within random and

aligned collagen ECM. Cells within aligned matrix showed faster elongation, acquisition of front-rear polarization, and net displacement than those within random matrix (Figure 3.6A), as cells within aligned ECM reached the thresholds for these behaviors (Figure3.6A; dashed lines) earlier than cells in random matrix. Following 24 h of spreading, cells exhibited a range of morphologies (Figure 3.6B), which were examined by measurement of single cells' aspect ratio and circularity, whereby rounded cells (low aspect ratio, high circularity), well-spread multipolar cells (low aspect ratio, low circularity), and well-spread bipolar cells (high aspect ratio, low circularity) could be distinguished. Interestingly, despite influencing the rate of initial cell spreading (Figure 3.6A), there was no difference in average aspect ratio and circularity between the two matrix conditions by 24 h (Figure 3.6C; horizontal and vertical lines, respectively). Additionally, although cells acquired front-rear polarized morphology faster in aligned matrix (Figure 3.6A) there was no difference in the fraction of polarized cells by 24 h (Figure 3.6D). However, matrix alignment induced a significant orientation bias on cell morphology: while ~65% of cells oriented within ±30° of the collagen axis in aligned ECM, those in random ECM showed no such directionality (Figure 3.6B,E). As indicated by comparable distributions of rounded, elongated, and polarized cells in random and aligned matrix by 24 h (Figure 3.6C,D), our data suggest that local matrix alignment does not influence a cell's ability to spread per se. Rather, local matrix alignment provides cues that accelerate (Figure 3.6A) and spatially direct cell spreading (Figure 3.6E).

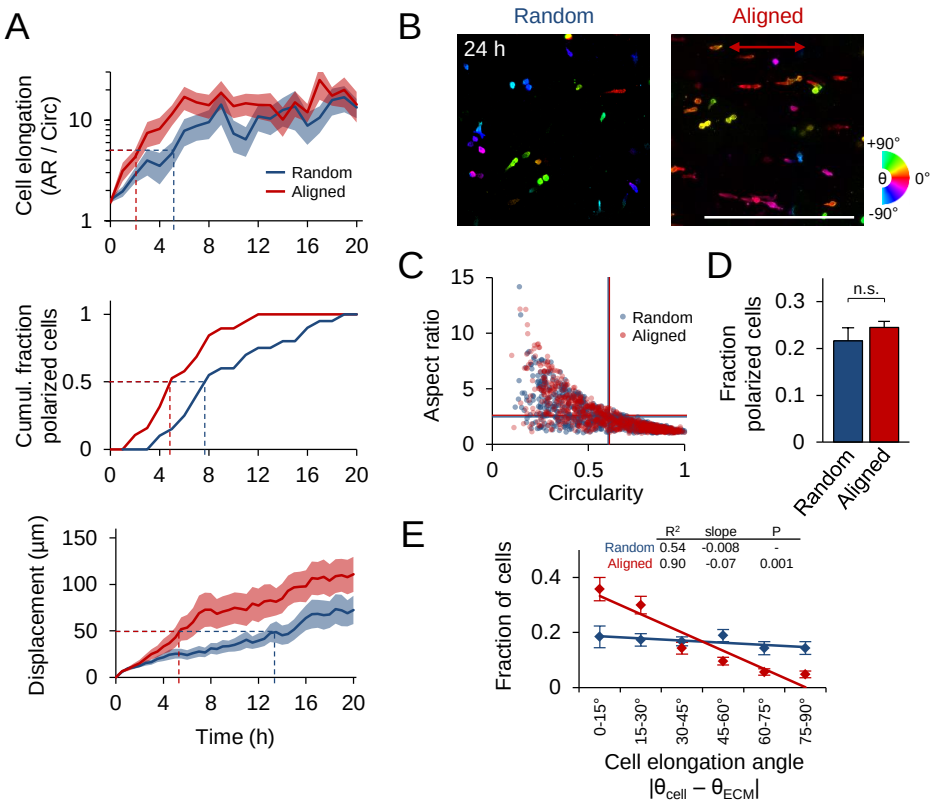

Figure 3.6. Guidance of 3D cell spreading by extracellular matrix alignment. (A) Time-lapse analysis of 3D cell spreading and migration initiation of MDA-MB-231 cells in random and aligned matrix. Elongation and displacement data are represented as mean ± SEM for 20 cells per matrix condition. Dashed lines indicate cell elongation threshold (aspect ratio / circularity = 5), half-maximum cell polarization response (50% polarized), and net cell displacement threshold (50 µm). **(B)** Alignment-pseudocolored images of phalloidin-labelled cells 24 h after seeding in 3D matrix. Red arrow indicates matrix alignment axis. Scale bar: 500 µm. **(C)** Cell morphology map of aspect ratio and circularity 24 h after seeding. Each data point represents an individual cell; horizontal and vertical lines represent average aspect ratio and circularity, respectively (no significant difference). **(D)** Fraction of cells showing front-rear polarization. n.s., not significant. **(E)** Distributions and linear regression analysis of cell elongation angle relative to matrix alignment. Cell elongation angle distributions were determined and mean ± SEM was computed for each angular bin. Linear regression analysis and associated goodness of fit (R^2), regression slope, and significance of comparison between random and aligned matrix are shown. Data in C-E are represented as mean ± SEM from n = 3 independent experiments (> 750 cells per condition).

ECM alignment causes spatial and temporal anisotropy of early matrix-probing protrusions

To expose the subcellular dynamics underlying the cellular response to aligned ECM, we investigated the matrix-probing protrusion dynamics of cells embedded within random and aligned collagen ECM. We monitored cells for 3-4 h after matrix polymerization, or until the cell elongated, since this event is associated with significant changes in cell behavior (Figure 3.3). Interestingly, while cells within random ECM generated isotropically distributed protrusions in all directions, cells in aligned ECM preferentially generated protrusions along the axis of collagen alignment (Figure 3.7A). These distinct angular distributions of protrusions were maintained over time (Figure 3.7B), indicating that even the earliest matrix probing is sensitive to matrix structure. Thus, while there was no discernible angular preference for protrusions in random matrix, approximately 80% of protrusions were within ±30° of the collagen axis in aligned matrix (Figure 3.7C). Notably, cells in aligned matrix also generated significantly fewer new protrusions during the matrix-probing phase (Figure 3.7D). Finally, we used regression analysis to examine maximum protrusion length and protrusion lifetime as a function of protrusion angle and found that matrix organization locally regulates protrusion dynamics (Figure 3.7E,F). Whereas aligned matrix induced anisotropy of protrusion dynamics, there was no angular dependence of protrusion length or lifetime in random matrix. Interestingly, cells in aligned collagen generated larger and longer-lived protrusions along the axis of matrix alignment and shorter, more transient protrusions orthogonal to this axis. Together with our earlier finding that “switching off” protrusion is critical for efficient 3D

migration, these data suggest that local matrix alignment accelerates cell spreading and motility acquisition by reducing the overall number of matrix-probing protrusions while spatially focusing those that form along the matrix alignment axis.

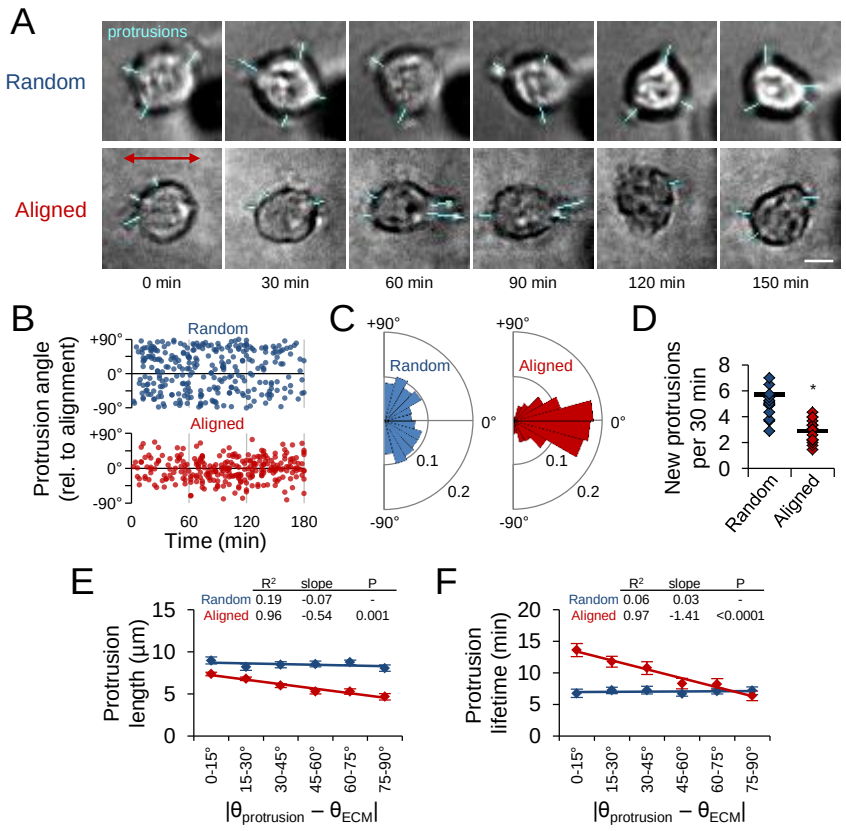

Figure 3.7. Spatial guidance of early protrusion dynamics by extracellular matrix alignment. (A) Representative time-lapse image series of matrix-probing protrusions generated by MDA-MB-231 cells during initial cell spreading in random and aligned collagen. Blue traces highlight protrusions. Red arrow indicates matrix alignment axis. Scale bar: 10 µm. **(B)** Angular distribution of protrusion formation over time. Data points represent the protrusion orientation and time of formation. **(C)** Rose plots illustrating distributions of protrusion orientation angle for data in B. **(D)** Protrusion formation rate for cells analyzed in B. Each data point represents a single cell. Black bars indicate means. *, $P < 0.001$. **(E)** Angular distributions and regression analysis of matrix-probing protrusion length. Protrusions in B were binned according to their orientation angle and mean ± SEM protrusion length was computed for each bin. **(F)** Angular distributions and regression analysis of matrix-probing protrusion lifetime as in E. Data in B-F are from n = 3 independent experiments (15 cells per condition).

The strong angular anisotropy of protrusion dynamics demonstrates that local ECM alignment also controls protrusion dynamics such that these on-axis protrusions are larger and more persistent.

ECM alignment induces cell migration anisotropy

Since cell morphodynamics are intimately tied to cell motility (Figure 3.2), we hypothesized that the matrix-induced anisotropy of early protrusion dynamics and cell morphology would ultimately translate to differences in cell migration. Indeed, reflective of the more rapid cell elongation, polarization, and displacement observed in aligned matrix (Figure 3.6A), motile fraction increased more rapidly and was significantly higher in aligned matrix (Figure 3.8A). While cells in random matrix showed no overall directional preference for their movement, greater than 60% of stepwise cell displacements in aligned matrix were within ±30° of the collagen orientation axis (Figure 3.8B), resulting in significantly different angular distributions by regression analysis. In addition to these differences in overall motility and movement direction, cell migration in aligned ECM was significantly faster than migration in random ECM (Figure 3.8C). Furthermore, matrix alignment-induced migration anisotropy was evident when stepwise cell speeds were considered along with the angle of the corresponding cell displacement (Figure 3.8D). Whereas stepwise cell speeds were distributed uniformly versus displacement angle in random matrix, higher stepwise speeds were observed at lower angles relative to the collagen orientation axis in aligned matrix. These results demonstrate that structural anisotropy

of a cell's local ECM can induce anisotropy of cell migration by promoting faster movement along the predetermined major axis of ECM organization.

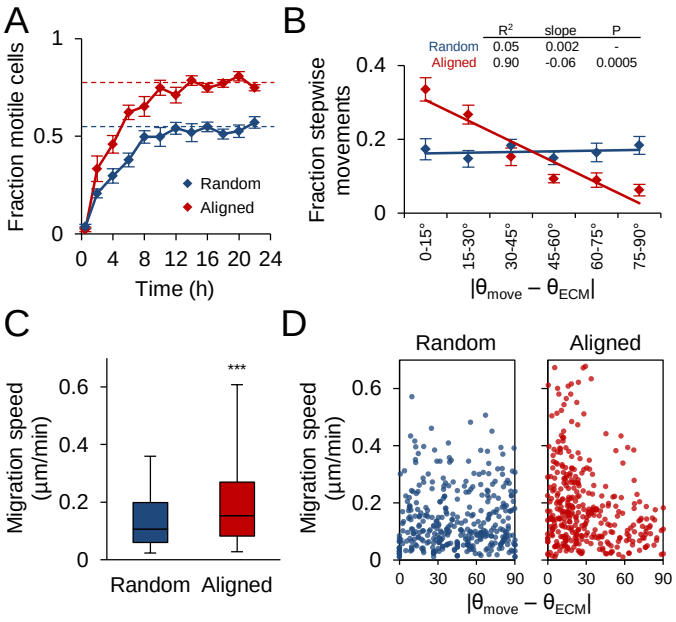

Figure 3.8. Guidance of 3D cell migration by extracellular matrix alignment. (A) Fraction of motile cells (mean ± SEM) in random and aligned matrix during the first 24 h of culture. Motile fraction was significantly higher ($P < 0.001$) in aligned matrix at all time points after 2 h, including at steady state (dashed lines; average of 12-24 h). **(B)** Angular distributions and regression analysis of stepwise cell movements from 12-18 h after seeding. Stepwise angular displacement distributions were binned as indicated and mean ± SEM was determined for each bin. **(C)** Stepwise cell migration speeds. Box and whisker plots show medians, $25^{th}/75^{th}$, and $5^{th}/95^{th}$ percentiles. ***, $P < 0.0001$. **(D)** Stepwise migration speed versus stepwise displacement angle relative to matrix alignment axis. All data are from n = 3 independent experiments (cells per condition: A, > 150 cells; B-D, 25 cells).

FAK and Rac1 activity enable matrix alignment-induced behavioral anisotropy

We next aimed to define the molecular mechanisms governing the subcellular morphodynamic response to matrix alignment. Cells perceive 3D matrix properties through integrin signaling [105, 217], which is spatially influenced by 3D matrix fiber structure and alignment [214]. Here, we found that matrix structure spatially directs

the formation of cell-matrix adhesions and localization of focal adhesion kinase (FAK) activity during 3D cell spreading (Figure 3.9A). Whereas pFAK^{Y397} staining was diffuse immediately following aligned matrix polymerization, pFAK^{Y397} signal rapidly localized to small protrusions associated with aligned fibers at the cell periphery after 30 and 120 min of spreading (Figure 3.9A; arrowheads), and later localized to the leading edge of migrating cells (Figure 3.9B).

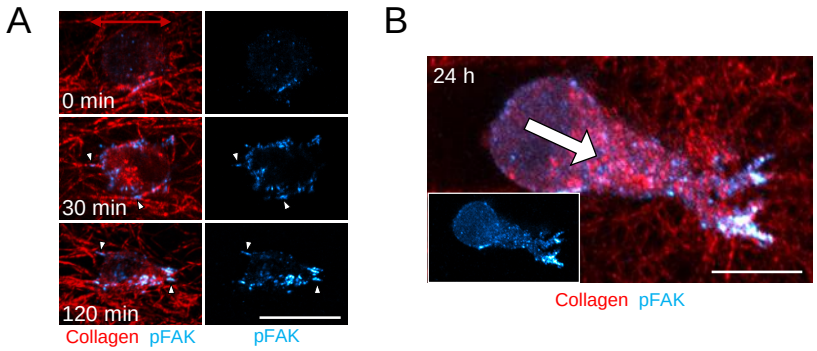

Figure 3.9. Guidance of 3D protrusion and adhesion formation by matrix structure. (A) Development of pFAK^{Y397}-containing adhesions (cyan; arrowheads) during early MDA-MB-231 cell spreading in aligned collagen matrix (red). Red arrow indicates matrix alignment axis. **(B)** Front-rear pFAK^{Y397} polarization in migrating cell 24 h after seeding. White arrow indicates migration direction. Scale bars: 20 μm.

These results provide evidence that matrix-directed adhesion signaling anisotropy occurs prior to spreading in aligned matrix and is maintained through 3D cell migration. Therefore, we investigated the role of β1-integrin, FAK, and Src, which can link adhesion signaling to Rho GTPases [218], as well as Rac1, in the cellular response to matrix alignment. Additionally, we tested whether PI3K, which is a major regulator of chemotactic migration guidance [143, 198], contributes to ECM-driven behavioral anisotropy and guidance.

Blocking β1-integrin ligation with the function-blocking antibody 4B4 significantly reduced protrusion formation (Figure 3.10A) and prevented cell spreading (data not shown), reaffirming the role of β1-integrin in mesenchymal 3D cell spreading [47, 57] and precluding β1-integrin-inhibited cells from further characterization of behavioral anisotropy in our system. Interestingly, while none of the other inhibitors significantly altered overall protrusion frequency during initial cell spreading (Figure 3.10A), we did observe significant differences in protrusion orientation under Rac1 and FAK inhibition (Figure 3.10B). While control cells showed a strong orientation bias for on-axis protrusion formation as demonstrated in Figure 3.7 (more protrusions at lower angles relative to ECM alignment), regression analysis indicated that Rac1 or FAK inhibition, but not Src or PI3K inhibition, resulted in significantly different angular distributions of matrix-probing protrusions. Notably, both Rac1 and FAK inhibition completely eliminated protrusion anisotropy (Figure 3.10B). Overall protrusion dynamics were also affected by both Rac1 inhibition, which decreased average protrusion length and lifetime, and FAK inhibition, which increased average protrusion length and lifetime (Figure 3.10C,E). To account for significant differences in average protrusion dynamics parameters, we used mean-normalized values for regression analysis. Interestingly, the orientation-indiscriminate protrusion directionality exhibited under Rac1 and FAK inhibition was accompanied by similarly alignment-insensitive protrusion dynamics (Figure 3.10D,F). Finally, neither PI3K nor Src inhibition significantly affected the angular dependence of protrusion dynamics (Figure 3.10A-F).

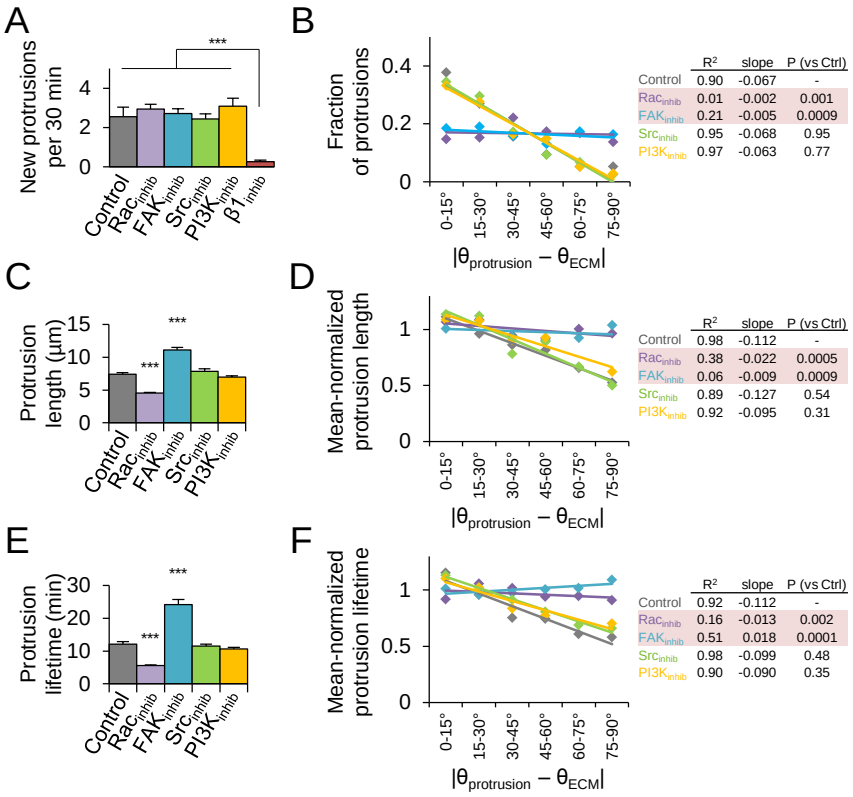

Figure 3.10. Regulation of 3D matrix alignment-induced protrusion anisotropy. **(A)** New protrusion formation rate within the first 4 h after seeding in aligned matrix. Cells were pretreated with the indicated inhibitors for 30 min before seeding. ***, $P < 0.0001$. **(B)** Angular distributions and regression analysis of matrix-probing protrusion formation. Protrusion orientation distributions were determined and means were computed for each angular bin. Rows highlighted in red are significantly different from Control. **(C)** Overall matrix-probing protrusion length. ***, $P < 0.0001$ compared to Control. **(D)** To account for significant differences in mean overall protrusion length, each treatment's data was mean-normalized before quantification of angular distributions and regression analysis as in Figure 3.7E. Rows highlighted in red are significantly different from Control. **(E)** Overall matrix-probing protrusion lifetime. ***, $P < 0.0001$ compared to Control. **(F)** Angular distributions and regression analysis of mean-normalized protrusion lifetimes analyzed and presented as in D. Rows highlighted in red are significantly different from Control. All data are from n = 3 independent experiments (12 cells, > 150 protrusions per treatment); data in B, D, and F are presented as mean ± SEM.

We next measured the morphology and migration of inhibitor-treated cells in aligned collagen matrix to determine if the observed differences in early matrix-probing

protrusions affected later behavioral anisotropy. We found that all treatments with the exception of Src inhibition induced significant changes in overall spread cell morphology 24 h after seeding (Figure 3.11A). Control cells showed morphologies ranging from rounded to bipolar elongated as indicated by the broad distribution in the aspect ratio versus circularity morphology map.

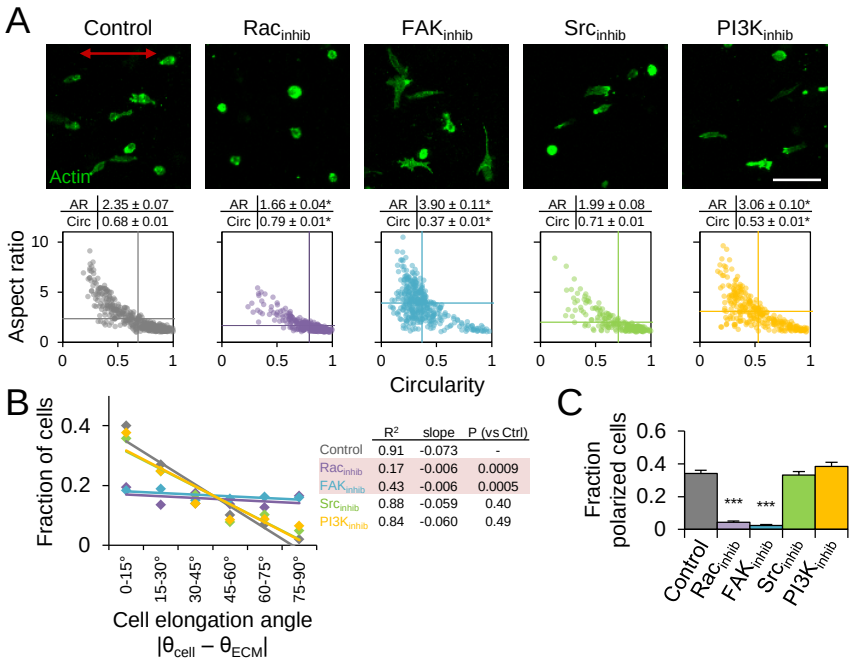

Figure 3.11. Regulation of 3D matrix alignment-induced morphology anisotropy. **(A)** Phalloidin-labelled cells (green) after 24 h of spreading in aligned collagen matrix treated as indicated. Red arrow indicates matrix alignment axis. Scale bar: 100 µm. Cell morphology maps of aspect ratio and circularity 24 h after seeding. Each data point represents an individual cell. Horizontal and vertical lines represent average aspect ratio and circularity, respectively. *, $P < 0.0001$ compared to Control. **(B)** Distributions and regression analysis of cell elongation angle for elongated cells (aspect ratio > 1.75). Elongation orientation distributions were determined and means were computed for each angular bin. Rows highlighted in red are significantly different from Control. **(C)** Fraction of cells (mean ± SEM) showing distinct front-rear polarization. ***, $P < 0.0001$ compared to Control. All data are from n = 3 independent experiments (cells per treatment: A, > 400 cells; B-C, > 150 cells).

Rac1-inhibited cells generally failed to elongate (low aspect ratio, high circularity), while FAK and PI3K inhibition induced bipolar/multipolar cell elongation (low/high aspect ratio, low circularity). We measured cell elongation angle, as defined by the major axis of elongated cells (aspect ratio > 1.75) relative to the matrix alignment axis, and found that Rac1 and FAK inhibition significantly reduced the anisotropy of 3D cell spreading observed in control cells (Figure 3.11B). Additionally, Rac1 and FAK inhibition significantly reduced front-rear polarization (Figure 3.11C) and 3D motility (Figure 3.12A) and reduced stepwise cell migration speeds to near or below the motility threshold limit (Figure 3.12B; dashed line).

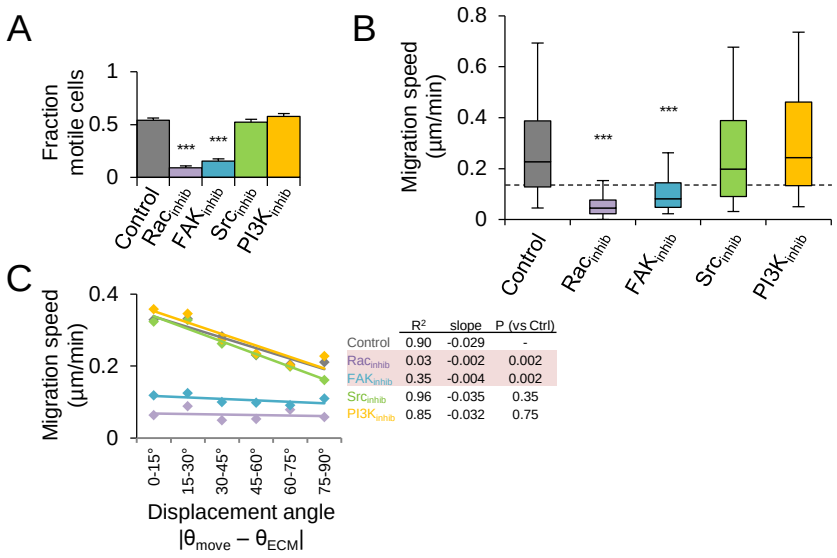

Figure 3.12. Regulation of 3D matrix alignment-induced migration anisotropy. **(A)** Steady state motile fraction (mean ± SEM) 12-18 h after seeding. ***, P < 0.0001. **(B)** Stepwise cell migration speeds. Box and whisker plots show medians, 25th/75th, and 5th/95th percentiles and dashed line indicates threshold migration speed of 0.125 μm/min (equivalent to 15 μm per 2 h, or the threshold for motility). ***, P < 0.0001 compared to Control. **(C)** Angular distributions and regression analysis of stepwise cell migration speed. Migration speeds were binned according to their associated displacement angle and mean migration speed was computed for each bin. Only migration speeds within each treatment's 95% confidence interval were included. Rows highlighted in red are significantly different from Control. All data are from n = 3 independent experiments (cells per treatment: A, > 150 cells; B-C, 40 cells).

Conversely, pharmacological targeting of Src signaling had no effect on 3D cell morphology and migration, and despite altering 3D morphology, PI3K inhibition did not affect front-rear polarization, motile fraction, or cell migration speed (Figure 3.11C, 3.12A,B). Finally, we analyzed stepwise cell migration speeds as a function of displacement angle and found that neither Src nor PI3K inhibition significantly affected the migration anisotropy induced by aligned collagen matrix (Figure 3.12C). In contrast, and in addition to significantly reducing overall cell migration speed, pharmacological inhibition of Rac1 or FAK eliminated ECM alignment-induced orientation bias of cell migration (Figure 3.12C). In summary, despite eliciting subtle changes in 3D morphology, inhibition of Src or PI3K signaling did not affect matrix alignment-induced anisotropy of matrix probing, cell spreading, and cell migration. Conversely, both Rac1 and FAK inhibition caused significant changes in protrusion dynamics and spreading as well as a substantial reduction in overall 3D motility. Notably, blocking Rac1 and FAK signaling completely eliminated ECM alignment-induced orientation bias during early matrix probing, spreading, and migration, indicating that Rac1 and FAK signaling are critical regulators of directional guidance of cell migration by 3D matrix alignment.

3.5 Discussion

The process of 3D cell migration is fundamental to cancer invasion and metastasis [44, 50]. Notably, 3D migration is sensitive to extracellular regulation [69] and the interstitial connective tissue that tumor cells negotiate during invasion contains physical features including tissue interfaces, cell-scale microtracks, and well-

organized fibrillar matrix that provide guidance cues and enable 3D cancer cell migration [13, 27, 37, 40, 41]. Despite a longstanding historical appreciation for the effects of contact guidance and matrix alignment-induced morphological and migration anisotropy [203, 210, 211, 219] as well as more recent association of highly aligned stromal ECM with poor breast cancer patient outcome [39], the mechanisms by which cancer cells detect and respond to 3D ECM alignment remain to be determined [143]. Critically, understanding the effects of such pro-invasive extracellular stimuli on cancer cell migration could enable the development of more effective targeted therapies to combat interstitial invasion. Here, we demonstrate that 3D matrix alignment induces spatial anisotropy of early 3D matrix-probing protrusions that leads to oriented cell spreading. This asymmetry of cellular morphodynamics and subsequent directed 3D migration is dependent on FAK and Rac1 signaling, implicating polarized adhesion signaling and active cell protrusion response as major drivers of 3D matrix guidance.

3D matrix alignment as an inducer of cell anisotropy

Directional cell migration results primarily from asymmetry of the extracellular cues perceived by a cell [143]. While many of the principles of directional migration have been determined by studying cell response to gradients of soluble factors (chemotaxis), cell migration can also be directed by asymmetry of physical microenvironmental factors including fluid flow (rheotaxis), stiffness (durotaxis) and adhesion ligands (haptotaxis). Regardless of the nature of the stimulus, directional migration requires both 1) the formation of a leading edge via establishment and

maintenance of a front-rear polarization axis and 2) orientation of this front-rear axis in response to the stimulus [143, 220]. We show here that 3D ECM anisotropy in the form of coordinated fiber alignment is a potent inducer of directional migration that contributes to both leading edge formation and cell orientation. In our system, 3D matrix alignment allows cells to quickly establish and orient a major axis along which they restrict much of their subsequent protrusion, spreading, and movement. Interestingly, while cells in random collagen ECM eventually elongate, polarize, and begin to migrate, by comparing the morphodynamics of cells within random and aligned matrix, we found that ECM alignment accelerates all of these critical behaviors. This finding, together with the observations that cells in aligned matrix generate fewer protrusions overall and are more migratory than those in random matrix, suggests that coordinated ECM cues such as alignment may allow cells to spread and migrate efficiently without needing to "explore" off-axis ECM features. Indeed, this hypothesis is consistent with the migration initiation-associated "switching off" of protrusion as well as the negative correlation between protrusion formation rate and migration speed we report in Figure 3.3. Therefore, 3D matrix alignment may promote leading edge formation and enable efficient oriented migration by spatially suppressing off-axis cell protrusion, thus preventing indiscriminate exploration of the pericellular space that slows 3D cell migration.

Molecular regulation of ECM alignment-induced cellular anisotropy

Studies in chemotaxing cells have revealed a critical role for polarized PI3K signaling in establishing and preserving the leading edge in response to soluble factor signaling

[221]. Notably, local PI3K activation results in signaling through secondary messengers that in turn activates the GTPase Rac1, which participates in regulation of cytoskeleton dynamics to drive directed migration [89, 198, 222]. Interestingly, we show here that Rac1 activity, but not PI3K activity, is required for 3D cell spreading and the anisotropic cellular response to 3D matrix alignment, indicating that the Rac1 activation required for chemical and structural guidance of migration may be achieved through distinct mechanisms. Thus, pathways other than PI3K are likely responsible for controlling Rac1 activity that leads to protrusion, spreading, and migration in 3D matrix [89].

In our screen of cell motility inhibitors, we found that only β1-integrin inhibition prevents cells from generating 3D matrix-probing protrusions. This effect is consistent with the established role of β1-integrin-ECM ligation in mediating protrusion and migration in 3D environments [57, 223]. Thus, while β1-integrin likely plays a critical role in the detection of and response to 3D matrix structure [224], the effect of function-blocking treatment on mesenchymal-type protrusion and spreading behavior was too destructive to allow further characterization in our model. Interestingly, despite ultimately being required for 3D migration, neither Rac1 nor FAK signaling are needed for matrix probing as both Rac1- and FAK-inhibited cells retain the ability to generate matrix-probing protrusions during early spreading. However, Rac1 and FAK inhibition completely eliminates the orientation bias of matrix-probing protrusions in aligned ECM, indicating that matrix probing is not merely an indiscriminate and random exploration of the pericellular space. Rather, our results

suggest that cells regulate where 3D matrix-probing protrusions are formed and how these protrusions will behave using active Rac1- and FAK-dependent cellular feedback in response to local ECM structure.

Consistent with this model for matrix guidance of protrusions, we found that cells exhibit both transient filopodia-like projections that explore matrix pores and longer-lived protrusive structures that extend along ECM fibers. Considering the topography-sensing function of filopodia in 3D environments [225] and the critical role of 3D ECM architecture in regulating cell-matrix adhesion maturation and dynamics [214], these observations suggest that cells interrogate their immediate matrix microenvironment using dynamic filopodia that can subsequently ligate discrete matrix fibers, resulting in adhesion maturation and signaling that locally regulates protrusion dynamics. Indeed, on 2D substrates, Rac1 can be activated by integrin-ECM ligation [226] and the development of filopodia into pseudopodia requires integrin occupancy and downstream Rac1 signaling [227]. Furthermore, Shibue et al. reported that filopodia-like protrusions precede and enable maturation of 3D cell-matrix adhesion plaques to trigger adhesion signaling [228]. Although the authors of the previous study did not consider the role of ECM structure in physically guiding this process, recent work by Kubow et al. showed that the structure and orientation of 3D matrix fibers adjacent to a cell determine adhesion dynamics, size, and composition [214]. Together with our findings here that ECM fiber architecture adjacent to a spreading cell can spatially pre-pattern the formation of new cell-matrix

adhesion sites (Figure 3.9A,B), these results implicate cell-matrix adhesion signaling as a major regulator of ECM structure detection and response.

3D cell spreading as a reductionist model for mesenchymal migration

Defining the cellular and extracellular determinants of 3D cell migration will ultimately be critical to understanding how cancer cells invade and metastasize. Significant advances have been made toward a more comprehensive understanding of microenvironmental context-specific cell migration [1, 229], but continued work is required to more fully explore the mechanisms of extracellular matrix guidance of migration. While the roles of ECM parameters such as dimensionality, stiffness, and pore size are increasingly appreciated, the impact of structural ECM organization on 3D cell migration is generally underappreciated. Notably, the microarchitecture of 3D cell migration microenvironments can vary widely *in vitro* and *in vivo* [42], and can be further altered through cell-induced matrix remodeling during migration [129, 230]. These observations underscore the critical need to better understand the role of a cell's local ECM structure in determining cell behavior, but also make this problem particularly challenging. To unmask correlations between 3D matrix structure and 3D cell behavior, each of which is complex and dynamic, and each of which is constantly engaged in bidirectional interactions with the other, matrix remodeling mechanisms and matrix response mechanisms must be decoupled.

Here, we introduce a novel experimental approach to study the mechanisms of 3D cell migration by examining early 3D cell spreading within a naïve 3D ECM – that is, one

that has not yet been altered by the cell being studied. This model effectively decouples response to matrix, which occurs immediately, from matrix remodeling (and subsequent response to cell-modified matrix), which occurs over longer time scales. Since cells are analyzed from a common rounded-morphology starting point and the naïve pericellular matrix architecture can be determined microscopically and experimentally tuned, many of the challenges associated with defining determinants of 3D migration – diverse cellular states, unknown cell history, ECM properties that are locally heterogeneous, dynamic, and poorly defined [231] – are bypassed. Cell migration is fundamentally highly coordinated cell spreading [45], and the prevailing assumption of our model is that the mechanisms underlying a given subcellular behavior during early 3D cell spreading (e.g., protrusion stabilization by matrix fibers) are reflective of the mechanisms underlying that behavior during 3D migration. In its initial application here, we use the 3D cell spreading model to identify and study the effects of 3D ECM alignment on cell behavior. We anticipate that our reductionist model can be used to further decouple the "detection" and "response" elements of 3D matrix guidance by combining analysis of early cell signaling with the morphodynamic analysis framework presented here. Similar strategies involving time-course analysis of cell signaling and subcellular behaviors have proven effective for defining rate-limiting steps of complex cell processes including 2D cell spreading and adhesion-dependent survival signaling [215, 228, 232].

Broadly, the anisotropy of cell phenotype we observe within aligned matrix directly demonstrates the influence of a cell's local ECM structure on its protrusion, spreading,

and migration behaviors and suggests that the "randomness" of protrusions observed in random ECM environments may actually be a consequence of cells interacting deterministically with their randomly organized pericellular matrix. Thus, 3D cell migration that is presumed to be random may actually be directed by a predetermined "map" of microheterogeneities in the surrounding ECM structure. This notion is supported by recent evidence indicating that 3D cell migration does not follow a true random walk due in part to the directional anisotropy that is characteristic of migration within 3D environments [233]. Since in our 3D cell spreading experimental model, matrix alignment induces an "expected" matrix-dependent behavior (i.e., anisotropy of protrusions, spreading, and movement), our results here provide critical insight into the molecular mechanisms by which cells detect and respond to local ECM structure. For example, since FAK and Rac1 inhibition interfere with the expected anisotropic cellular response to aligned matrix, these pathways are likely required for cells to respond to matrix structure in general [234].

In summary, we find here that 3D matrix alignment induces adhesion- and Rac1-dependent anisotropy of cancer cell morphodynamics that leads to directional cell migration. Aligned ECM suppresses off-axis and promotes on-axis behaviors including early matrix-probing protrusion formation, cell elongation, and movement, resulting in the acceleration and increased efficiency of 3D migration. These findings underscore the importance of extracellular guidance of 3D cell migration and could have implications ranging from the study of 3D cell migration mechanisms *in vitro* to

the development of therapeutic strategies targeting contact guidance-mediated cancer invasion *in vivo*.

CHAPTER 4

COMPARATIVE MECHANISMS OF CANCER CELL MIGRATION THROUGH 3D MATRIX AND PHYSIOLOGICAL MICROTRACKS

This chapter was published in *American Journal of Physiology – Cell Physiology* [41].

Portions of the data in this chapter were contributed by Casey Kraning-Rush.

4.1 Abstract

Tumor cell invasion through the stromal extracellular matrix (ECM) is a key feature of cancer metastasis and understanding the cellular mechanisms of invasive migration is critical to the development of effective diagnostic and therapeutic strategies. Since cancer cell migration is highly adaptable to physiochemical properties of the ECM, it is critical to define these migration mechanisms in a context-specific manner. Although extensive work has characterized cancer cell migration in 2D and 3D matrix environments, the migration program employed by cells to move through native and cell-derived microtracks within the stromal ECM remain unclear. We previously reported the development of an *in vitro* model of patterned type I collagen microtracks that enable matrix metalloproteinase (MMP)-independent *microtrack migration*. Here, we show that collagen microtracks closely resemble channel-like gaps in native mammary stroma ECM and examine the extracellular and intracellular mechanisms underlying microtrack migration. Cell-matrix mechanocoupling, while critical for migration through 3D matrix, is not necessary for microtrack migration. Instead,

cytoskeletal dynamics including actin polymerization, cortical tension, and microtubule turnover enable persistent, polarized migration through physiological microtracks. These results indicate that tumor cells employ context-specific mechanisms to migrate and suggest that selective targeting of cytoskeletal dynamics, but not adhesion, proteolysis, or cell traction forces, may effectively inhibit cancer cell migration through pre-formed matrix microtracks within the tumor stroma.

4.2 Introduction

As one of the earliest steps of metastasis, local tissue invasion represents a critical transition from local deregulated cell growth to potentially lethal disease. Tissue invasion is a multi-step biophysical process during which carcinoma cells bypass the epithelial basement membrane and migrate through the underlying interstitial stroma [1, 9]. Classically, stromal invasion has been viewed as a challenging and highly selective stepwise process requiring an invading cell to actively breach the basement membrane, protrude into a collagen-rich stroma, and employ a diversity of mechanochemical migration mechanisms to overcome matrix and tissue barriers to effectively migrate [19, 235]. However, recent evidence suggests that the vast cellular and microenvironmental heterogeneity within and around tumors allows significant diversity in invasion programs [5], and the context-specific mechanisms governing local tissue invasion and metastasis remain only partially understood.

Cancer cell migration through 3D stromal microenvironments is adaptive and sensitive to regulation by both intracellular and extracellular determinants [229, 236]. While

transit of tumor cells through the 3D extracellular matrix (ECM) requires coordination of a physiochemical motility program that generally involves cytoskeleton, adhesion, and contractility mechanisms [1, 45], migration strategies are context-specific and the molecular mechanisms employed depend on biochemical and biophysical properties of the ECM. Notably, biophysical matrix parameters including porosity, alignment, and elasticity have emerged as key mediators of cell behavior and together determine the requirements for and nature of motility [237]. For example, Wolf et al. recently showed that matrix porosity integrates with nuclear deformability to define the requirement for integrin- and actomyosin-mediated mechanocoupling and ECM remodeling during 3D migration [47]. Furthermore, our group and others have demonstrated that the structural and biochemical nature of type I collagen matrix determines 3D migration efficiency and the requirement for proteolytic ECM remodeling by matrix metalloproteinase (MMP) activity [55, 144, 158, 238]. In addition to imposing steric constraints, fibrillar 3D ECM can exhibit structural anisotropy including matrix fiber alignment [27, 56, 206] and interfacial regions [36, 200] that provide topographical guidance cues to migrating cells. Nonetheless, while these and other studies have contributed greatly to our understanding of ECM-directed cell invasion strategies, conventional *in vitro* 3D ECM models for studying mechanisms of tumor cell behavior vastly overestimate the homogeneity of the stromal ECM and the effects of local heterogeneity in matrix structure on cell motility remain only marginally understood [40, 42].

Cell-scaled track-like structures in the interstitial matrix, which have been observed as conduits for trafficking tumor cells *in vivo,* provide both physical guidance and a path of least resistance to migrating cells and thus, have been implicated as critical determinants of tumor cell behavior [35, 37, 40, 48, 49]. These structures can broadly include interfaces between tissue components, gaps and clefts between aligned collagen bundles, and organized networks of ECM pores. Recently, our group and others have shown that both tumor and stromal cells can use mechanical and proteolytic matrix remodeling to generate cell-caliber microtracks through type I collagen matrix that facilitate proteinase-independent invasion of other cells [144, 208, 239, 240]. Regardless of whether matrix microtracks are native to interstitial tissue [42] or a result of MMP-mediated matrix degradation by tumor/stromal cells [144, 158, 208], their presence in tissue challenges the conventional interstitial invasion model in which migrating cells must negotiate a restrictive collagen-rich ECM. Instead, cells may co-opt sufficiently wide pre-formed matrix tunnels to migrate in an unimpeded, MMP-independent manner [241]. Notably, the presence of such migration-enabling matrix-free pathways could explain the limited ability of clinical MMP inhibition to prevent invasion and metastasis. Since these track-like structures in the ECM provide strong pro-invasive cues to tumor cells, understanding the mechanisms that govern cancer cell migration through cell-scale gaps in tissue will be critical to the development of therapeutic strategies to targeting metastasis.

We have previously developed an *in vitro* system of patterned collagen microtracks to model tumor cell migration through cell-sized gaps in the ECM [60]. The microtracks,

unlike previous designs made from PDMS and polyacrylamide [242, 243], offer the advantage of more closely mimicking the mechanical and chemical properties of native ECM. We found that patterned collagen microtracks recapitulate tube-like tumor cell-derived channels within a 3D collagen matrix and enable MMP-independent migration of otherwise poorly invasive mammary epithelial cells [60]. Here, we use this platform alongside fibrillar 3D collagen matrix to define and compare the mechanisms that govern cancer cell migration within each environment. We show that mechanical cell-matrix interactions are needed for migration through 3D matrix, but not microtracks, where cleared matrix-free pathways provide little resistance and eliminate the need for traction generation, matrix remodeling, and cell body deformation. Conversely, migration through 3D matrix and microtracks are similarly driven by polarized protrusions and elongation at the leading edge, which are mediated by actin polymerization and reinforced by the microtubule cytoskeleton. Collectively, our findings suggest that microtracks within the interstitial stroma may provide paths of least resistance that enable tumor cell invasion by reducing the molecular machinery required for efficient migration.

4.3 Materials and Methods

Cell culture and reagents

Highly metastatic MDA-MB-231 breast adenocarcinoma cells (HTB-26; ATCC, Manassas, VA) were maintained in Minimum Essential Medium (Life Technologies, Grand Island, NY) supplemented with 10% (v/v) fetal bovine serum (FBS; Atlanta Biologicals, Flowery Branch, GA), 100 U/mL penicillin, and 100 µg/mL streptomycin

(Life Technologies). GFP-expressing MDA-MB-231 cells (AKR-201; Cell Biolabs, San Diego, CA) were maintained in Dulbecco's Modified Eagle Medium (Life Technologies) supplemented with 10% FBS, 100 U/mL penicillin, 100 µg/mL streptomycin, and 0.1 mM MEM non-essential amino acids (Life Technologies). For inhibitor studies, complete medium was supplemented with 10 µM Y27632, 10µM ML7, 50 µM blebbistatin, 10µM nocodazole, 12 µM paclitaxel, 20 µM cytochalasin D, 2.5 µM latrunculin A, (all from Sigma-Aldrich, St. Louis, MO), 2 µg/mL CT04 (Cytoskeleton, Inc., Denver, CO), 2.5-10 µg/mL monoclonal antibody (mAb) 4B4/FITC-4B4 (Beckman Coulter, Brea, CA), or dimethyl sulfoxide (DMSO) vehicle. All cell culture was maintained at 37°C and 5% CO_2. Primary antibodies used were anti-α-tubulin (05-829; Millipore, Billerica, MA), anti-phosphorylated myosin light chain 2 (3674S; Cell Signaling Technology, Danvers, MA), and anti-GAPDH (mAb374; Millipore).

Murine mammary cancer model

Mice were maintained under barrier conditions according to Cornell University animal care guidelines (protocol 2009-0101; R.M. Williams). The murine mammary cancer model was established as previously described [212]. Briefly, 3-4-week old female NOD.Cg-Prkdc^{scid} Il2rg^{tm1Wjl}/SzJ mice (The Jackson Laboratory, Bar Harbor, ME) were placed in an induction chamber and anesthetized with 3% isoflurane (Butler Animal Health Supply, Dublin, OH) for 2-5 minutes and subsequently moved to a custom-designed surgical platform. Developing glandular tissue was removed from the 4th and 7th inguinal mammary glands and 10^5 - 10^6 GFP-expressing MDA-MB-231

cells were injected into each cleared fat pad. Surgical incisions were repaired using wound clips (Fisher Scientific, Atlanta, GA), mice were resuscitated, and monitored for 3 weeks prior to *in vivo* and *ex vivo* imaging.

In vivo multiphoton imaging

After 3 weeks of orthotopic tumor growth, *in vivo* imaging was performed. Mice were anesthetized as for surgery and immediately moved to a custom-designed imaging stage. Isoflurane concentration was adjusted to 2% in order to maintain respiration at ~60 breaths/minute [244]. Mice were vivisected to expose MDA-MB-231-derived mammary tumors and multiphoton (MP) and second harmonic generation (SHG) imaging were performed as previously described [195, 245]. An 880 nm beam from a mode-locked Ti:sapphire laser illuminated MDA-MB-231/GFP-derived tumors and the surrounding mammary stroma *in situ* on a modified Olympus AX-70 upright microscope equipped with a water-immersion 20×/0.95 NA Olympus objective. The emission signal was separated into two channels to collect the SHG signal from collagen and MP fluorescence from GFP-labeled MDA-MB-231 cells. Following *in situ* multiphoton imaging, MDA-MB-231-derived tumors and the surrounding mammary stromal tissue were harvested for *ex situ* imaging; tissues were either fixed for 30 minutes in 3.7% (v/v) formaldehyde in PBS or embedded within collagen matrix (see below) for time-lapse confocal imaging.

Preparation of collagen matrices and microtracks

Collagen matrices and microtracks were prepared as previously described using acid-extracted type I collagen from rat tail tendons [144]. Collagen stock solution (10 mg/ml) was diluted to the desired concentration (1.5 – 5 mg/ml) using ice-cold culture medium and neutralized with sodium hydroxide. For 3D matrix experiments, dissociated MDA-MB-231 cells were incorporated sparsely into neutralized collagen solution prior to polymerization for 30 minutes at 37°C. For *ex situ* time-lapse imaging, excised tumors were similarly embedded within collagen matrix for stabilization. Collagen microtracks with dimensions of 10 × 1100 × 20 μm ($w \times l \times d$) were prepared as previously described [60]. Briefly, micropatterned polydimethylsiloxane (PDMS) stamps were rendered non-adhesive with bovine serum albumin before being washed with neutralized collagen solution and inverted over a drop of neutralized collagen solution. Collagen was polymerized for 90 minutes at 37°C, PDMS stamps were removed, and MDA-MB-231 cells were seeded onto patterned collagen matrices at low density to minimize cell-cell interactions. Finally, patterned collagen matrices were covered with a collagen lid to form three-dimensional microtracks. Except where indicated in Figure 2, all *in vitro* studies were performed in 1.5 mg/ml collagen matrix (3D) and 3.0 mg/ml collagen microtracks.

Confocal and time-lapse imaging

Confocal fluorescence and reflectance images were acquired as previously described [144] using a Zeiss LSM700 confocal microscope on a Zeiss AxioObserver Z1 inverted stand equipped with a long working distance water-immersion C-Apochromat 40×/1.1 NA Zeiss objective. Fluorescent labeling and imaging of actin and

microtubules (α-tubulin) was performed as previously described [129]. The ImageJ (v. 1.49b, National Institute of Health, Bethesda, MD) plugin OrientationJ was used to quantify and colorize actin organization from confocal fluorescence images as previously described [144]. Briefly, greyscale images were analyzed using a 0.6 μm Gaussian window and angular distributions of pixel orientation were normalized to microtrack angle. The mean and standard deviation of distributions were quantified and compared for n = 8-10 cells per condition. Phase contrast images were acquired using a Zeiss Axio Observer Z1 inverted phase contrast microscope equipped with a Hamamatsu ORCA-ER camera. Time-lapse phase contrast and confocal imaging were performed in custom temperature-, humidity-, and CO_2-controlled microscope incubation chambers.

Cell migration studies and analysis

Following cell seeding, 3D matrices and microtracks were overlaid with complete culture medium and incubated for 6-8 hours to allow cell adhesion and spreading prior to time-lapse imaging. To study the molecular mechanisms underlying cell migration through 3D matrix and microtracks, inhibitors of cell-matrix adhesion, contractility, and cytoskeleton dynamics were either applied immediately prior to imaging or after 4-5 hours of control imaging. For phase contrast time-lapse imaging, images were acquired at 5-minute intervals for 16 hours. Cells that divided or interacted with other cells during this time were excluded from analysis, and ImageJ (v. 1.49b, National Institute of Health, Bethesda, MD) was used to measure cells' morphologies and track the positions of cell centroids over time. To account for heterogeneity of cell

migration behavior, two migration parameters were measured: motile fraction and migration speed. A cell was considered motile if its centroid moved more than one cell diameter during the observation period, and motile fraction was determined by dividing the number of motile cells by the total number of cells in each frame of view. Cell migration speed within microtracks was quantified for motile cells as previously reported [60]. Motile fraction and migration speed were quantified post-treatment for n > 40 cells per condition from 2-3 independent experiments. To quantify cell morphodynamics during microtrack migration, cells were classified as amoeboid (rounded; aspect ratio < 4) or mesenchymal (elongated; aspect ratio > 4) as indicated in Figure 3F. Cell aspect ratio during microtrack migration was tracked for ~35 cells/condition to measure the rate at which cells underwent amoeboid→mesenchymal and mesenchymal→amoeboid transitions.

Polyacrylamide gel synthesis and traction force microscopy

Polyacrylamide substrates with Young's moduli of 5 kPa were synthesized, functionalized with N-6-((acryloyl)amido)hexanoic acid, coated with 100 µg/mL type I rat tail collagen (Becton Dickinson, Franklin Lakes, NJ), and used for traction force microscopy (TFM) as previously described [129, 136, 246]. Cells were seeded on polyacrylamide substrates and allowed to adhere and spread for 6-8 hours before treatments were initiated. After 10 hours of treatment, TFM experiments were performed and the traction field was derived from bead displacements using the LIBTRC analysis library developed by Dr. Micah Dembo (Boston University, Boston,

MA) [136]. Data are presented as mean ± SEM of total force magnitude, |F|, which is the integral of the traction field over the area of the cell for 20-60 cells per condition.

Western blotting

Following cell seeding in 3D collagen matrices (1.5 mg/ml), samples were incubated for 24 h, then treated with inhibitors of cell contractility for 4 h. Total protein was extracted from snap-frozen gels with preheated (95°C) 2× Laemmli sample buffer and twenty microliters of protein extract was subjected to sodium dodecyl sulfate (SDS)-polyacrylamide gel electrophoresis. Protein was electro-transferred onto a polyvinylidene difluoride membrane and the blots were incubated with primary antibody overnight at 4°C followed by horseradish peroxidase-conjugated secondary antibody for 1 hour at room temperature. Peroxidase signal was revealed with the SuperSignal West Pico or West Femto kit (Thermo Scientific, Rockford, IL). For quantification, p-MLC signal was normalized to GAPDH before comparison to control (no treatment). Data are presented as mean ± SEM for two independent experiments.

Flow cytometry

Cell adhesion to ECM via β1 integrin was blocked with the mouse monoclonal function-blocking antibody 4B4. Surface expression of β1 integrin was determined using a 4B4-FITC conjugate and FACS analysis with a FACSAria high speed flow cytometer (BD Biosciences, Franklin Lakes, NJ). In separate experiments, MDA-MB-231 cells were transfected with GFP-LifeAct (kind gift from Jan Lammerding, Cornell

University, Ithaca, NY), isolated using a FACSAria high speed flow cytometer, and seeded into collagen microtracks for confocal imaging.

Statistical analysis

Data are presented as mean ± SEM or box and whisker plots, where boxes indicate medians and $25^{th}/75^{th}$ percentiles and bars represent $5^{th}/95^{th}$ percentiles. Means were compared using analysis of variance with a post-hoc Tukey's Honestly Significant Difference (HSD) test or Dunnett's test where appropriate using JMP software (v.10, SAS Institute, Cary, NC). Microtrack migration speeds were compared using a non-parametric Wilcoxon test. Amoeboid→mesenchymal and mesenchymal→amoeboid transition frequencies were compared by two-tailed Student's t-test. Actin alignment distributions were compared using Levene's test for equal variances. Statistical significance was considered with $p < 0.05$.

4.4 Results

Cell-sized gaps in native stromal ECM and microfabricated collagen tracks support malignant cell invasion

Previously, we showed that microfabricated collagen tracks closely mimic the tube-like proteolytic tracks created by metastatic cancer cells migrating in 3D collagen matrix [60]. Using this system as a model for "follower cell" migration, we found that microtracks provide three-dimensional space through collagen matrix that enables MMP-independent migration of highly metastatic MDA-MB-231 cells as well as migration of non-invasive MCF-10A mammary epithelial cells. Here, we used an

orthotopic murine mammary cancer model to observe interactions between breast cancer cells and the native stromal extracellular matrix during tumor invasion. Three weeks after implantation of GFP-expressing MDA-MB-231 cells into the cleared mammary fat pad, palpable tumors had grown and cancer cells had begun expanding into and invading through the stromal ECM. *Ex situ* confocal imaging (Figure 4.1A) and *in situ* multiphoton imaging (Figure 4.1B) revealed channel-like gaps in the collagenous stromal ECM adjacent to mammary tumors as indicated by absence of reflected light and second harmonic signals, respectively (Figure 4.1A,B; double arrowheads).

Since confocal reflectance microscopy depends on interfacial light scattering due to refractive index mismatch, lack of reflectance signal indicates a lack of light scattering material within the aqueous interstitial space [247]. Notably, cells at the tumor periphery were observed squeezing into and through these spaces (Figure 4.1A; right panel, asterisks). Confocal reflectance microscopy of patterned collagen microtracks showed that collagen matrix structure around *in vitro* microtracks resembled ECM structure around *in vivo* microtracks, with aligned ECM fibers bounding an approximately 10-15 μm wide track on all sides (Figure 4.1A,C,D). To monitor cell migration through the stromal ECM, tumors were excised and imaged *ex vivo* using time-lapse confocal imaging (Figure 4.1E), which revealed cells migrating through gaps in the ECM (Figure 4.1E; double arrowheads). Similarly, MDA-MB-231 cells readily migrated through patterned collagen microtracks *in vitro* (Figure 4.1F).

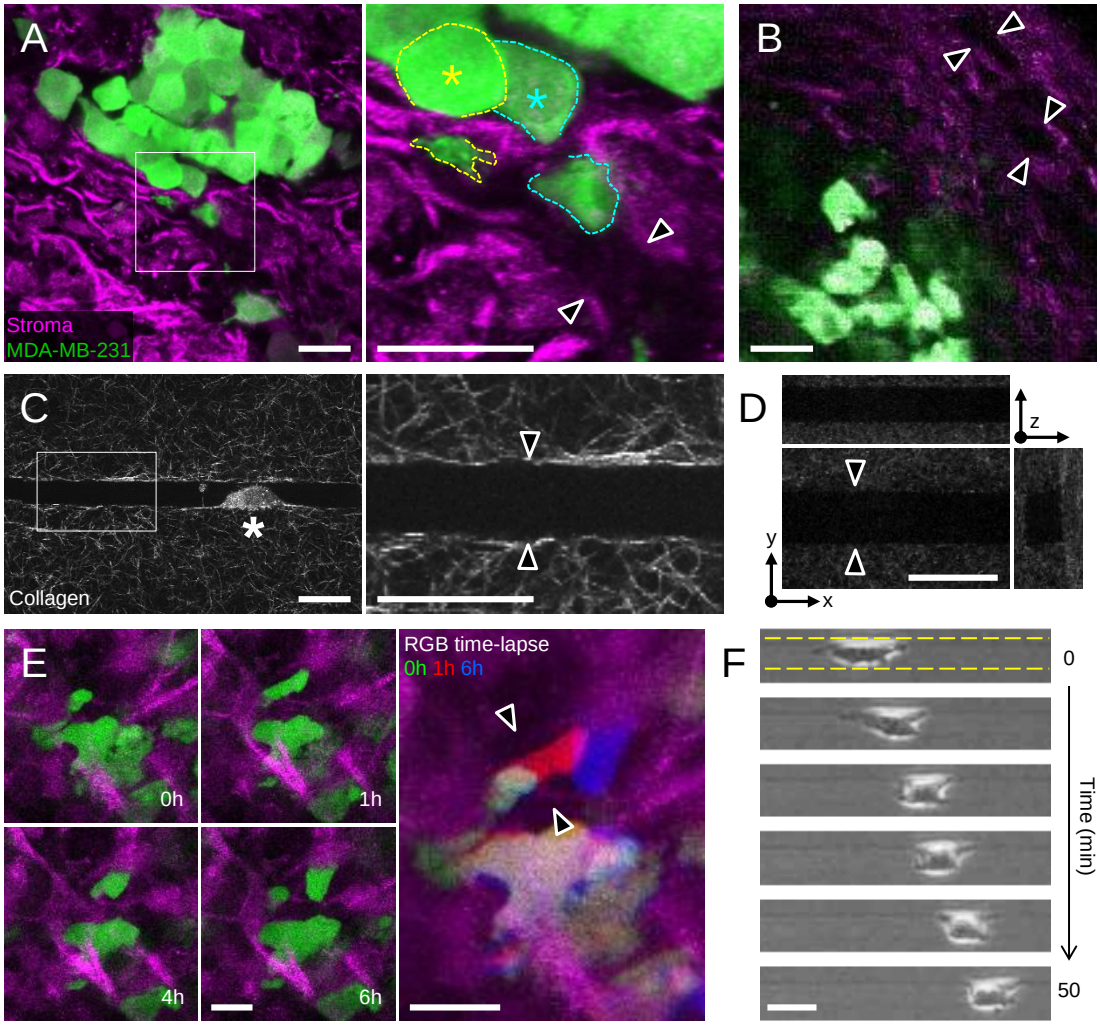

Figure 4.1. Channel-like gaps in stromal extracellular matrix and microfabricated collagen tracks. (A) *Ex situ* confocal images of GFP-expressing MDA-MB-231 cells (green) migrating through the stromal extracellular matrix (purple) in the murine mammary fat pad following 3 weeks of orthotopic tumor growth. 3× magnified image of cells and matrix at the indicated tumor/stroma interface. Asterisks and dashed outlines indicate tumor cells extending into open matrix pathway. **(B)** *In situ* two-photon image of mammary fat pad showing tumor cells and stromal extracellular matrix. **(C)** Confocal reflectance images of microtrack patterned in 3 mg/ml collagen. Asterisk indicates cell migrating within channel. **(D)** Orthogonal views of a patterned collagen microtrack. **(E)** Time-lapse *ex situ* confocal reflectance and fluorescence images of cells migrating through mammary stroma. RGB overlay of cell position over time. **(F)** Time-lapse phase contrast image series of MDA-MB-231 cell migrating through collagen microtrack. Dashed lines indicate microtrack edges. Arrowheads in A-E denote cell-scale gaps within the ECM. Scale bars: 25 µm.

Migration through collagen microtracks is independent of collagen matrix density

It has been established that native mammary stoma exhibits significant heterogeneity of biophysical and biochemical ECM properties at both the micro- and macro-scales [40]. Therefore, to investigate the effects of matrix density and tissue structure on metastatic cancer cell migration, cells were seeded in three-dimensional collagen matrix or collagen microtracks of varying collagen concentration. As shown by confocal reflectance microscopy, all matrices were composed of interconnected networks of collagen fibers and pores whose structure and organization were concentration-dependent: matrices of increasing density were more tightly packed and contained smaller fibers and pores (Figure 4.2A). Two motility metrics were used to quantify cell movement throughout the study: *motile fraction* describes what portion of the total cell population is migratory and *cell speed*. As previously shown, increasing collagen density significantly decreased motile fraction within 3D collagen matrices [47, 55], and less than 10% of cells were migratory within 5 mg/ml collagen matrices (Figure 4.2B). In contrast, collagen density did not significantly affect motile fraction (Figure 4.2B) or single-cell migration speed (Figure 4.2C) of cells within microtracks. For all collagen concentrations tested, 80-90% of cells were motile in microtracks and migration speeds consistently ranged from ~0.5-1.5 μm/min. While collagen density exerts a modest effect on patterned microtrack dimensions [60], these changes did not significantly impact microtrack migration. Together, these findings indicate that cell migration through microtracks is independent of the density of the surrounding matrix.

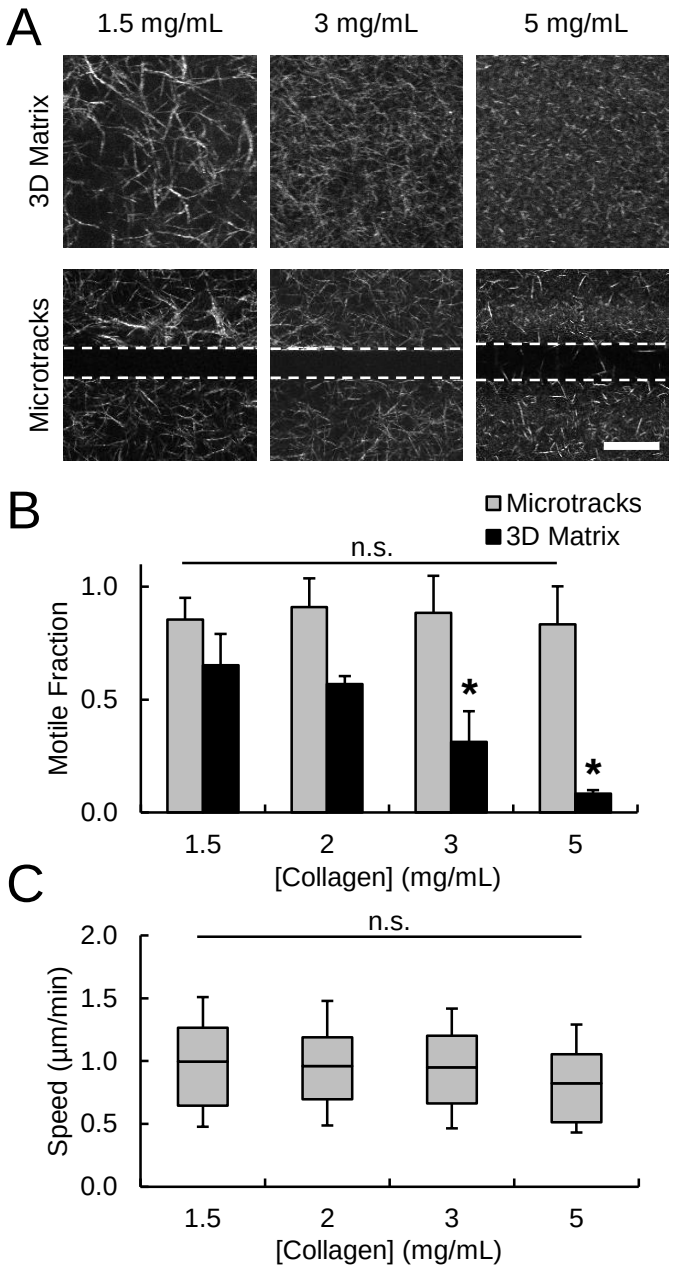

Figure 4.2. Density-dependent cell migration through 3D collagen matrix and microtracks. (A) Confocal reflectance images of collagen matrix structure in 3D matrix (top) and microtracks (bottom). Dashed lines indicate microtrack edges. Scale bar: 25 μm. **(B)** Fraction of motile cells within 3D matrix and collagen microtracks as a function of matrix density. **(C)** Single-cell speeds of motile cells within collagen microtracks.

β1 integrin adhesion mediates elongated microtrack migration

The independence of microtrack migration on matrix density suggests that cell-matrix interactions play a unique role in microtracks as compared to 2D and 3D environments. Therefore, the β1 integrin function-blocking monoclonal antibody 4B4 was used to probe the role of cell-matrix adhesion in cancer cell migration through 3D matrix and collagen microtracks. Flow cytometry was used to verify that maximal β1 integrin inhibition was achieved using 10 μg/mL 4B4 (Figure 4.3A).

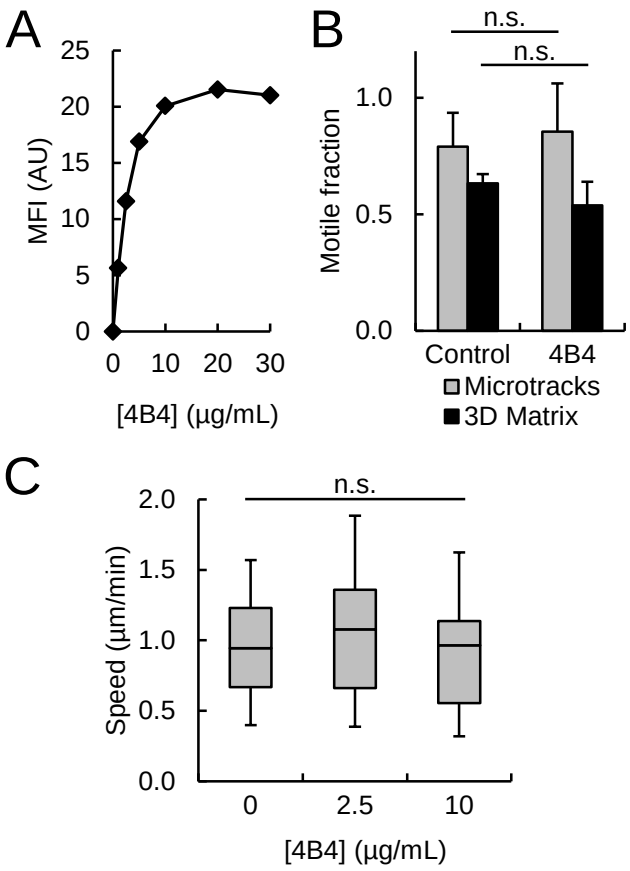

Figure 4.3. Effect of β1 integrin function blocking on cell migration. (A) Flow cytometry data showing fluorescence signal from cells treated with 0-30 μg/mL FITC-4B4. **(B)** Fraction of motile cells within 3D matrix and collagen microtracks treated with 10 μg/mL β1 integrin function-blocking antibody 4B4. **(C)** Single-cell speeds of motile cells within microtracks under increasing concentrations of 4B4.

Treatment with 4B4 did not significantly affect motile fraction in microtracks or 3D matrix, where ~85% and ~60% of cells were motile, respectively (Figure 4.3B). As previously shown [47, 57], inhibition of β1 integrin decreased cell elongation and migration speed in 3D matrix (Figure 4.4A). Interestingly, β1 integrin blocking did not affect single-cell migration speed in microtracks (Figure 4.3C), but treatment with 4B4 did alter the morphology of migrating cells (Figure 4.4B).

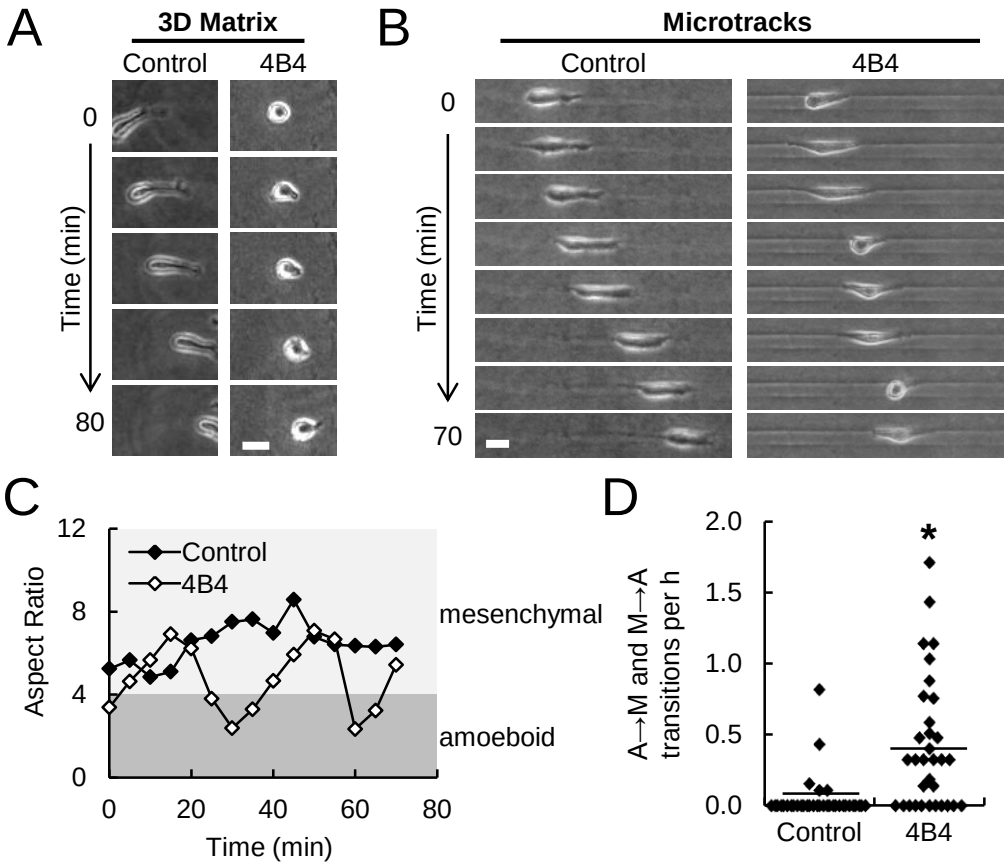

Figure 4.4. Regulation of elongated microtrack migration by β1 integrin. (A,B) Time-lapse image series of control and 4B4-treated (10 μg/mL) cells migrating in 3D matrix and microtracks. **(C)** Aspect ratios of cells in B. Aspect ratios < 4 correspond to rounded, amoeboid morphologies (dark gray region); aspect ratios > 4 correspond to elongated, mesenchymal morphologies (light gray region). **(D)** Frequency of amoeboid-mesenchymal ('A→M') and mesenchymal-amoeboid ('M→A') transitions during microtrack migration. Each data point represents an individual cell. Horizontal lines indicate means. Scale bars: 25 μm.

Whereas control cells exhibited consistently elongated, mesenchymal-like (high aspect ratio) morphologies during microtrack migration (Figure 4.4C; filled diamonds), β1-inhibited cells showed a saltatory pattern of morphology, oscillating between elongated, mesenchymal-like (high aspect ratio) and rounded, amoeboid-like (low aspect ratio) morphologies during migration (Figure 4.4C; open diamonds). Since the majority of control cells retained an elongated, mesenchymal morphology during microtrack migration, morphology switching was infrequent (0.04±0.02 transitions/h) as compared to 4B4-treated cells, which underwent morphology transitions ~10× more frequently (0.45±0.08 transitions/h) (Figure 4.4D). Thus, while β1 integrin adhesion is not required to maintain migration speed within microtracks, it does facilitate elongated mesenchymal morphology during migration.

Actomyosin contractility, but not traction generation, is required for efficient microtrack migration

Actomyosin-mediated contractility underlies several biomechanical functions central to invasive cell migration including cell body/nuclear deformation and traction force generation [1]. Myosin light chain (MLC) phosphorylation is the enabling molecular step in cell contractility and is controlled by several upstream regulators including the Rho-GTPase/Rho-associated kinase (ROCK) pathway and myosin light chain kinase (MLCK) [108]. To elucidate the role of cell contractility in microenvironment-dependent migration, pharmacological inhibitors targeting several players within the actomyosin contractility network were applied to cells in 3D matrix and microtracks.

Inhibition of Rho (CT04), ROCK (Y27632), MLCK (ML7), or myosin II (blebbistatin) significantly reduced motile fraction within 3D matrix, but had no effect on motile fraction within microtracks (Figure 4.5A), indicating a requirement for cell contractility during migration through restrictive 3D matrix environments.

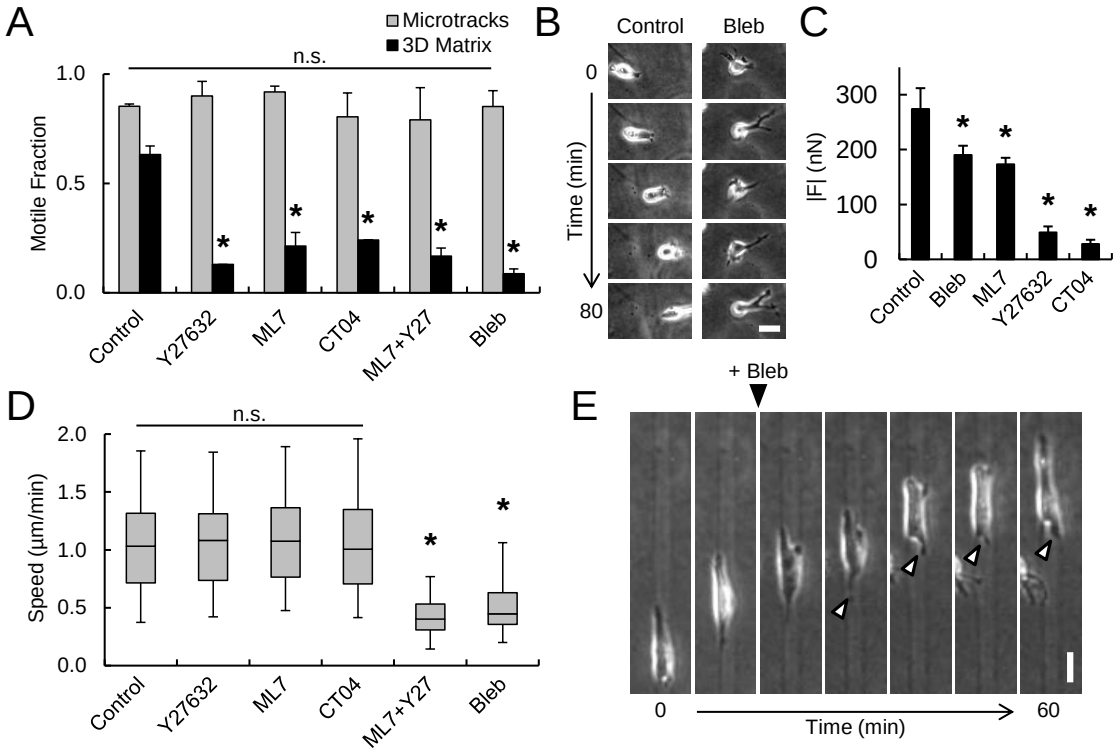

Figure 4.5. Role of cell contractility and traction forces in microtrack migration. **(A)** Fraction of motile cells within 3D matrix and collagen microtracks treated with: Y27632, ROCK inhibitor; ML7, MLCK inhibitor; CT04, Rho inhibitor; ML7 + Y27632; and blebbistatin (Bleb), myosin II inhibitor. **(B)** Representative frames from time-lapse series of cells migrating in 3D matrix under control and blebbistatin treatment. **(C)** Total traction force magnitude, |F|, of cells under treatments in A. **(D)** Single-cell speeds of motile cells within collagen microtracks under conditions in A. **(E)** Time-lapse image series of cell migrating in microtrack treated with blebbistatin at +20 minutes. Arrowheads indicate lagging cytoplasmic extensions after treatment. Scale bars: 25 μm.

As demonstrated by time-lapse imaging, contractility-deficient cells in 3D matrix exhibited a protrusive, non-motile phenotype characterized by: (1) extension of

anuclear, branching pseudopodia and (2) failure to translocate the cell nucleus and body (Figure 4.5B). Interestingly, while inhibition of Rho, ROCK, and MLCK alone significantly reduced cell traction forces (Figure 4.5C), these treatments had no effect on cell migration speed within microtracks (Figure 4.5D), indicating that traction forces are not explicitly required for microtrack migration. However, when both MLCK and ROCK were inhibited (ML7+Y27) or myosin II activity was inhibited directly (Bleb), microtrack migration speed was significantly reduced (Figure 4.5D), indicating that myosin activity contributes to maintenance of cell speed within microtracks. In addition to a significant reduction in traction force magnitude with blebbistatin treatment (Figure 4.5C), analysis of cell morphology prior to and following treatment indicated that the blebbistatin-induced decrease in microtrack migration speed was accompanied by impaired retraction of the trailing edge (Figure 4.5E; arrowheads). This behavior was also observed using other inhibitors of contractility. These results indicate that traction generation, 3D matrix migration, and microtrack migration can be pharmacologically decoupled and suggest that these behaviors may operate under the control of different mechanistic elements of the cell contractility pathway.

Since myosin light chain phosphorylation enables myosin ATPase activity that ultimately drives cell contractility, MLC phosphorylation was measured by Western blotting following 4 hours of treatment with contractility inhibitors. Treatment with Y27, CT04, and ML7+Y27 significantly reduced pMLC, but ML7, blebbistatin, and DMSO vehicle control did not significantly change pMLC signal (Figure 4.6A). These

treatments exhibited differential effects on cell behavior (Figure 4.5A-D), relative pMLC intensity was plotted against experimentally defined cell behaviors for each treatment to understand the relationship among MLC phosphorylation, cell migration, and traction generation (Figure 4.6B). Although ML7 inhibits MLCK, this treatment had no effect on MLC phosphorylation, suggesting that the effects of ML7 on 3D cell motility (Figure 4.5A) and traction force generation (Figure 4.5C) were due to off-target effects of the drug rather than a reduction in MLCK-dependent MLC phosphorylation. Alternatively, compensatory MLC phosphorylation under ML7 treatment could have been achieved through signaling pathways other than MLCK (e.g., ROCK) and/or the measured cell responses could exhibit different sensitivity to ML7 dose. Due to this uncertainty and the unknown mechanism of action on the measured behaviors, ML7 data was excluded from correlation analysis. MLC phosphorylation was not correlated with motile fraction within microtracks ($R^2 = 0.20$ for linear fit), motile fraction within 3D matrix ($R^2 = 0.13$ for linear fit), or microtrack migration speed ($R^2 = 0.01$ for linear fit), suggesting that MLC phosphorylation is not a unique regulator of cell migration. However, MLC phosphorylation was positively correlated with traction force generation ($R^2 = 0.86$ for linear fit), indicating pMLC promotes traction generation. Together, these results suggest that while myosin II activity downstream of MLCK and ROCK mediates migration through 3D matrix and retraction of the cell rear for efficient migration through microtracks, microtrack migration does not require MLC phosphorylation-dependent traction generation and is likely driven by parallel contractility mechanisms.

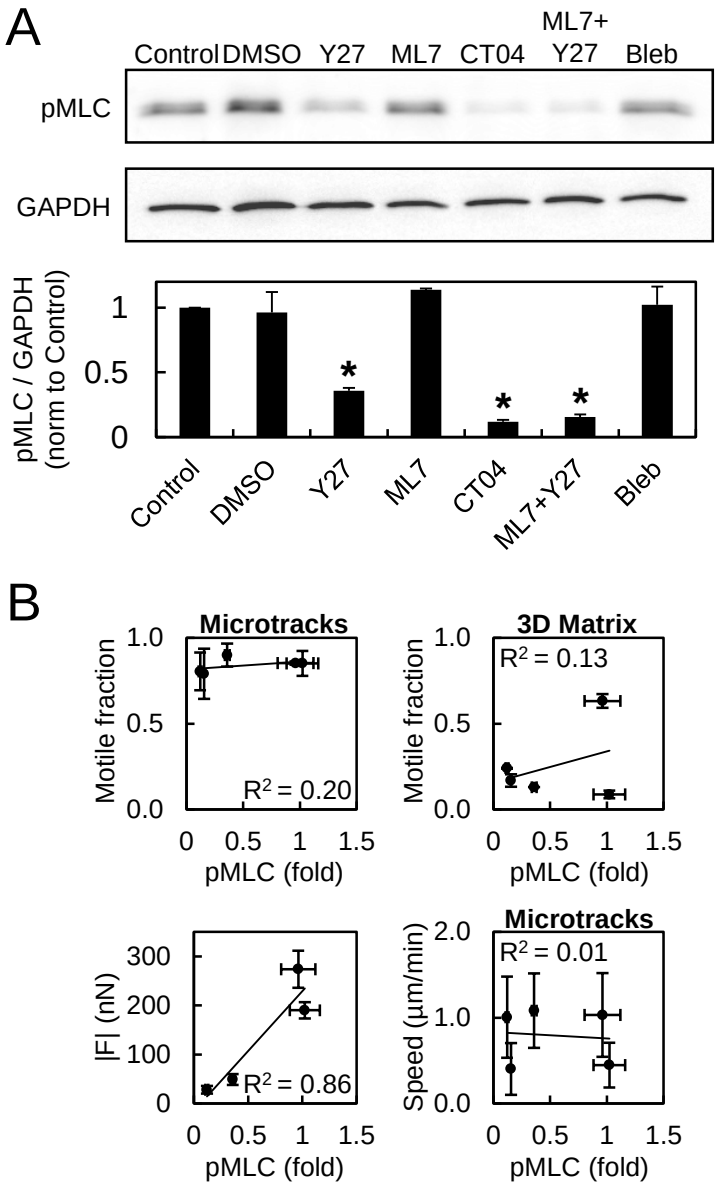

Figure 4.6. Role of MLC phosphorylation in regulating cell behaviors. (A) Western blot for pMLC in 3D matrix after 4 hours of treatment with inhibitors in Figure 4.5A. **(B)** Linear correlations between pMLC and: microtrack motile fraction, $R^2 = 0.20$; 3D matrix motile fraction, $R^2 = 0.13$; traction force magnitude, $R^2 = 0.86$; microtrack migration speed, $R^2 = 0.01$. Microtrack migration speed is represented as median ± SD; all other data are represented as mean ± SEM.

Actin and microtubule dynamics are required for microtrack migration

Cytoskeletal dynamics downstream of the ubiquitous Rho-family of GTPases are largely responsible for determination of cell morphology and motility [92, 232]. Since coordination of and crosstalk between the actin and microtubule (MT) cytoskeletons are particularly important for the initiation and development of cell protrusions [88, 248], the roles of actin and MT cytoskeleton dynamics in microtrack migration were assessed. Cells migrating within collagen microtracks contained primarily cortical F-actin and a polarized microtubule network aligned with the microtrack (Figure 4.7A). Inhibition of MT polymerization with nocodazole (Noco) and MT depolymerization with paclitaxel (Ptx) were verified by α-tubulin immunofluorescence (Figure 4.7A; right panels). Both treatments significantly decreased motile fraction in 3D matrix and microtracks (Figure 4.7B), reduced microtrack migration speed by approximately 50% (Figure 4.7C), and promoted more rounded cell morphology within microtracks (Figure 4.7A; right panels). Inhibition of F-actin polymerization with cytochalasin D (Cyto D) or latrunculin A (Lat A) prevented cell motility in both 3D matrix and microtracks (Figure 4.8A). To more closely examine the role of actin polymerization in microtrack migration, Lifeact-transfected cells in microtracks were imaged with time-lapse confocal microscopy before and after treatment with cytochalasin D. Migrating cells exhibited distinct front-back polarity of the actin cytoskeleton, with dynamic F-actin-rich protrusive structures at the leading edge (Figure 4.8B).

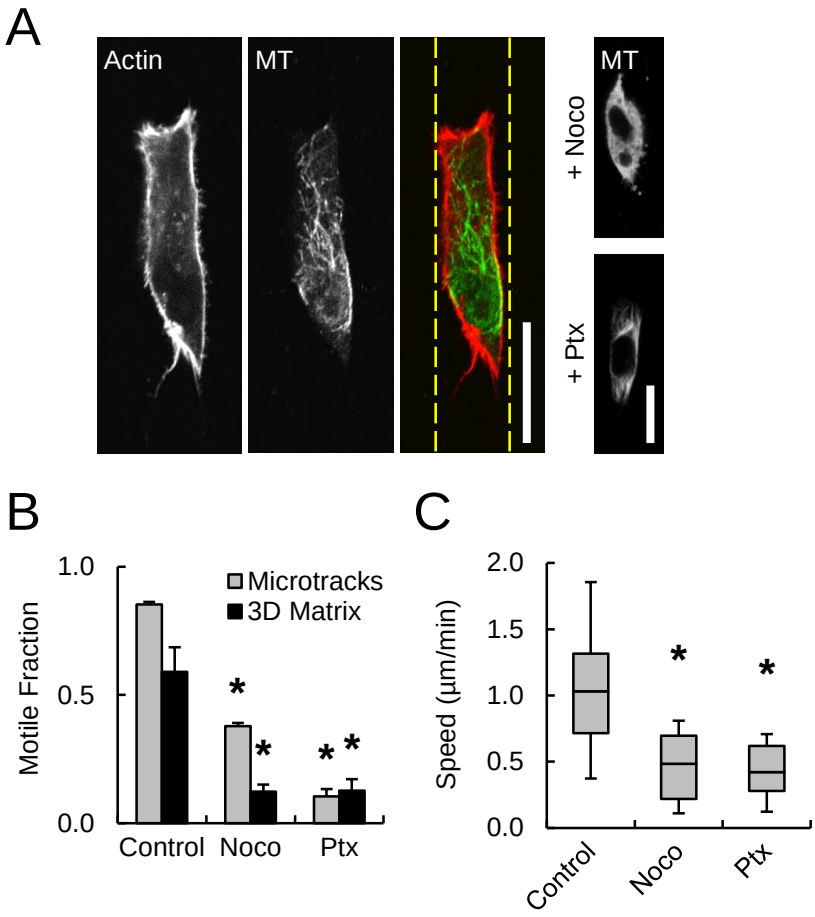

Figure 4.7. Requirement for microtubule dynamics during migration through physiological ECM. (A) Confocal fluorescence images of actin and microtubule organization in microtrack-migrating cells under control, + Noco, and + Ptx conditions. **(B)** Fraction of motile cells within 3D matrix and collagen microtracks treated with Nocodazole (Noco), microtubule polymerization inhibitor and Paclitaxel (Ptx), microtubule stabilizer. **(C)** Single-cell speeds of motile cells within collagen microtracks under conditions in A. Box and whisker plots show medians, $25^{th}/75^{th}$, and $5^{th}/95^{th}$ percentiles.

Upon treatment with cytochalasin D, cell migration was immediately arrested and the aligned cortical F-actin network dissociated into small, randomly oriented actin bundles throughout the cell body (Figure 4.8B; arrowhead). OrientationJ was used to pseudocolor actin as a function of feature orientation relative to the microtrack (Figure 4.8C).

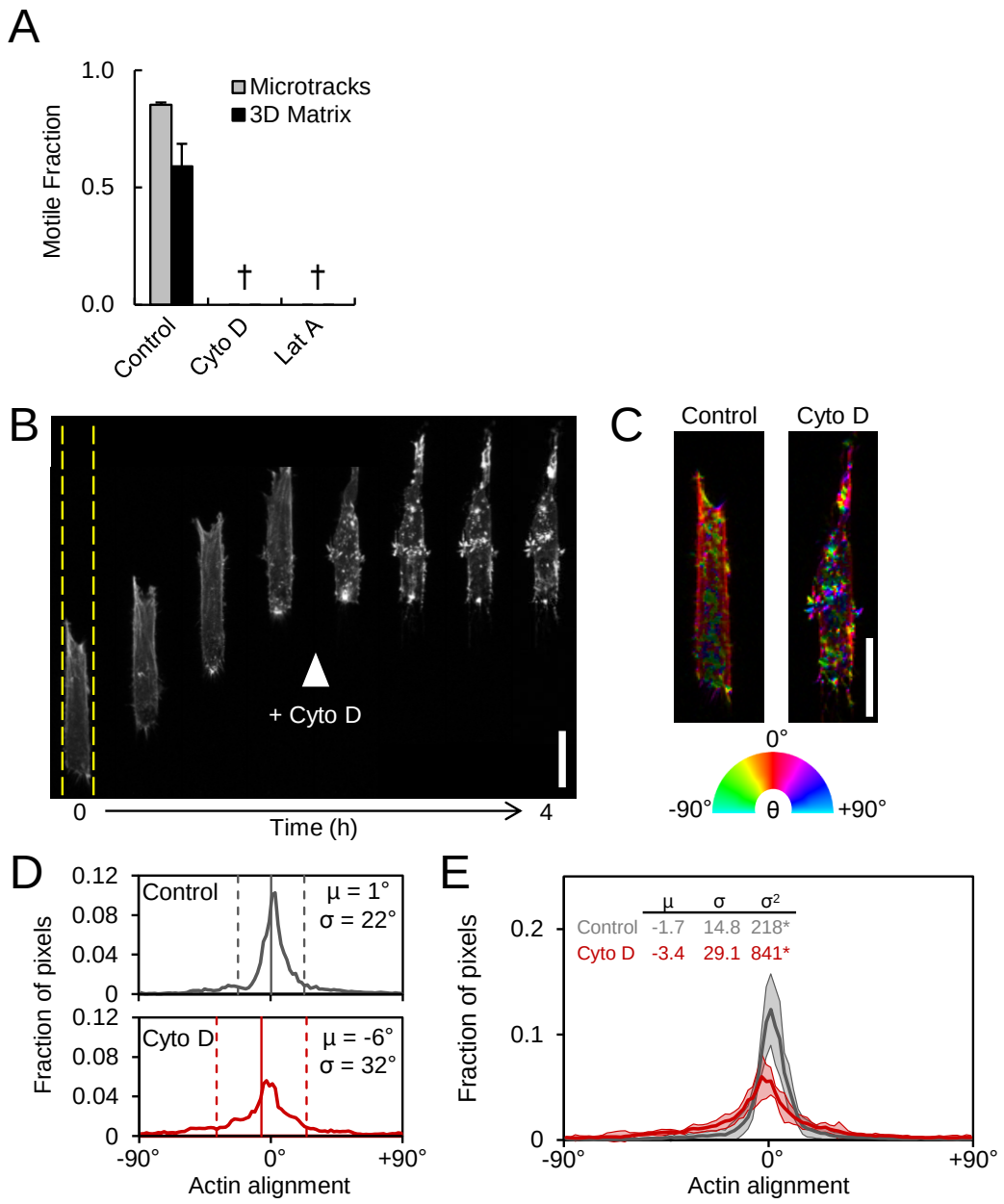

Figure 4.8. Requirement for actin cytoskeleton dynamics during migration through physiological ECM. (A) Fraction of motile cells within 3D matrix and collagen microtracks treated with actin polymerization inhibitors Cytochalasin D (Cyto D) and Latrunculin A (Lat A). †, no motile cells detected. **(B)** Confocal fluorescence time-lapse image series of Lifeact-transfected cell migrating through microtrack, with Cyto D added when indicated. **(C)** Selected panels from B pseudocolored to indicate actin alignment. Dashed yellow lines indicate microtrack edges. **(D)** Actin alignment distributions of control and cytochalasin D-treated cells in C. μ = distribution means (solid vertical lines); σ = distribution standard deviations (dashed vertical lines). **(E)** Actin alignment distributions and descriptive statistics from multiple cells. Scale bars: 25 μm.

To quantify alignment, the mean (μ) and standard deviation (σ) were extracted from actin orientation distributions (Figure 4.8D; vertical solid and dashed lines, respectively). While control and cytochalasin D-treated cells showed alignments centered around 0°, cytochalasin D treatment resulted in a significant increase in distribution variance as determined by Levene's test for equal variances, indicating that treatment significantly reduced actin alignment (Figure 4.8E). These results indicate that migration through physiological collagen microtracks: (1) is associated with a well-organized and aligned cortical actin cytoskeleton, (2) requires actin polymerization-driven protrusion, and (2) is enhanced by MT dynamics that support directional protrusion and elongation.

4.5 Discussion

Local tissue invasion is an inherently biophysical process that requires cells to coordinate adhesive, cytoskeletal, contractile, and proteolytic cellular machinery to negotiate matrix and tissue barriers in the tumor microenvironment. Tumor cell migration is highly adaptive, and the specific molecular mechanisms employed by cells to invade are determined largely by physiochemical properties of the stromal extracellular matrix including composition, architecture, and mechanics[48, 229]. Here, we used an *in vitro* collagen microtrack platform[60] to define the biochemical and biophysical mechanisms that mediate migration through physiologically relevant cell-scale tracks within interstitial tissue. We demonstrate that mechanisms of migration within collagen microtracks are distinct from those required for migration through 3D collagen matrix. Unlike mesenchymal tumor cell migration in 3D matrix,

microtrack migration is matrix density-independent and does not require β1 integrin adhesion. We show that migration through collagen microtracks, but not 3D matrix, can proceed in the absence of pMLC-dependent traction forces and that actin and microtubule cytoskeleton dynamics regulate cell migration through both collagen microtracks and 3D matrix. Together, these findings represent the first description of cell migration mechanisms within physiological collagen microtracks and suggest that once cells reach pre-formed paths of least resistance within the interstitial stroma, the molecular machinery required for efficient migration may be considerably reduced, effectively lowering the mechanistic threshold for local tissue invasion.

Modeling migration through the stromal extracellular matrix

The stromal ECM surrounding tumors primarily consists of type I collagen organized into interconnected fibrillar networks whose physiochemical properties, including stiffness [57, 81, 106], composition [58, 249] and architecture, regulate three-dimensional invasive behavior. While recent work has highlighted the roles of matrix porosity [47, 55], alignment [56, 206], and interfacial features [200] in modulating 3D migration, *in vitro* models for the study of migration through collagenous ECM generally overestimate matrix uniformity [42] and the effect of local heterogeneity in ECM structure remains poorly understood. Notably, cell-scale gaps in the stromal ECM, including clefts between ECM fibers, interfaces between tissue components, organized networks of ECM pores, and cell-derived proteolytic microtracks, have been identified as conduits for tumor cell migration both *in vitro* [144, 162, 208, 239, 250] and *in vivo* [37, 40, 48, 49]. Here, we show that microfabricated collagen tracks

closely resemble the channel-like gaps found in the native mammary gland stromal ECM, providing both a path of least resistance and highly aligned features that promote rapid, MMP-independent cancer cell migration [60].

Mechanisms of microtrack migration

During cancer progression, homeostatic ECM maintenance is lost, leading to deregulation of biophysical matrix properties [2, 13, 251]. Thus, invasive carcinoma stroma exhibits a desmoplastic response [29] that can include increased collagen I density and crosslinking [105, 106]. While migration through 3D matrix is negatively regulated by matrix density due to increased steric resistance, we show here that microtracks overcome this restriction by providing cell-caliber space, enabling matrix-density-independent migration [47, 55, 162]. Since changes in matrix density can alter adhesion ligand availability, which has been shown to modulate cell migration in 2D [252] and 3D environments [57, 253], these results suggest that microtrack migration is ligand-density-independent. Furthermore, while β1 integrin inhibition in 3D matrix results in inefficient, rounded migration, microtrack migration speed is not affected by β1 integrin blocking. Together, these results are consistent with recent findings by Wolf et al. that sufficiently large pores in 3D collagen matrix reduce the need for matrix remodeling and integrin-mediated mechanocoupling during mesenchymal migration [47]. Interestingly, cells treated with mAb 4B4 oscillate between mesenchymal and amoeboid morphologies during migration, indicating that persistent cell elongation within microtracks requires β1 activity. Thus, while β1 integrin ligation is not required for microtrack migration per se, β1 integrin may function as

part of integrin signaling and trafficking pathways that integrate with Rho GTPases including Rac1 [254], whose activity promotes actin-dependent membrane protrusion and maintains cell polarity [96]. Our findings compliment previous work in 3D matrix illustrating that integrin blocking in mesenchymal cells restricts cell elongation and reduces migration speed [47, 57] and indicate that cell spreading and migration in microtracks involve cell-matrix interaction programs that are unique to those employed in 2D and 3D microenvironments.

The application of cytoskeletal tension to the extracellular matrix results in traction forces that enable cell and matrix deformation and promote migration through restrictive 3D microenvironments [47, 134]. Here, we show that inhibition of actomyosin contractility or its upstream regulators MLCK and Rho/ROCK significantly reduces cell traction force and abolishes 3D matrix migration. Excessive cell elongation and indiscriminate generation of branching cytoplasmic projections under contractility inhibition are consistent with release of cortical tension [255] and failure to deform the cell body and/or matrix to squeeze through pores [47]. Interestingly, inhibition of single upstream mediators of myosin II activity does not affect microtrack migration, but migration is hindered when myosin II is directly inhibited with blebbistatin or both MLCK and ROCK are inhibited with ML7 and Y27632. These results suggest that the MLCK and Rho/ROCK pathways may provide compensatory activation of myosin II to maintain rapid microtrack migration. Indeed, MLCK and Rho/ROCK have been shown to play distinct spatial and temporal roles during adhesion and migration [108, 256], and while we do not observe such

specificity in microtracks here, it remains that these upstream regulators may act on myosin II activity through parallel and compensatory pathways. In support of this hypothesis, the contractility inhibitors used here elicit a variety of effects on myosin light chain phosphorylation, which we show is a poor indicator of migration behavior. Conversely, pMLC is correlated with traction force generation, confounding the link between pMLC-dependent traction generation and migration through 3D matrix and microtracks. While we have previously observed traction generation and ECM displacement during microtrack migration [60], we demonstrate here that this behavior is not required for migration since inhibition of Rho with CT04 reduces traction forces and pMLC by ~90%, but has no effect on microtrack migration. Instead, as indicated by lagging cytoplasmic extensions in migration-deficient cells, actomyosin contractility is likely utilized in microtracks to retract the cell rear, which is a characteristic requirement of mesenchymal-type migration strategies [145, 257]. Notably, our group and others have shown that cell contractility is required for matrix reorganization [56, 206], and microtrack generation [144, 208], but not perception and response to matrix structure. The present results are consistent with this conclusion and together suggest that pre-formed space in the ECM alleviates the need for actomyosin-based matrix remodeling and pMLC-dependent traction generation in cancer cell motility, which is likely under the control of a number of parallel cell contractility pathways.

Our results indicate that cell-matrix mechanocoupling – which is critical for cancer cell migration in both planar and 3D setting [47, 141] – is largely dispensable for

migration within collagen microtracks. Alternatively, we show that actin and microtubule (MT) cytoskeletal dynamics mediate protrusive, polarized microtrack migration. Cells within microtracks exhibit a cortical actin network and polarized MT cytoskeleton which are disrupted by inhibitors of actin polymerization and MT dynamics, respectively. Inhibition of MT polymerization (nocodazole) or depolymerization (paclitaxel) limits cell spreading and reduces motility in 3D matrix and microtracks, which is consistent with previous work indicating MT dynamics enable 3D cell spreading [129] and promote elongated 3D cell protrusions [87, 88]. As previously suggested, MTs may provide means for intracellular delivery of molecular cargo needed for elongation and stabilization of actin-based protrusions [88]. In support of this hypothesis, slower, more rounded microtrack migration can continue with inhibition of MT dynamics, but migration is immediately arrested with inhibition of actin polymerization. Treatment with cytochalasin D terminates growth of actin-rich protrusions at the leading edge and results in the loss of cortical actin localization and alignment, suggesting actin dynamics contributes to both protrusion and maintenance of cortical actomyosin tension that drive microtrack migration [91, 255]. Together, these results indicate that pseudopodial protrusions at the leading edge, which are initiated by actin polymerization and supported by microtubules, provide the primary impetus for physiological collagen microtrack migration.

The ability to readily adapt cell phenotype (i.e. phenotypic plasticity) is a characteristic feature of many cancer cells [5, 95, 258]. It is presumed that such plasticity is advantageous to cancer cells as it enables cells to continue their objective

(to invade) under a variety of microenvironmental conditions. Here, we directly demonstrate that MDA-MB-231 cells adapt their mode of migration upon confronting different structural microenvironments (3D matrix versus microtracks) and when challenged pharmacologically. This well-documented switch of migration strategies by tumor cells can be induced by both cellular and extracellular influences [229, 236], and is accompanied by a shift in molecular mechanisms underlying migration [167, 259]. Briefly, amoeboid migration is generally observed in low-density ECM, where rounded, blebbing cells use low cell-ECM adhesion and strong propulsive forces and cytoskeletal contraction to negotiate matrix. Conversely, mesenchymal migration occurs in low-to-high density ECM, where elongated cells utilize stepwise and cyclical protrusion, adhesion, traction generation, and tail retraction to move through matrix [161]. Here, we show that microtrack migration can exhibit elements of both mesenchymal and amoeboid migration and further demonstrate that microtracks provide a microenvironmental context that enables cells to adapt their migration mode and thus potentially evade inhibitors of cell migration (e.g., integrin blocking and cell contractility inhibitors). The oscillatory migration strategy exhibited by 4B4-treated cells within microtracks provides direct evidence of this dynamic switching, and contrasts to the stable mesenchymal→amoeboid transition exhibited by cells treated with integrin and MMP inhibitors in 3D matrix [47, 57, 161]. Interestingly, the metric of motile fraction emerges as an indicator of migration plasticity since it describes the subset of the cell population that is able to move under a given experimental or microenvironmental condition. Thus, as motile fraction approaches 0 (e.g., high 3D matrix density, inhibition of cell contractility in 3D matrix, inhibition of actin

polymerization), cells have exhausted options for adaptation and cease migrating. Critically, our findings here that inhibition of microtubule dynamics or actin polymerization arrest cell migration are consistent with literature suggesting that RhoGTPases and cytoskeletal dynamics are required to coordinate migration mode plasticity [95, 167].

Ultimately, it will be necessary to transition findings back to an *in vivo* tumor/stroma model, but, in light of our results here and others' [48] highlighting the critical role of the microenvironment in regulating mechanisms of cell motility, this transition will require an increasingly thorough understanding of the *in vivo* stromal context. Since the composition and structure of *in vivo* stroma remain only marginally understood [37], rationally designed *in vitro* models of the tumor microenvironment represent an effective approach to defining the mechanisms of cell-matrix interactions during tumor invasion. Importantly, our collagen microtrack migration model differs from microfluidic models of confined migration fabricated from rigid, non-porous PDMS [260] and polyacrylamide [243] in that migrating cells are bounded by physiological, fibrillar collagen matrix on all sides within our system [60]. Recently, several independent studies showed that confinement within narrow microfluidic PDMS or polyacrylamide channels eliminates the need for cell contractility and actin polymerization in migration [242, 243, 260]. While these findings are in contrast to our results, they are consistent with a computational model of confined dendritic cell migration wherein a pressure buildup in the cell that is caused by the confinement induced by rigid channel walls is sufficient to produce forward movement [261]. This

model shows that migration under confinement relies on increasing friction caused by the pressure buildup, and is independent of substrate adhesion and cell contractility. An alternative model of confined cell migration suggests that water permeation across cell membranes leads to polarized changes in cell volume and migration in the absence of actin polymerization [260]. In the context of these experimental and theoretical models, our results suggest that collagen microtracks, being inherently compliant and porous substrates, may not be able to induce mechanical and osmotic pressures within the cell and therefore, require a cell to utilize actin polymerization for migration. This difference highlights the need to carefully consider all aspects of the microenvironment through which cells migrate when designing experimental models and interpreting results.

In summary, this study is the first to systematically analyze the mechanisms guiding cell migration within physiological collagen microtracks. Using a micropatterned collagen microtrack platform that recapitulates matrix-free space within the stromal ECM, we demonstrate that adhesion and contractility mechanisms uniquely regulate migration through 3D collagen matrix and collagen microtracks. Microtrack migration is insensitive to matrix density and is independent of cell-matrix mechanocoupling, both of which are significant regulators of migration within 3D matrix. Actin and microtubule cytoskeletal dynamics at the leading edge and actomyosin contractility at the cell rear promote morphological polarity that enables rapid, MMP-independent migration through microtracks. Collectively, our data provide insight into the unique collection of mechanisms required by tumor cells to migrate through pre-existing

spaces in the stromal ECM and indicate that path-following migration during leader-follower collective invasion and transit along pre-formed paths of least resistance are less mechanistically demanding strategies for local tissue invasion.

CHAPTER 5

LEADING MALIGNANT CELLS INITIATE COLLECTIVE EPITHELIAL CELL INVASION IN A 3D HETEROTYPIC TUMOR SPHEROID MODEL

This chapter was published in *Clinical and Experimental Metastasis* [144].

5.1 Abstract

Solid tumors consist of genetically and phenotypically diverse subpopulations of cancer cells with unique capacities for growth, differentiation, and invasion. While the molecular and microenvironmental bases for heterogeneity are increasingly appreciated, the outcomes of such intratumor heterogeneity, particularly in the context of tumor invasion and metastasis, remain poorly understood. To study heterotypic cell-cell interactions and elucidate the biological consequences of intratumor heterogeneity, we developed a tissue-engineered multicellular spheroid (MCS) co-culture model that recapitulates the cellular diversity and fully three-dimensional cell-cell and cell-matrix interactions that characterize human carcinomas. We found that "invasion-competent" malignant cells induced the collective invasion of otherwise "invasion-incompetent" epithelial cells, and that these two cell types consistently exhibited distinct leader and follower roles during invasion. Analysis of extracellular matrix microarchitecture revealed that malignant cell invasion was accompanied by extensive extracellular matrix remodeling including matrix alignment and proteolytic track-making. Inhibition of cell contractility- and proteolysis-mediated matrix

reorganization prevented leader-follower behavior and malignant cell-induced epithelial cell invasion. These results indicate that heterogeneous subpopulations within a tumor may possess specialized roles during tumor progression and suggest that complex interactions among the various subpopulations of cancer cells within a tumor may regulate critical aspects of tumor biology and affect clinical outcome.

5.2 Introduction

The tumor microenvironment contains a complex mixture of normal epithelial cells, highly heterogeneous malignant cells, stromal cells, and extracellular matrix (ECM) whose interactions are critical to cancer progression [28, 262]. Despite advances in *in vitro* models that have refined our understanding of how the cellular and noncellular components of the tumor microenvironment cooperate to promote or suppress disease, many tissue-engineered tumor models fail to accurately recapitulate the intratumor heterogeneity and three-dimensional tissue architecture that characterize human carcinomas [52, 235, 263]. Notably, biophysical and biochemical interactions among dissimilar cell types within the tumor microenvironment enable many key features of developing cancer including abnormal cell growth [264], enhanced angiogenesis [265], and tissue invasion and metastasis [208, 266, 267]. However, the importance of interactions among dissimilar cells *within* the tumor compartment remains to be determined. To better understand how a tumor's constituents cooperate to regulate critical phases of tumor progression, these processes should be studied using well-controlled *in vitro* tumor models that permit three-dimensional, *in vivo*-like interactions among the diverse cells and ECM that comprise the microenvironment.

Since cancer cells continually interact with other cells that are resident within or recruited to the tumor microenvironment, several experimental models have coupled malignant cells with cells such as stromal fibroblasts, endothelial cells, and immune cells to study the underlying mechanisms and clinically relevant outcomes of heterotypic cell-cell interactions. For example, Gaggioli et al. observed that stromal fibroblasts produce cell contractility- and proteolysis-dependent tracks within the ECM that are sufficient to induce squamous cell carcinoma invasion [208]. Additionally, activation of stromal fibroblasts by gastric cancer cells induces stromal expression of pro-angiogenic factors resulting in increased tumor vascularization [265]. Importantly, the cellular diversity of the tumor microenvironment is not limited to these distinct cell types, as cells of epithelial lineage within carcinomas exist along a spectrum ranging from normal epithelial cells to highly variable malignant cells [16]. In addition to the significant heritable diversity that neoplastic cells can exhibit due to the acquisition of genetic and epigenetic alterations during oncogenesis [268], cancer cells exhibit phenotypic plasticity, whereby a cell's genetic program is integrated with biochemical and biophysical cues from the extracellular microenvironment to regulate cellular phenotype [69, 105, 258]. The resulting cellular diversity within the epithelial compartment itself gives rise to substantial morphological, physiological, and behavioral intratumor heterogeneity whose functional consequences are poorly understood.

While it is clear that human carcinomas contain subpopulations of cancer cells with unique capacities for growth, differentiation, tissue invasion, and secondary tumor initiation [16, 268], the significance of interactions among cells in these various subgroups are unknown. Since local tissue invasion is both the first discernible step of metastasis and the basis for histopathological diagnosis of metastatic cancer, the invasive potential of tumor cells is of particular clinical relevance [1, 269]. During invasion, cancer cells physically dissociate from the primary tumor mass, bypass the epithelial basement membrane to move from the epithelial compartment into the stromal compartment, and negotiate the three-dimensional interstitial microenvironment on their way to a secondary site [9]. Migration through the three-dimensional stroma requires specialized cellular mechanisms including proteolysis- and cell contractility-based matrix remodeling to overcome steric hindrance imposed by the extracellular matrix [158, 174, 238, 270]. Tissue invasion is dependent upon cells' invasive fitness as well as cell-cell and cell-matrix interactions [58, 69]. For example, 3D extracellular matrix microarchitecture [55], alignment [27], and mechanics [106] regulate 3D migration efficiency [173]. Biophysical cell-cell and cell-matrix interactions including cell-cell adhesions and proteolytic matrix patterning provide additional control over the nature of invasion [69, 158, 270, 271]. Together, these findings have established important roles for extracellular control of invasion, but there remains a need to investigate cancer invasion in a more physiologically relevant heterogeneous cancer model where only a subset of cancer cells within a heterogeneous tumor may be "invasion-competent".

Tissue engineering approaches to cancer research have emerged as valuable intermediates between traditional 2D *in vitro* cell culture techniques, which often fail to accurately represent the microenvironmental complexity of tumors, and *in vivo* cancer models, whose extensive complexity can limit experimental control and confound findings [52, 272, 273]. Tissue-engineered platforms such as multicellular spheroids (MCS) incorporate cells and ECM in a three-dimensional physiological context, and thus, are able to effectively recapitulate tumor architecture and cancer cell function, which are coupled through regulation of cell-cell and cell-ECM interactions [14, 81, 274]. Thus, tumor spheroids have been widely used to investigate tumorigenesis [275], cellular mechanisms of cancer invasion [162, 238], and anticancer drug efficacy [276]. Importantly, MCS can be made to contain multiple cell types in co-culture and can be dynamically and quantitatively analyzed with confocal microscopy, making them an ideal experimental model with which to explore the functional importance of intratumor heterogeneity.

In this study, we investigated cancer invasion in the framework of intratumor heterogeneity using a tissue-engineered co-culture tumor model in which two dissimilar cell types derived from the epithelial compartment were incorporated into heterotypic multicellular spheroids. Co-culture MCS composed of the "invasion-competent" breast adenocarcinoma cell line MDA-MB-231 and the "invasion-incompetent" breast epithelial cell line MCF-10A were embedded within 3D collagen matrices that permitted *in vivo*-like cell-cell and cell-matrix interactions and, thus, supported physiological *in vitro* tumor progression. Using this co-culture platform, we

found that invasive malignant cells induced and led collective invasion of otherwise non-invasive epithelial cells, and that this leader-follower co-invasive behavior was dependent upon cell contractility- and proteolysis-based ECM remodeling by leading malignant cells.

5.3 Materials and Methods

Cell culture and reagents

Malignant MDA-MB-231 breast adenocarcinoma cells (HTB-26; ATCC, Rockville, MD) were maintained in DMEM (Invitrogen, Carlsbad, CA) supplemented with 10% fetal bovine serum (Atlanta Biologicals, Norcross, GA) and 1% penicillin-streptomycin (Invitrogen). MDA-MB-231/GFP cells (AKR-201; Cell Biolabs, San Diego, CA) were maintained in complete MDA-MB-231 media supplemented with 0.1 mM MEM Non-Essential Amino Acids (Invitrogen). MCF-10A mammary epithelial cells (CRL-10317; ATCC) and MCF-10CA1a malignant mammary epithelial cells (Barbara Ann Karmanos Cancer Institute, Detroit, MI) were maintained in DMEM:F12 (Invitrogen) supplemented with 5% horse serum (Invitrogen), 0.5 µg/ml hydrocortisone (Sigma-Aldrich, St. Louis, MO), 20 ng/ml hEGF (Invitrogen), 10 µg/ml insulin (Sigma-Aldrich), 100 ng/ml cholera toxin (Sigma-Aldrich), and 1% penicillin-streptomycin. PC-3 malignant prostate adenocarcinoma cells (CRL-1435; ATCC) were maintained in Ham's F-12K Medium (ATCC) supplemented with 10% fetal bovine serum and 1% penicillin-streptomycin. PrEC primary human prostate epithelial cells (CC-2555; Lonza, Walkersville, MD) were maintained in PrEGM prostate epithelial cell growth medium (Lonza) supplemented with SingleQuots

(Lonza) according to the manufacturer's recommended protocol. Mammary spheroid formation media consisted of complete MCF-10A media supplemented with 0.25% methylcellulose (H4100; StemCell Technologies, Vancouver, BC). Mammary spheroid growth media consisted of complete MCF-10A media supplemented with 0.25% methylcellulose and 1% Matrigel (Becton Dickinson; San Jose, CA). Prostate spheroid formation media consisted of complete PrEC media supplemented with 0.25% methylcellulose. Prostate spheroid growth media consisted of complete PrEC media supplemented with 0.25% methylcellulose and 1% Matrigel. All cell culture was maintained at 37°C and 5% CO_2.

At least 2 h prior to spheroid generation, epithelial cells (MCF-10A, PrEC) and malignant cells (MDA-MB-231, MCF-10CA1a, PC-3) were labeled with 10 µM CellTracker Orange CMRA (Invitrogen) and 10 µM Cell Tracer Green CMFDA SE (Invitrogen), respectively. GM6001 (EMD Millipore, Billerica, MA) and Y27632 (Sigma-Aldrich) were used at 20 µM and 10 µM, respectively.

Multicellular spheroid generation

To generate multicellular spheroids, fluorescently labeled cells were trypsinized as for cell passage and resuspended in spheroid formation media at 2.5×10^4 cells/ml. To prepare epithelial and malignant monoculture spheroids, 200 µl of the appropriate cell suspension (5×10^3 cells) was seeded into each well of non-adhesive round-bottom 96-well plates (Corning; Tewksbury, MA). For epithelial/malignant co-culture spheroids, volumetric mixtures of each cell suspension were seeded into each well. Plates were

centrifuged at 1000 rpm for 5 min and then incubated at 37°C and 5% CO_2 on an orbital shaker at ~60 rpm for 2 h. Spheroid formation media was then replaced with spheroid growth media to promote spheroid compaction.

3D spheroid invasion assay

After 48 h of compaction, spheroids were embedded in 1.5 mg/ml and 6.0 mg/ml type I collagen gels. Collagen gels were prepared as previously described [55]. Briefly, type I collagen was acid-extracted from rat tail tendons (Pel-Freez Biologicals, Rogers, AR), purified via centrifugation and lyophilization, and reconstituted at 10 mg/ml in 0.1% acetic acid. Stock collagen solution was diluted to either 1.5 mg/ml or 6.0 mg/ml by gently mixing with ice-cold DMEM, and the solution was neutralized to pH 7.0 with 1 N NaOH. Spheroids were removed from culture plates and individually embedded within 500 µl collagen gels in glass-bottom 24-well plates (MatTek, Ashland, MA). After 30 minutes of gel polymerization at 37°C, gels were overlaid with 500 µl of complete MCF-10A or PrEC media with or without pharmacological inhibitors.

Microscopy and image analysis

Real-time spheroid compaction and invasion were measured with time-lapse microscopy using a Zeiss AxioObserver Z1 inverted phase contrast microscope equipped with a Hamamatsu ORCA-ER camera. For compaction analysis, spheroids were imaged at 2-h intervals for 24 h in a temperature-, humidity-, and CO_2-controlled microscope incubation chamber using AxioVision software (v. 4.8, Carl Zeiss

MicroImaging GmbH, Jena, Germany). Spheroid cross-sectional area was measured using ImageJ (v. 1.43u, National Institute of Health, Bethesda, MD) and normalized to initial cross-sectional area for $n \geq 10$ spheroids per condition from at least three independent experiments. Simultaneous fluorescence and phase time-lapse microscopy (imaged at 20-min intervals for 24 h) were used to observe invasion of fluorescently labeled MDA-MB-231 and MCF-10A cells from co-culture mammary spheroids into 1.5 mg/ml collagen matrices. Intra-spheroid cell organization and spheroid invasion were imaged using a Zeiss LSM700 confocal microscope operated by ZEN software (v. 2010, Carl Zeiss). Low-power (×5-10) fluorescent images of spheroids presented herein are maximum intensity z-projections of confocal image stacks acquired from the bottom surface of the spheroid to the spheroid center. Spheroid invasion was calculated by measuring the projected spheroid area immediately after collagen embedding (A_0) and the projected spheroid area following culture within collagen matrix for 48 h (A_{Inv}). Invasive Index was defined as (A_{Inv} / A_0) - 1 for $n \geq 10$ spheroids per condition from at least three independent experiments. Maximal invasion distance was determined by measuring the radial distance (in μm) from the spheroid edge to the invasive cells furthest from the spheroid for $n \geq 10$ spheroids per condition (four cells measured per spheroid) from at least three independent experiments. To further investigate invasion from co-culture mammary spheroids, the number of epithelial cell-containing invasive strands per spheroid was quantified for $n \geq 10$ co-culture spheroids after 48 h of invasion.

For E-cadherin immunofluorescence, mammary spheroids composed of MDA-MB-231/GFP and unlabeled MCF-10A cells were embedded in 1.5 mg/ml collagen and either fixed immediately or allowed to invade for 48 h before fixation. Briefly, samples were fixed with 3.7% (v/v) formaldehyde in PBS, permeabilized with 1% (v/v) Triton (JT Baker, Phillipsburg, NJ) in PBS, and blocked with 0.5% (v/v) Tween (JT Baker) with 3% (w/v) bovine serum albumin (Sigma-Aldrich) in PBS. An anti-E-Cadherin primary antibody (sc-7870; Santa Cruz Biotechnology Inc., Santa Cruz, CA) was used at (1:50) in 1% (w/v) BSA in PBS and an Alexa Fluor 568 conjugated secondary antibody (Santa Cruz) was used at (1:100) in 1% (w/v) BSA. Nuclei were stained with 4,6-diamidino-2-phenylindole (DAPI; Sigma-Aldrich).

Cell localization/immunofluorescence and collagen fiber organization before and during spheroid invasion were assessed with high-power (×40) fluorescence and reflectance confocal microscopy, respectively. Confocal reflectance images of collagen fibers are 1-μm thick confocal slices acquired as previously described near the spheroid "equator" [55]. The ImageJ plugin OrientationJ was used as previously described to measure collagen fiber orientation from confocal reflectance images [277]. Greyscale confocal reflectance images of collagen fibers were analyzed and colorized with OrientationJ such that pixel hue corresponded to the angle of local fiber orientation, which could range from -90° to +90° relative to horizontal. To quantify collagen fiber organization, collagen fiber angle (θ_{Fiber}) relative to the tangent of the original spheroid surface (θ_{Sph}) was determined for each pixel in the given region of interest using the algorithm $|\theta_{Fiber} - \theta_{Sph}|$. Using this analysis, the minimum angular

difference was 0°, which corresponded to a tangentially aligned fiber; the maximum angular difference was 90°, which corresponded to a radially aligned fiber. Results are graphed as frequency distributions of the angular difference, binned in 10-degree increments, between collagen fibers and the spheroid surface for all pixels within the indicated regions of interest.

Statistical analysis

Data was compared by one-way analysis of variance (ANOVA) with post-hoc Tukey HSD tests using JMP Pro software (v. 9.0.2, SAS Institute, Cary, NC). All numeric data is presented as mean ± SEM; statistical significance was considered with $p < 0.01$.

5.4 Results

Multicellular spheroid generation and characterization

To experimentally recapitulate intratumor heterogeneity and study heterogeneity-associated phenomena, a multicellular spheroid model was developed. Fluorescently labeled epithelial cells (labeled red) and malignant cells (labeled green) were seeded in round-bottom 96-well plates (Figure 5.1A; 0 h) and allowed to spontaneously coalesce and compact over 24 h to form multicellular spheroids (Figure 5.1A; insets). Fluorescence confocal microscopy and transmitted light microscopy were used to probe cellular distribution and spheroid morphology, respectively. MCF-10A epithelial monoculture spheroids were densely compacted, while MDA-MB-231 malignant monoculture spheroids were more loosely aggregated. Co-culture spheroids

(1:1 mixture of MCF-10A cells and MDA-MB-231 cells) exhibited intermediate compaction (Figure 5.1A; 24 h).

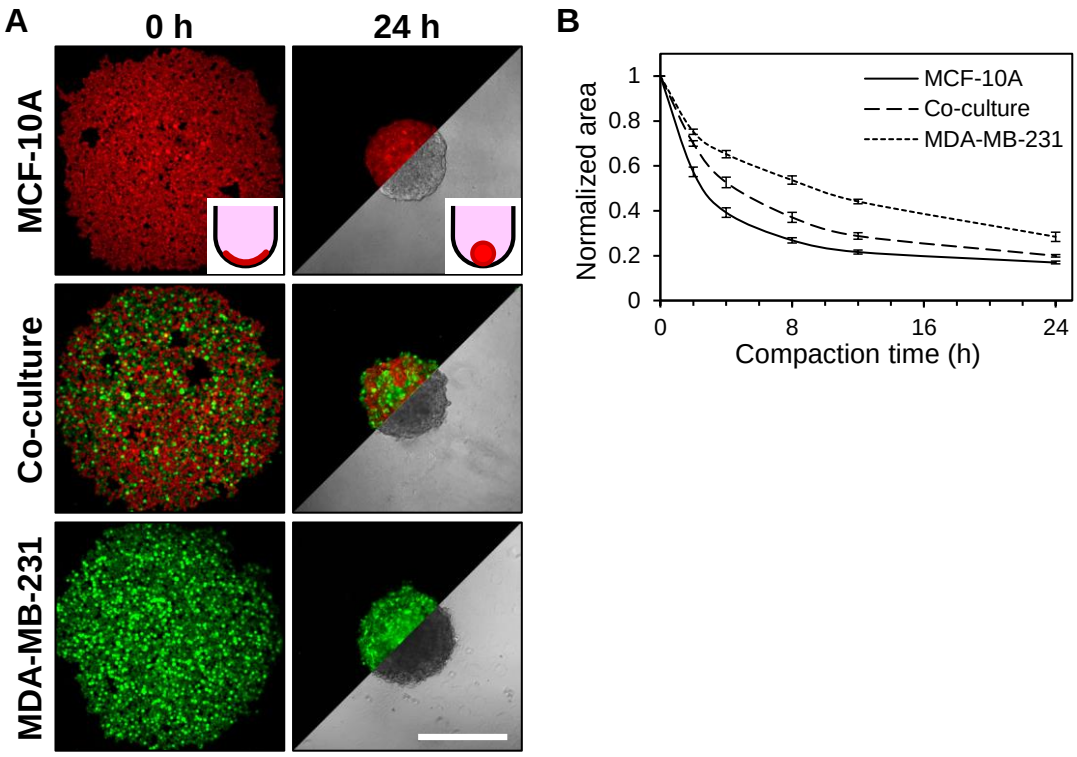

Figure 5.1. Multicellular spheroid compaction. (A) Representative confocal fluorescence images show cell compaction during formation of MCF-10A mammary epithelial cell monoculture (red), MDA-MB-231 malignant breast cell monoculture (green), and MCF-10A/MDA-MB-231 co-culture spheroids. Phase images illustrate spheroid morphologies after 24 hours of culture. Insets provide cartoon representation of cells (red) compacting within non-adhesive round-bottom wells to form spheroids. Scale bar: 500 μm. **(B)** Quantification of spheroid cross-sectional area during compaction; data are presented as spheroid cross-sectional area normalized to initial cross-sectional area for $n \geq 11$ spheroids from at least three independent experiments.

Tracking of spheroid area over 24 h showed that spheroid compaction, and thus, final spheroid size, was dependent on cellular composition (Figure 5.1B). Purely epithelial spheroids compacted rapidly and had final cross-sectional areas of 16.9 ± 0.8% of the initial cell pellet. Co-culture spheroids compacted more slowly and had final cross-

sectional areas of 19.9 ± 0.5% of the initial cell pellet. Purely malignant spheroids exhibited slower compaction than spheroids containing epithelial cells and had cross-sectional areas of 28.4 ± 2.1 % of the initial cell pellet.

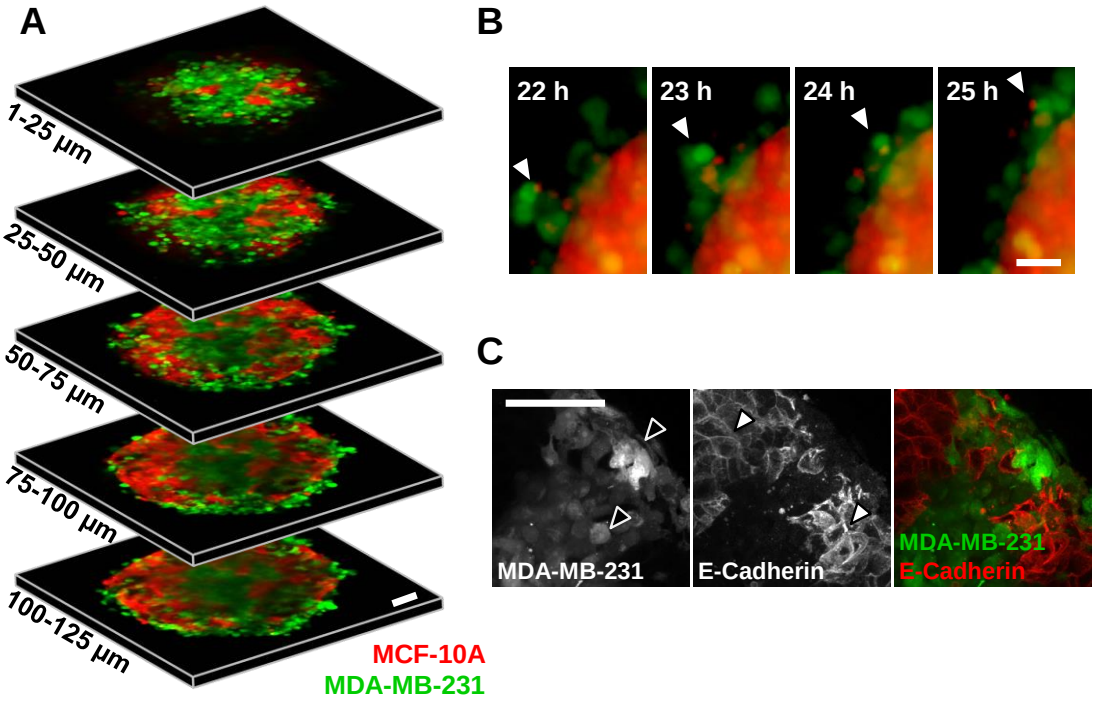

Figure 5.2. Cell organization within heterotypic co-culture spheroids. (A) Segmented 25-µm thick z-projections of a co-culture tumor spheroid consisting of fluorescently labeled MCF-10A (red) and MDA-MB-231 (green) cells after 24 h of compaction highlight localization of two cell types through partial thickness of spheroid. **(B)** Time-lapse imaging at peak spheroid compaction (22-25 h) shows compaction-independent intraspheroid movement of malignant MDA-MB-231 cells. Arrowheads track the movement of a highly motile cluster of malignant cells that have been excluded to the spheroid periphery. **(C)** Maximum intensity z-projection of co-culture tumor spheroid consisting of fluorescently labeled MDA-MB-231 and unlabeled MCF-10A cells. Black arrowheads highlight fluorescently labeled MDA-MB-231 cells and white arrowheads highlight E-cadherin-positive cell membranes of MCF-10A cells. Scale bars: 50 µm.

While epithelial and malignant monoculture spheroids contained homogeneous cellular distributions, epithelial/malignant co-culture spheroids contained clusters of each cell type. Confocal microscopy showed that these cell clusters were organized

into distinct regions of the spheroid (Figure 5.2A). Consistently, a core of malignant cells was encased in a shell of epithelial cells (Figure 5.2A; 100-125 μm), which was surrounded by an outer layer of malignant cells (Figure 5.2A; all slices). Time-lapse fluorescence microscopy demonstrated that malignant cells peripheral to the epithelial shell were highly motile at the conclusion of compaction (Figure 5.2B). E-cadherin was localized to MCF-10A cell membranes (Figure 5.2C; white arrowheads), but absent from fluorescently labeled MDA-MB-231 cells (Figure 5.2C; black arrowheads) in co-culture spheroids.

Three-dimensional multicellular spheroid invasion

To examine invasion from multicellular spheroids in a 3D physiological context, fluorescently labeled spheroids were fully embedded within collagen gels and imaged immediately and after 48 h. During this culture period, MCF-10A epithelial cells in monoculture spheroids remained non-invasive (Figure 5.3A), with these spheroids only undergoing some non-invasive expansive growth, as indicated by a small non-zero Invasive Index of 0.22 ± 0.04 (Figure 5.3B) and no detectable Maximal Invasion Distance (Figure 5.3C). In contrast, MDA-MB-231 malignant cells at the periphery of both epithelial/malignant co-culture and malignant monoculture spheroids extended exploratory cell protrusions and began to invade the matrix within 3 h after collagen embedding. After 48 h, co-culture and MDA-MB-231 malignant spheroids showed extensive collagen invasion (Figure 5.3A), resulting in statistically significant Invasive Indices of 2.3 ± 0.1 and 3.6 ± 0.2, respectively (Figure 5.3B). Cells invading from these spheroids exhibited statistically equivalent Maximal Invasion Distances of 276 ±

13 µm and 296 ± 14 µm, respectively (Figure 5.3C). MDA-MB-231 malignant cells (labeled green) invaded readily in a disorganized manner from both co-culture and

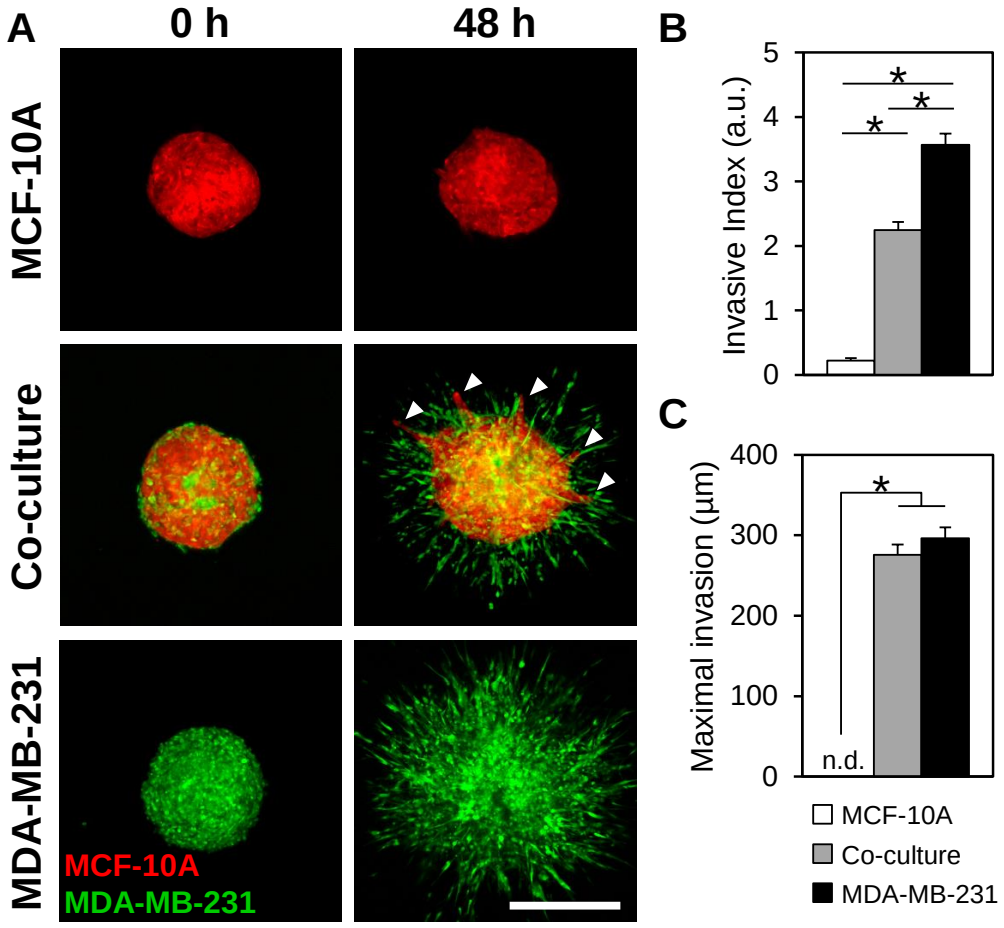

Figure 5.3. Three-dimensional multicellular tumor spheroid invasion. Fluorescently labeled spheroids were embedded within 1.5 mg/ml collagen gels and imaged immediately after embedding and at 48 h. **(A)** Representative confocal images of embedded MCF-10A monoculture, MCF-10A/MDA-MB-231 co-culture, and MDA-MB-231 monoculture spheroids at 0 h and 48 h. Arrowheads indicate strands of epithelial MCF-10A cells invading from co-culture spheroids. Scale bar: 500 µm. **(B)** Quantification of Invasive Index at 48 h; data are presented as spheroid cross-sectional area normalized to initial cross-sectional area at t = 0 h. **(C)** Quantification of maximal invasion distance at 48 h; data are presented as the radial distance from the spheroid edge to the invasive cells furthest from the spheroid. Data in B and C are from n ≥ 10 spheroids from at least three independent experiments.

malignant spheroids. Notably, when cultured with malignant cells in co-culture spheroids, normally non-invasive MCF-10A epithelial cells (labeled red) became invasive (Figure 5.3A; arrowheads).

Examination of cells invading from co-culture spheroids revealed that invading epithelial cells (Figure 5.4A; black arrowheads) were consistently organized in invasive strands that were led by one or more leading malignant cells (Figure 5.4A; white arrowheads).

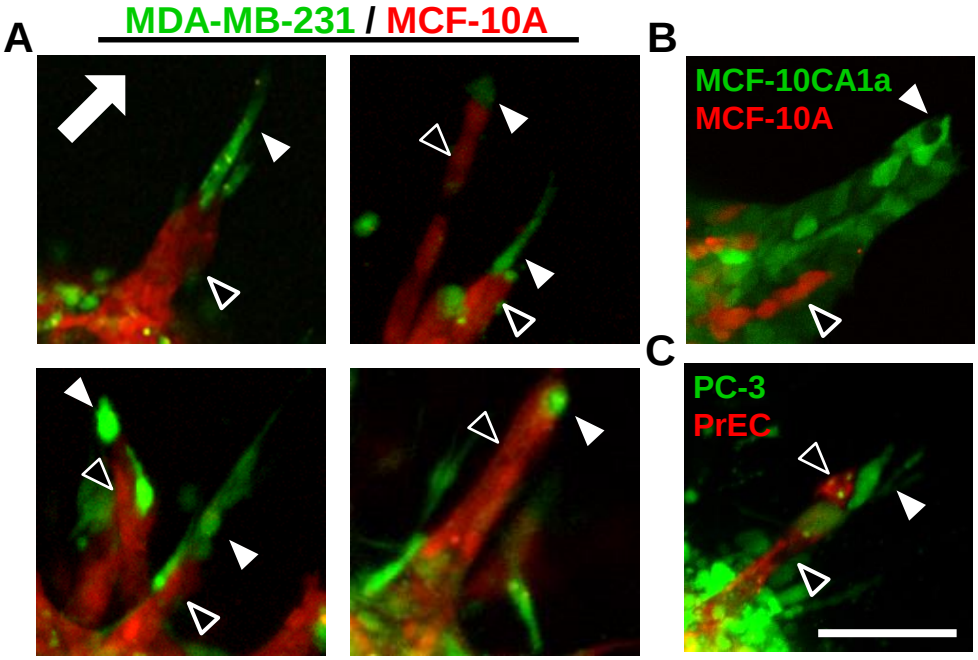

Figure 5.4. Leader-follower behavior in invasive strands. Confocal images of fluorescently labeled cells invading into 1.5 mg/ml collagen matrix from co-culture spheroids demonstrate leading malignant cells (green; white arrowheads) and following epithelial cells (red; black arrowheads). Co-culture combinations include: **(A)** MDA-MB-231 malignant breast adenocarcinoma cells (green) and MCF-10A mammary epithelial cells (red), **(B)** MCF10CA1a malignant mammary epithelial cells (green) and MCF-10A mammary epithelial cells (red), and **(C)** PC-3 malignant prostate adenocarcinoma cells (green) and PrEC primary prostate epithelial cells (red). Arrow indicates direction of invasion away from spheroids. Representative images from three independent experiments. Scale bar: 100 µm.

Another malignant mammary cell type, MCF-10CA1a, was similarly able to induce invasion of MCF-10A epithelial cells (Figure 5.4B). Additionally, PC-3 malignant prostate adenocarcinoma cells induced invasion of otherwise non-invasive (data not shown) PrEC primary prostate epithelial cells (Figure 5.4C). In each of these systems, malignant cells (MDA-MB-231, MCF10CA1a, or PC-3) were positioned at the tip of invasive strands (Figure 5.4A-C; white arrowheads) and epithelial cells (MCF-10A or PrEC) were trailing behind (Figure 5.4A-C; black arrowheads).

Extracellular matrix remodeling during spheroid invasion

To more closely examine the differential invasion observed from multicellular spheroids, confocal fluorescence and reflectance microscopy were used to probe cell localization and extracellular matrix organization at the spheroid-matrix interface, respectively. Immediately following collagen embedding, all spheroids were surrounded by uniform collagen matrices containing randomly organized fibers (Figure 5.5A; 0 h). After 48 h, collagen fiber reorganization and alignment were observed in all conditions (Figure 5.5A; 48 h, white arrowheads) as compared to naïve matrices at 0 h. The non-invasive expansive growth exhibited by MCF-10A epithelial spheroids was accompanied by reorganization of collagen fibers tangential to the spheroid surface such that fibers were wrapped around the spheroid (Figure 5.5A; 48 h). Quantitative analysis of fiber alignment using OrientationJ confirmed that the fibers in the indicated region of interest were preferentially aligned parallel to the epithelial spheroid surface, as shown by a small difference between θ_{Fiber} and θ_{Sph}

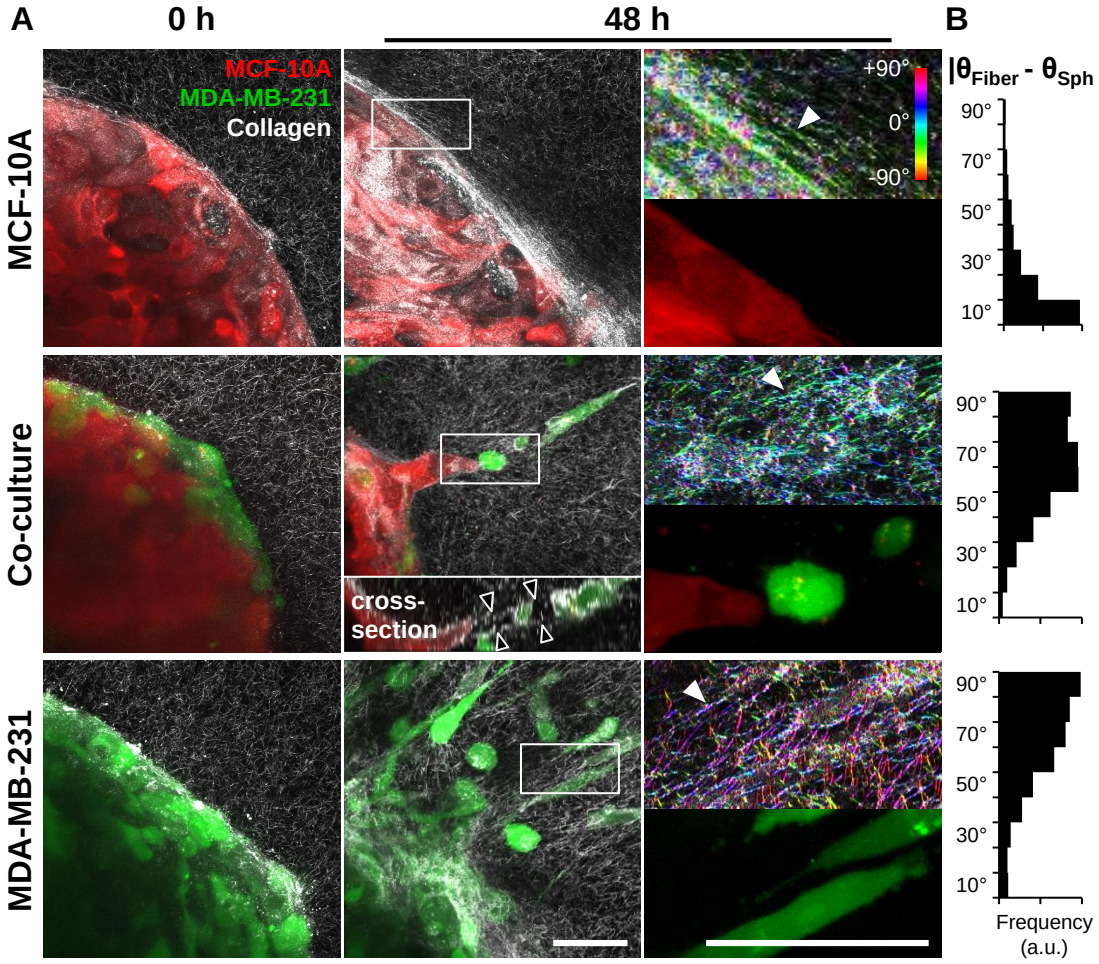

Figure 5.5. Matrix reorganization associated with malignant cell invasion. (A) Maximum intensity z-projections of multicellular tumor spheroids composed of epithelial MCF-10A cells (red) and malignant MDA-MB-231 cells (green), embedded within 1.5 mg/ml collagen matrix (white fibers imaged by confocal reflectance microscopy), and imaged immediately after embedding (0 h, left panels) and following culture (48 h, middle panels). Regions of interest at 48 h are indicated in middle panels by white boxes and are magnified 3× in right panels. Confocal reflectance images in right panels were colorized with OrientationJ as described in Materials and Methods. White arrowheads highlight areas of collagen fiber alignment. Inset in center panel is cross-sectional view along the invasive strand. Black arrowheads indicate boundaries of matrix microtrack generated by invading malignant leader cells. **(B)** Quantitative analysis of collagen fiber alignment relative to the spheroid surface. Briefly, local collagen fiber orientations (θ_{Fiber}) were determined with OrientationJ and compared to the angle given by the original spheroid surface (θ_{Sph}), resulting in alignment distributions representative of all fibers in the regions of interest. Scale bars: 50 µm.

(Figure 5.5B; MCF-10A). Cellular invasion from epithelial/malignant co-culture and MDA-MB-231 malignant monoculture spheroids was associated with remodeling of collagen fibers perpendicular to the spheroid surface (Figure 5.5A; 48 h). Quantification of ECM alignment in the proximity of invading cells with OrientationJ verified that collagen fibers were oriented orthogonal to the spheroid surface, as indicated by relatively large differences between θ_{Fiber} and θ_{Sph} (Figure 5.5B; Co-culture and MDA-MB-231). Consistently, leading malignant cells were elongated and radially oriented. Malignant and epithelial following cells tended to show rounded morphologies, with the latter forming cohesive invasive strands. Notably, invading malignant MDA-MB-231 leader cells left cell-scale microtracks in the matrix behind them, as indicated by regions of high collagen reflectance surrounding regions devoid of extracellular matrix (Figure 5.5A; 48 h, black arrowheads in cross-section inset).

Time-lapse imaging revealed the time-course and dynamics of invasion from co-culture spheroids and showed that leading malignant MDA-MB-231 cells persisted at the tips of invasive strands (Figure 5.6A; white arrowheads). Co-invasion was maintained even when transient gaps (Figure 5.6A; black arrowheads) formed between leading MDA-MB-231 cells and following MCF-10A cells. Trailing epithelial cells exhibited two general induced-invasion strategies: (i) MCF-10A cells fill matrix tunnels (Figure 5.6B; black arrowheads) left by invading MDA-MB-231 cells; and (ii) MCF-10A cells invade directly behind and adjacent to leading MDA-MB-231 cells. E-cadherin was consistently detected between following MCF-10A epithelial cells

(Figure 5.6B,C; white arrowheads), but not in leading MDA-MB-231 cells or between adjacent MDA-MB-231 cells (Figure 5.6C,D).

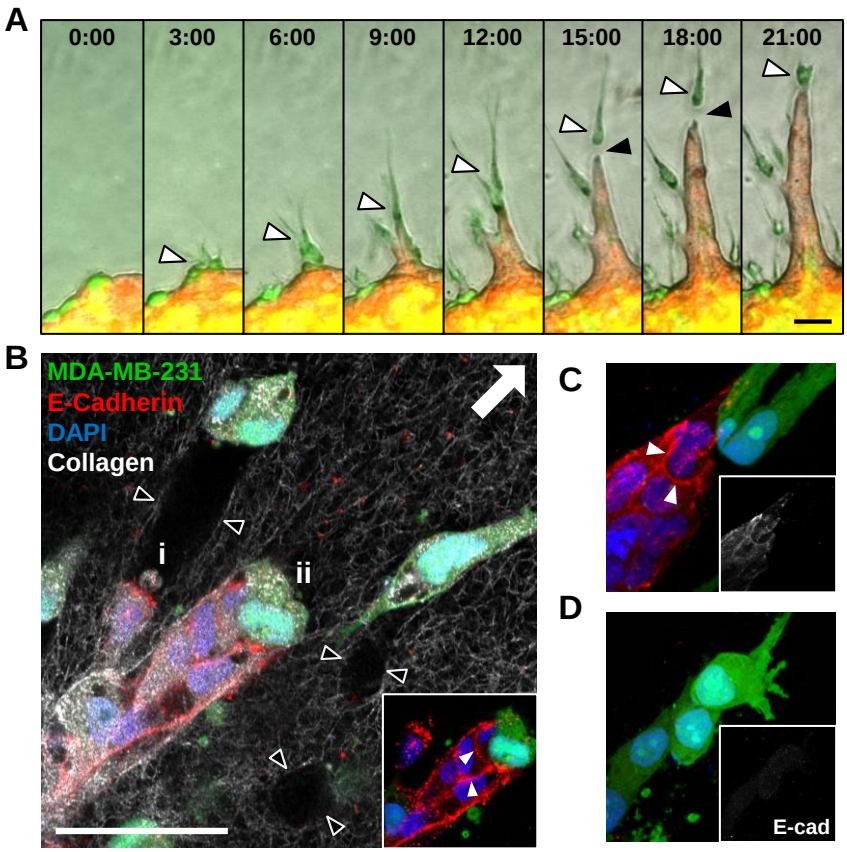

Figure 5.6. Intercellular interactions during co-invasion. (a) Time-lapse imaging of an invading co-culture spheroid. White arrowheads highlight MDA-MB-231 cell (green) leading an invasive strand of MCF-10A cells (red). Black arrowheads show transient gap between leading and following cells. Time in hours after embedding. **(B)** Confocal section of spheroid composed of MCF-10A cells and fluorescently labeled MDA-MB-231 cells (green) stained for E-cadherin (red) and nuclei (DAPI; blue) after 48 h of invasion. Inset highlights E-cadherin-positive cell-cell adhesions between MCF-10A cells (white arrowheads). Black arrowheads indicate boundaries of matrix microtracks generated by invading leader cells. Two induced-invasion strategies are demonstrated: (i) MCF-10A cells fill matrix tunnels left by invading MDA-MB-231 cells; (ii) MCF-10A cells remain adjacent to leading MDA-MB-231 cells, but with no detectable E-cadherin-based adhesions between the two cell types. **(C)** E-cadherin-positive (white arrowheads) cohort of MCF-10A cells following leading MDA-MB-231 cells. **(D)** Lack of E-cadherin-positive cell-cell adhesions between adjacent singly invading MDA-MB-231 cells. Arrow indicates direction of invasion away from spheroids for panels B-D. Scale bars: 50 µm.

Since fiber reorganization and proteolytic track-making were associated with cell invasion and malignant MDA-MB-231 cells consistently led invasive strands of epithelial MCF-10A cells during invasion from co-culture spheroids, we hypothesized that extracellular matrix remodeling by leading malignant cells was required for 3D invasion from multicellular spheroids. To test this hypothesis, co-culture spheroids were embedded within 1.5 mg/ml collagen matrices and treated with GM6001 (20 μM) to inhibit MMP activity or Y-27632 (10 μM) to inhibit ROCK-based cell contractility. Confocal reflectance imaging around invading cells at the spheroid-matrix interface showed that collagen fiber alignment and matrix microtracks, which were prominent in control conditions, were absent under MMP and ROCK inhibition (Figure 5.7A; black arrowheads). Quantification of ECM alignment indicated that treatment with GM6001 or Y27632 attenuated the fiber alignment observed in control conditions. Briefly, fibers within control ECM tended to be oriented perpendicular to the spheroid surface (large difference between θ_{Fiber} and θ_{Sph}) while fibers within GM6001- and Y27632-treated matrices showed reduced preferential orientation (Figure 5.7C).

MDA-MB-231 invasion past the original spheroid boundary (Figure 5.8A; dashed white lines) persisted under both MMP and ROCK inhibition (Figure 5.8A). However, the extent of invasion was decreased: MMP and ROCK inhibition significantly reduced Invasive Index from 2.3 ± 0.1 to 1.5 ± 0.2 and 1.4 ± 0.2 , respectively (Figure 5.8C), and significantly reduced Maximal Invasion Distance from 276 ± 13 μm to 217 ± 19 μm and 146 ± 15 μm, respectively (Figure 5.8D). Similar trends of reduced

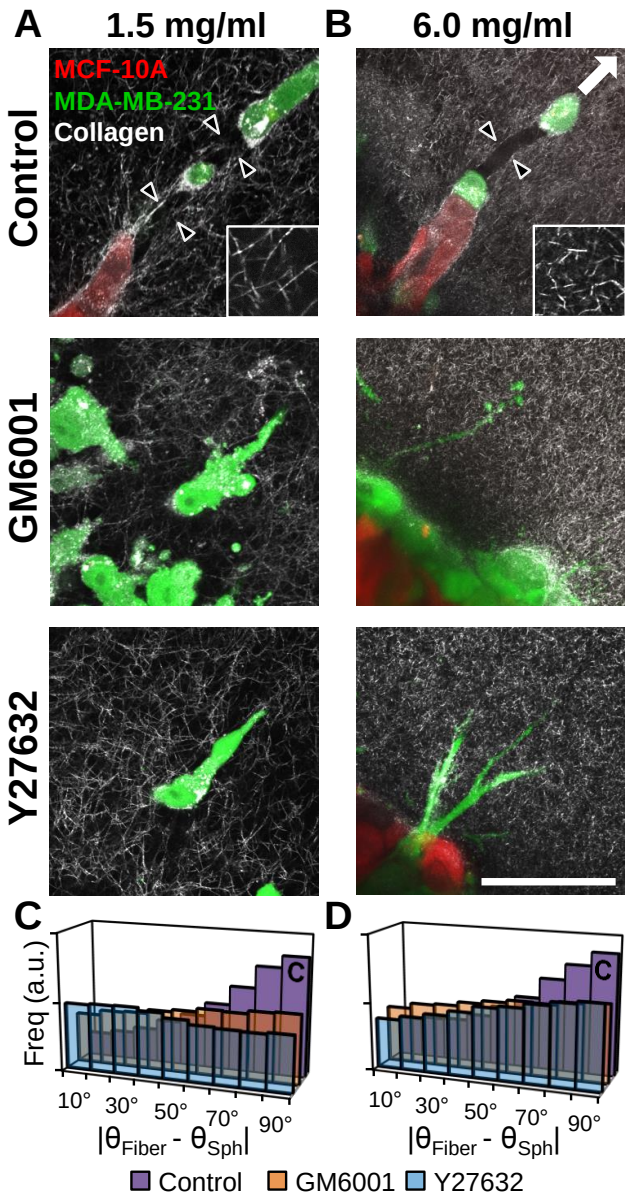

Figure 5.7. Effects of proteolysis and cell contractility on matrix reorganization during invasion. Confocal images of cells invading from co-culture spheroids into **(A)** 1.5 mg/ml or **(B)** 6.0 mg/ml collagen matrices under control conditions or treated with inhibitors of MMPs (GM6001; 20 μM) and ROCK (Y-27632; 10 μM). Black arrowheads indicate boundaries of matrix microtracks generated by leading malignant cells. Insets are high-magnification (20μm x 20μm) images of 1.5 and 6.0 mg/ml collagen matrices to highlight fiber and pore microarchitecture. Quantification of collagen fiber orientation relative to the spheroid surface at the spheroid-matrix interface within **(C)** 1.5 mg/ml or **(D)** 6.0 mg/ml collagen matrices under control conditions (purple bars), MMP inhibition with GM6001 (orange bars), or ROCK inhibition with Y27632 (blue bars). Scale bar: 50μm.

invasion under MMP and ROCK inhibition were observed in MDA-MB-231 monoculture spheroid studies (Figure 5.9A-C).

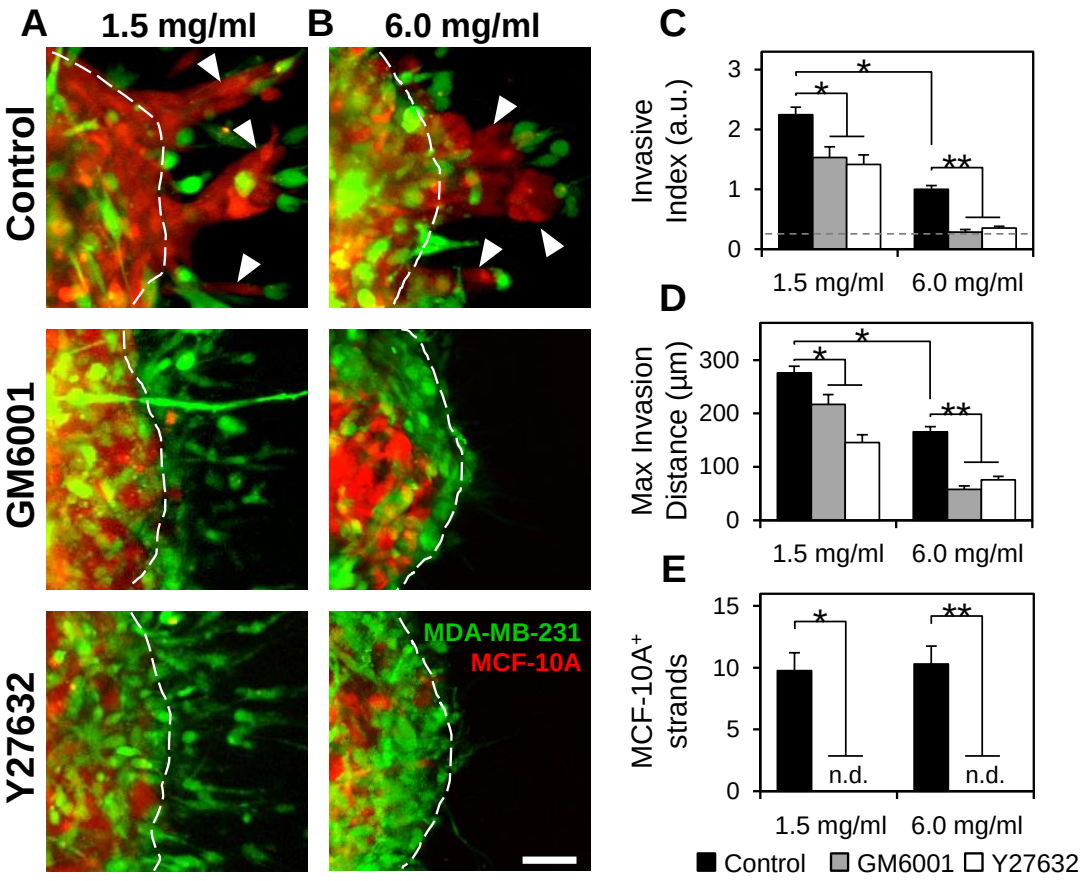

Figure 5.8. Role of proteolysis and cell contractility in induced collective epithelial cell invasion. Maximum intensity z-projections of co-culture multicellular spheroids embedded within **(A)** 1.5 mg/ml or **(B)** 6.0 mg/ml collagen gels and treated with GM6001 (20 μM) or Y-27632 (10 μM). Arrowheads indicate epithelial cell-containing invasive strands. Dashed lines indicate original spheroid boundaries. Quantification of **(C)** Invasive Index, **(D)** Maximal Invasion Distance, and **(E)** the incidence of MCF-10A-positive invasive strands under control conditions (black bars), GM6001 treatment (gray bars), and Y27632 treatment (white bars). Dashed gray line in C denotes Invasive Index of non-invasive epithelial monoculture spheroids. MCF-10A-positive invasive strands were not detected under GM6001 or Y27632 treatment (n.d.). * indicates statistical significance compared to control 1.5 mg/ml condition; ** indicates statistical significance compared to control 6.0 mg/ml condition. Scale bar: 50 μm.

Notably, co-culture spheroids exhibited 9.8 ± 1.5 MCF-10A^{+} invasive strands per spheroid (Figure 5.8A; white arrowheads), but no such epithelial cell-positive invasive strands were observed under MMP or ROCK inhibition (Figure 5.8A,E).

To investigate the role of matrix microarchitecture in regulating invasion, co-culture spheroids were embedded within high-density 6.0 mg/ml collagen matrices. These matrices have a more confined microarchitecture consisting of a tight meshwork of short collagen fibers and small pores (Figure 5.7B; inset) as compared to low-density 1.5 mg/ml collagen matrices, which contain larger fibers and pores (Figure 5.7A; inset). As in low-density gels, matrix remodeling was prominent in control conditions (Figure 5.7B; black arrowheads), but was reduced in cultures subjected to MMP or ROCK inhibition, which showed no matrix microtracks and reduced collagen fiber alignment (Figure 5.7B,D). Invasion into high-density matrices, as indicated by Invasive Index and Maximal Invasion Distance, was significantly reduced by 55% and 40%, respectively, compared to invasion into low-density matrices under control conditions (Figure 5.8C,D); however, matrix density did not change the frequency of MCF-10A^{+} invasive strands under control conditions (Figure 5.8E). Similar to as in low-density matrices, inhibition of MMP or ROCK activity mitigated invasion into high-density matrices (Figure 5.8B-D). MMP and ROCK inhibition significantly reduced the Invasive Indices to 0.28 ± 0.04 and 0.35 ± 0.03, respectively, which were close to the Invasive Index exhibited by non-invasive MCF-10A epithelial monoculture spheroids (Figure 5.8C; dashed line). Max invasion distance was reduced from 165 ± 10 to 58 ± 7 and 76 ± 6 by MMP and ROCK inhibition, respectively

(Figure 5.8D). These values are consistent with the observation that malignant cells extended thin protrusions from the spheroid periphery into the matrix, but did not translate completely past the spheroid boundary into the matrix (Figure 5.8B; dashed white lines). As in low-density matrix, inhibition of MMP and ROCK activity prevented the development of MCF-10A^{+} co-invasive strands in 6.0 mg/ml matrices (Figure 5.8B,E).

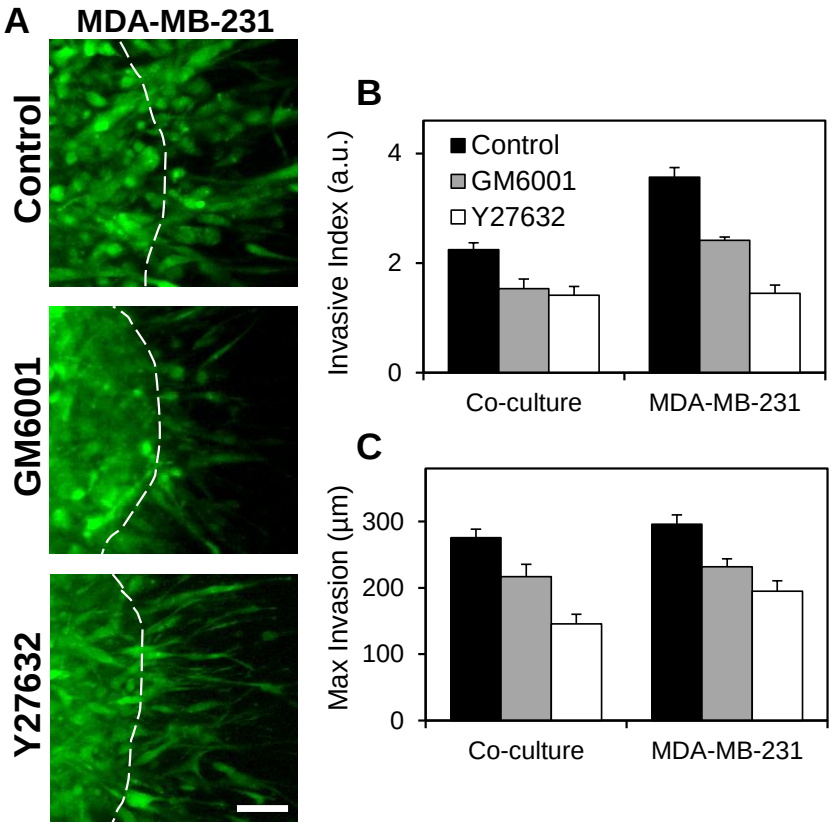

Figure 5.9. Effects of MMP and ROCK inhibition on co-culture and malignant spheroid invasion. (A) Maximum intensity z-projections of malignant MDA-MB-231 multicellular spheroids embedded within 1.5 mg/ml collagen gels and treated with inhibitors of MMPs (GM6001; 20 µM) and ROCK (Y-27632; 10 µM) for 48 h. Dashed lines indicate original spheroid boundaries. Quantification of **(B)** Invasive Index and **(C)** Maximal Invasion Distance show similar attenuation of invasion by both metrics in co-culture and monoculture malignant spheroids. Scale bar: 50 µm.

5.5 Discussion

Solid tumors, which initially arise by clonal expansion of transformed cells, contain diverse subpopulations that result from genetic instability, microenvironmental selective pressures, and the reinforcement of enabling phenotypes [268, 278, 279]. Such heritable diversity, when coupled with the phenotypic plasticity that characterizes cancer cells [258], results in substantial intratumor heterogeneity that can obscure the study, diagnosis, and treatment of cancer [263, 280]. To study the functional consequences of such cellular variety in a controlled *in vitro* system, we have developed a tissue-engineered model of intratumor heterogeneity using two dissimilar mammary cell types in co-culture multicellular spheroids. Using this platform, we have established a new model for collective cancer cell invasion in which invasive malignant cells can initiate the invasion of otherwise non-invasive cells within the tumor through cell contractility- and proteolysis-dependent matrix remodeling. To our knowledge, this is the first study that links the distinct leader and follower roles inherent in collective cancer cell invasion to differential invasiveness and intratumor heterogeneity. Thus, this study provides new insight into interactions between cell subpopulations within heterogeneous tumors.

Development and characterization of a fundamental in vitro model of intratumor heterogeneity

To generate a well-defined *in vitro* model of intratumor heterogeneity, co-culture multicellular spheroids were made by mixing equal numbers of fluorescently labeled cells from two dissimilar mammary cell lines: the malignant breast adenocarcinoma

cell line MDA-MB-231 and the breast epithelial cell line MCF-10A. These two cell lines were used throughout this study to represent two discrete subpopulations of cells within a tumor and were chosen because of their distinct invasive/metastatic potentials as well as their considerable historical and scientific significance within the field of breast cancer research. While MCF-10A cells exhibit a more basal phenotype than epithelial cells from normal breast tissue [281], these cells are non-tumorigenic in mice and, because they possess many features of normal mammary epithelial cells, they are extensively used as a model of normal epithelial cells *in vitro* [282, 283]. Malignant and epithelial monoculture spheroids were used throughout the study to demonstrate these cells' behavior in monoculture as a reference. To expand upon the co-culture spheroid system, an alternate malignant mammary epithelial cell line, MCF-10CA1a, was used in co-culture with MCF-10A epithelial cells. The MCF-10CA1a cell line was derived from a metastatic subpopulation of Ha-ras-overexpressing MCF-10A cells [284]. PC-3 malignant prostate adenocarcinoma cells and PrEC primary prostate epithelial cells were used to investigate intratumor heterogeneity in other tissue systems.

Using the MDA-MB-231 and MCF-10A cell lines, characterization of MCS compaction showed that the rate and extent of spheroid aggregation was dependent upon cell composition. Epithelial MCF-10A spheroids showed the fastest and most extensive compaction while malignant MDA-MB-231 spheroids showed the slowest and least extensive compaction; as expected, co-culture MCF-10A/MDA-MB-231 spheroids exhibited intermediate compaction. These differences in compaction were

likely due to differences in the cell-cell and cell-matrix adhesions that participated in aggregation since epithelial cell aggregation is primarily mediated by E-cadherin and malignant cell aggregation is directed by β1 integrin-ECM interactions [285, 286]. Indeed, E-cadherin was only detected on the cell membranes of epithelial MCF-10A cells, and was absent from malignant MDA-MB-231 cells within co-culture spheroids. Such disparity in intercellular adhesiveness is the basis for the differential adhesion hypothesis and, in part, may underlie the cell sorting that was observed in heterotypic co-culture spheroids [287]. Consistently, intermixed cells segregated to form distinct regions of each cell type: a core of malignant cells was encased within a densely packed shell of epithelial cells, which was surrounded by an outer rim of highly motile malignant cells. The presence of such mobile malignant cells at the spheroid periphery is supported by previous findings [288] and suggests that these cells were actively remodeling their adhesions to reach the physical configuration that maximized adhesion [287]. Consistent with this hypothesis, peripheral malignant cells eventually settled onto and adhered to the spheroid surface. While the specific mechanisms regulating cellular organization within co-culture spheroids remain to be determined, the time course of spheroid formation suggests that differential adhesion and cell sorting, as opposed to proliferation and apoptosis, are responsible for the rapid establishment of cellular organization [289]. An inclusive characterization of the mechanisms governing, and outcomes of, differential cell adhesion, sorting, and survival within heterotypic spheroids was not the aim of this work, and thus, a more comprehensive and rigorous analysis of cell physiology within co-culture spheroids remains an open challenge. Notably, co-culture spheroids can serve as a

physiologically relevant model system within which to study how microenvironmental factors such as cell-matrix interactions, heterotypic cell-cell interactions, and spatially defined nutrient and growth signals differentially influence cell behaviors relevant to cancer progression [290].

Physiological 3D invasion from an in vitro model of intratumor heterogeneity

Intratumor heterogeneity is thought to have considerable biological and clinical implications due to vast differences in growth, invasive, and differentiation potential among a tumor's cells [16, 263]. During tissue invasion, which is one of the earliest rate-limiting steps of metastasis, malignant cells must spatially and temporally coordinate proteolysis with changes in adhesion, contractility, and cell shape to physically disseminate from the primary tumor [1, 9]. Thus, due to the molecular specialization that is required for efficient invasion, we and others have hypothesized that cells within the tumor may possess different capacities for invasion and metastasis based on their phenotypic abilities [19, 172, 190, 269]. To test this hypothesis experimentally, malignant and epithelial cell lines were used in co-culture multicellular spheroids to represent cell subpopulations within a tumor having distinct invasive capacities.

When compacted spheroids were embedded into three-dimensional collagen matrices that mimic the *in vivo* tumor stroma [42], MCF-10A cells in monoculture epithelial spheroids were unable to invade the matrix and instead exhibited some non-invasive expansive growth. While extracellular cues including matrix stiffness [81], cellular

density [291], and growth factors [292] can promote an invasive mesenchymal phenotype in MCF-10A cells, cells in monoculture MCF-10A spheroids maintained a non-invasive epithelial phenotype, and thus, these cells represented an "invasion incompetent" subpopulation. Conversely, "invasion-competent" MDA-MB-231 cells in monoculture form malignant spheroids that readily invaded into the surrounding ECM by first extending exploratory cell projections into the matrix and subsequently translating the cell body away from the spheroid. These opposing behaviors, which were expected based on previous work with these cell types in 3D culture [158, 293], validated the physiological relevance of our 3D culture system. When heterotypic co-culture spheroids were embedded into 3D collagen matrix, they initially showed a pattern of invasion similar to malignant monoculture spheroids, with malignant cells promptly invading into the ECM. After 48 h of culture, the extent of invasion as indicated by measurement of the Invasive Index – the normalized area of invasion – was dependent upon the amount of malignant cells in each culture. Assessment of Maximal Invasion Distance revealed that malignant cells in co-culture spheroids are equally as invasive as malignant cells in monoculture malignant spheroids, indicating that epithelial cells did not restrain malignant cells' invasive capacity in co-culture.

Interestingly, when co-cultured with malignant MDA-MB-231 cells, otherwise non-invasive epithelial MCF-10A cells were triggered to invade into the matrix in cohesive strands following one or more leading malignant cells. This pattern of "co-invasion", with distinct leader cells and cohesive strands or masses of invading follower cells, is indicative of collective migration, which occurs during development, regeneration,

and epithelial cancer invasion [51, 158, 208, 271, 294, 295]. An alternate malignant mammary epithelial cell line, MCF-10CA1a, was similarly able to induce and lead invasion of MCF-10A cells and PC-3 malignant prostate cells led invasive strands of normally non-invasive PrEC primary prostate epithelial cells. While there were clear differences in cellular phenotypes and the nature of co-invasion among the cell lines used, the emergence of leader-follower collective invasion and consistent presence of malignant cells at the tips of invasive strands indicate that this phenomenon is not limited to MDA-MB-231/MCF-10A co-cultures. Additionally, the incidence of leader-follower co-invasion in prostate co-cultures suggests that this behavior extends to other tissue systems and that non-invasive primary cells can be induced to invade by malignant leader cells *in vitro*. Notably, a defining feature of collective cell migration is the preservation of cell-cell adhesions, and thus, an epithelial phenotype, in migrating cells [62, 69]. Here, we found that epithelial follower cells, but not malignant leader cells, retained such cell-cell cohesion when invading from co-culture spheroids. E-cadherin was maintained at cell-cell junctions between adjacent MCF-10A cells both within the spheroid mass and within invasive strands, indicating retention of an epithelial phenotype in co-invading MCF-10A cells. Thus, using our co-culture system, we demonstrate for the first time that the leader and follower roles characteristic of collective cancer invasion can be assumed by two distinct cellular subpopulations within a tumor.

Collective cell migration through physiological three-dimensional matrices requires that matrices contain adequately large pores through which strands or clusters of cells

can pass [69]. However, in the present study as well as in many tissues throughout the body [42], cell diameter can exceed ECM pore diameter, thus providing a barrier to 3D migration that requires cell-mediated extracellular matrix remodeling to permit invasion [241]. The concurrence and interdependence of 3D cell invasion and extracellular matrix remodeling has been extensively documented both *in vitro* and *in vivo* [27, 158, 208, 238, 270, 296, 297]. Notably, the Weiss group showed that cancer cells use the membrane-anchored proteinase MT1-MMP to cleave collagen and migrate through cross-linked collagen gels *in vitro* and interstitial ECM *in vivo* [270]. In defining the spatiotemporal dynamics of pericellular proteolysis during 3D invasion, Wolf et al. showed that malignant cells migrating through 3D matrices can proteolytically generate tunnel-like cell-scale microtracks that facilitate further cellular infiltration and proteolysis, eventually leading to the formation of macrotracks and the emergence of collective cell invasion [158]. Using a co-culture tumor model, Gaggioli et al. showed that cell-contractility and proteolysis-dependent matrix remodeling by stromal fibroblasts can induce the invasion of squamous cell carcinoma cells and that these cancer cells retain an epithelial phenotype as they collectively advance through matrix tunnels left by fibroblasts [208].

In the current study, confocal reflectance microscopy was used to assess the organization of collagen fibers around spheroids embedded within physiological fibrillar matrices. Collagen fibers around invading malignant and co-culture spheroids were preferentially aligned orthogonal to the spheroid surface while fibers surrounding non-invasive epithelial spheroids were aligned tangential to the spheroid surface.

Since naïve collagen matrices and matrix far from spheroids consisted of networks of isotropically oriented fibers, these results indicate that local ECM remodeling at the spheroid-matrix interface occurred in all conditions. The circumferential alignment of fibers around non-invasive MCF-10A epithelial spheroids suggests that the growing spheroid applied outward pressure to compress the matrix [298]. Similar matrix alignment was observed in work by Provenzano et al. that identified tangentially organized ECM around non-invasive mammary tumors *in vivo* [27]. The radial matrix organization associated with invasion in malignant monoculture and epithelial/malignant co-culture spheroids was due to active cell-mediated ECM remodeling by cells at the spheroid-matrix interface. Since cells in 3D physiological matrices exert traction forces on the ECM that can result in long-range physical changes in the surrounding matrix [129] and fibers up to several hundred microns from invading cells showed radial realignment in our model, we concluded that malignant cells caused cell contractility-mediated matrix reorganization in our system. Previous work has shown that such Rho-ROCK-based cell contractility is required for collagen fiber alignment at the tumor-stroma interface [56]. This alignment promotes contact guidance and invasion *in vivo* [27], and thus, may serve a similar role in our model. Furthermore, invading malignant cells also produced cell-scale microtracks through the matrix as reported elsewhere [158, 270], and in co-culture spheroids, cohorts of epithelial cells infiltrated these microtracks. Such microtracks have been shown to enable non-proteolytic cell infiltration [60, 162]. Notably, E-cadherin was only detected between adjacent following MCF-10A epithelial cells and transient gaps between leading and following cells opened and closed during co-invasion. These

results suggest that E-cadherin may be required for cohesive MCF-10A migration but that matrix tunnels, rather than cell-cell adhesions between leading and following cells, enable the induced invasive phenotype. Since we cannot rule out the possibility that malignant and epithelial cells interact using other adhesion molecules [285, 286, 289], future work should further define the mechanisms of leader-follower collective invasion in this system.

The use of cell traction forces and pericellular proteolysis to generate paths of least resistance is a general property of leader cells during three-dimensional collective migration in several systems [158, 295, 299, 300]. To determine if matrix remodeling by leading malignant cells in our co-culture system was required for the development of epithelial cell-positive co-invasive strands, cultures were treated with inhibitors of MMPs (GM6001) and ROCK-mediated cell contractility (Y27632). As expected, these inhibitors prevented the formation of matrix microtracks and quantitatively reduced matrix alignment at the spheroid-matrix interface, validating the efficacy of inhibition. While MMP and ROCK inhibition quantitatively reduced the efficiency of malignant cell invasion in both monoculture MDA-MB-231 and co-culture spheroids, presumably because the repertoire of 3D migration strategies available to cells was limited [68], these treatments completely prevented induced epithelial co-invasion. Together with our matrix remodeling observations, these findings support the hypothesis that matrix remodeling by leading invasive cancer cells was necessary for the induction of collective invasion by otherwise non-invasive cells.

Previously, we showed that 3D migration of MDA-MB-231 malignant cells is sensitive to matrix microarchitecture [55], so we used high-density 6.0 mg/ml collagen matrices to investigate the relationship between matrix structure, matrix remodeling, and invasion. Consistent with previous work showing that matrix density negatively correlates with 3D invasion efficiency [55, 158], here, we found that invasion from spheroids was less efficient in high-density matrices. Notably, while MDA-MB-231 cells were able to invade low-density matrix under MMP and ROCK inhibition, malignant cells at the periphery of spheroids embedded in high-density collagen matrix only extended thin protrusions into the surrounding matrix when treated with MMP and ROCK inhibitors, suggesting that high-density collagen matrices, but not low-density matrices, provided a barrier to MMP- and ROCK-independent invasion. The finding that MDA-MB-231 cells within low-density matrices retained their invasive phenotype under MMP and ROCK inhibition is supported by previous work with these cells [56], and suggests that malignant cells were sufficiently deformable to squeeze through the pores in low-density collagen matrices [153]. In support of this hypothesis, we observed that low-density collagen matrices were heterogeneous and contained a wide distribution of pore sizes, including sufficiently large pores that could potentially serve as "pro-invasive" microdomains through which malignant cells could migrate without matrix remodeling. While the absolute requirement for extracellular proteolysis during cell invasion through physiological 3D matrices remains a topic of debate, it is evident that this requirement is dependent upon local physical properties of the matrix (e.g., pore size and the presence of intermolecular

crosslinks) that determine the degree to which the matrix serves as a barrier to invasion [161, 238, 270].

ROCK-mediated cell contractility has been shown to serve many functions in three-dimensional cell migration including driving cell deformation for amoeboid movement and the generation of cell tension and strengthening of adhesions for matrix remodeling [56, 134, 141, 145, 259]. Interestingly, Sahai and Marshall showed that rounded amoeboid cell motility, but not elongated protrusive movement, has a significant requirement for Rho-ROCK activity [259]. Consistent with this, we found that malignant cells, which adopted an elongated mesenchymal motile phenotype, were still able to invade within permissive low-density matrices under ROCK inhibition. Thus, as previously shown [56], these results suggest that ROCK-mediated contractility was primarily responsible for matrix alignment and remodeling in our system, which acted to enhance, but was not required for, malignant cell invasion. Interestingly, we found that inhibition of force-mediated matrix remodeling prevented the formation of matrix microtracks by malignant cells, and thus, blocked induced MCF-10A invasion in co-cultures. These findings, which are supported by previous work by Gaggioli et al. with matrix-remodeling fibroblasts [208], suggest that coordinated proteolytic- and cell force-mediated matrix remodeling were critical for the formation of invasion-inducing microtracks. Indeed, regardless of matrix density, MCF-10A cells were only induced to co-invade when malignant cells were able to both invade into and remodel the surrounding matrix. This co-invasion occurred at the same frequency in low- and high-density matrices, and was similarly associated with

extracellular matrix remodeling, suggesting that the ability of leading MDA-MB-231 cells to generate matrix tunnels under control conditions was not sensitive to the matrix densities used in this study.

Our conclusion that proteolytic- and cell force-mediated matrix priming by leading invasive cells promoted the invasion of otherwise non-invasive cells is consistent with previous work in other experimental systems [208, 250]. While the use of global inhibitors of MMPs and ROCK prevents us from definitively ruling out the possibilities that (i) the epithelial follower cells themselves required ROCK and/or MMP activity to invade or that (ii) global MMP and ROCK inhibition indirectly altered off-target aspects of cell physiology [197], our data and others' suggest that the limiting factor for induced collective epithelial invasion in this model was the efficient generation of matrix tunnels by leading malignant cells. Nonetheless, future work should seek to more selectively down-regulate cell contractility and proteolytic machinery in a cell-type and isoform-specific manner to systematically define the molecular mechanisms required for leader-follower collective invasion and limit off-target effects.

We propose the following model for malignant cell-induced epithelial cell invasion in our novel heterotypic spheroid system. First, Rho-ROCK-based cell contractility enables ECM alignment by malignant cells that extend into the matrix at the spheroid periphery. This matrix priming facilitates efficient 3D migration of malignant cells into the surrounding matrix, where they can couple their migration with pericellular

proteolysis to generate cell-scale microtracks through the ECM. Finally, invasion-incompetent epithelial cells infiltrate matrix tunnels as cohesive strands or clusters of cells, resulting in collective invasion. In this paradigm, ROCK and MMP activity are required for distinct but integrated matrix remodeling functions by leading malignant cells that together lead to efficient generation of matrix tunnels and thus, induced epithelial cell invasion. Our results demonstrate a previously unappreciated instance of intratumor cellular cooperation [263] whereby invasion-competent cancer cells could provide ready-made matrix tunnels to be used by other cells that otherwise lack the ability to invade and negotiate the stromal ECM. In support of this concept, Hanahan and Weinberg recently proposed that, since heterogeneous subpopulations of cells within and around the tumor are likely to be significantly involved in all stages of cancer progression, it is unlikely that progression through the invasion-metastasis cascade is a cell-autonomous process [16]. Additionally, clear genetic differences have been detected among cells from separate but histologically similar regions of single metastatic tumors [268, 280], suggesting that invasive carcinomas can possess tremendous molecular and phenotypic cellular diversity that remains poorly understood. While the cell types used herein were chosen to represent two tumor subpopulations with distinct invasion capabilities, these results may also give an indication of how malignant cells could affect the remaining non-transformed epithelium within the tumor. Considering the critical role of homotypic epithelial cell-cell interactions in maintaining normal epithelial tissue homeostasis [14, 81], it is conceivable that the heterotypic cell-cell interactions characteristic of heterogeneous tumor cell populations could play a role in promoting the dysfunctional cell behavior

and tissue structure observed in invasive carcinomas [301]. Ultimately, the relevance of this *in vitro* model to the metastatic process could be validated *in vivo* to determine if a subpopulation of invasive cells can similarly enable the local invasion, dissemination, and metastasis of otherwise non-invasive cells. Further characterization of heterotypic cell-cell interactions and their functional outcomes within well-defined, tissue-engineered tumor heterogeneity models should provide additional insight into the biological and clinical consequences of intratumor heterogeneity.

CHAPTER 6

SORTING OUT TUMOR CELL HETEROGENEITY: PHENOTYPIC ISOLATION OF DIFFERENTIALLY INVASIVE MDA-MB-231 SUBPOPULATIONS

Portions of the data in this chapter were contributed by Marsha Lampi, Alexandra Braun, Karen Martin, and Zachary Goldblatt.

6.1 Abstract

Cellular heterogeneity is a characteristic feature of cancer that has recently been implicated as a driving force behind many aspects of tumor progression. In addition to obscuring cancer diagnosis and management in the clinical setting, such cellular diversity can confound the study of disease mechanisms by masking the behavior and therapeutic response of subpopulations of interest within a vast and heterogeneous population. Here, we developed a phenotypic cell purification technique designed to sort cells based on invasive fitness. We found that the parental MDA-MB-231 population contains subpopulations of cells that are both efficient (MDA^{INV}) and poor (MDA^{NON}) migrators, and that this differential invasive fitness is heritable. Our behavior-based sorting strategy enabled us to define key traits of the most invasive cells, which included proficient coordination of 3D protrusion and polarization, nascent adhesions containing active FAK at the cell periphery, Src-dependent membrane dynamics, and enhanced traction force generation and 3D matrix remodeling. Our results validate behavior-based cell sorting as an effective strategy by

which to decipher cellular heterogeneity and indicate that invasiveness is a cell-intrinsic attribute that can vary widely across a cell population.

6.2 Introduction

The activation and maintenance of cancer cell invasion through the tumor stroma is a critical hallmark of solid tumor progression towards metastatic disease [16]. To effectively negotiate the 3D stromal extracellular matrix, migrating cancer cells must coordinate protrusive, adhesive, contractile, and matrix remodeling behaviors [1, 47, 198], yet the specific molecular mechanisms utilized by migrating cells are adaptive and context-dependent [5, 41, 46]. Since a comprehensive understanding of the regulators of tumor cell invasiveness is critical to both the identification of biomarkers of invasion and metastasis as well as the development of therapeutic strategies to prevent invasion, characterization of the mechanisms underlying 3D cancer cell motility remains an open challenge.

Solid tumors are inherently heterogeneous and contain substantial cellular diversity due to both genetic and non-genetic variability [16, 268]. To minimize this heterogeneity, most mechanistic cell migration studies utilize established malignant cell lines such as MDA-MB-231 (breast adenocarcinoma), HT-1080 (fibrosarcoma), and U-87 MG (glioblastoma). Critically, even within the well-defined *in vitro* environments used to study cell migration mechanisms, cancer cell lines exhibit considerable population-wide variability in migration speed and efficiency, as well as heterogeneity in the nature and mode of migration. For example, numerous studies have reported single-cell 3D migration speeds that span an order of magnitude across a

cell population [47, 57, 95, 161]. This heterogeneity is likely due to both deterministic or cell-intrinsic diversity across the cell lines [231] as well as stochastic fluctuations in gene expression [302] and protein expression and activation [303]. Additional migration variability is likely a result of cellular plasticity in response to spatially and temporally fluctuating microenvironmental cues [5]. Critically, such temporal noise (i.e., variability in an individual over time) and population noise (i.e., diversity across the population) can confound population-averaged cellular and molecular measurements [231, 302, 304]. Thus, controlling and accounting for this heterogeneity is key to the effective identification and study of regulators of cell behavior including 3D cell motility. Notably, *in vitro* subcloning experiments in which single tumor cells are expanded into distinct subpopulations [305, 306] as well as landmark studies pioneered by Fidler and Kripke in which subtypes of differentially metastatic cells were isolated from a parent population of malignant cells together indicate that elements of invasive fitness are cell-intrinsic and heritable [307].

Here, we sought to unmask population-wide heterogeneity within the parental MDA-MB-231 cell population to define unique properties of highly and poorly invasive cancer cells. Because efficient 3D cell migration requires coordination of many sub-cellular behaviors which are driven by vast interconnected networks of molecular components [1], we developed a novel *in vitro* cell sorting technique based on 3D collagen I invasive fitness. We first sorted parental MDA-MB-231 cells (MDA^{PAR}) into collagen invasive (MDA^{INV}) and non-invasive (MDA^{NON}) subpopulations, which we then independently enriched through repeated rounds of sorting. To characterize

the purified subpopulations, we assessed 3D invasiveness within physiological collagen matrices as well as migration-associated behaviors. Notably, the purified subpopulations showed considerably divergent migration phenotypes in 3D collagen migration models: while MDA^{INV} showed efficient migration, MDA^{NON} showed defective migration in both 3D collagen matrix and collagen microtracks. Quantitative analysis showed that MDA^{INV} and MDA^{NON} cell morphologies and migration were within the upper and lower bounds, respectively, of the MDA^{PAR} population, indicating that the sorted subpopulations were indeed selected from within the heterogeneous parental population. Divergent cell phenotypes were maintained through freeze/thaw cycles and many population doublings, suggesting that the heterogeneity of invasive fitness observed in the parental MDA-MB-231 population is at least in part cell intrinsic and heritable. Ultimately, cell sorting and multi-parameter analyses of divergent cell phenotypes allowed us to identify several characteristic behaviors unique to efficient 3D migrators including coordination of 3D protrusion dynamics, 3D cell polarization, membrane ruffling, traction generation, and 3D matrix remodeling.

6.3 Materials and Methods

Cell culture and reagents

MDA-MB-231 breast adenocarcinoma cells (HTB-26; ATCC, Rockville, MD) were maintained in Dulbecco's modified Eagle's medium (DMEM; Life Technologies, Grand Island, NY) supplemented with 10% fetal bovine serum (FBS; Atlanta Biologicals, Flowery Branch, GA), 100 U/ml penicillin, and 100 µg/ml streptomycin

(Life Technologies). All cell culture and time-lapse imaging was performed at 37°C and 5% CO_2.

The following antibodies and reagents were used for Western blot analysis and fluorescent imaging: polyclonal anti-FAK (3285; Cell Signaling Technology, Danvers, MA), polyclonal anti-pFAK^{Y397} (3283; Cell Signaling Technology); polyclonal anti-Src (2108; Cell Signaling Technology, Danvers, MA), polyclonal anti-pSrc^{Y416} (2101; Cell Signaling Technology); monoclonal anti-GAPDH (MAB374; Millipore, Billerica, MA); anti-rabbit and anti-mouse conjugated to horseradish peroxidase (Rockland Immunochemicals, Limerick, PA); monoclonal anti-vinculin (V9131; Sigma-Aldrich, St. Louis, MO) polyclonal anti-MT1-MMP (AB6004; Millipore); polyclonal anti-cortactin (sc-11408; Santa Cruz Biotechnology, Santa Cruz, CA); Alexa Fluor 568-conjugated anti-rabbit (A-11036, Life Technologies); Alexa Fluor 488-conjugated anti-mouse (A-11001, Life Technologies); Alexa Fluor 488-conjugated phalloidin (Life Technologies); DAPI (Sigma-Aldrich). The MMP inhibitor GM6001 (20–100μM; Millipore), ROCK inhibitor Y27632 (10μM; Sigma-Aldrich), and Src kinase inhibitor 4-amino-5-(4-methylphenyl)-7-(t-butyl)pyrazolo-d-3,4-pyrimidine (PP1) (10μM; Sigma-Aldrich) were used as described below.

Cell migration studies and analysis

For 3D migration assessment, MDA-MB-231 cells were seeded sparsely within 1.5 mg/ml collagen matrices and 3 mg/ml collagen microtracks prepared from acid-solubilized type I rat tail tendon collagen as previously described [41]. Following

polymerization at 37°C, matrices were overlaid with culture media. Time-lapse phase contrast imaging was performed at ×10 or ×20 using a Zeiss Axio Observer Z1 inverted microscope equipped with a Hamamatsu ORCA-ER camera. Images were acquired >200 μm above the bottom surface of 3D matrices. All image analysis was performed using ImageJ (version 1.49b, National Institutes of Health, Bethesda, MD).

To accurately represent heterogeneity in the 3D migration phenotype, all cells were included in motility analysis unless they divided or interacted with other cells during the indicated observation period. For determination of the fraction of motile cells, matrices were imaged at 20-min intervals for 24 h immediately following polymerization. A cell was considered motile if the cell body displaced at least one cell diameter during a 2-h period, and motile fraction was defined as the ratio of motile cells to total cells. Following 12 h of spreading in 3D matrix and 4 h of spreading in microtracks, single cell migration speeds were quantified from stepwise (total speed) and net (net speed) cell body displacements during 4-8 h observation periods as indicated. Three-dimensional cell morphology and protrusions during migration were monitored from time-lapse image sequences.

Phenotypic cell sorting

To purify differentially invasive cells, parental MDA-MB-231 cells (MDA^{PAR}) were seeded in a custom-designed collagen invasion assay. Briefly, a thin 1 mg/ml collagen gel (~10 μm thickness) was polymerized in an 8-μm pore Transwell insert (Corning Life Sciences, Lowell, MA) for 15 min and the coated insert was equilibrated in

serum-free DMEM. Cells were plated at 40,000 cells/cm^2 on the gel surface in DMEM + 0.5% FBS, and the insert was placed in a well plate containing DMEM + 10% FBS. On day 2 of culture, the media in the upper reservoir was replaced with fresh DMEM + 0.5% FBS. On day 4 of culture, media was removed from both the upper Transwell insert and lower well plate and reserved. Adherent cells were removed from both compartments with 0.25% Trypsin-EDTA (Life Technologies) and cell suspensions were pooled with their respective reserved media. Invasive (MDA^{INV}) and non-invasive (MDA^{NON}) cell subpopulations were recovered by centrifugation from the lower and upper compartment solutions, respectively. Purifying cell sorting was achieved by repeatedly seeding MDA^{INV} and MDA^{NON} cells on separate freshly prepared collagen invasion assays as described above. For purification of MDA^{INV} cells, invasive cells were recovered and reseeded; for purification of MDA^{NON} cells, non-invasive cells were recovered and reseeded. Twenty rounds of purification were performed, during which time MDA^{PAR} cells were maintained and passaged every 4 d. Invasive fraction was calculated as the number of invaded cells in the lower compartment divided by the total number of cells in the upper and lower compartments on day 4. Subpopulations were used in experiments for up to 8 passages following purification (up to 15 passages to validate retention of invasiveness in Figure 6.2B) with no discernible changes in behavior.

Matrix metalloproteinase activity was inhibited in the collagen invasion assay by addition of the broad spectrum MMP inhibitor GM6001 to the upper chamber of the Transwell at 0–100 μM, where 0 μM samples were treated with the 100μM equivalent

of dimethylsulfoxide (DMSO) vehicle. For MT1-MMP knockdown experiments, MDA^{INV} cells were transfected with 25nM MT1-MMP siRNA (accession number NM_004995.2; targeting sequence: 5′-CCUACGAGAGGAAGGAUGGCAAAUU-3′) or control siRNA (non-targeting sequence: 5′-UUCCUCUCCACGCGCAGUACAUUUA-3′) using Lipofectamine 2000 (2μg/ml; Life Technologies).

Imaging and morphology quantification

Two-dimensional (2D) cell morphologies were assessed by measuring area and circularity of cells 24 h after seeding on tissue culture plastic. Phalloidin- and DAPI-stained samples were used to determine F-actin organization, and cells were categorized as having actin organized into ruffling lamellipodia, stress fibers, or both lamellipodia and stress fibers. For adhesion immunofluorescence, cells were stained for vinculin, pFAK, and DAPI or F-actin and pFAK. Control and PP1-treated samples (24 h treatment) were stained for F-actin and MT1-MMP or cortactin. Fluorescent images are maximum projections and were acquired using a Zeiss LSM700 at ×40.

Protrusion assay

Cells were seeded sparsely on tissue culture plastic and allowed to spread for 24 h before being serum starved for 16 h with DMEM + 0% FBS. Cell areas were measured from phase contrast images acquired immediately before and 2 h after media was replaced with DMEM + 10% FBS.

Cell contractility assays

To assess 3D matrix remodeling ability, cells were seeded at 300,000 cells/ml in floating 1.5 mg/ml collagen matrices. To quantify contraction, gel areas at d 4 were compared to the initial gel area and the change in gel area was normalized to MDA^{PAR} control. Confocal reflectance of collagen matrix at d 4 was performed on DAPI-stained samples using a ×40/1.1 water-immersion lens on a Zeiss LSM700 as previously described [129].

To measure traction force generation, cells were seeded on 5 kPa polyacrylamide substrates coated with 100µg/ml type I rat tail collagen (Becton Dickinson, Franklin Lakes, NJ). Traction force experiments were performed as previously described [136, 246] and traction fields were obtained from bead displacements using the LIBTRC analysis library developed by Dr. Micah Dembo. Data area presented as total force magnitude |F|, which is equal to the integral of the traction field over the area of the cell.

Western blotting

Protein was extracted from serum-starved (0% FBS) cells on tissue culture plastic using preheated (95°C) 2× Laemmli sample buffer and subjected to SDS-PAGE as previously described [41]. Horseradish peroxidase signal was revealed with the SuperSignal West Pico or West Femto kit (Thermo Scientific, Rockford, IL). Densitometry was performed using ImageJ. For quantification of total protein expression, total protein signal was normalized to GAPDH loading control. For

quantification of protein activation by phosphorylation, $pSrc^{Y416}$ or $pFAK^{Y397}$ signal was first normalized to GAPDH, then to its respective GAPDH-normalized total protein signal.

Statistical analysis

Data are shown as means ± SEM or box-and-whisker plots, where boxes represent medians and $25^{th}/75^{th}$ percentile and bars indicate the 5^{th} and 95^{th} percentiles. Means were compared using analysis of variance (ANOVA), with a post hoc Tukey's honestly significant difference test using JMP software. Cell migration speeds, cell area change, and traction forces were compared using a nonparametric Wilcoxon test.

6.4 Results

Three-dimensional cancer cell migration is heterogeneous and heritable

Following seeding in fibrillar 3D collagen matrix, MDA-MB-231 cells began to spread and migrate, and the motile fraction plateaued by 12 h, indicating that following a phase of initial cell spreading, 65% of cells were migratory (Figure 6.1A; dashed line). Once this steady state was reached, cells exhibited a range of migration proficiency (Figure 6.1B), which is reflected by the distributions of both total migration speed (95% confidence interval: 0.12-0.62 μm/min) and net migration speed (95% confidence interval: 0.01-0.22 μm/min) (Figure 6.1C). Of note, 3D migration was generally inefficient, as indicated by net migration speeds (derived from stepwise movement) significantly less than total migration speeds (derived from total displacement) (Figure 6.1C). Interestingly, despite this extensive variability in cell

motility across the population, 3D migration fitness was conserved through cell division, as indicated by a positive correlation (R^2 = 0.62 for linear fit) of mother and daughter cells' total migration speed (Figure 6.1D). Taken together, these data suggest that the diversity of 3D migration fitness exhibited by MDA-MB-231 cells may be a result of heritable cell-intrinsic differences between cells.

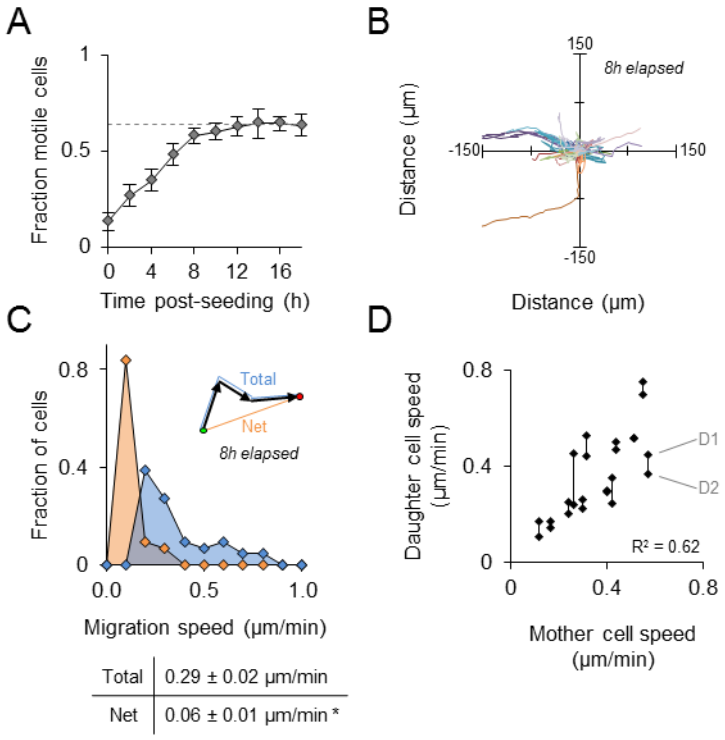

Figure 6.1. Heterogeneity and heritability of 3D migration in parental MDA-MB-231 cells. (A) Fraction of motile MDA-MB-231 cells following seeding in 1.5 mg/ml collagen matrix. Dashed line indicates maximal motile fraction achieved by steady state. **(B)** Single-cell migration paths and **(C)** total and net cell migration speeds over 8 h. Quantification of mean ± SEM total and net migration speeds. *, P < 0.0001. **(D)** Correlation of total cell migration speed before and after mitosis. Each pair of daughter cells, D1 and D2, is connected by a vertical line, and the average daughter cell speed was used to determine correlation (R^2 = 0.62).

Purification of stable cell subpopulations based on invasive capacity

To purify differentially invasive subpopulations of cells, parental MDA-MB-231 cells were seeded in a collagen gel Transwell invasion assay (Figure 6.2A). In this assay, invasive cells migrate through a collagen gel and 8-µm membrane pores into the lower compartment of the well, while non-invasive cells remain in the upper compartment adhered to the gel surface.

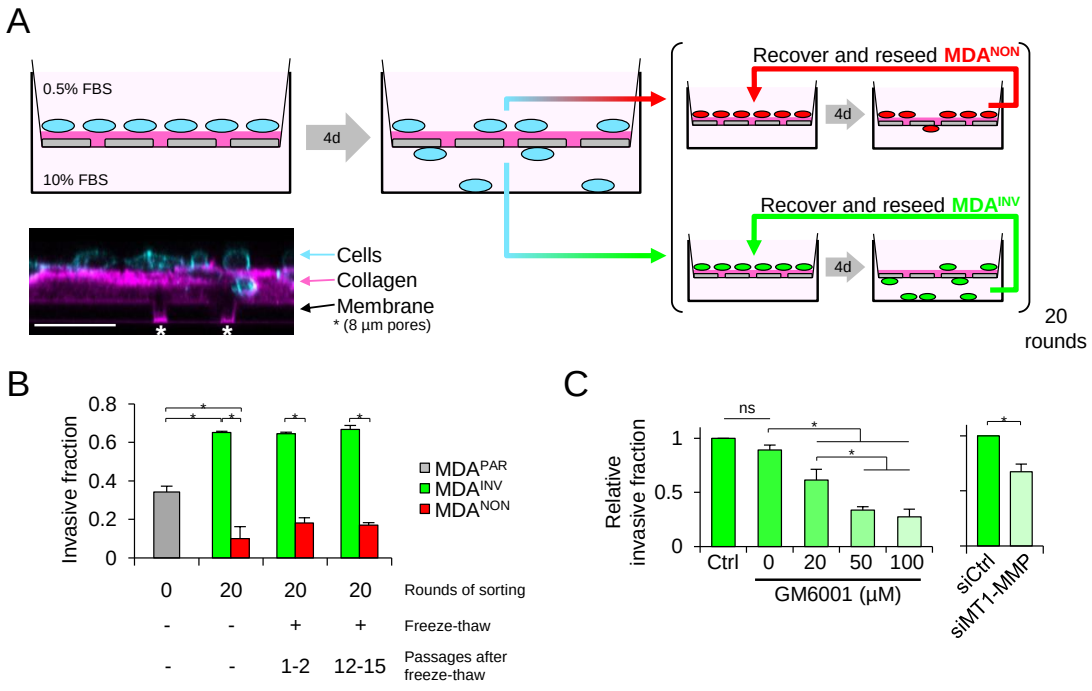

Figure 6.2. Phenotypic cell sorting to purify differentially invasive MDA-MB-231 subpopulations. (A) Schematic of behavioral cell sorting technique. Cells seeded on a collagen gel invade through matrix into the lower chamber of the Transwell. After 4 d, cells in each compartment were removed and seeded in separate invasion assays, and the process was repeated for 20 rounds of selection. Orthogonal confocal view showing cells (cyan) seeded on collagen matrix (magenta). * indicate 8 µm pores in Transwell membrane. Scale bar: 25 µm. **(B)** Invasive fraction (mean ± SEM) calculated as $n_{invaders}$ / ($n_{invaders}$ + $n_{non\text{-}invaders}$) for the indicated populations after 4 d of invasion. *, $P < 0.05$. **(C)** Invasive fraction of MDA^{INV} cells treated with GM6001 or MT1-MMP siRNA. Data are represented as mean ± SEM from n = 2-3 independent. *, $P < 0.05$; ns, not significant.

After 4 d of culture, the invasive (MDA^{INV}) and non-invasive (MDA^{NON}) cell populations were recovered and reseeded separately for the next round of cell sorting. Following 20 rounds of purification, MDA^{INV} and MDA^{NON} cells exhibited significantly divergent invasive capacities as compared to parental MDA-MB-231 cells. These differences in invasive fitness were maintained through a freeze-thaw cycle and over many passages of growth on tissue culture plastic (Figure 6.2B). While ~30% of parental MDA^{PAR} cells were invasive, ~65% of MDA^{INV} and less than ~20% of MDA^{NON} invaded into the lower compartment of the Transwell. Notably, the enhanced invasiveness of MDA^{INV} cells was dependent on MT1-MMP activity as indicated by dose-dependent decreases in invasive fraction with both broad spectrum MMP inhibition and siRNA knockdown of MT1-MMP (Figure 6.2C). These results indicate that our cell sorting technique effectively separated two subpopulations of cells with stable and opposing collagen-invasive capacity.

Purified MDA-MB-231 subpopulations exhibit differences in 3D migration

We next examined whether differential invasiveness through the cell sorting assay translated to differential cell migration within 3D collagen microenvironments. When seeded in 3D collagen matrix, MDA^{INV}, but not MDA^{NON}, initiated 3D motility. Maximum motility was achieved by 16 h, when 83% of MDA^{INV} and only 5% of MDA^{NON} cells were motile (Figure 6.3A), both of which were significantly different from the 64% of MDA^{PAR} cells that were motile (Figure 6.3A; dashed lines). These results indicate a shift in population-wide motility whereby the MDA^{INV} population is enriched for migratory cells and the MDA^{NON} population contains few migratory cells.

Single cell tracking after 16 h showed that MDA^{INV} cells migrated persistently while MDA^{NON} showed little cell body displacement (Figure 6.3B). These differences in 3D migration were reflected in quantification of total and net migration speeds, which were both significantly lower for MDA^{NON} (Figure 6.3C).

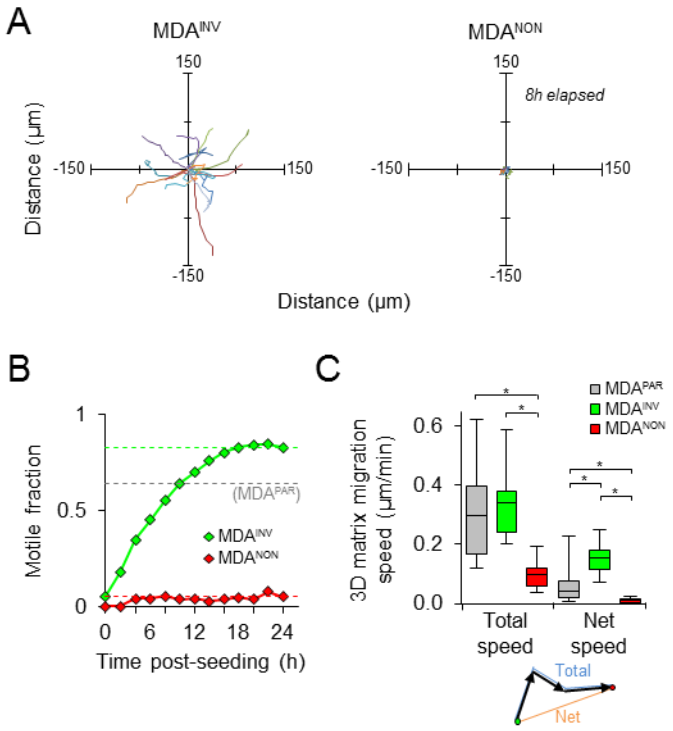

Figure 6.3. 3D matrix migration of purified MDA-MB-231 subpopulations. (A) Fraction of motile MDA^{INV} and MDA^{NON} cells following seeding in 1.5 mg/ml collagen matrix. Dashed green (MDA^{INV}), red (MDA^{NON}), and gray (MDA^{PAR}) lines indicate maximal motile fraction achieved by steady state. $P < 0.0001$, all pairs. **(B)** Single-cell migration paths and **(C)** total and net migration speeds of MDA-MB-231 subpopulations. Box and whisker plots show medians, 25th/75th, and 5th/95th percentiles. *, $P < 0.0001$.

Assessment of net speed confirmed that MDA^{NON} were defective at cell body displacement in 3D and indicated that these cells' non-zero total migration speed was due to small oscillatory movements of the cell centroid around the initial cell position. Both the total and net migration speeds of the MDA^{INV} and MDA^{NON} subpopulations

were within or near the 95% confidence interval of MDA^{PAR} migration speeds (Figure 6.3C), indicating selection of the best and worst migrating cells from the heterogeneous parental population. Analysis of cell morphodynamics in 3D collagen demonstrated that both MDA^{INV} and MDA^{NON} were able to generate protrusions into the surrounding matrix, but only MDA^{INV} elongated, polarized, and displaced the cell body (Figure 6.4A). Interestingly, while MDA^{INV} and MDA^{NON} cells showed equivalent 3D protrusion formation during early cell spreading (0-3 h post-seeding) (Figure 6.4B), only MDA^{INV} transitioned to a low-protrusion, high-displacement state by 12-18 h (Figure 6.4C).

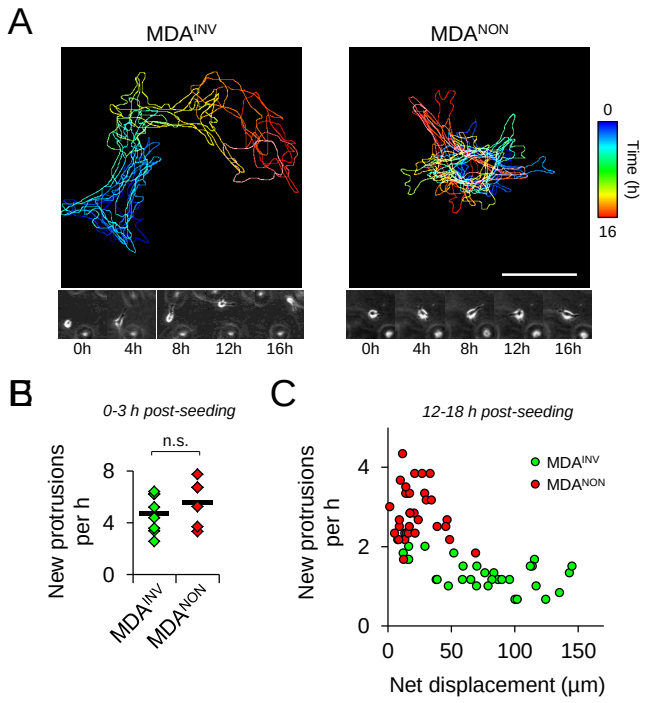

Figure 6.4. 3D morphodynamics of purified subpopulations. (A) Morphodynamic analysis of MDA^{INV} and MDA^{NON} cells. Cell contours from 0-16 h were color coded blue-red and overlaid. Scale bar: 25 μm. **(B)** Protrusion formation rate during early cell spreading from 0-3 h following seeding in collagen; each point represents an individual cell. n.s., not significant. **(C)** Protrusion formation rate during steady state (12-8 h post-seeding) versus net cell displacement; each point represents an individual cell.

To test whether MDA^{NON} cells' defective 3D migration was due to the restrictive nature of 3D collagen matrix, we analyzed cell migration in collagen microtracks, which mimic matrix-free spaces within interstitial tissue and provide cell-scale paths of least resistance that drastically reduce the mechanistic threshold required for efficient 3D migration [41]. We previously showed that parental MDA-MB-231 cells adhere to physiological collagen matrix on all sides when seeded within tube-like microtracks, where they undergo efficient, MMP-independent migration [41, 60]. Here, we found that both MDA^{INV} and MDA^{NON} elongate and move within microtracks (Figure 6.5A), and MDA^{INV} showed significantly faster migration speeds than MDA^{NON} (Figure 6.5B). As in 3D matrix, the invasive and non-invasive subpopulations' total migration speeds fit within the range of previously reported parental MDA-MB-231 migration speeds (Figure 6.5B; dashed gray lines) [41]. As in 3D matrix, MDA^{NON} microtrack migration was inefficient and oscillatory, resulting in significantly lower net displacement speed than total migration speed (Figure 6.5B). Interestingly, assessment of cell morphology during migration analysis indicated that MDA^{NON} cells failed to acquire front-rear polarization characteristic of efficiently migrating MDA^{INV} cells in both 3D matrix and microtracks (Figure 6.5C). Notably, MDA^{PAR} showed a mixed phenotype, with an intermediate fraction of front-rear polarized cells. Together, these data indicate that the purified subpopulations are representative of the most (MDA^{INV}) and least (MDA^{NON}) migratory cells in the heterogeneous parental MDA-MB-231 population. Dynamic analysis of cell behavior in 3D collagen matrix and microtracks suggests that the differential 3D migration

phenotypes shown by the MDA^{INV} and MDA^{NON} subpopulations are due to differences in the cells' abilities to coordinate migration machinery.

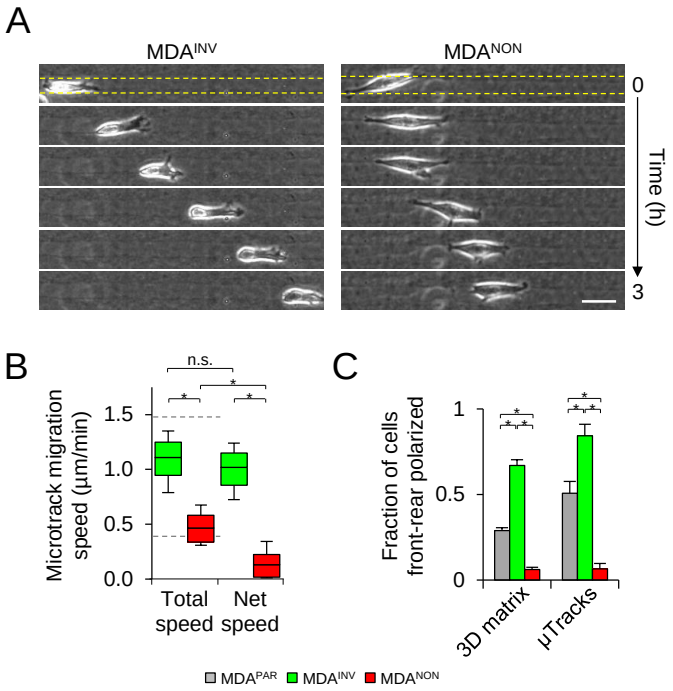

Figure 6.5. 3D collagen microtrack migration of purified subpopulations. (A) Time-lapse image series of MDA^{INV} and MDA^{NON} cells migrating in collagen microtracks for 3 h. Dashed yellow lines indicate microtrack edges. Scale bar: 25 µm. **(B)** Total and net microtrack migration speeds. Dashed gray lines indicate 5th and 95th percentiles of MDA^{PAR} total microtrack migration speed. *, $P < 0.0001$; n.s., not significant. **(C)** Fraction of cells showing front-rear polarization in 3D collagen matrix and microtracks (µTracks). Representative polarized (MDA^{INV}) and non-polarized (MDA^{NON}) cells are shown in Figure 6.4A (3D matrix) and Figure 6.5A (microtracks). *, $P < 0.0001$.

Purified subpopulations exhibit divergent cell morphology, adhesion signaling, and membrane dynamics

Cytoskeleton organization and dynamics are key regulators of cancer cell migration in 2D and 3D environments [91]. Thus, we hypothesized that the purified subpopulations would exhibit differences in morphology and cytoskeleton organization. Indeed,

parental and purified MDA-MB-231 subpopulations were morphologically distinct on tissue culture plastic (Figure 6.6A). MDA^{INV} cells were smaller and showed more lamellipodia (thus, lower circularity) than MDA^{NON} cells (Figure 6.6B; vertical and horizontal lines represent mean area and circularity, respectively). Notably, the MDA^{PAR} population contained cells that resembled those purified in the MDA^{INV} and MDA^{NON} subpopulations (Figure 6.6A,B; green and red arrowheads, respectively). Approximately 60% of MDA^{PAR}, MDA^{INV}, and MDA^{NON} cells contained F-actin organized in both peripheral stress fibers and ruffling lamellipodia (Figure 6.6C,D; black and white arrowheads, respectively). However, while the remainder of the MDA^{PAR} population contained both cells with ruffling lamellipodia only (10%) and cells with stress fibers only (29%), MDA^{INV} cells predominantly exhibited ruffling lamellipodia (36%) and MDA^{NON} primarily showed pronounced stress fibers (38%) (Figure 6.6C,D).

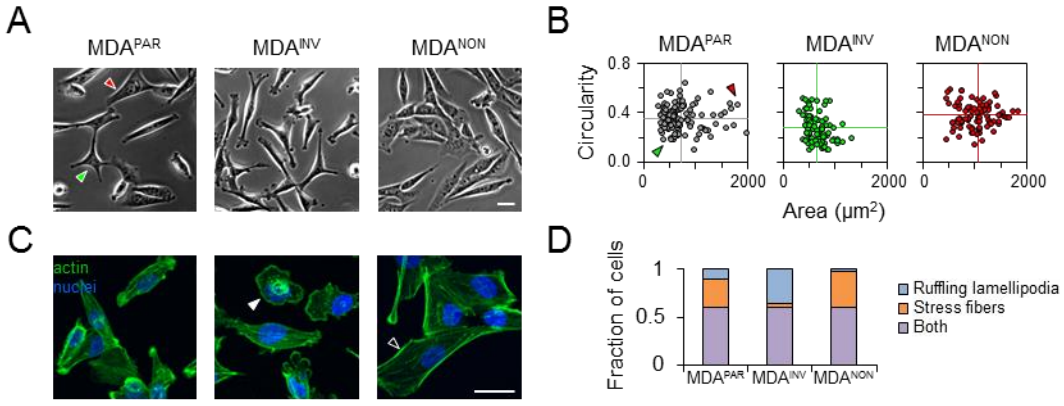

Figure 6.6. Differential cell morphology of purified subpopulations. (A) Representative two-dimensional morphologies and **(B)** distributions of cell area and circularity of the MDA-MB-231 subpopulations. Arrowheads indicate MDA^{INV}-like (green) and MDA^{NON}-like (red) cells in the MDA^{PAR} population. Vertical and horizontal lines in B indicate average cell area and circularity, respectively. **(C)** Actin cytoskeleton morphology and **(D)** quantification. Arrowheads indicate ruffling lamellipodia (white) and peripheral stress fibers (black). Scale bars: 25 μm.

Because of the interdependence of the actin cytoskeleton and cell-matrix adhesions, we hypothesized that the purified subpopulations would exhibit dissimilar adhesive structures and signaling [234]. MDA^{INV} cells showed accumulation of vinculin and $pFAK^{Y397}$ in relatively small, nascent adhesion complexes along the periphery of the ruffling membrane and within the lamellipodium (Figure 6.7A; white arrowheads) while MDA^{NON} cells contained larger, elongated focal adhesions at the ends of actin stress fibers (Figure 6.7A; black arrowheads).

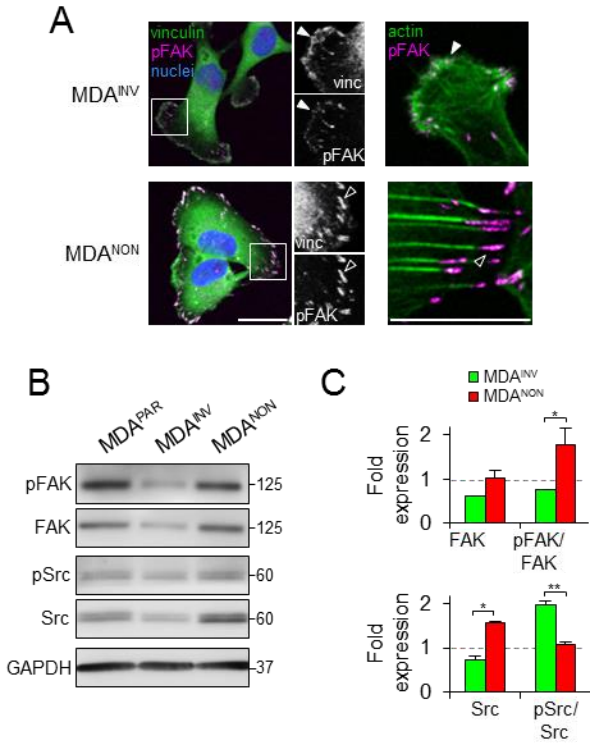

Figure 6.7. Differential adhesion signaling of purified subpopulations. (A) Representative vinculin (green) and pFAK (magenta) adhesion immunofluorescence images of MDA^{INV} and MDA^{NON} cells on 2D substrate. Insets show ×2 magnification to highlight different adhesion structures. Actin (green) and pFAK (magenta) show subpopulation-specific cytoskeleton/adhesion complex association. Arrowheads indicate small, nascent adhesions in MDA^{INV} (white) and large focal adhesions in MDA^{NON} (black). Scale bars: 25 µm. **(B)** Western blot analysis of signaling and **(C)** quantification of total and phosphorylated protein signal intensity normalized to GAPDH expression. Dashed gray lines indicate MDA^{PAR} expression levels. *, $P < 0.05$; **, $P < 0.001$.

These differences in adhesion organization were associated were alterations in FAK signaling between the purified subpopulations, with MDA^{NON} showing a significant increase in FAK activation over MDA^{INV} (Figure 6.7B,C). Active Src has been shown to localize to membrane ruffles and correlate with protrusion velocity [308]. Interestingly, while MDA^{NON} upregulated total Src expression as compared to MDA^{INV}, MDA^{INV} showed increased Src activation (Figure 6.7B,C).

Since 2D protrusion has been found to be predictive of cancer cell motility in 3D matrices [309], we assessed serum-induced protrusion of the isolated subpopulations. Upon serum stimulation, MDA^{INV} cells induced lamellipodia that resulted in a significant increase in 2D cell area after 2 h (Figure 6.8A,B). In contrast, MDA^{NON} cells showed no distinguishable protrusion response, suggesting these cells exhibit reduced cytoskeleton dynamics. Notably, only MDA^{INV} cells showed peripheral localization of cortactin and MT1-MMP to ruffling lamellipodia (Figure 6.8C) and both membrane ruffling and peripheral localization of cortactin and MT1-MMP in MDA^{INV} were Src-dependent (Figure 6.8C,D). Interestingly, Src inhibition converted MDA^{INV} cell morphology to that of MDA^{NON} cells by reducing actin-rich membrane ruffles and promoting peripheral actin stress fibers, but had no effect on MDA^{NON} morphology (Figure 6.8C,D). These data suggest that Src activation uniquely promotes both membrane dynamics and the localization of motility-associated proteins in MDA^{INV} cells. The pronounced effect of Src inhibition on MDA^{INV} cells and lack of effect on MDA^{NON} cells further indicates a divergence in adhesion signaling between the isolated subpopulations.

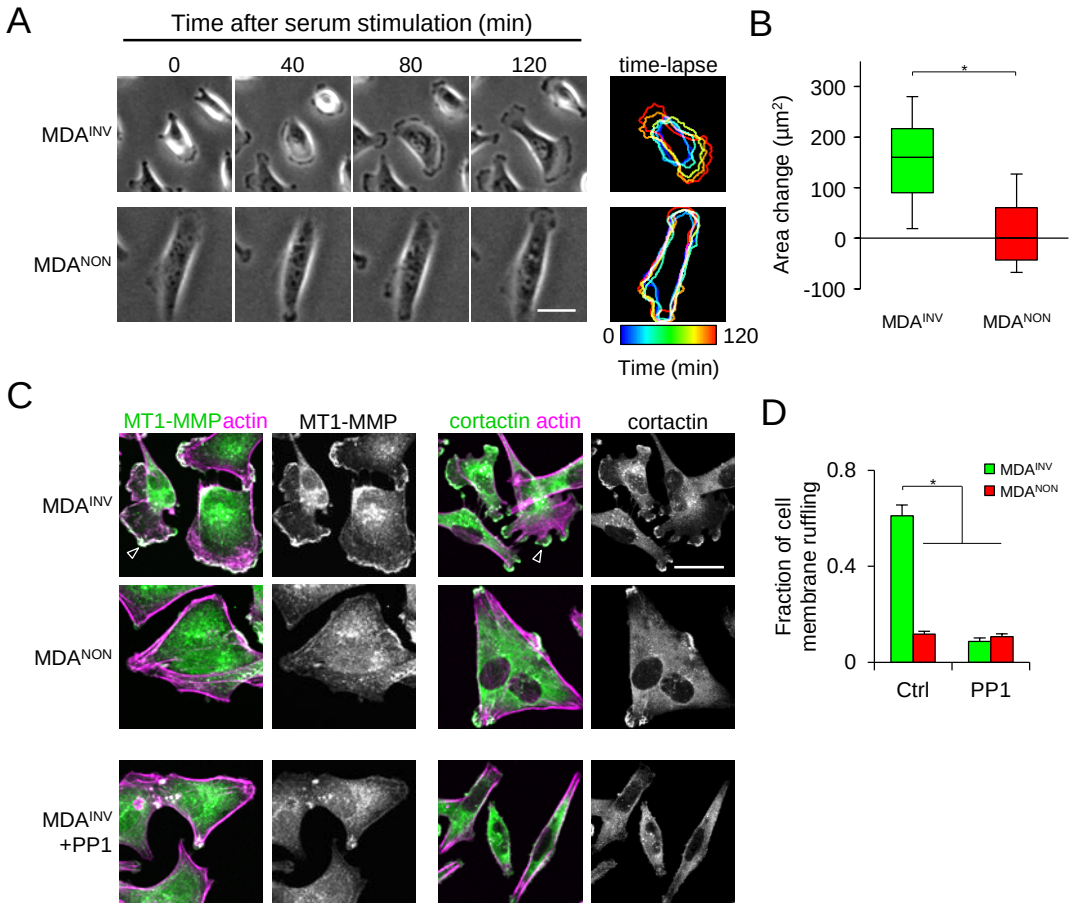

Figure 6.8. 2D protrusion and Src-dependent membrane dynamics. (A) Representative time-lapse image series of serum-stimulated MDA^{INV} and MDA^{NON} cells. Cell contours from 0 - 120 min were color coded blue-red and overlaid. **(B)** Quantification of single-cell area change ($A_{120\ min}$ / $A_{0\ min}$). Box and whisker plots show medians, $25^{th}/75^{th}$, and $5^{th}/95^{th}$ percentiles. *, $P < 0.0001$. **(C)** Representative MT1-MMP or cortactin (green) and actin (magenta) immunofluorescence images of MDA^{INV}, MDA^{NON}, and PP1-treated MDA^{INV} cells on 2D substrate. Black arrowheads indicate co-localization of MT1-MMP/cortactin with actin at the periphery of ruffling lamellipodia. **(D)** Quantification of cell membrane ruffling in control (Ctrl) and PP1-treated (10µM) MDA-MB-231 subpopulations, as determined by the fraction of peripheral cell membrane showing co-localization of cortactin and actin. *, $P < 0.0001$. Scale bars: 25 µm.

Taken together, these results provide insight into 2D behaviors that are indicative of efficient and inefficient 3D migration and invasion. Traits of good 3D migrators (MDA^{INV}) include the generation of nascent adhesions, Src activation, protrusiveness,

and peripheral localization of motility-associated proteins in membrane ruffles. Characteristics of poor 3D migrators (MDA^{NON}) include extensive actin stress fibers capped by large focal adhesions, elevated FAK signaling, deficient Src activation, and low cytoskeletal dynamics.

Invasive subpopulation generates enhanced traction forces, 3D contractility and matrix remodeling

Mesenchymal migration involves coordination of both protrusive and contractile behaviors, and the transmission of traction forces to fibrillar collagen is a critical feature of efficient migration through 3D matrices [41, 47]. Therefore, we tested the contractile properties of the parental and purified MDA-MB-231 populations. While single-cell traction forces measured by TFM were heterogeneous and varied widely from 100-1000nN, MDA^{INV} exerted significantly higher traction forces than both MDA^{PAR} and MDA^{NON} (Figure 6.9A). As indicated by non-zero relative gel contraction, all cell populations generated ROCK-dependent 3D cell traction to contract collagen gels (Figure 6.9B). However, MDA^{INV} exhibited significantly enhanced 3D matrix remodeling over both MDA^{PAR} and MDA^{NON} (Figure 6.9B). This enhanced bulk matrix contraction was associated with substantial compaction of collagen fibers around cells (Figure 6.9C; black arrowhead) that was dependent on ROCK activity (Figure 6.9C; inset), illustrating the increased collagen remodeling abilities of MDA^{INV}. Together, these results indicate that the invasive MDA^{INV} subpopulation is adept at traction force generation, particularly within a 3D collagen

environment, where force generation is a critical determinant of 3D migration competence.

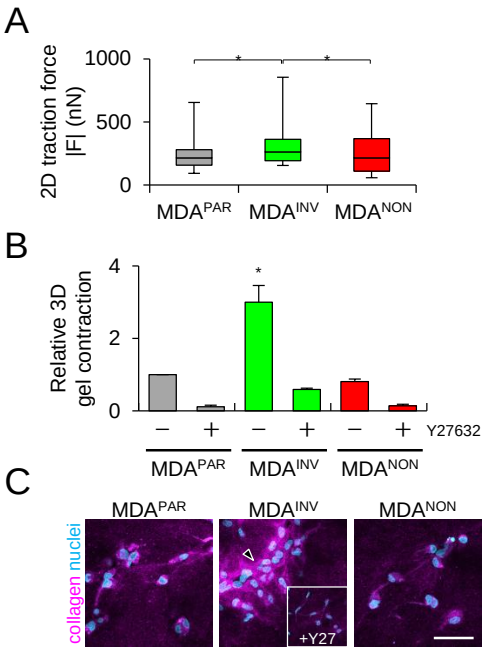

Figure 6.9. Cell contractility and ROCK-dependent matrix remodeling. (A) Total traction force magnitude, |F|, of MDA-MB-231 subpopulations. Data are represented as box and whisker plots showing medians, $25^{th}/75^{th}$, and $5^{th}/95^{th}$ percentiles of traction force measurements from $n > 45$ cells. *, $P < 0.05$. **(B)** Bulk collagen matrix contraction by MDA^{PAR}, MDA^{INV} and MDA^{NON} cells. Contraction is normalized to MDA^{PAR} control. *, $P < 0.001$ **(C)** Confocal reflectance images of collagen matrix (magenta) around embedded cells (cyan) following contraction. Black arrowhead indicates collagen fiber compaction as illustrated by increased reflectance signal. Inset highlights lack of matrix remodeling with Y27632 treatment. Scale bar: 25 µm.

6.5 Discussion

Three-dimensional cell migration is critical to many physiological and pathological processes, including cancer invasion and metastasis [44]. Defining the prevailing regulators of 3D motility is of considerable biological and clinical relevance [1], but the ability to do so is confounded by cellular heterogeneity that results from cell-intrinsic diversity [231], stochastic temporal and population variability [302], and

cellular adaptation and plasticity in response to microenvironmental cues [5]. While strides in *in vitro* microenvironment engineering and an increasing understanding of cellular plasticity have led to progress in defining context-specific cellular mechanisms of tumor cell motility [5, 229], intratumor heterogeneity continues to hinder both the investigation and treatment of cancer progression [263, 302, 310].

Therefore, the objective of this study was to unmask population-wide variability to better understand the cellular determinants of 3D tumor cell migration. To do so, we first sorted a heterogeneous parental population of malignant MDA-MB-231 cells into collagen-invasive (MDA^{INV}) and non-invasive (MDA^{NON}) subpopulations. We examined these cells' 3D migration phenotypes using time-lapse imaging and analysis of cell morphodynamics and found that the failure of MDA^{NON} cells to migrate in 3D collagen matrix was associated with an inability to coordinate 3D cell protrusion and polarize, implicating these processes as critical for 3D cell migration. The sorted MDA-MB-231 subpopulations exhibit differences in 2D cell morphology, actin cytoskeleton organization, and adhesion signaling and the most invasive cells show enhanced 2D protrusion and 2D/3D traction force generation. The purified subpopulations' divergent phenotypes and differential invasive behaviors are stable over many generations, indicating that the variability of 3D migration fitness shown by MDA-MB-231 cells can be attributed in part to heritable, cell-intrinsic differences across the inherently heterogeneous cell line.

The extensive molecular and phenotypic heterogeneity exhibited by cells within a tumor is becoming increasingly appreciated, and can contribute to disease progression by sustaining tumor growth [311], enabling the emergence of drug-resistant clones [310], and facilitating invasive migration [144, 312]. Intratumor heterogeneity is increasingly thought to be partially deterministic, that is, predetermined by cell-intrinsic or microenvironmental factors, the majority of which are thus far uncharacterized [231]. Recently, several powerful approaches have been developed to decipher heterogeneity at the transcript and protein levels *in situ* [313–316]. Alternative strategies exploit heterogeneity by using differential protein expression and/or activation to purify live cells that can then be used for further studies [303, 317]. However, most cell processes are multifactorial in that they result from the coordination of many molecular components and cellular subroutines. Thus, *in vitro* behavior-based cell sorting strategies can be used to isolate and study specific complex behaviors including chemotaxis, drug resistance, and invasiveness [306, 318, 319].

Although 3D cell migration is not driven by any one molecule or cell behavior in isolation, but rather the coordinated effort of many players across length and time scales [45], the process of behavioral sorting allowed us to define key subcellular behaviors indicative of efficient and inefficient 3D migrators. Specifically, we found that early 3D cell spreading is dominated by frequent protrusion into the surrounding ECM, and that MDA^{INV}, but not MDA^{NON} cells, down-regulate this indiscriminate protrusion formation and translate the cell body. These results suggest that moderation

of protrusion initiation enables efficient 3D migration. This finding is in contrast to previous work showing that protrusion frequency correlates positively with 3D cell speed [85]. However, this discrepancy can be attributed to substantial differences between experimental systems as the previous finding was derived by analysis of focal adhesion protein-depleted cells, which generally showed both decreased migration speed and protrusion frequency. We recently found that collagen microtracks significantly lower the mechanistic threshold for 3D cell migration by providing cell-scale space in which cells can spread, move, and readily adapt migration mode [41]. Here, we examined MDA-MB-231 subpopulation migration in microtracks to determine if the defective migration phenotype of MDA^{NON} cells is due to an inability to overcome 3D matrix confinement. Like parental and MDA^{INV} cells, MDA^{NON} cells are motile within microtracks, but show significantly impaired migration speed and efficiency, indicating a deficiency in coordination of migration mechanisms [45, 143]. Indeed, the inability of poorly migratory MDA^{NON} cells to polarize and establish a front-rear axis supports this hypothesis since this process is critical to cell migration and requires coordination among Rho GTPases, the cytoskeleton, and polarity proteins [199, 220, 320]. Together, our findings indicate that: 1) decreasing isotropic matrix exploration in favor of polarized cell elongation is a critical part of mesenchymal 3D migration initiation and maintenance, 2) the most efficient migrators undergo this transition adeptly, and 3) a cell's failure to polarize in 3D matrix environments is indicative of poor 3D migration fitness.

Membrane protrusion serves to physically advance the cell front during migration [45] while simultaneously enabling subcellular localization of migration-associated molecules [321]. Our finding that 2D protrusion correlates with 3D migration is consistent with previous work, and the MDA^{NON} cells' lack of protrusive response to serum stimulation indicates defective cytoskeletal dynamics [309]. Interestingly, consistent with MDA^{INV} cells' dynamic nature, these cells show localization of active FAK to nascent adhesions within membrane ruffles, where FAK has been shown to activate Rac and protrusion [322]. Conversely, MDA^{NON} cells exhibit high FAK and low Src activation and contain stress fibers and large fibrillar adhesions, which are characteristic of inefficiently migrating cells [323]. Since FAK-Src signaling promotes adhesion turnover and enables protrusion [116], this suggests that MDA^{NON} cells' deficient Src activation may prevent adhesion turnover, leading to the formation of large adhesions and resulting in low cytoskeleton and adhesion dynamics [234]. Interestingly, it has been posited that FAK can exist in distinct pools within lamellipodia and focal adhesions that differentially respond to extracellular stimuli [322]. In light of the diverse roles of FAK and Src in cell motility [324], our finding that the purified subpopulations differ so significantly in adhesion morphology and signaling prompts further investigation of adhesion dynamics and signaling in both 2D and 3D environments [214, 217, 325].

The observed disparities in kinase activation and sensitivity to Src inhibition indicate that the subpopulations exhibit fundamental differences in cell signaling, so future work should also aim to characterize the major regulatory networks that integrate with

adhesion signaling. One such regulatory network includes the ubiquitous Rho family of small GTPases, the balance among which plays a critical role in cancer cell migration [92]. Indeed, the stark differences in motility, signaling, and 2D cell morphology exhibited by MDA^{INV} and MDA^{NON} suggest subpopulation-specific differences in the balance of activity between Rho and Rac [326], which is normally tightly regulated during protrusion and migration [232]. In addition to contributing to the establishment of cell polarity, Rho GTPase activity regulates cytoskeletal dynamics that contribute to mechanotransduction, force generation, and cell deformation [148], all of which are important for cancer cell migration [1]. Here, we show that MDA^{INV} uniquely elicit extensive 3D matrix remodeling that is dependent on the Rho GTPase pathway. While the mechanisms by which the invasive subpopulation excels at 3D force generation remain to be determined, the differences in 2D cell-matrix adhesion structures and traction force measurements are consistent with previous work showing that small, nascent adhesions apply strong traction force that gradually attenuates as adhesions mature and grow larger [327]. Thus, MDA^{NON} cells may exert lower traction force because they are unable to turnover their large cell-matrix adhesions. Future work should use the purified subpopulations to more closely examine the relationship among cell-matrix adhesion and cytoskeleton dynamics, and force generation in 3D to more fully explain the invasion-enabling features of MDA^{INV}.

Here, our examination of quantitative single-cell metrics including 3D migration speed, 2D/3D morphology, and traction force generation suggests that our behavioral

sorting was selecting, rather than conditioning, subpopulations from within the parental MDA-MB-231 population. Notably, for the isolated subpopulations, each of these measurements falls within the bounds set by population-wide analysis of the parental population. While the invasive subpopulation contains *more* cells that invade and migrate in 3D (as measured by invasive fraction and motile fraction, respectively) and contract (as measured by 3D gel contraction) than the parental MDA-MB-231 population, the single-cell analogs of these measurements, cell migration speed and traction force generation, were within the limits of the parental population. Therefore, while we cannot rule out that cells are altered by the sorting process, the resulting subpopulations of cells do show 2D and 3D behaviors that are representative of the extremes of the parental population.

A common strategy to study cell migration mechanisms is to subject a population of cells to various pharmacological or molecular treatments to identify the role of a molecule, pathway, or subcellular behavior of interest. A key presumption of this technique is that the population being studied is uniform or at least that molecular and phenotypic diversity across the population will average to represent the behavior of the population as a whole. However, it is likely that screening large heterogeneous populations of cells could mask the behavior and/or experimental response of the most relevant cells [231]. Here, we demonstrate this consequence through multivariate examination of the cell populations. Morphological and molecular analyses (Figure 6.6-6.8) indicate that the parental MDA-MB-231 population includes MDA^{INV}-like cells, which exhibit a dynamic actin cytoskeleton, relatively low expression but high

activation of Src, and extensive Src-dependent membrane ruffling. Conversely, the parental MDA-MB-231 population also includes MDA^{NON}-like cells, which show peripheral stress fibers, high expression but low activation of Src, and no morphological response to Src inhibition. Considering the mixed morphology and intermediate Src signaling (Figure 6.7C; dashed lines) of MDA^{PAR}, these findings indicate that the parental MDA-MB-231 population could contain both PP1-sensitive and PP1-insensitive cells. While future work should seek to directly address the issue of differential pharmacological sensitivity, our results suggest that cellular diversity across the cell population of interest could at best, dilute an experimental effect, and at worst, completely mask an experimental effect. In addition to impeding *in vitro* mechanistic studies, such consequences are likely extended to the clinical setting, where cellular heterogeneity has been closely linked to drug resistance and therapy-driven tumor evolution [328–330].

In summary, we demonstrate that by sorting cells based on invasive fitness, we can not only purify differentially invasive subpopulations of cells, but also utilize these cells to unmask characteristic behaviors otherwise obscured by cellular heterogeneity. Thus, we were able to define distinguishing predetermining features of efficient and poor 3D migrators. Ultimately, future studies should seek to further define unique molecular and phenotypic signatures of the most invasive and migratory cells, as these cells may physically drive the processes of invasion and metastasis [144, 307, 312]. More broadly, our results suggest that phenotypic diversity could be exploited to study other

cellular processes by first selecting for, then characterizing the underlying mechanisms of, a cell behavior of interest.

CHAPTER 7

INDUCTION OF A MECHANOSENSITIVE INVASIVE EPITHELIAL PHENOTYPE BY 3D COLLAGEN MATRIX

Portions of the data in this chapter were contributed by Karen Martin.

7.1 Abstract

A critical step in breast cancer progression is local tissue invasion, during which cells pass from the epithelial compartment to the stromal compartment. We recently showed that malignant leader cells can promote the invasion of otherwise non-invasive epithelial follower cells, but the effects of this induced-invasion phenomenon on follower cell phenotype remain unclear. Notably, this process can expose epithelial cells to the stromal extracellular matrix (ECM), which is distinct from the ECM within the normal epithelial microenvironment. Here, we used a 3D epithelial morphogenesis model in which cells were cultured in biochemically and mechanically defined matrices to examine matrix-mediated gene expression and the associated phenotypic response. We found that 3D collagen matrix promoted expression of mesenchymal genes including MT1-MMP, which was required for collagen-stimulated invasive behavior. Epithelial invasion required matrix anchorage as well as signaling through Src, PI3K, and Rac1, and increasingly stiff collagen promoted dispersive epithelial cell invasion. These results suggest that leader cell-facilitated access to the stromal

ECM may trigger an invasive phenotype in follower epithelial cells that could enable them to actively participate in local tissue invasion.

7.2 Introduction

Local tissue invasion is a key transition in solid tumor progression toward metastatic disease during which cells from the epithelial compartment bypass the basement membrane and cross into the underlying interstitial stroma [9]. Since invasion involves suppression of normal homeostatic epithelial behaviors and orchestration of extracellular matrix (ECM) remodeling and cell motility programs, this process is mechanistically burdensome [1], and it is unlikely that all of the cells within a tumor are invasion-competent [16]. Notably, it has been suggested that cooperation among distinct cellular subtypes within the tumor microenvironment could facilitate several elements of cancer progression, including invasion and metastasis [263, 331]. Our group and others have provided experimental evidence for this notion, showing that extracellular matrix remodeling by invasive cells or stromal fibroblasts can induce a co-invasive phenotype by which otherwise non-invasive epithelial cells can enter and migrate through the stromal ECM [144, 208, 332]. During this process, proteolytic ECM patterning by leader cells can result in the formation of matrix microtracks that provide physical space to enable unimpeded, mechanistically simpler migration by follower cells [41, 60, 162]. However, the comprehensive effects of the induced-invasion phenomenon on follower cell phenotype remain to be determined, and it is unclear how escape from the protective epithelial compartment and transit into the stromal compartment affects non-transformed epithelial cells.

Among the most significant differences between the epithelial and stromal tissue compartments is the distinct extracellular matrix that comprises each [13]. Whereas epithelial basement membrane is a thin, dense meshwork primarily consisting of laminin and type IV collagen [7], the interstitial stromal ECM is a structurally heterogeneous fibrillar network dominated by type I collagen [333]. In developing, homeostatic, and diseased mammary tissue, basement membrane and interstitial ECM biochemistry, architecture, and mechanics are key regulators of epithelial cell phenotype [13, 14], acting primary through ECM-specific integrin-based adhesion and signaling [249, 334–336]. Critically, even during extensive physiological tissue remodeling, hyperplastic disorders, and carcinoma *in situ*, epithelial/carcinoma cells remain adherent to the epithelial basement membrane, only accessing the type I collagen-rich stroma during tumor invasion [9].

To model the effects of mammary epithelial cell exposure to stromal type I collagen ECM, we utilized an *in vitro* epithelial morphogenesis model. This strategy was not intended to model physiological epithelial branching morphogenesis or pathological matrix-directed disease progression [58, 106, 206, 282, 337], but rather, provide a simple 3D culture system with which to simultaneously examine collagen matrix-mediated gene expression as well as the resulting collagen matrix-directed epithelial cell phenotype. We found that, compared to culture in 3D basement membrane (Matrigel), 3D type I collagen matrix induced mesenchymal gene expression and

promoted an MT1-MMP-dependent invasive epithelial phenotype that was driven by protrusive signaling and sensitive to collagen ECM structure and mechanics.

7.3 Materials and Methods

Cell culture and reagents

MCF-10A mammary epithelial cells (CRL-10317; ATCC, Rockville, MD) and MCF-10A stably expressing GFP-tagged H2B (MCF-10A/H2B-GFP; kind gift from Warren Zipfel, Cornell University, Ithaca, NY) were maintained in DMEM:F12 medium (Life Technologies, Grand Island, NY) supplemented with 5% horse serum, 20 ng/ml hEGF, 100 U/ml penicillin, and 100 µg/ml streptomycin (all from Life Technologies), 0.5 µg/ml hydrocortisone, 10 µg/ml insulin, and 100 ng/ml cholera toxin (all from Sigma-Aldrich, St. Louis, MO). MCF-10A growth medium containing 5 ng/ml hEGF was used for 3D cultures. All cell culture and time-lapse imaging was performed at 37°C and 5% CO_2.

The following reagents were used for fluorescent imaging: anti-E-cadherin antibody (sc-7870), anti-laminin γ2 antibody (sc-25341), and anti-fibronectin antibody (sc-80559) from Santa Cruz Biotechnology, Santa Cruz, CA; anti-vimentin antibody (V6389; Sigma-Aldrich); Alexa Fluor 568-conjugated anti-rabbit secondary antibody (A-11036), Alexa Fluor 568-conjugated anti-mouse secondary antibody (A-11004), Alexa Fluor 488-conjugated phalloidin, and Alexa Fluor 568-conjugated phalloidin from Life Technologies; DAPI (Sigma-Aldrich). The broad spectrum MMP inhibitor GM6001 (0.1 µM; EMD Millipore, Billerica, MA), Rac1 inhibitor NSC23766 (25

μM; Santa Cruz Biotechnology), Src kinase inhibitor PP1 (5 μM; Sigma-Aldrich), PI3K inhibitor LY294002 (10 μM; EMD Millipore), and ROCK inhibitor Y27632 (10 μM; Beckman Coulter, Brea, CA) were used as described below.

For MT1-MMP knockdown experiments, cells were transfected with 1 nM MT1-MMP siRNA (accession number NM_004995.2; targeting sequence: 5′-CCUACGAGAGGAAGGAUGGCAAAUU-3′) or control siRNA (non-targeting sequence: 5′-UUCCUCUCCACGCGCAGUACAUUUA-3′) using Lipofectamine 2000 (2μg/ml; Life Technologies). Medium was changed following 4 h of transfection and cells were seeded for experiments the following day.

3D epithelial morphogenesis culture

MCF-10A cells were seeded in 3D ECM gels and cultured for 4 days to monitor matrix-dependent epithelial morphogenesis. Matrigel (growth factor-reduced, Corning Life Sciences, Lowell, MA) was diluted with 3D culture medium to a final matrix concentration of 4 mg/ml. Three-dimensional collagen matrix was prepared from acid-extracted rat tail tendon type I collagen as previously described [55]. Briefly, 10 mg/ml collagen stock was diluted with 3D culture medium to final matrix concentrations of 1.0 mg/ml or 1.5 mg/ml and neutralized with 1 M sodium hydroxide. Mixed collagen/Matrigel matrices were prepared using the above protocols to generate final concentrations of each component as indicated. Non-enzymatic glycation of collagen was performed as previously described [54]. Collagen stock solution was mixed with 0.5 M ribose in 0.1% acetic acid to form glycated collagen solutions

containing a final concentration of 0, 50, or 100 mM ribose and incubated at 4°C for 5 days. Glycated collagen solutions were buffered to final concentrations of 25 mM HEPES and 44 mM sodium bicarbonate, and neutralized with 1 M sodium hydroxide to form 1.5 mg/ml collagen gels. Cells were incorporated into diluted Matrigel or neutralized collagen solutions at 10^5 cells/ml and solutions were polymerized at 37°C before being overlaid with 3D culture medium, which was changed every other day during experiments. For 2D gene expression control, cells were seeded on type I collagen-coated (0.1 mg/ml) glass.

Quantitative real-time RT-PCR

Total RNA was extracted using the RNeasy Mini Kit (Qiagen, Valencia, CA) from cell pellets trypsinized from 2D tissue culture as indicated or from 3D samples following matrix digestion with collagenase/dispase (Roche, Indianapolis, IN) per manufacturer instructions. RNA was reverse transcribed into cNDA using qScript cDNA SuperMix (Quanta Biosciences, Gaithersburg, MD) according to manufacturer's instructions and quantitative RT-PCR was performed using SYBR Green SuperMix (Quanta Biosciences) and an iCycler IQ Real-Time PCR detection system (Bio-Rad Laboratories, Hercules, CA). Gene expression was normalized to GAPDH. Custom primers were obtained from Life Technologies: E-cadherin forward: 5′-TTGACGCCGAGAGCTACA-3′, E-cadherin reverse: 5′-GACCGGTGCAATCTTCAAA-3′; N-cadherin forward: 5′-ACCAGGTTTGGAATGGGACAG-3′, N-cadherin reverse: 5′-ATGTTGGGTGAAGGGGTGCTTG-3′; vimentin forward: 5′-

TGAAGGAGGAAATGGCTCGTC-3′, vimentin reverse: 5′-GTTTGGAAGAGGCAGAGAAATCC-3′; Snail forward: 5′-ATCGGAAGCCTAACTACAGCGAGC-3′, Snail reverse: 5′-CAGAGTCCCAGATGAGCATTGG-3′; fibronectin forward: 5′-GATAAATCAACAGTGGGAGC-3′, fibronectin reverse: 5′-CCCAGATCATGGAGTCTTTA-3′; MT1-MMP forward: 5′-CGCTACGCCATCCAGGGTCTCAAA-3′, MT1-MMP reverse: 5′-CGGTCATCATCGGGCAGCACAAAA-3′; GAPDH forward: 5′-CATGAGAAGTATGACAACAGCCT-3′, GAPDH reverse: 5′-AGTCCTTCCACGATACCAAAGT-3′.

Indirect immunofluorescence and imaging

For immunofluorescence imaging, 3D matrix samples were fixed with buffered 3.7% formaldehyde, rinsed, permeabilized with 0.1% Triton X-100, and blocked with bovine serum albumin (1% w/v) and 10% fetal bovine serum (10% v/v) in PBS before overnight incubation with primary antibody in blocking solution (1:50). Samples were washed extensively before overnight incubation with secondary antibody in blocking solution (1:100). Fixed samples were labelled with phalloidin and DAPI for organoid morphology characterization. All imaging was performed using a Zeiss LSM700 confocal scanning head on a Zeiss Axio Observer Z1 inverted microscope. A ×40 long working distance water immersion lens was used for immunofluorescence and collagen matrix imaging by confocal reflectance microscopy, and a ×10 lens was used for organoid morphology and time-lapse imaging. Brightfield images were acquired

by detection of transmitted laser light using a T-PMT. Collagen matrix structure was quantified by measurement of matrix pore cross sectional area from confocal reflectance images of matrix immediately following polymerization. Epithelial organoid morphology was quantified my measurement of organoid cross sectional area, circularity ($4\pi \cdot (\text{area} / \text{perimeter}^2)$), and protrusive structure lengths. Organoid circularity was used to categorize organoid morphology: acinar (round, non-invasive colonies; circularity > 0.8); protrusive acinar (acinar colonies with protrusions; circularity 0.6-0.8); invasive (protrusive and stellate colonies; organoid circularity < 0.6). All image analysis was performed using ImageJ (version 1.49b, National Institutes of Health, Bethesda, MD).

Statistical analysis

Data are presented as mean ± SEM, or box-and-whisker plots, where boxes represent medians and $25^{th}/75^{th}$ percentile and bars indicate the 5^{th} and 95^{th} percentiles. Means were compared by one-way analysis of variance (ANOVA) with a post hoc Tukey's HSD test using JMP (version 10; SAS Institute, Cary, NC).

7.4 Results

Three-dimensional collagen induces an invasive epithelial phenotype

To determine the effect of matrix composition on mammary epithelial phenotype, we used a 3D morphogenesis assay in which Matrigel and type I collagen represented the basement membrane and stromal extracellular matrix, respectively. After 4 days of

culture, single MCF-10A epithelial cells proliferated to form multicellular clusters of cells, or organoids, whose morphologies were matrix-dependent (Figure 7.1A).

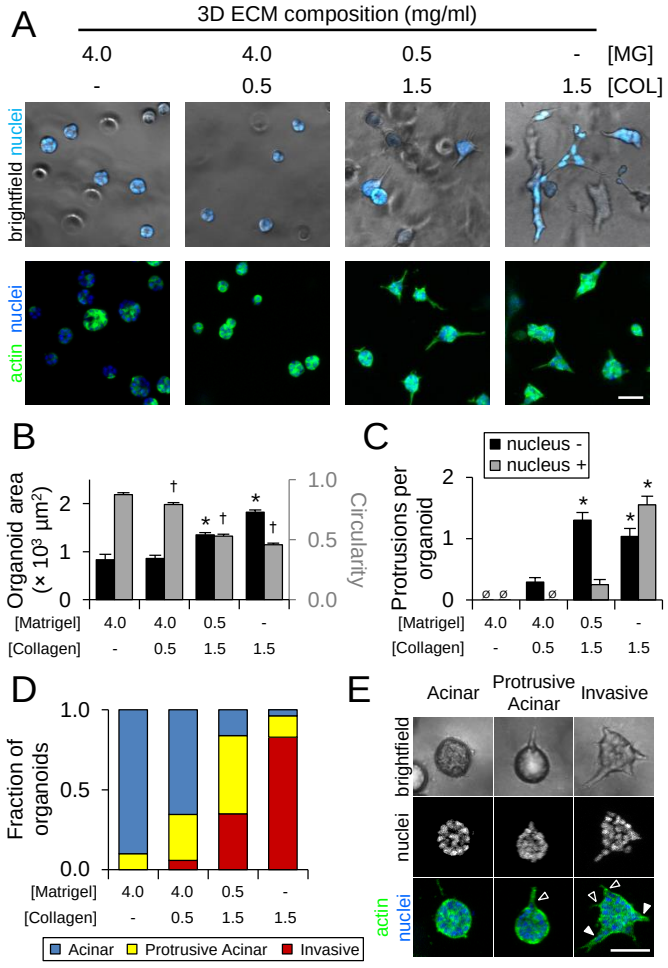

Figure 7.1. 3D matrix-induced epithelial cell phenotypes. **(A)** Brightfield and fluorescent images of MCF-10A epithelial organoids after 4 days of growth in the indicated ECM. **(B)** Quantification of organoid area (black bars) and circularity (grey bars). *, $P < 0.001$ as compared to Matrigel area; †, $P < 0.001$ as compared to Matrigel circularity. **(C)** Quantification of nucleus-free ('nucleus -', black bars) and nucleus-containing protrusions ('nucleus +', grey bars) exhibited by epithelial organoids. Ø, none detected. *, $P < 0.05$ as compared to no observed protrusions in Matrigel. **(D)** Quantification of organoid morphology. Circularity was used to determine organoid morphology as described in the text. Data in B-D was from n = 3 independent experiments (> 100 organoids per condition). **(E)** Representative images of acinar, protrusive acinar, and invasive MCF-10A epithelial organoids. Protrusive acinar and invasive organoids exhibit protrusions: nucleus-free, black arrowheads and nucleus-containing, white arrowhead. Scale bars: 50 µm.

Cells in pure Matrigel formed acinar organoids, and as collagen content was increased and Matrigel content decreased, organoids became increasing invasive, losing their rounded morphology and becoming stellate and protrusive. We quantified matrix-directed morphological changes to find that organoids in collagen were significantly larger and showed decreased circularity (Figure 7.1B), indicative of increased protrusivity. Whereas organoids in Matrigel and collagen-supplemented Matrigel showed no significant protrusions, organoids in Matrigel-supplemented collagen exhibited nucleus-free cytoplasmic protrusions, and organoids in pure collagen matrix uniquely generated both nucleus-free and nucleus-containing protrusions (Figure 7.1C). We measured the circularity of multicellular structures to categorize organoids as acinar (circularity > 0.8), protrusive acinar (circularity 0.6-0.8), and invasive (circularity < 0.6) and found that increasing collagen content and decreasing Matrigel suppressed acinar morphologies and promoted an invasive phenotype (Figure 7.1D). Overall, acinar structures were rounded and exhibited no protrusive extensions, protrusive acinar organoids were rounded and typically contained one or more nucleus-free protrusion (Figure 7.1E; black arrowhead), and invasive organoids were morphologically heterogeneous and generally contained one or more nucleus-free and nucleus-containing protrusion (Figure 7.1E; black and white arrowheads, respectively). Together, these results confirmed that the 3D collagen-induced invasive phenotype involves expansive outgrowth, protrusion, and cell body translation into the surrounding ECM.

Three-dimensional collagen promotes mesenchymal gene expression

To better understand how the ECM composition regulates epithelial cell behavior, we measured 3D matrix-dependent gene expression using quantitative real-time RT-PCR and indirect immunofluorescence. We found that collagen downregulates E-cadherin expression while inducing significant upregulation of the mesenchymal markers vimentin, fibronectin, and Snail (Figure 7.2A).

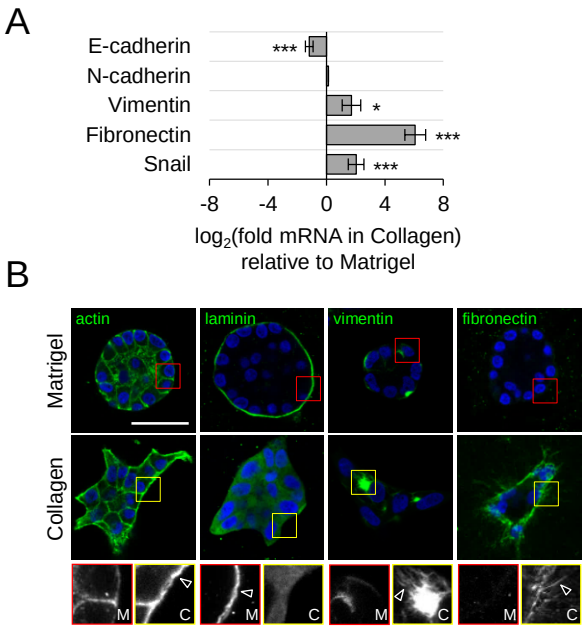

Figure 7.2. 3D matrix-dependent gene expression. (A) Gene expression of MCF-10A in 1.5 mg/ml collagen and 4.0 mg/ml Matrigel measured by quantitative real-time RT-PCR. Data are presented as $\log_2$(collagen expression / Matrigel expression) such that positive values indicate upregulation and negative values indicate downregulation relative to Matrigel. Data are mean ± SEM from at least n = 3 independent experiments. *, P = 0.01; ***, P < 0.0001. **(B)** Representative confocal images of actin, laminin, vimentin, and fibronectin staining in organoids developed in Matrigel and collagen. Insets and arrowheads highlight characteristic features in Matrigel (red) and collagen (yellow). Scale bar: 50 μm.

We observed striking matrix-dependent differences in protein expression and localization by confocal imaging (Figure 7.2B). F-actin was abundant and formed continuous trans-cellular cables around the periphery of invasive structures in collagen

matrix, but only weak cortical staining in acinar organoids formed in Matrigel. Laminin was deposited in a continuous basement membrane surrounding organoids in Matrigel, but not collagen. The intermediate filament vimentin showed considerable cell-to-cell variability in both Matrigel and collagen, but uniquely organized into filamentous networks in invasive organoids formed in collagen. Finally, whereas acinar organoids in Matrigel showed no fibronectin expression by immunofluorescence, invasive organoids in collagen matrix showed extensive extracellular deposition of fibrillar fibronectin. Together, these data indicate that the 3D collagen microenvironment promotes mesenchymal gene and protein expression.

3D collagen-induced MT1-MMP expression and activity is required for epithelial invasion through restrictive ECM

Since membrane type 1 matrix metalloproteinase (MT1-MMP) is the primary enzyme used by stromal and cancer cells to degrade and migrate through fibrillar collagen [158, 270] and the invasive epithelial phenotype involved cells moving outward through the surrounding collagen matrix, we next investigated whether MT1-MMP contributes to epithelial invasion in this system. We found that cells in 3D collagen matrix uniquely upregulated MT1-MMP expression, whereas cells in 3D Matrigel significantly downregulated MT1-MMP and cells seeded on 2D collagen-coated glass showed no change in MT1-MMP expression after 24 h (Figure 7.3A). Elevated MT1-MMP expression in 3D collagen matrix was maintained throughout the 96-h experiment (Figure 7.3B). To determine if MT1-MMP was responsible for invasive behavior, we knocked down MT1-MMP prior to cell seeding in collagen using siRNA.

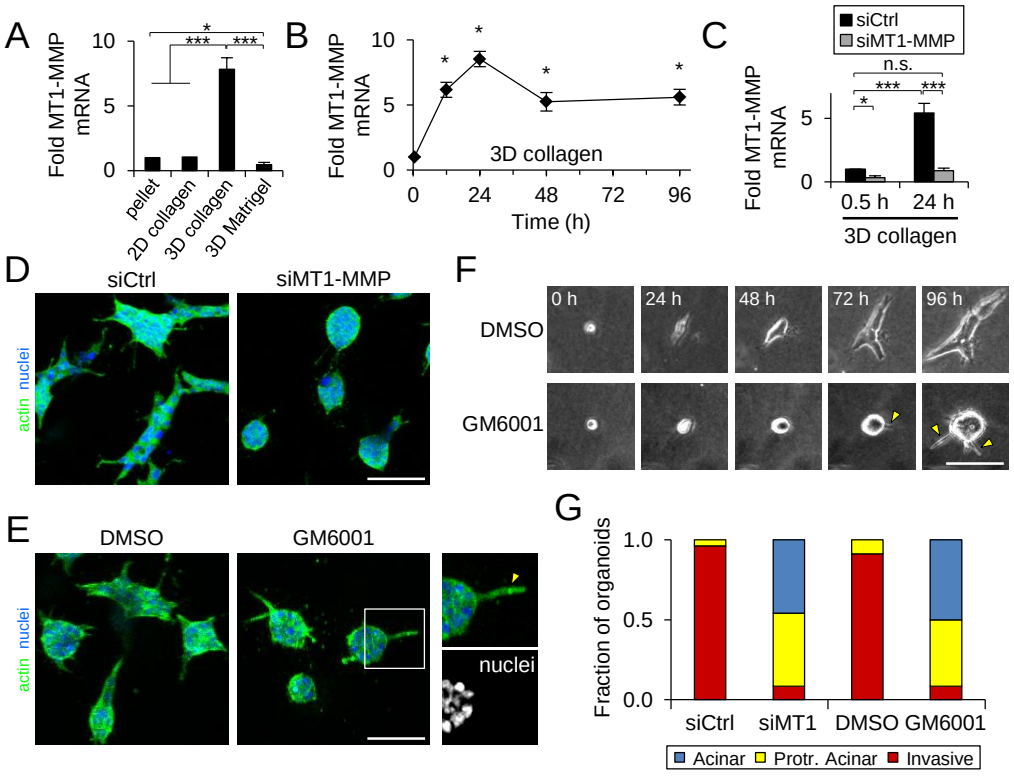

Figure 7.3. Regulation of invasive epithelial phenotype by matrix-induced MT1-MMP. (A) MT1-MMP gene expression by MCF-10A epithelial cells following 24 h of culture on 2D collagen-coated glass (0.1 mg/ml), in 3D collagen matrix (1.5 mg/mL), or in 3D Matrigel matrix (4.0 mg/mL). Data are normalized to cell pellet lysed prior to seeding. *, P = 0.04; ***, P < 0.0001. **(B)** MT1-MMP expression during 96 h of culture in 3D collagen matrix. *, P < 0.001 compared to 0.5 h. **(C)** MT1-MMP expression in cells treated with 1 nM MT1-MMP targeting or non-targeting control siRNA and seeded in 3D collagen for 0.5 h and 24 h. *, P = 0.02; ***, P = 0.002; n.s., not significant. Data in A-C are represented as mean ± SEM from at least n = 3 independent experiments. **(D)** siRNA-treated epithelial organoids after 4 days of 3D collagen culture. Scale bar: 100 µm. **(E)** Epithelial organoids after 4 days of 3D collagen culture treated with GM6001 (0.1 µM) or equivalent DMSO control. Inset and yellow arrowhead indicate nucleus-free protrusion characteristic of protrusive acinar organoids with MT1-MMP-targeting siRNA and GM6001 treatment. Scale bar: 100 µm. **(F)** Time-lapse image series of epithelial morphogenesis in 3D collagen matrix with GM6001 or DMSO control treatment. Yellow arrowheads indicate nucleus-free protrusions into the surrounding matrix with GM6001 treatment. Scale bar: 50 µm. **(G)** Quantification of organoid morphology from n = 2-3 independent experiments (> 50 organoids per treatment).

Treatment with 1 nM targeting siRNA significantly reduced MT1-MMP expression to ~30% of non-targeting siRNA levels in cell pellets prior to seeding and prevented collagen-induced upregulation of MT1-MMP at 24 h (Figure 7.3C). Notably, MT1-MMP knockdown suppressed epithelial invasion, reverting organoids to more acinar and protrusive acinar morphologies (Figure 7.3D). Since previous work has indicated MT1-MMP has critical non-proteolytic functions during epithelial branching morphogenesis [338], we tested whether the invasive epithelial phenotype we observed here was dependent on MMP activity by treating cells with the broad spectrum MMP inhibitor GM6001. Even low level GM6001 (0.1 μM) treatment suppressed invasive outgrowth of epithelial cells, indicating the proteolytic activity is required for epithelial invasion in our system (Figure 7.3E). Both MT1-MMP knockdown and GM6001 treatment induced long, actin-rich anuclear cell extensions at the periphery of some organoids, consistent with the protrusive acinar phenotype (Figure 7.3E; inset and arrowhead). Time-lapse imaging of organoid formation under DMSO vehicle treatment showed outward protrusion of cell bodies as epithelial cells proliferated, resulting in the characteristic invasive multicellular structure by day 4 (Figure 7.3F). GM6001 treatment prevented this outward cell movement during proliferation and limited protrusion into the surround matrix to long, cytoplasmic extensions (Figure 7.3F; arrowheads). Therefore, whereas cells treated with control siRNA and DMSO vehicle formed primarily invasive organoids, both MT1-MMP knockdown and GM6001 treatment resulted in formation of acinar and protrusive acinar epithelial organoids (Figure 7.3G).

The requirement for MMP activity during mesenchymal cell migration through three-dimensional matrix is dependent on matrix pore size, with larger pores permitting MMP-independent movement [47]. Therefore, we tested whether the requirement for MMP activity in epithelial invasion was similarly sensitive to matrix structure.

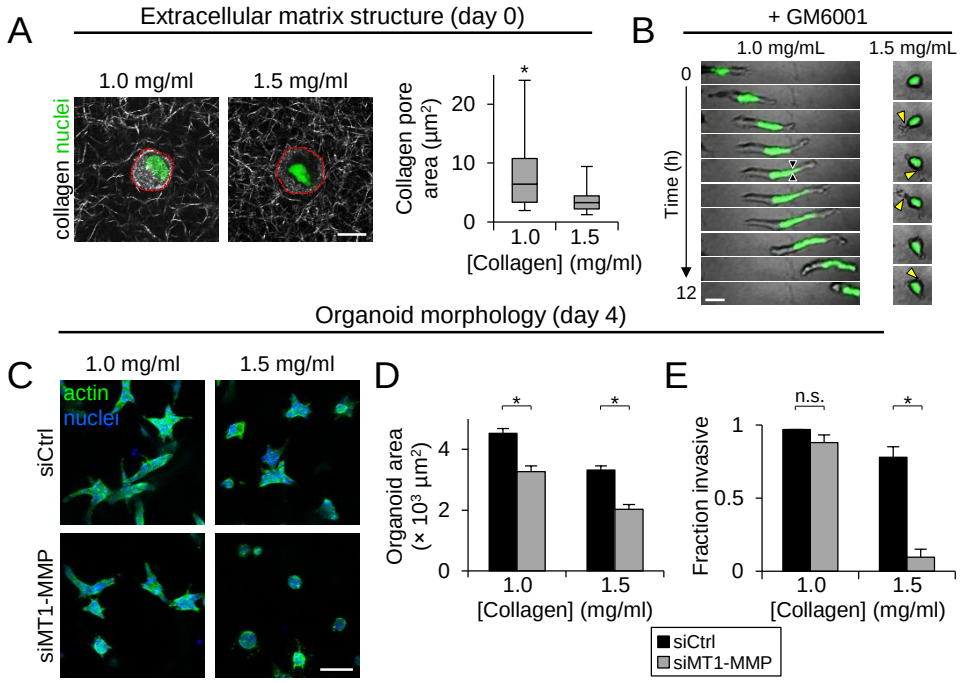

Figure 7.4. Matrix pore size-dependent epithelial cell migration and invasion. (A) Confocal fluorescence and reflectance images of MCF-10A/H2B-GFP cells in 1.0 mg/ml and 1.5 mg/ml collagen matrices demonstrating representative cell nuclei (green) and collagen structure (grey). Scale bar: 10 µm. Quantification of collagen matrix pore cross-sectional area from n = 2 independent experiments. *, $P < 0.0001$. **(B)** Black arrowheads indicate nucleus constriction site during MMP-independent migration in low density (large pore) matrix. Yellow arrowheads indicate transient cytoplasmic protrusions characteristic of MMP-inhibited cells in high density (small pore) matrix. Scale bar: 25 µm. **(C)** siRNA-treated (1 nM) epithelial organoids after 4 days of 3D culture in 1.0 mg/ml and 1.5 mg/ml collagen matrices. Scale bar: 100 µm. **(D)** Epithelial organoid area and **(E)** fraction of invasive epithelial organoids. Data in D-E are represented as mean ± SEM from n = 2 independent experiments (> 100 organoids per condition). *, $P < 0.01$; n.s., not significant.

We seeded cells in 1.0 mg/ml in addition to 1.5 mg/ml collagen matrix and used confocal reflectance microscopy to image the collagen ECM surrounding cells

following matrix polymerization. As expected, the distributions of pore sizes were broad, and reducing collagen density significantly increased pore size (Figure 7.4A).Pore cross-sectional area ranged from ~1-10 μm^2 in 1.5 mg/ml collagen matrix and ~1-25 μm^2 in 1.0 mg/ml collagen matrix. Time-lapse imaging showed that GM6001 treatment prevented cell migration in higher density matrix, where cells were unable to translocate their nucleus and continually extended thin cytoplasmic protrusions into the surrounding matrix (Figure 7.4B; yellow arrowheads). Conversely, GM6001-treated cells in low density matrix retained their ability to migrate and notably showed transient pauses in migration during which the nucleus arrested and deformed (Figure 7.4B; black arrowheads), consistent with nuclear deformation through matrix pores during protease-independent 3D migration [47, 164]. The requirement for MT1-MMP during epithelial organoid morphogenesis was also dependent on collagen matrix structure (Figure 7.4C). Whereas MT1-MMP knockdown induced a small but significant decrease in organoid area in both matrix densities (Figure 7.4D), it caused a dramatic decrease in the fraction of organoids showing an invasive phenotype only in higher density 1.5 mg/ml matrix (Figure 7.4E). Together, these results indicate that 3D collagen induces upregulation of MT1-MMP, the activity of which is required for epithelial invasion through restrictive 3D matrix, but dispensable for epithelial cell movement through large pores in lower density matrix.

Invasive epithelial phenotype is driven by protrusive signaling

We next sought to identify molecular regulators of the MT1-MMP-dependent collagen-induced invasive epithelial phenotype. Since type I collagen can influence epithelial cell behavior through adhesion signaling and the Rho family of GTPases [104, 122, 128, 339], we examined mammary epithelial morphogenesis under pharmacological inhibition of these major signaling pathways. Inhibition of Src, PI3K, Rac1, and ROCK activity elicited diverse changes in epithelial morphogenesis that altered organoid morphology (Figure 7.5A).

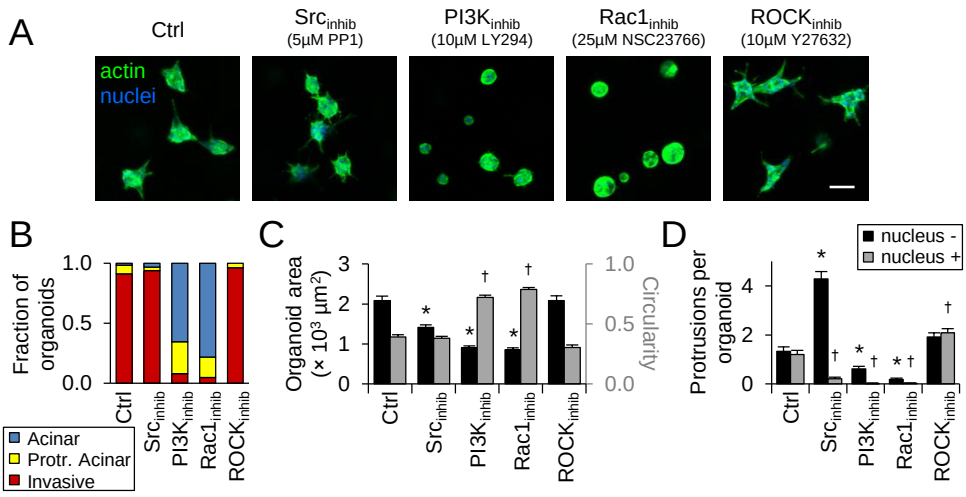

Figure 7.5. Molecular regulation of the invasive epithelial phenotype. (A) MCF-10A epithelial organoids after 4 days of culture in 1.5 mg/ml collagen treated as indicated. **(B)** Quantification of organoid morphology. **(C)** Quantification of organoid area (black bars) and circularity (grey bars). *, $P < 0.0001$ as compared to Ctrl area; †, $P < 0.0001$ as compared to Ctrl circularity. **(D)** Quantification of 'nucleus -' (black bars) and 'nucleus +' (grey bars) protrusions exhibited by epithelial organoids. *, $P < 0.0001$ as compared to Ctrl 'nucleus -'; †, $P < 0.0001$ as compared to Ctrl 'nucleus+'. Data in B-D was from n = 2 independent experiments (> 50 organoids per treatment).

Whereas control, Src-inhibited, and ROCK-inhibited cells primarily formed invasive structures, PI3K and Rac1 inhibition suppressed epithelial invasion, resulting in acinar and protrusive acinar organoids (Figure 7.5B). Inhibition of Src, PI3K, and Rac1

activity significantly reduced organoid size, and PI3K and Rac1 inhibition increased organoid circularity (Figure 7.5C), indicative of the more rounded acinar structures formed with these treatments. Notably, Src inhibition significantly reduced nucleus-containing protrusion and increased nucleus-free protrusion (Figure 7.5D), mimicking the MMP-inhibited protrusive acinar phenotype. Thus, while the enhanced formation of anuclear protrusions with Src inhibition decreased circularity to cause an apparent increase in organoid invasiveness (Figure 7.5B), Src inhibition prevented cell migration from organoid structures. Since Src, PI3K, and Rac1 inhibition effectively eliminated nucleus-containing protrusions, these pathways are required for invasive collagen-induced cellular outgrowth from epithelial organoids (Figure 7.5D).

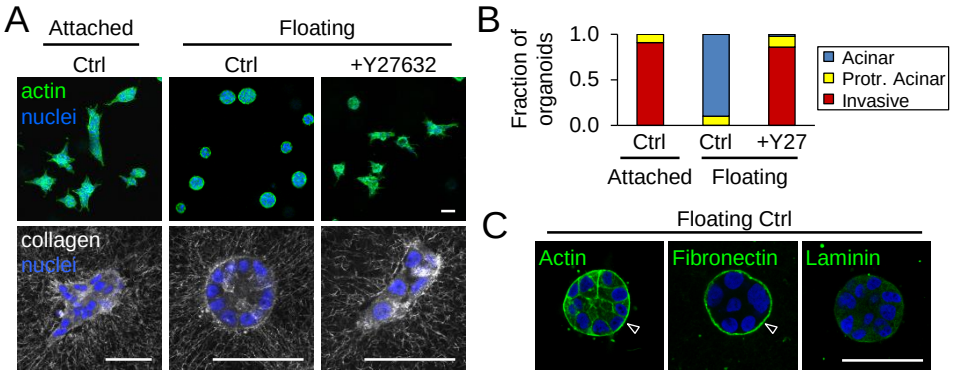

Figure 7.6. Role of cell and matrix mechanics in regulating invasive epithelial phenotype. (A) Top panels: Epithelial organoids formed in attached and floating collagen matrices. Bottom panels: Confocal reflectance images of collagen matrix (grey) surrounding organoids. **(B)** Quantification of organoid morphology from n = 3 independent experiments (> 60 organoids per condition). **(C)** Representative images of actin, fibronectin, and laminin localization in organoids formed in floating collagen matrices. Arrowheads indicate strong localization of actin and fibronectin at the organoid periphery. Scale bars: 50µm.

Interestingly, the only measured effect of ROCK inhibition on the invasive epithelial phenotype was an increase in the number of nucleus-containing protrusions per

organoid, suggesting that ROCK activity is not required for invasive outgrowth and may actually act as an invasion restrictor in this system. Since ROCK-mediated cell contractility plays critical functions in both 3D cell migration and detection of 3D matrix properties [41, 122], this finding led us to question the role of ECM mechanics in regulating the collagen-induced invasive epithelial phenotype. We found that epithelial invasion was prevented by floating the collagen matrix following polymerization to release intra-matrix tension (Figure 7.6A; top panels). However, ROCK inhibition rescued the invasive phenotype in floating matrix (Figure 7.6B), further supporting the hypothesis that ROCK activity suppresses epithelial invasion in this model. Notably, the phenotypic conversion to acinar organoid morphology in floating collagen matrix was not associated with a complete reversion to Matrigel-like epithelial acini. Similar to invasive organoids in attached collagen matrix (Figure 7.2B), rounded organoids in floating collagen showed strong peripheral staining of actin and deposited fibronectin, but not laminin (Figure 7.6C; arrowheads). Interestingly, invasive and acinar organoids in attached and floating matrix, respectively, showed radial alignment of collagen at the organoid periphery (Figure 7.6A; bottom panels). ROCK inhibition prevented this fiber realignment, indicating that local matrix remodeling is ROCK-dependent, but is neither required nor sufficient for invasion. Taken together, these results provide evidence that the collagen-induced invasive epithelial phenotype requires intra-matrix tension and is driven by protrusive signaling rather than cell contractility and matrix remodeling.

Stiffening of collagen ECM promotes epithelial dispersion

The requirement for attached collagen matrix indicated that the invasive epithelial phenotype is mechanosensitive. To investigate this further and simulate the effects of increasingly stiff stromal extracellular matrix associated with tumor progression [106], we examined the behavior of MCF-10A cells cultured in collagen matrix of increasing stiffness. As previously reported, collagen matrix was stiffened via non-enzymatic glycation by incubating acidified collagen solution with varying amounts of ribose prior to cell embedding, resulting in compressive moduli of 175 Pa (0 mM), 340 Pa (50 mM), and 515 Pa (100 mM) [54]. By examining epithelial collagen cultures after 4 days, we found that 3D epithelial phenotype was dependent on the mechanical properties of the ECM (Figure 7.7A).

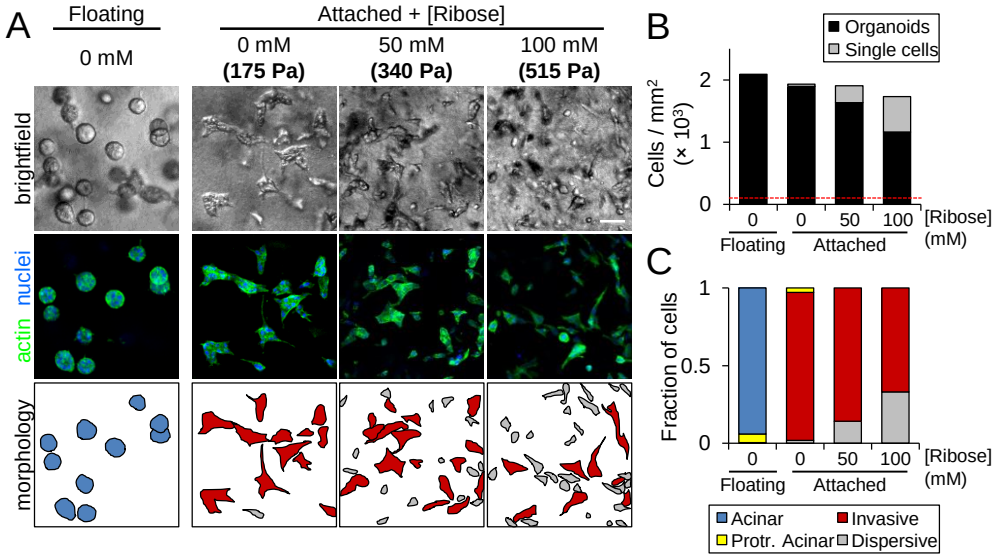

Figure 7.7. Mechanosensitivity of the invasive epithelial phenotype. (A) MCF-10A epithelial organoids after 4 days of culture in floating collagen matrix and attached collagen matrix of increasing stiffness. Brightfield, fluorescence, and cartoon representation of cell/organoid morphologies. Scale bar: 100 μm. **(B)** Quantification of cell density and cell organization as single cells (hashed bars) or into multicellular organoids (filled bars) from n = 2 independent experiments (> 700 cells per condition). **(C)** Quantification of single cell/organoid morphologies for cells in B.

Whereas all cells were part of multicellular organoids in floating collagen matrices, stiffening of attached collagen matrix increased the number of dispersed single epithelial cells (Figure 7.7B). Notably, while increasing matrix stiffness caused a reduction in overall cell density, presumably due to decreased proliferation and/or increased cell death in stiffer matrix, this effect was not large enough to account for the abundance of single cells since seeding density was equivalent to ~100 cells/mm^2 (Figure 7.7B; dashed red line). Thus, both epithelial cells' ability to form multicellular structures and the nature of multicellular organoid structures were dependent on 3D collagen matrix mechanics (Figure 7.7C and 7.7A; cartoon schematic). Together, these data suggest that epithelial cell exposure to increasingly stiff collagen ECM converts the cohesive invasive phenotype to a dispersive invasive phenotype.

7.5 Discussion

The infiltration of cells from the epithelial compartment into the stromal extracellular matrix is a critical event in tumor progression that serves as an important clinical indicator and determinant of management strategy [1, 22]. Motivated by recent findings that malignant and stromal cells can act as path-making leader cells to induce stromal invasion of otherwise invasion-incompetent cells [144, 208, 332], the focus of the current study was to examine the effect of exposure to stromal type I collagen on 3D mammary epithelial cell behavior to determine if access to the stromal compartment during invasion is sufficient to induce an aberrant epithelial phenotype in the absence of cell transformation. We demonstrate that culture in 3D collagen matrix induces expression of mesenchymal genes including fibronectin and vimentin, as well

as MT1-MMP, which is required for protrusive outgrowth of epithelial cells through matrix pores in the surrounding collagen ECM. Protrusive signaling and collagen matrix mechanics serve as critical determinants of the collagen-induced invasive epithelial phenotype. These results suggest that escape from the protective basement membrane-enveloped epithelial compartment and transit into the collagen-rich stromal microenvironment could induce an invasive, mesenchymal-type phenotype in epithelial cells.

The epithelial microenvironment is widely appreciated as a fundamental regulator of mammary cell phenotype during development, functional differentiation, the deregulation of nontransformed epithelium, and invasive cell migration [81, 236, 340, 341]. We show here that inappropriate exposure of nontransformed mammary epithelial cells to type I collagen ECM induces expression of the mesenchymal genes vimentin, fibronectin, Snail, and MT1-MMP, and downregulates E-cadherin relative to culture in 3D Matrigel. Although the existence of a complete epithelial-mesenchymal transition (EMT) in cancer progression is controversial [63], there is substantial evidence that the cellular microenvironment can promote the acquisition of mesenchymal gene expression and phenotypes in epithelial cells through growth factor signaling as well as ECM mechanics and composition [65, 249, 342–344]. The ECM-mediated mesenchymal shift and enhanced invasiveness we observe here are consistent with previous work showing that both fibronectin and type I collagen induce mesenchymal gene expression in epithelial cells [344–346], which increases mammary epithelial cell cytoskeletal dynamics and migration [347]. Although ECM

properties could modulate growth factor signaling to elicit these changes [81, 346, 348], there is also evidence that type I collagen promotes mesenchymal traits directly via β1-integrin [249] and PI3K-Rac1-JNK signaling [339]. These findings are consistent with previous work indicating that β1-integrin activates PI3K to enhance Rac1 activity [104] as well as our result here that the characteristic induction of protrusive behavior by 3D collagen matrix is PI3K- and Rac1-dependent. Interestingly, both type I collagen and aberrant PI3K-Rac1 activity disrupt mammary epithelial polarity [104, 349]. Since Rac1 activity plays a crucial role in epithelial cell-cell adhesion, basement membrane deposition, and protrusion [350, 351], further investigation of type I collagen-dependent Rac1 signaling in driving epithelial phenotype is warranted.

Our results show distinct Matrigel- and type I collagen-mediated gene expression in mammary epithelial cells. Previous work in which matrix-dependent migration phenotypes were observed in Matrigel and type I collagen reported no EMT-like molecular response to collagen [58]. However, the authors acknowledge that since RNA was extracted from whole cultures that included large numbers of cells within the interior of epithelial organoids that initially contained 200-1,000 cells, molecular changes in the cells directly contacting ECM may not have been detectable [58]. In our model, all organoids start as single cells contacting the ECM, allowing us to detect differential matrix-dependent gene expression. The collagen-induced mesenchymal shift we observe here is important because it directly illustrates an ECM-mediated destabilization of the mammary epithelial phenotype and suggests that the acquisition

of mesenchymal gene expression by exposure to type I collagen could enable epithelial cells to then invade autonomously (if they were led into the stroma in the first place) or exacerbate existing basement membrane defects (if focal loss of basement membrane exposed cells to stromal ECM). In support of this notion, transient and localized loss of basement membrane at the invasive front is correlated with increased metastasis and poor patient survival [23], indicating there need not be a widespread dissolution of basement membrane for invasion. Based on our results that collagen I upregulates expression and deposition of fibronectin, which promotes its own expression in mammary epithelium [345], and MT1-MMP, which functions broadly in the proteolytic processing of ECM, cell surface, and soluble substrates [352], it is therefore tempting to speculate that a collagen-induced mesenchymal shift could initiate feed-forward mechanisms to drive tumor invasion. Thus, future work using our model will define the molecular mechanisms through which basement membrane and stromal ECM drive epithelial and mesenchymal phenotypes, respectively.

MT1-MMP is a membrane-tethered proteinase whose substrates include ECM components, cell surface receptors, and other MMPs [352]. Notably, MT1-MMP has been shown to serve both pericellular collagenolytic and other roles during epithelial branching [338, 353] as well as collagen-invasive migration of epithelial cells [354]. Critically, MT1-MMP was recently identified as a major regulator of the transition from *in situ* to invasive carcinoma [355], is upregulated at the invasive front of tumor cells [158], and is required for blood vessel invasion and metastasis of breast cancer

cells [356]. Here, we show that MT1-MMP expression is induced by 3D collagen and suppressed by 3D Matrigel in nontransformed mammary epithelial cells, and demonstrate that MT1-MMP activity is required for outward cell body translation and the formation of nucleus-containing protrusions in stroma-like ECM. Type I collagen-dependent MT1-MMP upregulation has been observed in endothelial [357], mesothelioma [358], and carcinoma cells [359] and is suspected to occur via β1-integrin-dependent Src signaling that upregulates the transcription factor Egr-1 to promote MT1-MMP expression [359]. Since MT1-MMP expression has also been shown to be controlled by MEK/ERK and PI3K/Akt signaling in different cell types and under varying stimuli [360, 361], the mechanisms by which type I collagen promotes MT1-MMP upregulation in mammary epithelial cells remain to be determined.

While our finding that MT1-MMP is only required for invasion through small ECM pores is consistent with a recent study by Wolf et al. [47], these results contrast with work by Mori et al. indicating that MT1-MMP knockdown prevents epithelial branching morphogenesis in both dense (3.0 mg/ml) and sparse (1.0 mg/ml) collagen matrix [338]. One possible explanation for this apparent discrepancy is that our MT1-MMP knockdown may not be as complete as that achieved by Mori et al. Indeed, we found that more extensive MT1-MMP knockdown (5-25 nM siRNA) prevents 3D, but not 2D, cell proliferation and results in considerable 3D cell death by day 4. Notably, in our culture model, organoid formation is proliferation-dependent, so this effect was unacceptable. Conversely, in the model employed by Mori et al., multicellular

epithelial aggregates are formed outside matrix and then embedded in collagen, and it is unclear the extent to which the outgrowth/branching phenotype depends on proliferation. Therefore, our results do not contest those of Mori et al., but rather suggest that our relatively modest knockdown may leave sufficient MT1-MMP remaining to accomplish its non-proteolytic functions including integrin signaling that Mori et al. showed to be required for invasion and branching in sparse collagen matrix [338]. In support of this hypothesis, we found a similar trend with inhibition of MMP activity whereby low level GM6001 treatment (0.1 μM) allows proliferation and protrusive acinar organoid formation, and higher treatment levels (1-20 μM) causes cell death in 3D. Together, these findings are aligned with previous work showing that MT1-MMP activity is required for 3D cell growth [197], and suggest that the catalytic activity of MT1-MMP is required for proliferation and invasive outgrowth of epithelial cells in restrictive 3D collagen matrix within our culture model.

Interestingly, we show here that a small amount of Matrigel in collagen matrix promotes anuclear protrusions while suppressing nucleus-containing protrusions. This phenotype closely resembles the MMP- and Src-inhibited phenotypes, suggesting that cells across these treatments may share a similar deficiency in matrix remodeling behaviors that enable outward cell body movement. Indeed, we found that culture in 3D Matrigel downregulates MT1-MMP, which is aligned with previous work showing MT1-MMP inhibition by certain α-chains of type IV collagen [362, 363]. Additionally, it was previously shown that Src both mediates collagen-induced MT1-MMP expression and directly phosphorylates MT1-MMP to enable its localization

during cell migration [359, 364]. Notably, membrane localization is one of several critical post-translational modifications that regulate MT1-MMP activity, and the ECM can play a role in both MT1-MMP localization and activity [25, 365, 366]. Thus, while our findings support MT1-MMP as a rate-limiting enabler for epithelial cell movement through 3D collagen matrix, future work should explore the transcriptional, translational, and post-translational mechanisms by which specific mammary epithelial extracellular matrices regulate MT1-MMP.

Mammary epithelial cell phenotype is significantly dependent the mechanical properties of the ECM microenvironment [81, 105, 106, 367]. We show here that 3D collagen matrix mechanics play a critical role in determining whether epithelial cells acquire an invasive epithelial phenotype as well as the nature of that phenotype. We first demonstrate by floating collagen matrices that intra-matrix tension is a requirement for the invasive epithelial phenotype, which unto itself is not surprising as cell-matrix mechanocoupling is a central determinant of epithelial phenotype [81]. Interestingly, inhibition of cell contractility via ROCK inhibition overcomes this suppression and promotes protrusion to rescue the invasive epithelial phenotype. This finding suggests that the potential for invasion is maintained in floating matrix, but is suppressed by ROCK activity when matrix tension is released. Indeed, we found that MCF-10A cells deposit fibronectin and not laminin in floating collagen matrix, which is consistent with ECM deposition in attached collagen matrix and suggests that collagen ECM provides signaling to drive mesenchymal gene expression independently of matrix anchorage. Notably, Paszek et al. demonstrated that soft ECM

promotes mammary epithelial cell-cell cohesion as indicated by enhanced stability of adherens junctions in cells on soft ECM as compared to cells on stiff ECM [81]. Of particular relevance to our results, it was recently reported that relaxation of myosin-II contractility weakens cell-cell cohesion [367] and enhances Rac1 activity in mammary epithelial cells [368]. Together with our findings here, these results suggest that epithelial cells in our model may generate enhanced contractility to stabilize cell-cell adhesions in soft floating matrix, which restricts Rac1-dependent invasion. Thus, ROCK inhibition might serve to destabilize cell-cell adhesion and reactivate Rac1 to promote protrusive invasion, which is consistent with a release of cortical tension leading to protrusive activity [255].

Interestingly, although we show here that Rac1 is required for the formation of protrusive structures in 3D type I collagen, it has also been shown that Rac1 activity downstream of β1-integrin adhesion regulates mammary epithelium polarity [104] and differentiation [369] in basement membrane culture. These seemingly opposing roles for Rac1 in mediating epithelial phenotype suggest that ECM composition might modulate signaling upstream and/or downstream of Rac1 to promote distinct matrix-dependent cell behaviors. Notably, Chaudhuri et al. demonstrated that constitutive activation of Rac1 in soft basement membrane ECM promotes a protrusive malignant phenotype while suppression of Rac1 activity prevents invasive behavior in stiff basement membrane ECM [337]. Together, these results indicate that matrix mechanics and composition provide critical signaling inputs that ultimately define the effect of Rac1 signaling on mammary epithelial cell phenotype. Considering recent

findings in mammary epithelial cells that type I collagen enhances Rho activity as compared to Matrigel, and matrix-dependent Rac1 activity can be tuned through regulation of Rho activity [368], the ECM context-dependent expression and activation of Rho GTPases is of particular interest.

We found that increasing 3D collagen matrix stiffness via non-enzymatic glycation promotes an increasingly dispersive invasive phenotype in mammary epithelial cells. This finding is consistent with previous work showing that increased 3D collagen matrix stiffness enhances cell outgrowth [54]. While we did not examine the mechanisms by which enhanced 3D matrix stiffness downregulates cell-cell cohesion to promote epithelial dispersion here, it is likely that Rho GTPases play a significant role in this behavior [81, 106, 370], and these mechanisms are currently under investigation. Indeed, it was recently shown that enhanced Rac1 activity is associated with increased 3D epithelial cell scattering following mitosis [351]. Of note, our finding that increasing 3D ECM stiffness alone is sufficient to induce significant phenotypic changes in epithelial cells is in contrast to work by Levental et al. in which both matrix stiffening and oncogene induction were required to drive invasive behavior [106]. This dissimilarity is likely due to significant differences in experimental models. Since our model is intended to model the effects of epithelial cell exposure to type I collagen-rich stromal ECM, our epithelial morphogenesis model contains only 3D collagen matrix. Conversely, Levental et al. cultured cells in mixed basement membrane/collagen matrices to model matrix stiffness-induced disruption of homeostatic epithelial structures [106]. Furthermore, we used relatively

high ribose concentrations (up to 100 μM) to achieve a three-fold increase in collagen stiffness via "pre-glycation", that is, treatment of the collagen prior to incorporation with cells and matrix polymerization [54]. Since Levental et al. crosslinked ECM surrounding established epithelial colonies using long-term (28 days) ribose treatment, it is likely that cell viability was adversely affected by treatment above 15 μM ribose, and as such, matrix stiffening was relatively limited. Nonetheless, these results suggest that additional "hits" (e.g., oncogene induction) may be required to fully drive invasive epithelial behavior in response to smaller increases in ECM stiffness and/or in the presence of an established basement membrane. These findings further indicate that ECM composition and mechanics co-regulate mammary epithelial phenotype, and imply that future studies should continue to explore this relationship more deeply.

Finally, the distinct matrix-dependent gene expression patterns in Matrigel and collagen as well as the intermediate phenotypes observed in mixed Matrigel/collagen culture suggest that basement membrane and type I collagen may stimulate opposing cell signaling and phenotypic responses in epithelial cells. Indeed, specific integrin-ligand combinations can lead to distinct signaling and phenotypic outcomes [371], and ECM composition can regulate integrin expression and signaling in mammary epithelial cells [249, 372]. Especially since complete basement membrane dissolution is not necessary for invasion and cells can re-express basement membrane at secondary sites during metastasis [23], it is conceivable that epithelial/carcinoma cells perceive mixed ECM signals during both early epithelial tissue destabilization and later metastatic seeding. However, the extent to which basement membrane protects

and type I collagen deregulates normal epithelial cell phenotype remains unclear. Thus, future work using rationally designed composite ECM models to identify the relative contributions of basement membrane and collagen I in regulating epithelial signaling and phenotype would provide further insight to our findings here as well as to both developmental and tumorigenic epithelial cell processes in general.

CHAPTER 8

CONCLUSIONS AND FUTURE DIRECTIONS

8.1 Conclusions

In this dissertation, we set out to define cellular and extracellular determinants of the invasive cancer cell phenotype. Drawing inspiration from various elements of the tumor microenvironment including diverse structural ECM features in the tumor stroma and cellular heterogeneity, we examined 3D cell migration within rationally designed *in vitro* models and developed novel strategies to study cancer heterogeneity. Together, our results identified pro-invasive extracellular determinants, described microenvironment-contextualized mechanisms of 3D cell migration, and demonstrated sources and outcomes of invasive heterogeneity.

Given the diversity of 3D ECM pore and fiber structure in the mammary tumor stroma [42], we first investigated the role of 3D matrix microarchitecture in determining 3D cancer cell migration in Chapter 2. We found that collagen ECM microarchitecture directly regulates cell migration independently of bulk scale gel density (concentration), with cell spreading and motility promoted in matrices with larger pores and fibers and suppressed in matrices with smaller pores and fibers. Secondary to this finding, we showed that ECM microarchitecture is gel thickness- and media

type-dependent, emphasizing the importance of monitoring gel structure in 3D assays of cell behavior.

Interestingly, we found in Chapter 2 that despite showing limited cell body translation, cells within restrictive, small-pore 3D matrices continue to extend and retract pseudopodial "matrix probing" protrusions. We therefore hypothesized that ECM structure regulates cells' transition from matrix probing to motility in 3D. To test this hypothesis directly in Chapter 3, we developed and implemented a method to study cellular and extracellular mechanisms of 3D migration using early cell spreading as a reductionist model for the complex and heterogeneous process of migration. While similar strategies have been effective in analysis of 2D cell spreading and migration [215, 216], this work was the first demonstration of a simplified *in vitro* model for cell migration in complex 3D microenvironments. Using this approach, we monitored cell and protrusion morphodynamics during early cell spreading and found that cells "turn off" exploratory matrix probing protrusions as they choose a direction, elongate, and begin to migrate. This novel finding was consistent with our observation that the most efficiently migrating cells generate fewer protrusions, and led us to question the mechanisms by which a cell's local ECM drives this transition.

We applied our 3D cell spreading model to cells within anisotropic, aligned collagen matrix, which was dually motivated by two critical observations. First, consistent with work by the Keely group [27], we found substantial matrix alignment at the tumor-stroma interface *in vivo*, as well as at the spheroid-ECM and even single cell

protrusion-ECM boundaries *in vitro*. Second, we simultaneously visualized protrusion dynamics and pericellular matrix structure and found that local ECM structure guides and stabilizes cell protrusions during early spreading. Thus, aligned ECM allowed us to investigate matrix-directed cell spreading and migration initiation in cells exposed to defined ECM structure. We showed that local ECM alignment induces spatial anisotropy of cell morphodynamics, promoting on-axis and suppressing off-axis behaviors to accelerate and direct spreading and migration. Finally, we demonstrated that matrix-directed polarization of adhesion signaling and active cell protrusion response drive ECM alignment-mediated guidance. This work allowed us to define the elements of 3D spreading and migration that are sensitive to ECM structure and was the first mechanistic study of 3D ECM alignment response in single cell migration.

Track-like ECM structures in the tumor stroma have been observed as conduits for migrating cancer cells [37, 48, 49]. Our group previously showed that an *in vitro* model of such structures – collagen microtracks – removed the need for pericellular proteolysis during 3D cancer cell migration [60], and we hypothesized here that microtracks may also affect the requirement for other migration mechanisms. We directly compared cancer cell migration within isotropic 3D collagen matrix and collagen microtracks, finding that cells in these two environments employ fundamentally different mechanisms to migrate. Since inhibition of cell-matrix adhesion and cell contractility prevent cell movement in 3D matrix but not in physiological microtracks, we concluded that matrix-free channels facilitate migration by reducing the mechanistic burden for cell-matrix mechanocoupling. Consequently,

we identified actin and microtubule cytoskeleton dynamics as critical regulators of cell motility in microtracks, which was in contrast to previous work using rigid, impermeable PDMS channels [242]. Nonetheless, since our collagen microtracks closely mimic the structure and composition of track-like ECM found *in vivo*, we are confident in the biological and clinical relevance of our findings that preformed paths of least resistance within the ECM reduce the mechanistic threshold for cancer cell migration.

While our previous work explored the mechanisms by which cancer cells exploit matrix microtracks, it did not address the formation of such track-like structures, which are suspected to arise from normal tissue assembly as well as ECM remodeling by fibroblasts and macrophages [37, 40, 250]. Interestingly, throughout the aforementioned work, we found that malignant cells actively create matrix-free microtrack structures in their wake as they migrate through 3D collagen matrix [60]. Given these findings, the widely accepted existence of intratumor heterogeneity, and the likelihood that invasive and metastatic potential vary widely across a tumor [307], we hypothesized that matrix remodeling by particularly invasive cells in a tumor might influence the migration of other, less invasive cells within the tumor. Therefore, in Chapter 5 we studied cell-cell interactions within a heterotypic co-culture multicellular spheroid model to elucidate consequences of intratumor heterogeneity on invasive progression. We found that "invasion-competent" malignant cells enable invasion by otherwise "invasion incompetent" cells, and showed that this induced invasion consistently occurs as follow-the-leader collective invasion. As hypothesized,

we demonstrated that invasion induction occurs due to the formation of matrix microtracks generated by contractility- and proteolysis-mediated ECM remodeling by leading malignant cells. Our results indicated for the first time that through the generation of invasion-enabling microtracks, select subpopulations of tumor cells may be able to promote invasion of otherwise non-invasive cells. These findings provided the impetus to further investigate invasive heterogeneity in Chapter 6 and study outcomes of induced invasion in Chapter 7.

Throughout the work in Chapters 2-5, we found considerable cell-to-cell variability in the 3D migration phenotype of the malignant breast cell line MDA-MB-231. Specifically, we observed that even at steady state following an initial phase of 3D spreading, only a fraction of cells are motile, and migration speeds vary widely, often spanning an order of magnitude across the population. Furthermore, in Chapter 5, we found that some, but not all, malignant cells serve as leader cells. These observations led us to question whether cells within this population possess deterministic, cell-intrinsic traits that make them particularly effective or ineffective invaders. In Chapter 6, we developed a novel phenotypic cell sorting technique that isolates the most and least collagen-invasive cells and enabled us to establish invasive (MDA^{INV}) and non-invasive (MDA^{NON}) subpopulations of MDA-MB-231 cells. MDA^{INV} and MDA^{NON} exhibit distinct differences in 3D migration phenotype, as well as morphology, adhesion signaling, cytoskeleton dynamics, and traction force generation that are conserved through generations, indicating that inherent differences in these key traits might contribute to the observed differential invasive fitness. Since MDA^{NON} remain

in a matrix-probing state in 3D, these studies indicated that in addition to being directed by local ECM structure (Chapter 3), the transition from matrix probing to motility is a cell-intrinsic attribute. Finally, these results indicated that our novel use of behavioral cell sorting to separate cells is effective in unmasking obscured phenotypes and their underlying mechanisms and may also be useful to test therapeutic effect in a cell population of interest (e.g., invasive cells).

In addition to raising questions about the determinants of effective 3D migrators and leader cells, our finding of follow-the-leader invasion in Chapter 5 led us to investigate how induced invasion affects follower cells. Since the epithelial basement membrane provides polarity and differentiation cues that are important for the maintenance of epithelial homeostasis [72], and cells of epithelial origin only cross over the basement membrane into the mammary stroma during invasive progression [9], we hypothesized in Chapter 7 that access to stroma-like type I collagen ECM would deregulate epithelial phenotype. We employed a simple *in vitro* model to study 3D matrix-mediated gene expression and the associated phenotypic response and found that collagen matrix induces mesenchymal gene expression, protrusive activity, and proteolytic remodeling resulting in a characteristically invasive phenotype. This invasive behavior is sensitive to collagen matrix mechanics since invasion is suppressed by releasing intra-matrix tension and enhanced by stiffening the collagen matrix. Our findings uniquely suggest that access to stromal ECM activates an invasive phenotype in mammary epithelial cells that could potentially enable these cells to participate in matrix remodeling and further interstitial tissue invasion.

Ultimately, the results presented in this dissertation provide novel insight into the factors that influence cancer cell invasiveness. Our findings support a definition of the "invasive phenotype" that includes both a cell's inherent intracellular programming state as well as the local 3D extracellular matrix in the vicinity of the cell, as the integration of these two key elements ultimately determines cancer cell migration behavior. Together, our results indicate that cellular and/or ECM heterogeneity can lead to dramatic diversity in invasiveness, and suggest that the most effective therapeutic targets by which to prevent invasive progression are likely the key rate-limiting subcellular processes and pro-invasive extracellular matrix features that enable cancer cell invasion.

8.2 Future Directions

In addition to defining pro-invasive extracellular determinants, microenvironment-specific mechanisms of 3D cell migration, and outcomes of cellular heterogeneity, we have also developed and/or refined several biologically inspired experimental platforms that can be used to further study these problems. These include:

- 3D collagen matrices with tunable porosity and alignment microarchitecture and physiological collagen microtracks for the study of matrix-directed 3D cell migration
- Heterotypic multicellular spheroids for the study of cell cooperation during invasion
- Phenotypic cell sorting strategy to isolate differentially invasive cell subpopulations for the study of intratumor heterogeneity and invasive fitness

- Tunable 3D collagen/Matrigel matrices for determination of matrix-driven epithelial cell gene expression and phenotype

There are several open questions remaining in three broad areas that can be addressed by expanding upon the use of the aforementioned experimental systems.

Matrix-directed 3D cell migration

1) What is the stepwise sequence of molecular events that enables matrix guidance?

More detailed analysis of the molecular mechanisms involved in alignment detection and response could provide critical information regarding the sequence of signaling events that underlie matrix guidance. Dynamic analysis of Rho GTPases, polarity proteins, and the actin and microtubule cytoskeletons [199, 220, 232] within the 3D cell spreading model presented in Chapter 3 would provide considerable mechanistic insight establishment of 3D cell polarity. Based on our finding that anisotropic adhesion signaling and active protrusion is required for the cellular response to 3D matrix structure, a proposed mechanistic role for the Rho GTPases in the matrix-guidance response is shown in Figure 8.1. The sequence of signaling underlying matrix guidance could be determined by molecularly/pharmacologically perturbing suspected pathways (e.g., adhesion signaling, Rho GTPases), and monitoring indicators such as cell-matrix adhesion and Rho GTPase effector localization that may be either upstream or downstream of the targeted pathway [223].

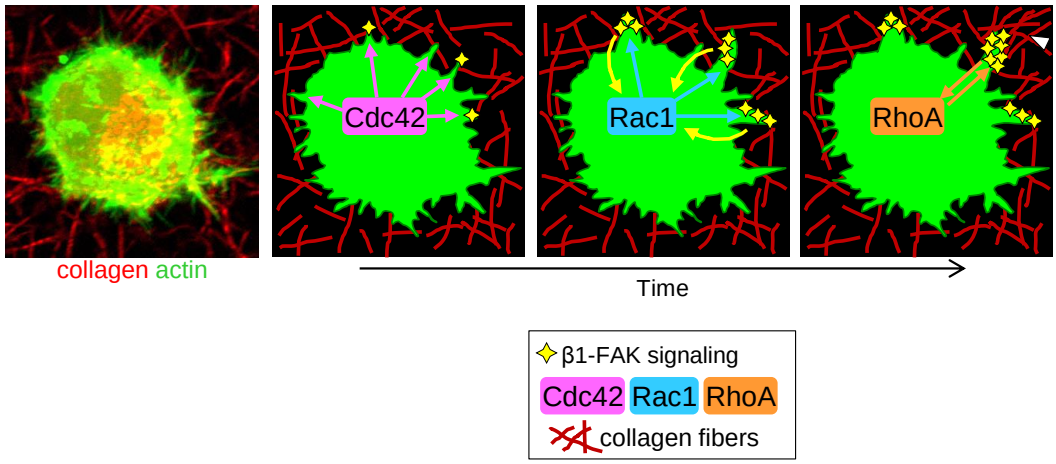

Figure 8.1. Adhesion signaling and Rho GTPases in 3D cell spreading. Proposed mechanistic function of integrin signaling and Rho-GTPases in matrix-guidance response.

2) What are the relative roles of ECM microstructure and micromechanics?

We definitively show the importance of matrix structure in regulating cell morphodynamics during early 3D cell spreading. Future work can address the sensitivity of protrusion dynamics and morphodynamics to matrix properties including ECM microarchitecture (fiber and pore size) and stiffness. These studies could begin to address the important relationship between ECM microstructure and micromechanics and determine the extent to which cells' response to ECM is due to mechanical feedback and physical guidance. Interestingly, the structural/mechanical relationship of 3D matrix has been shown to affect migration mechanisms [373], so these studies would be of broad interest to 3D cell migration.

3) Can cells predetermine their migration through anisotropic ECM remodeling?

In Chapter 3, we demonstrate that the 3D ECM structure surrounding a cell directs its spreading and migration and provide some evidence that these responses drive cell morphodynamics even in random matrix. Future work can explore this hypothesis directly by mapping the random ECM surrounding a cell prior to spreading and subsequently analyzing "on-fiber" and "off-fiber" cell behaviors as "on-axis" and "off-axis" behaviors were assessed in Chapter 3. Additionally, future studies can investigate the role of dynamic cell autologous-remodeling of this "ECM map" during spreading and migration. Preliminary results suggest that cells may be able to direct their spreading and migration by first remodeling their surrounding matrix and then responding to this matrix using a process we refer to as *autologous mechanotaxis*. We have found that cells in randomly structured 3D collagen matrix are surrounded by isotropic ECM immediately after seeding (Figure 8.2A; left), and can induce anisotropy of ECM density and orientation (Figure 8.2A; right) prior to spreading, which is directed along the previously defined axis of anisotropy (Figure 8.2B). This observation is consistent with the results we present in Chapter 3 as well as previous work showing that interstitial flow can induce upstream rheotaxis through matrix-induced polarization of adhesion signaling [223]. Therefore, integrating the results and analysis techniques in Chapter 3 with the molecular and structure/mechanics analyses described above will allow for a mechanistic understanding of *autologous mechanotaxis*, which we hypothesize is a fundamental aspect of 3D cell migration in fibrillar matrix environments.

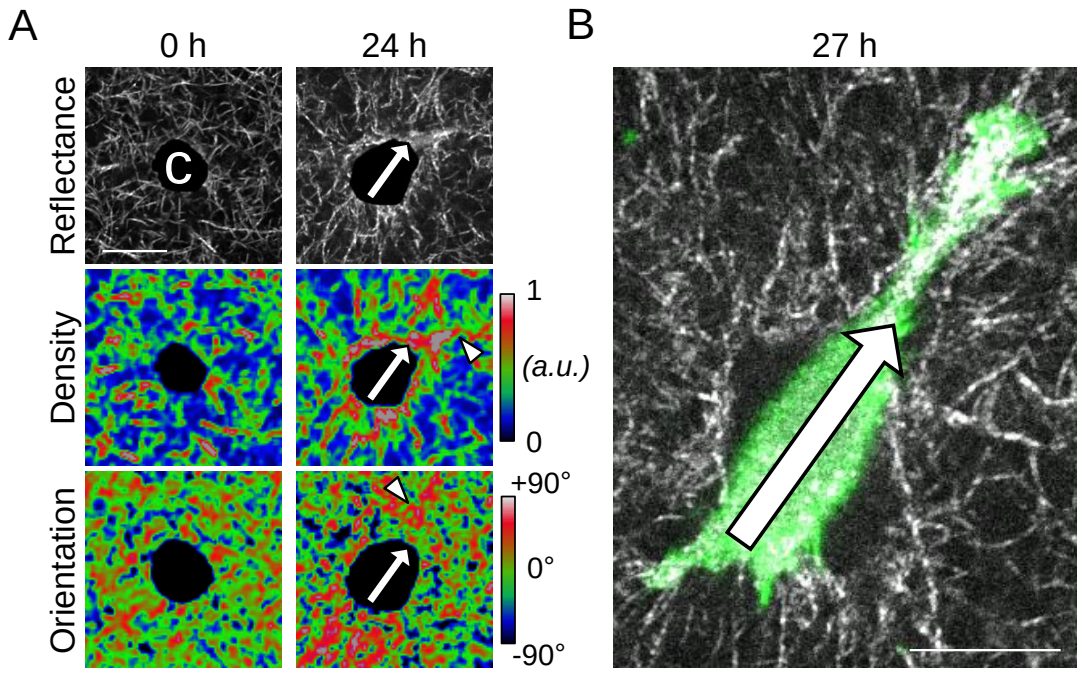

Figure 8.2. Autologous mechanotaxis. (A) Extracellular matrix structure (top) and heat maps of ECM density (middle), orientation (bottom) around a spreading MDA-MB-231 cell ('c') 0 h and 24 h after seeding in collagen. Arrows indicate direction of matrix anisotropy and arrow heads highlight regions of increased density and fiber organization at 24 h. **(B)** Spreading of cell in A at 27 h in response to matrix anisotropy. Scale bars: 20 μm.

Cancer cell heterogeneity:

1) **What are the underlying molecular differences between invasive and non-invasive cells?**

Preliminary experiments have indicated that, in addition to the differences demonstrated Chapter 6, the invasive and non-invasive subpopulations exhibit differential gene expression (Figure 8.3). Transcriptome/proteome/phosphoproteome analysis could complement our phenotypic analysis to define key molecular signatures of invaders and non-invaders. Because of their importance in cell migration,

expression and dynamics of cell-matrix adhesions, Rho GTPases, and the cytoskeleton will be of particular interest [92, 374, 375].

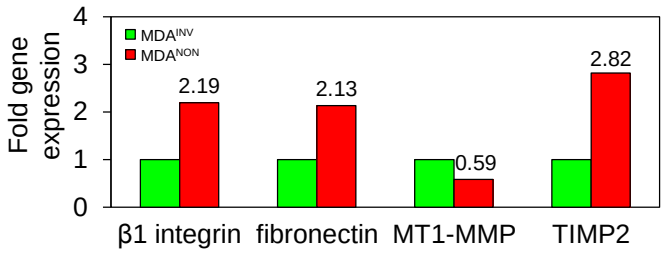

Figure 8.3. Differential gene expression in MDA^{INV} and MDA^{NON} cells.

2) What are the effects of invasion heterogeneity in vivo?

It will be important to determine how our findings regarding the sources and outcomes of heterogeneity in Chapters 5 and 6 translate to the *in vivo* setting. Principles of follow-the-leader invasion could be explored further in the *ex vivo* peritoneal basement membrane invasion model or chorioallantoic membrane invasion model, both of which provide native, physiological ECM through which cells must invade [24, 270]. Additionally, cell cooperation during invasive progression could be assessed *in vivo* by injecting luciferase-expressing invasion-incompetent cells into the murine mammary fat pad with or without invasion-competent cells and subsequently monitoring the effect of invasive cells on tumor growth, hematogenous dissemination of invasion-incompetent cells (through blood draws), and the metastatic capacity of invasion-incompetent cells (through bioluminescent imaging of whole animals or target organs).

Matrix-driven mammary epithelial phenotype:

1) How does basement membrane protect and type I collagen deregulate epithelial phenotype?

To build off of our findings that type I collagen induces mesenchymal gene expression that leads to an invasive phenotype, more thorough characterization. A more thorough characterization of the induction of mesenchymal gene expression by type I collagen will allow for the identification of critical signaling nodes that can subsequently be targeted molecularly as has been recently demonstrated for other extracellular inducers of mesenchymal induction [343–345].

A complementary strategy to investigate the relative and seemingly opposing contributions of basement membrane and type I collagen to regulating epithelial phenotype will be to measure gene expression of epithelial cells within the mixed ECM gels used in Chapter 7. We have established that classic epithelial and mesenchymal markers are differentially regulated in the two ECMs. Figure 8.4 demonstrates anticipated results, where epithelial (blue) and mesenchymal (red) genes are differentially induced by basement membrane and collagen, respectively. By examining gene expression in the gradient region, it will be possible whether the expression of a given gene is either:

A. Controlled primarily by basement membrane-derived signaling. This type of gene is expected to exhibit expression signatures similar to the dashed blue and red lines since even small amounts of basement membrane maintain gene expression.

B. Controlled primarily by collagen-derived signaling. This type of gene is expected to exhibit expression signatures similar to the solid blue and red lines since even small amounts of collagen maintain gene expression.

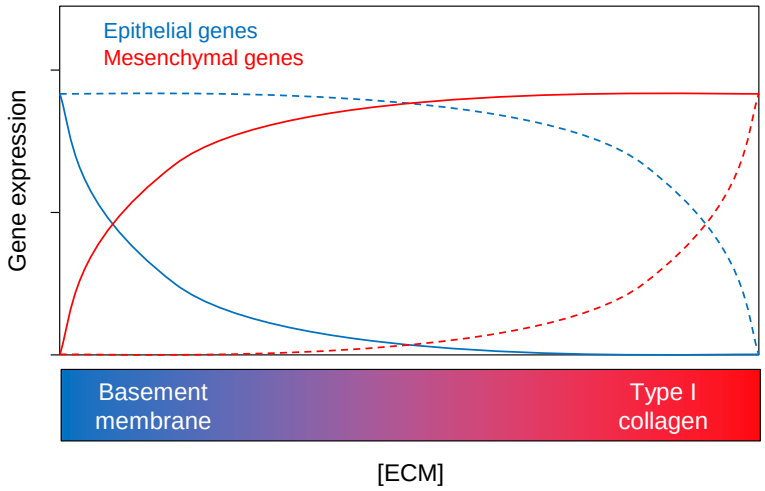

Figure 8.4. Anticipated results of matrix-induced gene expression studies. Epithelial (blue) and mesenchymal (red) gene expression is indicated as a function of 3D matrix composition. Genes that show expression patterns like the dashed lines are basement membrane-mediated. Genes that show expression patterns like the solid lines are collagen-mediated.

2) How do ECM structure and composition cooperate to influence epithelial phenotype?

Our group previously showed that MCF-10A migrate readily in collagen microtracks [60]. Given our finding here that collagen induces mesenchymal gene expression including fibronectin and vimentin, both of which influence MCF-10A migration [345, 376], it will be interesting to determine if epithelial motility in collagen microtracks depends on mesenchymal induction. Therefore, a well-designed series of experiments studying MCF-10A migration in microtracks formed using the gradient

matrices discussed above will determine if MCF-10A migration is simply stimulated by open space in the ECM or if it requires open space plus a collagen-induced mesenchymal phenotype.

3) How does ECM regulate MT1-MMP from transcription to activity?

Our finding that 3D collagen matrix uniquely up-regulates MT1-MMP transcription that is required for invasive behavior can be greatly expanded upon by studying the matrix-dependent regulation of MT1-MMP protein expression and the many steps of post-translational regulation that control MT1-MMP activity [25, 359, 377]. Since we showed that Matrigel downregulates MT1-MMP, performing these studies in mixed ECM gels will indicate to what extent type I collagen induces and basement membrane suppresses MT1-MMP expression and activity.

4) What are the mechanisms underlying the mechanosensitivity of the invasive epithelial phenotype?

It will be important to further explore the mechanisms by which collagen matrix stiffness regulates gene expression and epithelial invasion. Analysis of stiffness-dependent signaling and subsequent pharmacological and molecular targeting of key signaling networks should reveal the governing pathways [105]. Finally, although MCF-10A cells are used widely as a model of non-transformed mammary epithelial cells, it will be important to test if the observed matrix-dependent behaviors occur in other cell models and/or primary mammary epithelium [58].

Appendix A

Epithelial and malignant breast cell culture

This protocol is for the care and maintenance of MCF-10A and MDA-MB-231 cells as recommended by the Physical Sciences Oncology Center (PS-OC).

I. Cell culture supplies:

- Sigma (Use Krackeler)
  - Bovine insulin powder; 50 g (I6634-50MG) lasts 10 bottles
  - Hydrocortisone; 1 g (H-0888-1G*) lasts 4000 bottles
  - Cholera toxin; 0.5 mg (C8052-0.5MG) lasts 10 bottles

- Invitrogen (Supply Center)
  - DMEM; 500 mL (11965-092)
    4.5 g/L glucose (high) / + glut / - NaPyruvate
  - DMEM:F12; 500 mL (11320-033)
  - Horse Serum; 100 mL (16050-130) lasts 4 bottles
  - hEGF; 100 µg (PHG-0311) lasts 10 bottles
  - 0.05% and 0.25% trypsin, 0.53 mM EDTA (20) 5-mL aliquots
    100 mL (25200-056)

- Atlanta Biologicals
  - Fetal Bovine Serum (S11095)

II. Aliquoting and storage:

- hEGF (100 µg; in -20°C freezer)
  Resuspend at 100 µg/mL in sterile dH_2O or PBS. Store at -20°C in (10) 100 µL aliquots.
- Hydrocortisone (at RT)
  Resuspend at 1 mg/mL in 200-proof EtOH. Store at -20°C in 250 µL aliquots.
- Cholera toxin (0.5 mg; in 4°C)
  Resuspend at 1 mg/mL (500µL) in sterile dIH_2O; allow to reconstitute for 10 minutes. Store at 4°C in (10) 50 µL aliquots.
- Insulin (50 mg; in -20°C)

Resuspend at 10 mg/mL in sterile dIH_2O with 1% glacial acetic acid; shake solution and allow to reconstitute for 10-15 minutes. Store at -20°C in (10) 500 µL aliquots.

- Prepare 1% acetic acid solution (50 µL glacial acetic acid in 5 mL dIH_2O)
- Add ~ 3 mL to insulin bottle, wait 10 minutes, remove to 15-mL conical tube.
- Add remaining 2 mL 1% acetic acid to insulin bottle, remove to conical tube.
- Refrigerate overnight at 4°C overnight; should be clear next day

- Horse serum (100 mL; in -20°C)
  Thaw at 4°C before transferring into (4) 25 mL aliquots. Store at -20°C.
- Fetal bovine serum (500 mL; in -20°C)
  Thaw at 4°C before transferring into (10) 50 mL aliquots. Store at -20°C.

III. Complete growth medium preparation:

- <u>MDA-MB-231</u>

DMEM (11965-092)	(1) 500 mL bottle
10% FBS (S11095)	(1) 50 mL aliquot; thaw in refrigerator
100 U/mL each Pen/Strep	(1) 5 mL aliquot; ⋯

- Remove **55 mL** DMEM
- Add FBS and Pen/Strep
- Do not filter (per PSOC) → (10) 50 mL aliquots

- <u>MCF-10A</u>

DMEM:F12 (11320-033)	(1) 500 mL bottle
5% Horse serum (16050-130)	(1) 25 mL aliquot; thaw in refrigerator
20 ng/mL hEGF	(1) 100 µL aliquot; ⋯
0.5 µg/mL Hydrocortisone	(1) 250 µL aliquot; ⋯
10 µg/mL Insulin	(1) 500 µL aliquot; ⋯
100 U/mL each Pen/Strep	(1) 5 mL aliquot; ⋯
100 ng/mL Cholera toxin	(1) 50 µL aliquot; at 4°C

- Remove **30.9 mL** DMEM
- Add above ingredients
- Do not filter (per PSOC) → (10) 50 mL aliquots

IV. Passing/Maintaining cells:

- Complete growth medium (above)

- Trypsin/EDTA
- Sterile PBS

1. Place media and trypsin in 37°C water bath for at least 15 minutes
2. Aspirate media off cells, rinse twice with 5 mL PBS
3. Remove PBS, add 1.0 mL trypsin/EDTA (0.05% for MCF-10A; 0.25% for MDA-MB-231)
4. Incubate at 37°C until cells dissociate from plate (MDA-MB-231: ~2 min; MCF-10A: ~15 min)
5. Add 2-4 mL media to plate and transfer full volume to 15-mL conical tube
6. Centrifuge at 1000 rpm at RT for 5 min
7. Carefully aspirate or pour off supernatant from cell pellet
8. Resuspend in 1 mL of media, pipette gently to mix
9. Add desired volume to flask containing pre-warmed media
10. Culture at 37°C, 5% CO_2, feeding every 2 days, pass every 3-4 days

Note: MCF-10A cells grow much faster than MDA-MB-231 cells. For coordinated growth, pass MCF-10A cells ~1:20 and MDA-MB-231 cells ~1:5.

V. Thawing cells:

- Complete growth medium (above)

1. Place media in 37°C water bath for at least 15 minutes
2. Retrieve (and record in log) vial of cells from liquid nitrogen
3. Immediately thaw vial in 37°C water bath for ~2 min. Once cells are thawed, thoroughly sterilize vial with 70% EtOH and move to sterile biosafety cabinet
4. Add 10 mL media to 15-mL conical tube
5. To this, add contents of vial (should be ~1 mL)
6. Centrifuge at 1000 rpm for 5 min
7. Aspirate supernatant and resuspend cells in 1 mL pre-warmed media
8. Transfer cell suspension to flask
9. Maintain cells at 37°C, 5% CO_2
10. Change media day after thawing to remove any unattached/dead cells
11. Pass as early as 2 days post-thawing depending on cells.

VI. Freezing cells:

- Freezing medium (complete growth medium + 10% (V/V) DMSO)
- Trypsin/EDTA
- Sterile PBS
- Cell freezing vial and container (Mr. Frosty)

1. Place freezing media on ice
2. Label vial(s) for freezing with passage number, approximate cell number, date, initials
3. Follow passaging protocol above to step 7
4. Freeze either by cell number or freezing dilution (~1:3)
    - For 1:3 dilution, resuspend in 1 mL *growth media*. For each vial, add 333 µL *cell suspension* to 566 µL *growth media*, then add 100 µL *DMSO*
    - Otherwise, add 10% DMSO to entire cell suspension and aliquot into separate
5. Place vials on ice for 5 min
6. Transfer vials into cell freezing container at RT, move to -80°C for 24 hours
7. Transfer vials to liquid nitrogen tank (record in log)

Appendix B

Type I collagen isolation and purification

Materials:

- Frozen rat tails (Pel-Freez until 6/2013, then switched to Rockland Immunochemicals)
- Sterile 0.1% acetic acid (1:1000 glacial acetic acid in MilliQ H_20)
- 70% ethanol

- Scalpel or dissecting scissors
- Hemostat
- Rat-toothed microdissecting forceps
- Large Petri dish
- 250 ml beaker
- Sterile 400 ml / 1 L glass bottles
- 50 ml conical tubes
- Centrifuge
- Lyophilizer

Methods:

Part 1: Rat tail tendon extraction

The protocol should be performed in a sterile biosafety cabinet.

1. Autoclave glass bottles, 250 ml beaker, and dissection tools to ensure sterility.
2. Fill the beaker and petri dish with 70% ethanol.
3. Submerge frozen rat tails in ethanol in the petri dish to thaw for 5-10 minutes.
4. Cut off the tips of the tail at both ends and make a shallow incision along the entire length of the tail (only cut through the skin). Peel the skin away either by hand or using the hemostat/forceps.
5. Four bundles of shiny white tendons should now be visible along the length of the tail. Hold the tail at the base with your non-dominant hand and use the hemostat or rat-toothed forceps in your dominant hand to grab one of the tendon bundles about 1/3 of the way down from the tip of the tail (you should be able to get underneath the tendon bundle to separate it from the muscle). Remove the tendons by pulling the bundle towards the tip. Do not pull towards the tail base as the tendons will likely break. Place the isolated tendons in the beaker of ethanol.

6. Repeat this process for the remainder of this bundle by grabbing the tendons ~1/3 of the way down from the tip of the remaining tendon.
7. Repeat for each of the four tendon bundles.

Part 2: Acid-solubilization of collagen I from rat tail tendons

1. Once extraction is complete, dry the tendons with Kimwipes and weigh them in sterile 50 ml conical tubes.
2. Place the tendons in sterile bottles, and add 0.1% acetic acid at 150 ml/g of tendon. **For Rockland rat tail tendons, add acetic acid at 300 ml/g**
3. Allow acetic acid to solubilize collagen I for at least 48 hours at 4°C. The tendons will swell and become translucent as the collagen goes into solution.

Part 3: Purification and reconstitution of collagen I

1. Pipet the collagen/tendon/tissue material into 50 ml conical tubes. Weigh the tubes to ensure that opposing tubes are well balanced (± 0.1 g). Centrifuge for 90 minutes at 4°C to remove insoluble tissue from solubilized collagen I.
    a. If using the NBTC centrifuge, set centrifuge to highest settings: 9000 rpm, fast ramp up, fast ramp down.
    b. Alternatively, use fastest centrifuge available: ~4600 rpm.
2. Carefully collect the clear supernatant and discard the pellet. Replace conical tube caps with clean Kimwipe or move to and freeze the solution. Flash freeze in liquid nitrogen; -80°C for 30 minutes, or -20°C overnight.

→ Collagen is most stable at this stage; hold here at -20°C or -80°C if necessary ←

3. Place tubes in lyophilizer for at least 48 hours (may be longer for larger volumes).
4. Immediately after removal from lyophilizer, mass the collagen product in new sterile conical tubes and reconstitute in 0.1% acetic acid at the desired concentration (typically 10 mg/ml or 20 mg/ml).

Notes:

1. *Part I* should yield 0.3-0.6 g of tendon/tail (depends on tail and efficiency of isolation)
2. Although the solution at the end of *Part 2* will theoretically remain stable at 4°C indefinitely, we try to use it within 1-2 months.
3. The "purified" supernatant solution at *Step 3.2* is approximately 1-2 mg/ml.
    a. Thus, 100 ml of this solution should yield approximately 100-200 mg of pure collagen I after lyophilization.
4. *Very* rough estimate of ~100 mg of pure collagen I per tail. This is highly variable, but is a good estimate for resource management.

Appendix C

3D collagen matrix alignment

Protocol co-authored by Zachary Goldblatt

I. Create device

1. Pour 44g of PDMS into square petri dish (40g Sylgard 184 silicon elastomer base, 4g Sylgard 184 silicon elastomer curing agent).
2. Vacuum out bubbles and let cure for 4 hours in oven at 60°C.
3. Cut out approximately 20x20mm PDMS squares with scalpel. PDMS should be around 3-5mm thick.
4. Cut out two "C" shaped wells on opposite sides of PDMS square to create an H shape. Cut out should be about 10x10mm.
5. Use glass etcher to cut 22x22mm glass slides into roughly 20x8mm to 20x10mm (the width and height of the PDMS) rectangle pieces of glass. This glass serves as the fourth wall in order to enclose the well.
6. Glue the rectangular glass to the two edges of the wall with Superflex Clear RTV Silicone Adhesive Sealant. This glue will make glass permanently stick to the PDMS. Make sure glass is perfectly flat on bottom and in line with PDMS in order to create best seal possible.

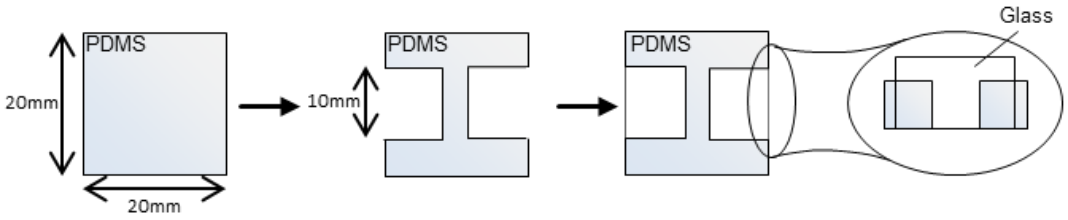

II. Activate the device (adapted from Activation Protocol by Brooke Mason)

1. Clean the PDMS devices very well with a water/alconox rinse and ethanol rinse. Let air dry in clean petri dish until no liquid droplets are present.
2. Line PDMS devices onto edges of petri dish, minimizing the amount of PDMS in contact with the petri dish plastic.
3. Line a second petri dish with parafilm (used in step 7-12).
4. Put petri dish with PDMS devices into plasma cleaner, close door, turn on vacuum pump, and turn on plasma.

5. Once chamber turns purple, allow plasma to be on for 2 minutes.
6. After 2 minutes, remove petri dish from plasma cleaner and lay PDMS devices flat in second petri dish with parafilm.
7. Incubate wells with 1% PEI in MilliQ water solution for 10 minutes. Add as much liquid is needed in order to fill entire well.
8. Remove PEI solution and properly dispose in appropriate waste container.
9. Rinse wells with MilliQ water (3 x 5min incubations).
10. Incubate wells with 0.1% glutaraldehyde in PBS solution for 30 minutes. Add as much liquid is needed in order to fill entire well.
11. Remove glutaraldehyde solution and properly dispose in appropriate waste container.
12. Rinse wells with MilliQ water (3 x 5min incubations).
13. Let dry overnight
14. After cleaning with water/alconox, activation effects decrease dramatically. Suggest activating before each use of single device.

III. Seeding cells in media collagen

1. Rinse PDMS device with ethanol to sterilize before using in culture hood.
2. Using vacuum grease, attach PDMS device to glass slide. Glass that was glued to PDMS (I.6) should make tight seal with bottom glass slide.
3. Lay PDMS and glass slide into a large petri dish or onto aluminum foil inside culture hood. Place neodymium magnet (BZX0Y0X0-N52; K&J Magnetics, Pipersville, PA) next to devices. Glass wall should be touching magnet.

   Caution: Magnet is very strong. Keep anything metal away from magnet and remove metal jewelry if wearing.

   Create 20x paramagnetic polystyrene bead stock (PM-20-10; Spherotech, Lake Forest, IL)

   a. Dilute metal beads at 1:20 with sterile PBS

4. Prepare MDA-MB-231 cells for seeding

   a. Remove media from T-25 flask of cultured cells
   b. Rinse with sterile PBS
   c. Add 1mL of trypsin into T-25 flask for 2min at 37°C *(do not over-trypsinize)*
   d. Neutralize trypsin with 4mL media; transfer to 15 mL tube
   e. Centrifuge cells at 1000 rpm for 5 min
   f. Aspirate supernatant and resuspend cells in 1 mL culture media; count cells

5. Pretreat cells with effectors if desired.

a. Make 200µL cell suspension comprising 125,000cells and the appropriate amount of inhibitor.
b. Incubate for 30 min in incubator on rocker.

6. For aligned matrix, seed MDA-MB-231 cells into 1.5mg/mL media collagen with metal beads at a cell density of 125,000cells/mL collagen.

   Create 1.5mg/mL collagen with metal beads.
   a. 150µL 10mg/mL Rat Tail Collagen I
   b. (800–cell suspension)µL DMEM Complete Media
   c. 3µL NaOH
   d. 50µL Metal Bead solution (1%v/v)
   e. Cell suspension to achieve 125,000cells

7. Pipette collagen/metal bead/cell solution into well touching magnet until solution is almost at top of well (~400µL).
8. For random matrix, seed MDA-MB-231 cells into 1.5mg/mL media collagen with no metal beads at a cell density of 125,000cells/mL collagen.
9. Pipette collagen/cell solution into well opposite of magnet until solution is almost at top of well (~400µL).
10. Allow to polymerize for 30 min at room temperature in culture hood.

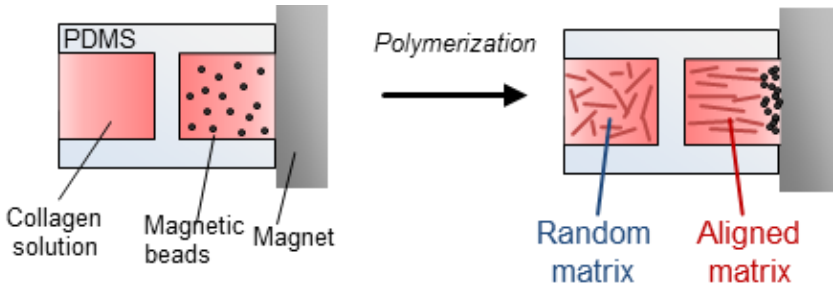

IV. Transferring PDMS devices with cells in collagen to microscope for time-lapse imaging.

1. After polymerization, remove magnet from culture hood. Spray with ethanol to resterilize before putting away.
2. Remove bottom glass slide from PDMS device. Don't slide it off. Since activated, collagen should stick to sides of PDMS well and not fall out.
3. Apply more vacuum grease to bottom of device and insert into 6 well plate. Apply enough pressure to firmly secure PDMS device to bottom of plastic well.
4. Overlay with 5-7mL of DMEM Complete Media, or until device is completely submerged in media. If cells were pretreated with an inhibitor, overlay 5-7mL of DMEM Complete Media with the appropriate amount of inhibitor added, over the specific devices consisting of inhibited cells.
5. Transport 6 well plate with devices to microscope for time-lapse imaging.

V. Time-lapse imaging and fixing

1. Set microscope to Phase_Timelapse experiment.
2. Set objective to x20 and time interval to 2min for protrusion dynamic imaging.
3. Set objective to x20 and time interval to 10-20min for single cell migration imaging.
4. Set objective to x10 and time interval to 10-20min for cell population imaging.
5. Choose positions that are at least >200μm above the bottom surface.
6. Chose as many positions as desired (*Note: 30 positions take about a min to image*).
7. After time-lapse imaging or at any time point during culture in incubator, collagen gels in device can be fixed.

   Fix cells in collagen gel
   a. Rinse gels in device with PBS (3x)
   b. Fix cells with 3.7% formaldehyde in PBS for 10min
   c. Remove formaldehyde solution and properly dispose in appropriate waste container.
   d. Rinse wells with PBS (3 x 5min incubations).

8. At this point, collagen gels can remain inside device or can be removed.

Appendix D

Multicellular spheroids

I. General protocol

1. Coordinate growth of cells
2. Label cells with vital dye (maintain unlabeled flasks for further propagation)
3. Allow cells to recover for 3-24 hours
4. Trypsinize cells, add appropriate number of cells to complete media/0.25% Methocult
5. Mix cell suspensions in appropriate ratios in round-bottom 96-well plate (200 µL/well)
6. Incubate at 37°C for 2 hours on orbital shaker (~60rpm)
7. Replace media with complete media / 0.25% Methocult / 1% Matrigel after shaking and every 2-3 days thereafter

II. Live cell labeling

CMFDA CellTracker Green (C7025)

Prepare 10 mM stock (50 µg lyophilized powder in 9 µL DMSO); store at -20°C

1. Remove media from T-25 flask by aspiration
2. Rinse 1X with sterile PBS
3. Add 1 mL working solution (**10 µM CMFDA in PBS**)
4. Incubate 15 min
5. Replace working solution with fresh pre-warmed media
6. Incubate 30 min
7. Rinse 1X with sterile PBS
8. Replace fresh pre-warmed media

CMRA SE CellTracker Orange (C34551)

Prepare 10 mM stock (50 µg lyophilized powder in 9 µL DMSO); store at -20°C

1. Remove media from T-25 flask by aspiration
2. Rinse 1X with sterile PBS
3. Add 1 mL pre-warmed working solution (**10 µM CMRA in PBS**)
4. Incubate 30 min

5. Replace working solution with fresh pre-warmed media
6. Incubate 30 min
7. Rinse 1X with sterile PBS
8. Replace fresh pre-warmed media

Alternatively, cells can be labeled in suspension:

1. Trypsinize and centrifuge cells as for passaging
2. Resuspend pellet (including desired cell number) in working solution for 10-15 minutes at 37°C
3. Centrifuge to pellet cells, and resuspend in PBS
4. Centrifuge to pellet cells, and resuspend in desired growth medium

Note: MDA-MB-231 cells are extremely sensitive to the DMSO in the working solution; minimize their exposure by labeling these cells with the CMFDA (shorter incubation required)

III. Spheroid Reagents

Matrigel ("MG") [BD 356234; Lot 15900] – ordered from Krackeler

11. Thaw MG at 4°C overnight on ice
    Note: Avoid multiple freeze-thaws
12. Freeze 20-200µL sterile pipette tips and centrifuge tubes at -20°C
13. **On ice**, aliquot into appropriate volumes
    For 1% MG: 144 µL MG per 14.4 mL complete media (enough for 150 µL x 96 wells)
14. Quickly transfer aliquots to cold -20°C freezer box; store at -20°C
15. Immediately before use, remove from -20°C, thaw on ice, dilute in cold media on ice

Methocult ("MC") [H4100] – ordered from Stem Cell

1. Thaw MC overnight at 4°C
2. Add 98 mL of complete culture media to MC (2.6%); solution now 0.75%, store at 4°C

Note:
Use MCF-10A media for both MDA-MB-231 and MCF-10A monoculture and co-culture spheroids. MDA-MB-231 form much better in MCF-10A media than in MDA-MB-231 media (reason unknown; likely EGF, hydrocortisone, or insulin?)

IV. Spheroid Protocol

6. Remove media from T-25 flask of cultured cells

7. Rinse 1X with sterile PBS
8. Trypsinize cells at 37°C *(do not over-trypsinize)*
9. Neutralize trypsin with 3-5 mL media; transfer to 15 mL tube
10. Centrifuge cells at 1000 rpm for 5 min
11. Aspirate supernatant and resuspend cells in 1 mL culture media; count cells
12. Mix MC by swirling bottle and pipetting up and down (do not introduce bubbles)
13. Make media / 0.25% MC by mixing 1 part MC with 2 parts media:

    per 96-well plate (200 µL/well) (includes extra 2.8 mL buffer volume):

0.75% MC	7.33 mL
Complete media	14.66 mL
	22 mL media / 0.25% MC

14. Add desired number of cells to media/0.25% MC; cell concentration should be desired number of cells per 200 µL (i.e. for 5,000-cell spheroids, 5,000 cells/200 µL)

    Note: If volume of cell suspension to add is more than 500 µL, repellet and suspend in media / 0.25%MC

15. Pour cell suspension into sterile reagent reservoir
16. Use multichannel pipette to add 200 µL suspension to each well of a non-treated, round bottom, 96-well plate
17. Centrifuge at 1000rpm, 5 min at room temp
18. Incubate at 37°C, 5% CO_2 for 2 hours on orbital shaker (~60rpm)
19. Remove from shaker and incubate at 37°C, 5% CO_2
20. *Optional:* For poorly cells lines immediately replace culture media with **complete media / 0.25% MC / 1% MG**
    Notes:
    - *Do not shake with MG-containing media*
    - *In my experience, adding Matrigel to MDA-MB-231 spheroids doesn't seem to make much difference in compaction and can often just cause issues if it partially polymerizes during handling. I prefer to leave it out.*

21. Feed spheroids every 2-3 days by removing and replacing 150-175 µL media

V. Co-culture Spheroid Protocol

Spheroids can be made to include multiple cell types by dividing the spheroid-making solution (22 mL of media / 0.25% MC / cell suspension) between the two cell types. For 50/50 mixed spheroids, 11 mL of spheroid-making solution would be required for each cell type, and 100 µL of each solution would be added to each well.

For several different ratios of cell type A and B, the relative amounts of each must be determined:

I: 100% cell type A
II: 50% cell type A, 50% cell type B
III: 1% cell type A, 99% cell type B
IV: 100% cell type B

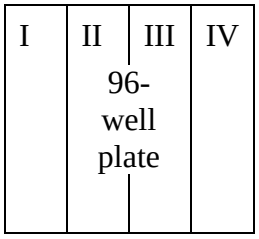

Solution A: 1.5 / 4 = 0.375 → **8.25 mL**
(~1.5 / 4 of the plate is type A, requiring 8.25 mL of solution A)

Solution B: 2.5 / 4 = 0.625 → **13.75 mL**
(~2.5 / 4 of the plate is type B, requiring 13.75 mL of solution B)

Per (1) plate of 5k-cell co-culture spheroids as shown above:

MCF-10A solution (13.75 mL):

0.75% MC	4.58 mL	
Complete media/cells	9.17 mL	(including 344k cells)

MDA-MB-231 solution (8.25 mL):

0.75% MC	2.75 mL	
Complete media/cells	5.50 mL	(including 206k cells)

Feeding solution (14.4 mL of media / 0.25% MC / 1% MG):

0.75% MC	4.8 mL
Complete media	9.6 mL
MG	144 µL

Appendix E

siRNA transfection of MCF-10A and MDA-MB-231 cells

Overview:
d1 Seed cells in plate for transfection
d2 siRNA transfection
d3 Media change
d4 Seed cells in experiment

I. Seed cells in plate for transfection (d1)

Seeding density is cell type-dependent and is shown below optimized for maximum cell output at d4. Volumes and cell numbers can be adjusted in proportion to well surface area for different plates (e.g. 24-well → 2 cm^2; 12-well → 4 cm^2; 6-well → 10 cm^2).

1. Trypsinize cells from culture flask per protocol
2. Resuspend in pen/strep-free media
3. Plate cells:

d1	Seed 37.5k cells/cm^2 (MDA-MB-231) Seed 15k cells/cm^2 (MCF-10A)
d2	Transfect
d3	Media change
d4	~90% confluent

For example, seed at 150k MDA-MB-231 cells/well in 12-well plate; 0.8 mL media/well (see Step II for explanation of volume)

II. siRNA transfection (d2)

As above, volumes of reagents are shown optimized for siRNA transfection in 12-well plates with a total media volume of 1 mL. Concentration of Lipofectamine and siRNA in transfection solution are cell type- and siRNA-dependent and can be adjusted accordingly.

	Stock concentration	*Final concentration*	*Volume of stock (in 1mL)*
Lipofectamine	1 mg/mL	2 µg/mL	2 µL
siRNA	20 µM (20 pmoles/µL)	25 nM (25 pmoles/mL)	1.25 µL
OptiMEM			100 µL + 100 µL

1. Check plate seeded on d1 for cell attachment and viability
2. Prepare transfection solution (final concentrations: 25nM siRNA; 2µg/mL Lipofectamine):
   Per **12-well plate** well:
   a. Add 1.25 µL siRNA stock solution to 100 µL OptiMEM; mix and rest at room temperature for 3-5 minutes
   b. Add 2 µL Lipofectamine stock solution to 100 µL OptiMEM; mix and rest at room temperature for 3-5 minutes
   c. Combine above solutions; mix and rest at room temperature for 20 minutes
3. Add transfection solution dropwise to cells in 0.8 mL media; total volume now 1 mL
   (do not change media before adding reagents unless there is poor cell attachment)
4. Depending on cells, a media change 4 h after may improve viability
   MCF-10A greatly prefer 4 h transfection

III. Media change (d3) – if not changed after 4 h on d2

1. Aspirate media/transfection solution
2. Add 1 mL (or appropriate volume) of pen/strep-free media to each transfected well

IV. Seed cells in experiment (late d3 / d4)

Cells can be seeded in experiment, assayed for protein expression, etc. either 8-12 h following media change or the next day. Ideal timeline post-transfection should be determined for the specific experiment.
Generally, maximal mRNA knockdown is seen 24-48 h after transfection, while maximal protein and phenotypic responses require 48-96 h (per Life Technologies).

Appendix F

Extraction of mRNA from 3D matrix samples

Protocol for extracting total mRNA from 3D collagen and Matrigel samples. Customary cDNA synthesis and qRT-PCR can be used for downstream applications.

Materials:

- RNase-free pipettes, tubes, Petri dishes, etc.
- RNaseZap-treated razor blade
- RNeasy Mini Kit (Qiagen #74104)
- Collagenase type IV (Worthington Biochemial #CLS-4)
  - Make working solution immediately prior to use: 300 U/mL in sterile PBS
- Collagenase/dispase (Roche # 10269638001)
  - Make 1 mg/mL working solution in sterile PBS. Aliquot and freeze at -20°C

Methods:

I. Matrix digestion

Note:
Collagenase and collagenase/dispase volumes can be adjusted accordingly to larger or smaller gels. Longer incubations are required for higher concentration collagen/Matrigel.

1. Aspirate media from gel, rinse twice with PBS
2. Transfer gel from well to petri dish and dice with razor blade. ~15 seconds of rapid up-and-down movement should be sufficient
3. Use cell scraper to pool liquid and gel pieces and transfer solution to 15 mL conical tube
4. Digest gel:

   For **COLLAGEN**
   a. Add 1 mL of 300 U/mL collagenase type IV working solution to conical tube (per 0.5 mL gel)
   b. Use wide-bore pipet to mix
   c. Incubate on orbital shaker (~60 rpm) at 37°C for 10 min (1 mg/mL gel) to 30 min (5 mg/mL gel), or until gel pieces are no longer visible
      Note: Depending on collagenase quality, incubation times may vary slightly.

For **MATRIGEL** or mixed **MATRIGEL/COLLAGEN**

a. Thaw 1 mL aliquot of collagenase/dispase and add to gel
b. Use wide-bore pipet to mix
c. Incubate on orbital shaker (~60 rpm) at 37°C for 1 h

5. Once chunks of matrix are no longer visible (cells and cell clusters should still be visible as tiny specks floating through solution), add several mL of complete media to dilute solution and centrifuge at 1000 rpm for 5 min to pellet cells
6. Aspirate supernatant, add 5 mL of complete media, and centrifuge to pellet
7. Aspirate supernatant and quickly proceed to next section.

II. Cell pellet lysis

Note:

Move to RNase-free work space and use benchtop microcentrifuge for remaining steps. Follow protocol from Qiagen RNeasy Mini Kit (included below).

1. Add 350 µL RLT Buffer to cell pellet
2. Add 1 volume (equal to volume of remaining liquid) of 70% ethanol; pipette well to mix
3. Transfer 700 µL of solution to RNeasy column, centrifuge 15 s at >8000xg; discard flow-through
4. Repeat step 6 as needed, adding remaining solution 700 µL at a time to same RNeasy spin column
5. Add 700 µL Buffer RW1 to RNeasy column, centrifuge 15 s at >8000xg; discard flow-through
6. Add 500 µL Buffer RPE to RNeasy column, centrifuge 15 s at >8000xg; discard flow-through
7. Add 500 µL Buffer RPE to RNeasy column, centrifuge 15 s at >8000xg; discard flow-through
8. Remove RNeasy spin column from collection tube and place in new 1.5 mL collection tube
9. Add 30 µL RNase-free water directly to spin column membrane, centrifuge for 1 min at >8000xg to elute RNA from membrane
10. Measure RNA concentration and purity
11. Use 0.5-1 µg RNA for first strand synthesis using qScript cDNA Synthesis Kit (Quanta Biosciences #95047-100)

Appendix G

Immunofluorescence of 3D samples

Protocol for staining cells in 3D collagen gels with one primary antibody, phalloidin, and DAPI

1. Aspirate media and rinse the samples 3x with PBS.
2. To fix samples, add 1 mL of 3.7% formaldehyde in PBS to each gel for:
    a. **30 min** at **RT** on rocker
    b. **Overnight** at **4°C** on rocker is also acceptable
3. Carefully flip gels over so that all solutions are applied to "imaging" surface of gel.
4. Wash 3x with PBS for **5-10 min** each on rocker.
   Note: Samples can be stored in PBS at 4°C at this point for a couple of days if necessary
5. To permeabilize cells, add 1 mL 1% Triton in PBS for **10-30 min** at RT on rocker.
   *** Can go directly to step 17 if only staining with phalloidin**
6. Wash 3x with 0.02% Tween 20 in PBS for **5-10 min** each at RT on rocker.
7. To block samples, wash 1x with 0.02% Tween 20/3% BSA/10%FBS for **3 h** at RT on rocker.
8. Prepare 1° antibody in blocking solution. Dilute antibodies according to the manufacturers' recommendation. 1:50 is often a good starting dilution.
9. Add 1° antibody solution (~10-50% gel volume) to samples.
10. Incubate samples **overnight** at **37°C** with gentle shaking.

11. Wash 3x with 0.02% Tween for **30-60 min** each on rocker
    *** This washing can continue for several more hours to reduce background staining**

12. Prepare 2° antibodies in blocking solution. Dilute according to the manufacturers' recommendation. 1:100-1:500 is often a good dilution. Centrifuge 2° antibody at 14k xg for 2 min at 4ºC before use.
13. Add 2° antibody solution (~10-50% gel volume) to samples.
14. Incubate samples **overnight** at **37°C** with gentle shaking.

15. Wash 2x with 0.02% Tween for **30-60 min** each on rocker
16. Wash 2x with PBS for **30-60 min** each on rocker (to remove unbound immunologicals)

*** This washing can continue for several more hours to reduce background staining**

Staining for F-actin

17. Prepare phalloidin solution (1:50-1:100 in PBS) and add (10-50% gel volume) to samples.
18. Incubate for **2 h** at RT on rocker.
19. Wash 3x with PBS for **5-10 min** each on rocker.

Staining for nuclei

20. Prepare DAPI solution (0.02-0.1 mg/mL in MilliQ water) and add (10-50% gel volume).
21. Incubate for **20 min** at RT on rocker.
22. Wash 3x with PBS for **5-10 min** each on rocker.
23. Flip gels back over for imaging

IF solutions

- 3.7% (v/v) formaldehyde *make fresh*
  1:10 dilution of stock formaldehyde (37%) in PBS

- 1% (v/v) Triton (octyl phenol ethoxylate) *make fresh*
  1:100 dilution of stock Triton in PBS

- 0.02% (v/v) Tween 20 (polyoxyethylene 20 sorbitan monolaurate)
  1:500 dilution of Tween in PBS

- 0.02% (v/v) Tween 20 / 3% (w/v) BSA / 10% FBS *make fresh*
  0.03 g BSA + 0.1 mL FBS per 1 mL 0.02% Tween 20

Appendix H

Phenotypic cell sorting

Protocol co-authored with Zachary Goldblatt and Alexandra Braun

I. Setting up collagen–coated Transwell

1. Insert 8μm pore membrane Transwell into a 6 well plate.
2. Coat top of Transwell membrane with 75μL of 1mg/mL collagen. This produces around a 10μm thick collagen layer.

    a. 100μL 10mg/mL Rat Tail Collagen I
    b. 900μL of base serum-free DMEM (0% FBS)
    c. 2μL NaOH

3. Polymerize for 15min in incubator at 37°C.
4. After 15min, fill Transwell with media. Keep in incubator until ready to use.

    a. Fill the bottom of the 6 well with 2.5mL of DMEM Complete Media (10% FBS).
    b. Fill the top of the Transwell with 1mL of serum-free DMEM.

    Note: Want to have media inside Transwell and inside 6 well at similar levels to minimize fluid movement through Transwell.

5. Prepare cells for seeding.

    g. Remove media from T-25 flask of cultured cells
    h. Rinse with sterile PBS
    i. Add 1mL of trypsin into T-25 flask for 2min at 37°C *(do not over-trypsinize)*
    j. Neutralize trypsin with 4mL media; transfer to 15 mL tube
    k. Centrifuge cells at 1000 rpm for 5 min
    l. Aspirate supernatant and resuspend cells in 1 mL serum-starved DMEM (0.5% FBS); count cells

6. Remove serum-free media from top of Transwell.
7. Seed 200,000 cells suspended in serum-starved DMEM onto top of Transwell.

8. Add serum-starved DMEM until volume reaches 1mL.
9. Incubate at 37°C for 2 days.
10. After 2 days, remove media from top of Transwell.
11. Replace with fresh serum-starved DMEM on top of Transwell.
12. Incubate at 37°C for 2 more days.

II. Collecting cells from Transwell

1. Collect media from the inside (NON) and outside (INV) of the Transwell into two separate 15mL tubes.
2. Rinse outside of Transwell with 2mL of PBS, and inside of Transwell with 1mL of PBS.
3. Collect the PBS and pipette into the respective tubes.
4. Add 2-2.5mL of 0.25% trypsin-EDTA into outside of Transwell and 1mL to the inside of the Transwell.
5. Incubate 6 well plate at 37°C on rocker for 3-4min.
6. Add DMEM Complete Media to the inside and outside of each Transwell to neutralize trypsin.
7. Remove media/trypsin from inside of Transwell first and put into NON tube. Remove Transwell from 6 well and collect as much media from inside as possible.
8. Run PBS over inside of Transwell and collect PBS into NON tube as well.
9. Run media from 6 well plate over outside of Transwell 3x, to collect any loosely attached cells.
10. Remove media/trypsin from 6 well and put into INV tube.
11. Run PBS over 6 well and collect PBS into INV tube.
12. Centrifuge cells at 1000rpm for 5min
13. Remove supernatant and resuspend pellet in 1mL of media*; count cells

    * Type of media will be determined by what cells are used for next.
    If reseeding cells for another Transwell assay, resuspend in serum-starved DMEM.
    If seeding cells into a T-25 flask for culture, resuspend in DMEM Complete Media.
    If just counting the number of cells, resuspend in Base DMEM.

III. Purification

1. For additional rounds of purification, seed INV cells and NON cells at 200,000cells/well into separate Transwells in order to create the invasive and non-invasive population respectively.
2. Repeat steps from “II”.
3. Only reseed the INV cells from the invasive population and the NON cells from the non-invasive population.

IV. Analysis of purity

1. Label INV cells with CMFDA CellTracker
2. Label NON cells with CMRA CellTracker

    a. Prepare 10mM stock solution of cell tracker.
    b. Dilute in 1mL of PBS.
    c. After step II.12, resuspend cell pellet in 1mL PBS/cell tracker solution.
    d. Incubate cell suspension at 37°C on rocker for 10min.
    e. Add 3mL of DMEM Complete Media to each cell suspension and mix.
    f. Centrifuge at 1000rpm for 5min.
    g. Remove supernatant and resuspend pellet in 1mL of serum-starved media; count cells

3. Seed 100,000 cells/well for each subpopulation. The two subpopulations will mix making original 200,000 cells/well.
4. Repeat steps in "II" in order to get an INV and NON population again.
5. Seed INV and NON cells into separate 6 well plate wells at similar cell densities and add DMEM Complete Media until 2mL of media are in the well.
6. Wait 4 hours to allow cell adherence and image on Zeiss LSM700 confocal microscope at x10.

REFERENCES

1. Carey SP, D'Alfonso TM, Shin SJ, Reinhart-King CA (2012) Mechanobiology of tumor invasion: engineering meets oncology. Crit Rev Oncol/Hematol 83:170–83

2. Carey SP, Charest JM, Reinhart-King CA (2011) Forces during cell adhesion and spreading: implications for cellular homeostasis. In: Gefen A (ed) Cell Biomol Mech Mechanobiol. Springer-Verlag, Berlin and Heidelberg, pp 29–69

3. Weigelt B, Peterse JL, van 't Veer LJ (2005) Breast cancer metastasis: markers and models. Nat Rev Cancer 5:591–602

4. Hood JD, Cheresh DA (2002) Role of integrins in cell invasion and migration. Nat Rev Cancer 2:91–100

5. Friedl P, Alexander S (2011) Cancer invasion and the microenvironment: plasticity and reciprocity. Cell 147:992–1009

6. Sahai E (2005) Mechanisms of cancer cell invasion. Curr Opin Genet Dev 15:87–96

7. LeBleu VS, Macdonald B, Kalluri R (2007) Structure and function of basement membranes. Exp Biol Med 232:1121–9

8. Lohi J (2001) Laminin-5 in the progression of carcinomas. Int J Cancer 94:763–7

9. Liotta LA, Stetler-Stevenson WG (1991) Tumor invasion and metastasis: an imbalance of positive and negative regulation. Cancer Res 51:5054s–9s

10. Fu HL, Moss J, Shore I, Slade MJ, Coombes RC (2002) Ultrastructural localization of laminin and type IV collagen in normal human breast. Ultrastruct Pathol 26:77–80

11. Chang HY, Chi J-T, Dudoit S, Bondre C, van de Rijn M, Botstein D, Brown PO (2002) Diversity, topographic differentiation, and positional memory in human fibroblasts. Proc Natl Acad Sci USA 99:12877–82

12. Kalluri R, Zeisberg M (2006) Fibroblasts in cancer. Nat Rev Cancer 6:392–401

13. Lu P, Weaver VM, Werb Z (2012) The extracellular matrix: a dynamic niche in cancer progression. J Cell Biol 196:395–406

14. Bissell MJ, Rizki A, Mian IS (2003) Tissue architecture: the ultimate regulator of breast epithelial function. Curr Opin Cell Biol 15:753–62

15. Rønnov-Jessen L, Petersen OW, Bissell MJ (1996) Cellular changes involved in conversion of normal to malignant breast: importance of the stromal reaction. Physiol Rev 76:69–125

16. Hanahan D, Weinberg RA (2011) Hallmarks of cancer: the next generation. Cell 144:646–74

17. Wang W, Goswami S, Lapidus K, Wells AL, Wyckoff JB, Sahai E, Singer RH, Segall JE, Condeelis JS (2004) Identification and testing of a gene expression signature of invasive carcinoma cells within primary mammary tumors. Cancer Res 64:8585–94

18. Polyak K (2010) Molecular markers for the diagnosis and management of ductal carcinoma in situ. J Natl Cancer Inst 210–3

19. Liotta LA, Tryggvason K, Garbisa S, Hart I, Foltz CM, Shafie S (1980) Metastatic potential correlates with enzymatic degradation of basement membrane collagen. Nature 284:67–8

20. Gusterson BA, Warburton MJ, Mitchell D, Ellison M, Neville AM, Rudland PS (1982) Distribution of myoepithelial cells and basement membrane proteins in the normal breast and in benign and malignant breast diseases. Cancer Res 42:4763–70

21. Adriance MC, Inman JL, Petersen OW, Bissell MJ (2005) Myoepithelial cells: good fences make good neighbors. Breast Cancer Res 7:190–7

22. Lerwill MF (2004) Current practical applications of diagnostic immunohistochemistry in breast pathology. Am J Surg Pathol 28:1076–91

23. Spaderna S, Schmalhofer O, Hlubek F, Berx G, Eger A, Merkel S, Jung A, Kirchner T, Brabletz T (2006) A transient, EMT-linked loss of basement membranes indicates metastasis and poor survival in colorectal cancer. Gastroenterology 131:830–40

24. Hotary K, Li X, Allen E, Stevens SL, Weiss SJ (2006) A cancer cell metalloprotease triad regulates the basement membrane transmigration program. Genes Dev 20:2673–86

25. Poincloux R, Lizárraga F, Chavrier P (2009) Matrix invasion by tumour cells: a focus on MT1-MMP trafficking to invadopodia. J Cell Sci 122:3015–24

26. Mueller MM, Fusenig NE (2004) Friends or foes - bipolar effects of the tumour stroma in cancer. Nat Rev Cancer 4:839–49

27. Provenzano PP, Eliceiri KW, Campbell JM, Inman DR, White JG, Keely PJ (2006) Collagen reorganization at the tumor-stromal interface facilitates local invasion. BMC Med 4:38

28. Dvorak HF, Weaver VM, Tlsty TD, Bergers G (2011) Tumor microenvironment and progression. J Surg Oncol 103:468–74

29. Kumar V, Abbas A, Fausto N, Aster J (2010) Robbins and Cotran Pathologic Basis of Disease, 8th ed. Elsevier Saunders, Philadelphia

30. Shao ZM, Nguyen M, Barsky SH (2000) Human breast carcinoma desmoplasia is PDGF initiated. Oncogene 19:4337–45

31. Iacobuzio-Donahue CA, Argani P, Hempen PM, Jones J, Kern SE (2002) The desmoplastic response to infiltrating breast carcinoma : gene expression at the site of primary invasion and implications for comparisons between tumor types. Cancer Res 62:5351–7

32. Kawashiri S, Tanaka A, Noguchi N (2009) Significance of stromal desmoplasia and myofibroblast appearance at the invasive front in squamous cell carcinoma of the oral cavity. Head Neck 31:1346–53

33. Tamimi SO, Ahmed A (1987) Stromal changes in invasive breast carcinoma: an ultrastructural study. J Pathol 153:163–70

34. De Wever O, Demetter P, Mareel M, Bracke M (2008) Stromal myofibroblasts are drivers of invasive cancer growth. Int J Cancer 123:2229–38

35. Goetz JG, Minguet S, Navarro-Lérida I, et al (2011) Biomechanical remodeling of the microenvironment by stromal caveolin-1 favors tumor invasion and metastasis. Cell 146:148–63

36. Weigelin B, Bakker G-J, Friedl P (2012) Principles of interface guidance and microvesicle dynamics: Intravital third harmonic generation microscopy of collective melanoma cell invasion. Intravital 1:32–43

37. Alexander S, Weigelin B, Winkler F, Friedl P (2013) Preclinical intravital microscopy of the tumour-stroma interface: invasion, metastasis, and therapy response. Curr Opin Cell Biol 25:659–71

38. Sidani M, Wyckoff J, Xue C, Segall JE, Condeelis J (2006) Probing the microenvironment of mammary tumors using multiphoton microscopy. J Mammary Gland Biol Neoplasia 11:151–63

39. Conklin MW, Eickhoff JC, Riching KM, Pehlke CA, Eliceiri KW, Provenzano PP, Friedl A, Keely PJ (2011) Aligned collagen is a prognostic signature for survival in human breast carcinoma. Am J Pathol 178:1221–32

40. Gritsenko PG, Ilina O, Friedl P (2012) Interstitial guidance of cancer invasion. J Pathol 226:185–99

41. Carey SP, Rahman A, Kraning-Rush CM, Romero B, Somasegar S, Torre OM, Williams RM, Reinhart-King CA (2015) Comparative mechanisms of cancer cell migration through 3D matrix and physiological microtracks. Am J Physiol Cell Physiol 308:C436–47

42. Wolf K, Alexander S, Schacht V, Coussens LM, von Andrian UH, van Rheenen J, Deryugina E, Friedl P (2009) Collagen-based cell migration models in vitro and in vivo. Semin Cell Dev Biol 20:931–41

43. Ray MR, Jablons DM (2009) Hallmarks of Metastasis. In: Keshamouni V, Arenberg D, Kalemkerian G (eds) Lung Cancer Metastasis. Springer New York, New York, NY, pp 29–46

44. Doyle AD, Petrie RJ, Kutys ML, Yamada KM (2013) Dimensions in cell migration. Curr Opin Cell Biol 25:642–9

45. Lauffenburger DA, Horwitz AF (1996) Cell migration: a physically integrated molecular process. Cell 84:359–69

46. Petrie RJ, Yamada KM (2013) At the leading edge of three-dimensional cell migration. J Cell Sci 125:5917–26

47. Wolf K, te Lindert M, Krause M, Alexander S, te Riet J, Willis AL, Hoffman RM, Figdor CG, Weiss SJ, Friedl P (2013) Physical limits of cell migration: control by ECM space and nuclear deformation and tuning by proteolysis and traction force. J Cell Biol 201:1069–84

48. Tozluoğlu M, Tournier AL, Jenkins RP, Hooper S, Bates PA, Sahai E (2013) Matrix geometry determines optimal cancer cell migration strategy and modulates response to interventions. Nat Cell Biol 15:751–62

49. Condeelis J, Segall JE (2003) Intravital imaging of cell movement in tumours. Nat Rev Cancer 3:921–30

50. Yamaguchi H, Wyckoff J, Condeelis J (2005) Cell migration in tumors. Curr Opin Cell Biol 17:559–64

51. Alexander S, Koehl GE, Hirschberg M, Geissler EK, Friedl P (2008) Dynamic imaging of cancer growth and invasion: a modified skin-fold chamber model. Histochem Cell Biol 130:1147–54

52. Yamada KM, Cukierman E (2007) Modeling tissue morphogenesis and cancer in 3D. Cell 130:601–10

53. Cukierman E, Pankov R, Yamada KM (2002) Cell interactions with three-dimensional matrices. Curr Opin Cell Biol 14:633–9

54. Mason BN, Starchenko A, Williams RM, Bonassar LJ, Reinhart-King CA (2013) Tuning three-dimensional collagen matrix stiffness independently of collagen concentration modulates endothelial cell behavior. Acta Biomater 9:4635–44

55. Carey SP, Kraning-Rush CM, Williams RM, Reinhart-King CA (2012) Biophysical control of invasive tumor cell behavior by extracellular matrix microarchitecture. Biomaterials 33:4157–65

56. Provenzano PP, Inman DR, Eliceiri KW, Trier SM, Keely PJ (2008) Contact guidance mediated three-dimensional cell migration is regulated by Rho/ROCK-dependent matrix reorganization. Biophys J 95:5374–84

57. Zaman MH, Trapani LM, Sieminski AL, MacKellar D, Gong H, Kamm RD, Wells A, Lauffenburger DA, Matsudaira P (2006) Migration of tumor cells in 3D matrices is governed by matrix stiffness along with cell-matrix adhesion and proteolysis. Proc Natl Acad Sci USA 103:10889–94

58. Nguyen-Ngoc K-V, Cheung KJ, Brenot A, Shamir ER, Gray RS, Hines WC, Yaswen P, Werb Z, Ewald AJ (2012) ECM microenvironment regulates collective migration and local dissemination in normal and malignant mammary epithelium. Proc Natl Acad Sci USA 109:E2595–604

59. Harley BAC, Kim H-D, Zaman MH, Yannas I V, Lauffenburger DA, Gibson LJ (2008) Microarchitecture of three-dimensional scaffolds influences cell migration behavior via junction interactions. Biophys J 95:4013–24

60. Kraning-Rush CM, Carey SP, Lampi MC, Reinhart-King CA (2013) Microfabricated collagen tracks facilitate single cell metastatic invasion in 3D. Integr Biol 5:606–16

61. Makale M (2007) Cellular mechanobiology and cancer metastasis. Birth Defects Res C 81:329–43

62. Thiery JP (2002) Epithelial-mesenchymal transitions in tumour progression. Nat Rev Cancer 2:442–54

63. Tarin D, Thompson EW, Newgreen DF (2005) The fallacy of epithelial mesenchymal transition in neoplasia. Cancer Res 65:5996–6000

64. Christofori G (2006) New signals from the invasive front. Nature 441:444–50

65. Lee JM, Dedhar S, Kalluri R, Thompson EW (2006) The epithelial-mesenchymal transition: new insights in signaling, development, and disease. J Cell Biol 172:973–81

66. Klymkowsky MW, Savagner P (2009) Epithelial-mesenchymal transition: a cancer researcher's conceptual friend and foe. Am J Pathol 174:1588–93

67. Thomson S, Petti F, Sujka-Kwok I, Mercado P, Bean J, Monaghan M, Seymour SL, Argast GM, Epstein DM, Haley JD (2011) A systems view of epithelial-mesenchymal transition signaling states. Clin Exp Metastasis 28:137–55

68. Friedl P, Wolf K (2003) Tumour-cell invasion and migration: diversity and escape mechanisms. Nat Rev Cancer 3:362–74

69. Friedl P, Wolf K (2010) Plasticity of cell migration: a multiscale tuning model. J Cell Biol 188:11–9

70. Nelson CM, Khauv D, Bissell MJ, Radisky DC (2008) Change in cell shape is required for MMP-induced EMT of mammary epithelial cells. J Cell Biochem 105:25–33

71. Gomez EW, Chen QK, Gjorevski N, Nelson CM (2010) Tissue geometry patterns epithelial-mesenchymal transition via intercellular mechanotransduction. J Cell Biochem 110:44–51

72. Ryan MC, Lee K, Miyashita Y, Carter WG (1999) Targeted disruption of the LAMA3 gene in mice reveals abnormalities in survival and late stage differentiation of epithelial cells. J Cell Biol 145:1309–23

73. Coopman PJ, Do MTH, Thompson EW, Mueller SC (1998) Phagocytosis of cross-linked gelatin matrix by human breast carcinoma cells correlates with their invasive capacity. Clin Cancer Res 4:507–15

74. Chen W-T (1989) Proteolytic activity of specialized surface protrusions formed at rosette contact sites of transformed cells. J Exp Zool 251:167–85

75. Kelly T, Yan Y, Osborne RL, Athota AB, Rozypal TL, Colclasure JC, Chu WS (1998) Proteolysis of extracellular matrix by invadopodia facilitates human breast cancer cell invasion and is mediated by matrix metalloproteinases. Clin Exp Metastasis 16:501–12

76. Wang W, Wyckoff JB, Frohlich VC, et al (2002) Single cell behavior in metastatic primary mammary tumors correlated with gene expression patterns revealed by molecular profiling. Cancer Res 62:6278–88

77. Yamaguchi H, Lorenz M, Kempiak S, et al (2005) Molecular mechanisms of invadopodium formation: the role of the N-WASP-Arp2/3 complex pathway and cofilin. J Cell Biol 168:441–52

78. Weaver AM (2006) Invadopodia: specialized cell structures for cancer invasion. Clin Exp Metastasis 23:97–105

79. Stylli SS, Kaye AH, Lock P (2008) Invadopodia: at the cutting edge of tumour invasion. J Clin Neurosci 15:725–37

80. Alexander NR, Branch KM, Parekh A, Clark ES, Iwueke IC, Guelcher SA, Weaver AM (2008) Extracellular matrix rigidity promotes invadopodia activity. Curr Biol 18:1295–9

81. Paszek MJ, Zahir N, Johnson KR, et al (2005) Tensional homeostasis and the malignant phenotype. Cancer Cell 8:241–54

82. Provenzano PP, Inman DR, Eliceiri KW, Knittel JG, Yan L, Rueden CT, White JG, Keely PJ (2008) Collagen density promotes mammary tumor initiation and progression. BMC Med 6:11

83. Schedin P, Keely PJ (2010) Mammary gland ECM remodeling, stiffness, and mechanosignaling in normal development and tumor progression. Cold Spring Harb Perspect Biol 3:a003228

84. Oser M, Eddy R, Condeelis J (2010) Actin-based motile processes in tumor cell invasion. In: Carlier M-F (ed) Actin-based Motil. Springer Netherlands, pp 125–64

85. Fraley SI, Feng Y, Krishnamurthy R, Kim D, Celedon A, Longmore GD, Wirtz D (2010) A distinctive role for focal adhesion proteins in three-dimensional cell motility. Nat Cell Biol 12:598–604

86. Dikovsky D, Bianco-Peled H, Seliktar D (2008) Defining the role of matrix compliance and proteolysis in three-dimensional cell spreading and remodeling. Biophys J 94:2914–25

87. Kikuchi K, Takahashi K (2008) WAVE2- and microtubule-dependent formation of long protrusions and invasion of cancer cells cultured on three-dimensional extracellular matrices. Cancer Sci 99:2252–9

88. Schoumacher M, Goldman RD, Louvard D, Vignjevic DM (2010) Actin, microtubules, and vimentin intermediate filaments cooperate for elongation of invadopodia. J Cell Biol 189:541–56

89. Hall A (1998) Rho GTPases and the actin cytoskeleton. Science 279:509–14

90. Yamaguchi H, Condeelis J (2007) Regulation of the actin cytoskeleton in cancer cell migration and invasion. Biochim Biophys Acta 1773:642–52

91. Olson MF, Sahai E (2009) The actin cytoskeleton in cancer cell motility. Clin Exp Metastasis 26:273–87

92. Parri M, Chiarugi P (2010) Rac and Rho GTPases in cancer cell motility control. Cell Commun Signal 8:1–14

93. Nakahara H, Otani T, Sasaki T, Miura Y, Takai Y, Kogo M (2003) Involvement of Cdc42 and Rac small G proteins in invadopodia formation of RPMI7951 cells. Genes Cells 8:1019–27

94. Ada-Nguema AS, Xenias H, Hofman JM, Wiggins CH, Sheetz MP, Keely PJ (2006) The small GTPase R-Ras regulates organization of actin and drives membrane protrusions through the activity of PLC-epsilon. J Cell Sci 119:1307–19

95. Sanz-Moreno V, Gadea G, Ahn J, Paterson H, Marra P, Pinner S, Sahai E, Marshall CJ (2008) Rac activation and inactivation control plasticity of tumor cell movement. Cell 135:510–23

96. Yamazaki D, Kurisu S, Takenawa T (2009) Involvement of Rac and Rho signaling in cancer cell motility in 3D substrates. Oncogene 28:1570–83

97. Cai Y, Biais N, Giannone G, et al (2006) Nonmuscle myosin IIA-dependent force inhibits cell spreading and drives F-actin flow. Biophys J 91:3907–20

98. Shankar J, Messenberg A, Chan J, Underhill TM, Foster LJ, Nabi IR (2010) Pseudopodial actin dynamics control epithelial-mesenchymal transition in metastatic cancer cells. Cancer Res 70:3780–90

99. Vial E, Sahai E, Marshall CJ (2003) ERK-MAPK signaling coordinately regulates activity of Rac1 and RhoA for tumor cell motility. Cancer Cell 4:67–79

100. Geiger B, Bershadsky A, Pankov R, Yamada KM (2001) Transmembrane extracellular matrix-cytoskeleton crosstalk. Nat Rev Mol Cell Bio 2:793–805

101. Mercurio AM, Rabinovitz I (2001) Towards a mechanistic understanding of tumor invasion - lessons from the alpha6/beta4 integrin. Semin Cancer Biol 11:129–41

102. Guo W, Giancotti FG (2004) Integrin signalling during tumour progression. Nat Rev Mol Cell Bio 5:816–26

103. White DE, Kurpios NA, Zuo D, Hassell JA, Blaess S, Mueller U, Muller WJ (2004) Targeted disruption of beta1-integrin in a transgenic mouse model of human breast cancer reveals an essential role in mammary tumor induction. Cancer Cell 6:159–70

104. Liu H, Radisky DC, Wang F, Bissell MJ (2004) Polarity and proliferation are controlled by distinct signaling pathways downstream of PI3-kinase in breast epithelial tumor cells. J Cell Biol 164:603–12

105. Provenzano PP, Inman DR, Eliceiri KW, Keely PJ (2009) Matrix density-induced mechanoregulation of breast cell phenotype, signaling and gene expression through a FAK-ERK linkage. Oncogene 28:4326–43

106. Levental KR, Yu H, Kass L, et al (2009) Matrix crosslinking forces tumor progression by enhancing integrin signaling. Cell 139:891–906

107. Clarke M, Spudich JA (1977) Nonmuscle contractile proteins: the role of actin and myosin in cell motility and shape determination. Annu Rev Biochem 46:797–822

108. Totsukawa G, Yamakita Y, Yamashiro S, Hartshorne DJ, Sasaki Y, Matsumura F (2000) Distinct roles of ROCK (Rho-kinase) and MLCK in spatial regulation of MLC phosphorylation for assembly of stress fibers and focal adhesions in 3T3 fibroblasts. J Cell Biol 150:797–806

109. Amano M, Ito M, Kimura K, Fukata Y, Chihara K, Nakano T, Matsuura Y, Kaibuchi K (1996) Phosphorylation and activation of myosin by Rho-associated kinase (Rho-kinase). J Biol Chem 271:20246–9

110. Kawano Y, Fukata Y, Oshiro N, Amano M, Nakamura T, Ito M, Matsumura F, Inagaki M, Kaibuchi K (1999) Phosphorylation of myosin-binding subunit (MBS) of myosin phosphatase by Rho-kinase in vivo. J Cell Biol 147:1023–37

111. Vega FM, Fruhwirth G, Ng T, Ridley AJ (2011) RhoA and RhoC have distinct roles in migration and invasion by acting through different targets. J Cell Biol 193:655–65

112. Fritz G, Just I, Kaina B (1999) Rho GTPases are over-expressed in human tumors. Int J Cancer 81:682–7

113. Sahai E, Marshall CJ (2002) Rho-GTPases and cancer. Nat Rev Cancer 2:133–42

114. Schlaepfer DD, Hauck CR, Sieg DJ (1999) Signaling through focal adhesion kinase. Prog Biophys Mol Bio 71:435–78

115. Klemke RL, Cai S, Giannini AL, Gallagher PJ, de Lanerolle P, Cheresh DA (1997) Regulation of cell motility by mitogen-activated protein kinase. J Cell Biol 137:481–92

116. Webb DJ, Donais K, Whitmore LA, Thomas SM, Turner CE, Parsons JT, Horwitz AF (2004) FAK-Src signalling through paxillin, ERK and MLCK regulates adhesion disassembly. Nat Cell Biol 6:154–61

117. Helfman DM, Pawlak G (2005) Myosin light chain kinase and acto-myosin contractility modulate activation of the ERK cascade downstream of oncogenic Ras. J Cell Biochem 95:1069–80

118. Bhadriraju K, Yang M, Ruiz SA, Pirone D, Tan J, Chen CS (2007) Activation of ROCK by RhoA is regulated by cell adhesion, shape, and cytoskeletal tension. Exp Cell Res 313:3616–23

119. Jaalouk DE, Lammerding J (2009) Mechanotransduction gone awry. Nat Rev Mol Cell Bio 10:63–73

120. Wozniak MA, Chen CS (2009) Mechanotransduction in development: a growing role for contractility. Nat Rev Mol Cell Bio 10:34–43

121. Discher DE, Janmey P, Wang Y-L (2005) Tissue cells feel and respond to the stiffness of their substrate. Science 310:1139–43

122. Wozniak MA, Desai R, Solski PA, Der CJ, Keely PJ (2003) ROCK-generated contractility regulates breast epithelial cell differentiation in response to the

physical properties of a three-dimensional collagen matrix. J Cell Biol 163:583–95

123. Polte TR, Eichler GS, Wang N, Ingber DE (2004) Extracellular matrix controls myosin light chain phosphorylation and cell contractility through modulation of cell shape and cytoskeletal prestress. Am J Physiol - Cell Ph 286:C518–28

124. Yeung T, Georges PC, Flanagan LA, Marg B, Ortiz M, Funaki M, Zahir N, Ming W, Weaver V, Janmey PA (2005) Effects of substrate stiffness on cell morphology, cytoskeletal structure, and adhesion. Cell Motil Cytoskel 60:24–34

125. Giannone G, Sheetz MP (2006) Substrate rigidity and force define form through tyrosine phosphatase and kinase pathways. Trends Cell Biol 16:213–23

126. Peyton SR, Ghajar CM, Khatiwala CB, Putnam AJ (2007) The emergence of ECM mechanics and cytoskeletal tension as important regulators of cell function. Cell Biochem Biophys 47:300–20

127. Buxboim A, Ivanovska IL, Discher DE (2010) Matrix elasticity, cytoskeletal forces and physics of the nucleus: how deeply do cells "feel" outside and in? J Cell Sci 123:297–308

128. Provenzano PP, Keely PJ (2011) Mechanical signaling through the cytoskeleton regulates cell proliferation by coordinated focal adhesion and Rho GTPase signaling. J Cell Sci 124:1195–205

129. Kraning-Rush CM, Carey SP, Califano JP, Smith BN, Reinhart-King CA (2011) The role of the cytoskeleton in cellular force generation in 2D and 3D environments. Phys Biol 8:015009

130. Wang N, Ingber DE (1994) Control of cytoskeletal mechanics by extracellular matrix, cell shape, and mechanical tension. Biophys J 66:2181–9

131. Döbereiner H-G, Dubin-Thaler BJ, Giannone G, Sheetz MP (2005) Force sensing and generation in cell phases: analyses of complex functions. J Appl Physiol 98:1542–6

132. Laevsky G, Knecht DA (2003) Cross-linking of actin filaments by myosin II is a major contributor to cortical integrity and cell motility in restrictive environments. J Cell Sci 116:3761–70

133. Fischer RS, Gardel M, Ma X, Adelstein RS, Waterman CM (2009) Local cortical tension by myosin II guides 3D endothelial cell branching. Curr Biol 19:260–5

134. Wyckoff JB, Pinner SE, Gschmeissner S, Condeelis JS, Sahai E (2006) ROCK- and myosin-dependent matrix deformation enables protease-independent tumor-cell invasion in vivo. Curr Biol 16:1515–23

135. Guck J, Lautenschläger F, Paschke S, Beil M (2010) Critical review: cellular mechanobiology and amoeboid migration. Integr Biol 2:575–83

136. Dembo M, Wang Y-L (1999) Stresses at the cell-to-substrate interface during locomotion of fibroblasts. Biophys J 76:2307–16

137. Reinhart-King CA, Dembo M, Hammer DA (2003) Endothelial cell traction forces on RGD-derivatized polyacrylamide substrata. Langmuir 19:1573–9

138. Du Roure O, Saez A, Buguin A, Austin RH, Chavrier P, Silberzan P, Ladoux B (2005) Force mapping in epithelial cell migration. Proc Natl Acad Sci USA 102:2390–5

139. Califano JP, Reinhart-King CA (2010) Substrate stiffness and cell area predict cellular traction stresses in single cells and cells in contact. Cell Mol Bioeng 3:68–75

140. Gunzer M, Friedl P, Niggemann B, Brocker E-B, Kampgen E, Zanker KS (2000) Migration of dendritic cells within 3-D collagen lattices is dependent on tissue origin, state of maturation, and matrix structure and is maintained by proinflammatory cytokines. J Leukoc Biol 67:622–9

141. Mierke CT, Rösel D, Fabry B, Brábek J (2008) Contractile forces in tumor cell migration. Eur J Cell Biol 87:669–76

142. Meshel AS, Wei Q, Adelstein RS, Sheetz MP (2005) Basic mechanism of three-dimensional collagen fibre transport by fibroblasts. Nat Cell Biol 7:157–64

143. Petrie RJ, Doyle AD, Yamada KM (2009) Random versus directionally persistent cell migration. Nat Rev Mol Cell Bio 10:538–49

144. Carey SP, Starchenko A, McGregor AL, Reinhart-King CA (2013) Leading malignant cells initiate collective epithelial cell invasion in a three-dimensional heterotypic tumor spheroid model. Clin Exp Metastasis 30:615–30

145. Poincloux R, Collin O, Lizárraga F, Romao M, Debray M, Piel M, Chavrier P (2011) Contractility of the cell rear drives invasion of breast tumor cells in 3D matrigel. Proc Natl Acad Sci USA 108:1943–8

146. Oliver T, Dembo M, Jacobson K (1999) Separation of propulsive and adhesive traction stresses in locomoting keratocytes. J Cell Biol 145:589–604

147. Suresh S (2007) Biomechanics and biophysics of cancer cells. Acta Biomater 3:413–38

148. Fletcher DA, Mullins RD (2010) Cell mechanics and the cytoskeleton. Nature 463:485–92

149. Elson EL (1988) Cellular mechanics as an indicator of cytoskeletal structure and function. Annu Rev Biophys Bio 17:397–430

150. Stamenović D, Coughlin MF (1999) The role of prestress and architecture of the cytoskeleton and deformability of cytoskeletal filaments in mechanics of adherent cells: a quantitative analysis. J Theor Biol 201:63–74

151. Baker EL, Lu J, Yu D, Bonnecaze RT, Zaman MH (2010) Cancer cell stiffness: integrated roles of three-dimensional matrix stiffness and transforming potential. Biophys J 99:2048–57

152. Guck J, Schinkinger S, Lincoln B, et al (2005) Optical deformability as an inherent cell marker for testing malignant transformation and metastatic competence. Biophys J 88:3689–98

153. Cross SE, Jin Y-S, Rao J, Gimzewski JK (2007) Nanomechanical analysis of cells from cancer patients. Nat Nanotechnol 2:780–3

154. Ochalek T, Nordt FJ, Tullberg K, Variants MC, Burger MM (1988) Correlation between cell deformability and metastatic potential in B16-F1 melanoma cell variants. Cancer Res 48:5124–8

155. Lekka M, Laidler P, Gil D, Lekki J, Stachura Z, Hrynkiewicz AZ (1999) Elasticity of normal and cancerous human bladder cells studied by scanning force microscopy. Eur Biophys J 28:312–6

156. Beil M, Micoulet A, von Wichert G, et al (2003) Sphingosylphosphorylcholine regulates keratin network architecture and visco-elastic properties of human cancer cells. Nat Cell Biol 5:803–11

157. Swaminathan V, Mythreye K, O'Brien ET, Berchuck A, Blobe GC, Superfine R (2011) Mechanical stiffness grades metastatic potential in patient tumor cells and in cancer cell lines. Cancer Res 71:5075–80

158. Wolf K, Wu YI, Liu Y, Geiger J, Tam E, Overall C, Stack MS, Friedl P (2007) Multi-step pericellular proteolysis controls the transition from individual to collective cancer cell invasion. Nat Cell Biol 9:893–904

159. Farina KL, Wyckoff JB, Rivera J, Lee H, Segall JE, Condeelis JS, Jones JG (1998) Cell motility of tumor cells visualized in living intact primary tumors using green fluorescent protein. Cancer Res 58:2528–32

160. Wolf K, Müller R, Borgmann S, Bröcker E-B, Friedl P (2003) Amoeboid shape change and contact guidance: T-lymphocyte crawling through fibrillar collagen is independent of matrix remodeling by MMPs and other proteases. Blood 102:3262–9

161. Wolf K, Mazo I, Leung H, Engelke K, von Andrian UH, Deryugina EI, Strongin AY, Bröcker E-B, Friedl P (2003) Compensation mechanism in tumor cell migration: mesenchymal-amoeboid transition after blocking of pericellular proteolysis. J Cell Biol 160:267–77

162. Ilina O, Bakker G-J, Vasaturo A, Hoffman RM, Friedl P (2011) Two-photon laser-generated microtracks in 3D collagen lattices: principles of MMP-dependent and -independent collective cancer cell invasion. Phys Biol 8:015010

163. Guilak F, Tedrow JR, Burgkart R (2000) Viscoelastic properties of the cell nucleus. Biochem Bioph Res Co 269:781–6

164. Friedl P, Wolf K, Lammerding J (2011) Nuclear mechanics during cell migration. Curr Opin Cell Biol 23:55–64

165. Croft DR, Sahai E, Mavria G, Li S, Tsai J, Lee WMF, Marshall CJ, Olson MF (2004) Conditional ROCK activation in vivo induces tumor cell dissemination and angiogenesis. Cancer Res 64:8994–9001

166. Rösel D, Brábek J, Tolde O, et al (2008) Up-regulation of Rho/ROCK signaling in sarcoma cells drives invasion and increased generation of protrusive forces. Mol Cancer Res 6:1410–20

167. Panková K, Rösel D, Novotný M, Brábek J (2010) The molecular mechanisms of transition between mesenchymal and amoeboid invasiveness in tumor cells. Cell Mol Life Sci 67:63–71

168. Butcher DT, Alliston T, Weaver VM (2009) A tense situation: forcing tumour progression. Nat Rev Cancer 9:108–22

169. Ulrich TA, de Juan Pardo EM, Kumar S (2009) The mechanical rigidity of the extracellular matrix regulates the structure, motility, and proliferation of glioma cells. Cancer Res 69:4167–74

170. Bergamaschi A, Tagliabue E, Sørlie T, et al (2008) Extracellular matrix signature identifies breast cancer subgroups with different clinical outcome. J Pathol 214:357–67

171. Han X, Burke RM, Zettel ML, Tang P, Brown EB (2008) Second harmonic properties of tumor collagen: determining the structural relationship between reactive stroma and healthy stroma. Opt Express 16:1846–59

172. Kraning-Rush CM, Califano JP, Reinhart-King CA (2012) Cellular traction stresses increase with increasing metastatic potential. PLoS One 7:e32572

173. Pedersen JA, Swartz MA (2005) Mechanobiology in the third dimension. Ann Biomed Eng 33:1469–90

174. Pathak A, Kumar S (2011) Biophysical regulation of tumor cell invasion: moving beyond matrix stiffness. Integr Biol 3:267–78

175. Gelse K (2003) Collagens - structure, function, and biosynthesis. Adv Drug Deliv Rev 55:1531–46

176. Kuntz RM, Saltzman WM (1997) Neutrophil motility in extracellular matrix gels: mesh size and adhesion affect speed of migration. Biophys J 72:1472–80

177. O'Brien FJ, Harley BA, Yannas I V, Gibson LJ (2005) The effect of pore size on cell adhesion in collagen-GAG scaffolds. Biomaterials 26:433–41

178. Roeder BA, Kokini K, Robinson JP, Voytik-Harbin SL (2004) Local, three-dimensional strain measurements within largely deformed extracellular matrix constructs. J Biomech Eng-T ASME 126:699–708

179. Raub CB, Unruh J, Suresh V, Krasieva T, Lindmo T, Gratton E, Tromberg BJ, George SC (2008) Image correlation spectroscopy of multiphoton images correlates with collagen mechanical properties. Biophys J 94:2361–73

180. Roeder BA, Kokini K, Voytik-Harbin SL (2009) Fibril microstructure affects strain transmission within collagen extracellular matrices. J Biomech Eng 131:031004

181. Raub CB, Suresh V, Krasieva T, Lyubovitsky J, Mih JD, Putnam AJ, Tromberg BJ, George SC (2007) Noninvasive assessment of collagen gel microstructure and mechanics using multiphoton microscopy. Biophys J 92:2212–22

182. Sander EA, Stylianopoulos T, Tranquillo RT, Barocas VH (2009) Image-based multiscale modeling predicts tissue-level and network-level fiber reorganization

in stretched cell-compacted collagen gels. Proc Natl Acad Sci USA 106:17675–80

183. Yang YL, Kaufman LJ (2009) Rheology and confocal reflectance microscopy as probes of mechanical properties and structure during collagen and collagen/hyaluronan self-assembly. Biophys J 96:1566–85

184. Bailey JL, Critser PJ, Whittington C, Kuske JL, Yoder MC, Voytik-Harbin SL (2011) Collagen oligomers modulate physical and biological properties of three-dimensional self-assembled matrices. Biopolymers 95:77–93

185. Van Goethem E, Poincloux R, Gauffre F, Maridonneau-Parini I, Le Cabec V (2010) Matrix architecture dictates three-dimensional migration modes of human macrophages: differential involvement of proteases and podosome-like structures. J Immunol 184:1049–61

186. Hakkinen K, Harunaga J, Doyle AD, Yamada KM (2011) Direct comparison of the morphology, migration, cell adhesions, and actin of fibroblasts in four different three-dimensional extracellular matrices. Tissue Eng Part A 17:713–24

187. Pizzo AM, Kokini K, Vaughn LC, Waisner BZ, Voytik-Harbin SL (2005) Extracellular matrix (ECM) microstructural composition regulates local cell-ECM biomechanics and fundamental fibroblast behavior: a multidimensional perspective. J Appl Physiol 98:1909–21

188. Harjanto D, Maffei JS, Zaman MH (2011) Quantitative analysis of the effect of cancer invasiveness and collagen concentration on 3D matrix remodeling. PLoS One 6:e24891

189. Miron-Mendoza M, Seemann J, Grinnell F (2010) The differential regulation of cell motile activity through matrix stiffness and porosity in three dimensional collagen matrices. Biomaterials 31:6425–35

190. Baker EL, Srivastava J, Yu D, Bonnecaze RT, Zaman MH (2011) Cancer cell migration: integrated roles of matrix mechanics and transforming potential. PLoS One 6:e20355

191. Yang YL, Sun C, Wilhelm ME, Fox LJ, Zhu J, Kaufman LJ (2011) Influence of chondroitin sulfate and hyaluronic acid on structure, mechanical properties, and glioma invasion of collagen I gels. Biomaterials 32:7932–40

192. Ulrich TA, Jain A, Tanner K, MacKay JL, Kumar S (2010) Probing cellular mechanobiology in three-dimensional culture with collagen-agarose matrices. Biomaterials 31:1875–84

193. Gobeaux F, Mosser G, Anglo A, Panine P, Davidson P, Giraud-Guille M, Belamie E (2008) Fibrillogenesis in dense collagen solutions: a physicochemical study. J Mol Biol 376:1509–22

194. Yang YL, Motte S, Kaufman LJ (2010) Pore size variable type I collagen gels and their interaction with glioma cells. Biomaterials 31:5678–88

195. Williams RM, Ellenson LH, Connolly DC, Hamilton TC, Nikitin AY, Zipfel WR, Flesken-Nikitin A (2010) Strategies for high-resolution imaging of epithelial ovarian cancer by laparoscopic nonlinear microscopy. Transl Oncol 3:181–94

196. Petersen NO, Höddelius PL, Wiseman PW, Seger O, Magnusson KE (1993) Quantitation of membrane receptor distributions by image correlation spectroscopy: concept and application. Biophys J 65:1135–46

197. Hotary KB, Allen ED, Brooks PC, Datta NS, Long MW, Weiss SJ (2003) Membrane type I matrix metalloproteinase usurps tumor growth control imposed by the three-dimensional extracellular matrix. Cell 114:33–45

198. Ridley AJ, Schwartz MA, Burridge K, Firtel RA, Ginsberg MH, Borisy G, Parsons JT, Horwitz AR (2003) Cell migration: integrating signals from front to back. Science 302:1704–9

199. Iden S, Collard JG (2008) Crosstalk between small GTPases and polarity proteins in cell polarization. Nat Rev Mol Cell Bio 9:846–59

200. Bordeleau F, Tang LN, Reinhart-King CA (2013) Topographical guidance of 3D tumor cell migration at an interface of collagen densities. Phys Biol 10:065004

201. Sundararaghavan HG, Masand SN, Shreiber DI (2011) Microfluidic generation of haptotactic gradients through 3D collagen gels for enhanced neurite growth. J Neurotrauma 28:2377–87

202. Hadjipanayi E, Mudera V, Brown RA (2009) Guiding cell migration in 3D: A collagen matrix with graded directional stiffness. Cell Motil Cytoskeleton 66:121–8

203. Dickinson RB, Guido S, Tranquillo RT (1994) Biased cell migration of fibroblasts exhibiting contact guidance in oriented collagen gels. Ann Biomed Eng 22:342–56

204. Beerling E, Ritsma L, Vrisekoop N, Derksen PWB, van Rheenen J (2011) Intravital microscopy: new insights into metastasis of tumors. J Cell Sci 124:299–310

205. Kim A, Lakshman N, Petroll WM (2006) Quantitative assessment of local collagen matrix remodeling in 3-D culture: the role of Rho kinase. Exp Cell Res 312:3683–92

206. Brownfield DG, Venugopalan G, Lo A, Mori H, Tanner K, Fletcher DA, Bissell MJ (2013) Patterned collagen fibers orient branching mammary epithelium through distinct signaling modules. Curr Biol 23:703–9

207. Shi Q, Ghosh RP, Engelke H, Rycroft CH, Cassereau L, Sethian JA, Weaver VM, Liphardt JT (2014) Rapid disorganization of mechanically interacting systems of mammary acini. Proc Natl Acad Sci U S A 111:658–63

208. Gaggioli C, Hooper S, Hidalgo-Carcedo C, Grosse R, Marshall JF, Harrington K, Sahai E (2007) Fibroblast-led collective invasion of carcinoma cells with differing roles for RhoGTPases in leading and following cells. Nat Cell Biol 9:1392–400

209. Riching KM, Cox BL, Salick MR, et al (2014) 3D Collagen Alignment Limits Protrusions to Enhance Breast Cancer Cell Persistence. Biophys J 107:2546–2558

210. Tranquillo RT, Durrani MA, Moon AG (1992) Tissue engineering science: consequences of cell traction force. Cytotechnology 10:225–50

211. Weiss P (1934) In vitro experiments on the factors determining the course of the outgrowing nerve fiber. J Exp Zool 68:393–448

212. Deome KB, Faulkin LJ, Bern HA, Blair PB (1959) Development of mammary tumors from hyperplastic alveolar nodules transplanted into gland-free mammary fat pads of female C3H mice. Cancer Res 19:515–20

213. Guo C, Kaufman LJ (2007) Flow and magnetic field induced collagen alignment. Biomaterials 28:1105–14

214. Kubow KE, Conrad SK, Horwitz AR (2013) Matrix microarchitecture and myosin II determine adhesion in 3D matrices. Curr Biol 23:1607–19

215. Dubin-Thaler BJ, Hofman JM, Cai Y, Xenias H, Spielman I, Shneidman A V., David LA, Döbereiner HG, Wiggins CH, Sheetz MP (2008) Quantification of cell edge velocities and traction forces reveals distinct motility modules during cell spreading. PLoS One 3:e3735

216. Giannone G, Dubin-Thaler BJ, Döbereiner HG, Kieffer N, Bresnick AR, Sheetz MP (2004) Periodic lamellipodial contractions correlate with rearward actin waves. Cell 116:431–43

217. Cukierman E, Pankov R, Stevens DR, Yamada KM (2001) Taking cell-matrix adhesions to the third dimension. Science 294:1708–12

218. Huveneers S, Danen EHJ (2009) Adhesion signaling - crosstalk between integrins, Src and Rho. J Cell Sci 122:1059–69

219. Dunn GA, Ebendal T (1978) Contact guidance on oriented collagen gels. Exp Cell Res 111:475–9

220. Etienne-Manneville S (2008) Polarity proteins in migration and invasion. Oncogene 27:6970–80

221. Wang F (2009) The signaling mechanisms underlying cell polarity and chemotaxis. Cold Spring Harb Perspect Biol 1:1–16

222. Welch HCE, Coadwell WJ, Stephens LR, Hawkins PT (2003) Phosphoinositide 3-kinase-dependent activation of Rac. FEBS Lett 546:93–7

223. Polacheck WJ, German AE, Mammoto A, Ingber DE, Kamm RD (2014) Mechanotransduction of fluid stresses governs 3D cell migration. Proc Natl Acad Sci 111:2447–52

224. Jokinen J, Dadu E, Nykvist P, et al (2004) Integrin-mediated cell adhesion to type I collagen fibrils. J Biol Chem 279:31956–63

225. Albuschies J, Vogel V (2013) The role of filopodia in the recognition of nanotopographies. Sci Reports 3:1658

226. Price LS, Leng J, Schwartz MA, Bokoch GM (1998) Activation of Rac and Cdc42 by integrins mediates cell spreading. Mol Biol Cell 9:1863–71

227. Guillou H, Depraz-Depland A, Planus E, Vianay B, Chaussy J, Grichine A, Albigès-Rizo C, Block MR (2008) Lamellipodia nucleation by filopodia depends on integrin occupancy and downstream Rac1 signaling. Exp Cell Res 314:478–88

228. Shibue T, Brooks MW, Fatih Inan M, Reinhardt F, Weinberg RA (2012) The outgrowth of micrometastases is enabled by the formation of filopodium-like protrusions. Cancer Discov 2:706–21

229. Willis AL, Sabeh F, Li X-Y, Weiss SJ (2013) Extracellular matrix determinants and the regulation of cancer cell invasion stratagems. J Microsc 251:250–60

230. Bloom RJ, George JP, Celedon A, Sun SX, Wirtz D (2008) Mapping local matrix remodeling induced by a migrating tumor cell using three-dimensional multiple-particle tracking. Biophys J 95:4077–88

231. Snijder B, Pelkmans L (2011) Origins of regulated cell-to-cell variability. Nat Rev Mol Cell Biol 12:119–25

232. Machacek M, Hodgson L, Welch C, Elliott H, Pertz O, Nalbant P, Abell A, Johnson GL, Hahn KM, Danuser G (2009) Coordination of Rho GTPase activities during cell protrusion. Nature 461:99–103

233. Wu P-H, Giri A, Sun SX, Wirtz D (2014) Three-dimensional cell migration does not follow a random walk. Proc Natl Acad Sci U S A 111:3949–54

234. Schwarz US, Gardel ML (2012) United we stand - integrating the actin cytoskeleton and cell-matrix adhesions in cellular mechanotransduction. J Cell Sci 125:3051–60

235. Fidler IJ (1978) Tumor heterogeneity and the biology of cancer invasion and metastasis. Cancer Res 38:2651–60

236. Friedl P, Wolf K (2010) Plasticity of cell migration: a multiscale tuning model. J Cell Biol 188:11–9

237. Wolf K, Friedl P (2011) Extracellular matrix determinants of proteolytic and non-proteolytic cell migration. Trends Cell Biol 21:736–44

238. Sabeh F, Shimizu-Hirota R, Weiss SJ (2009) Protease-dependent versus - independent cancer cell invasion programs: three-dimensional amoeboid movement revisited. J Cell Biol 185:11–9

239. Fisher KE, Sacharidou A, Stratman AN, Mayo AM, Fisher SB, Mahan RD, Davis MJ, Davis GE (2009) MT1-MMP- and Cdc42-dependent signaling co-regulate cell invasion and tunnel formation in 3D collagen matrices. J Cell Sci 122:4558–69

240. Alcoser TA, Bordeleau F, Carey SP, Lampi MC, Kowal DR, Somasegar S, Varma S, Shin SJ, Reinhart-King CA (2015) Probing the biophysical properties of primary breast tumor-derived fibroblasts. Cell Mol Bioeng 8:76–85

241. Friedl P, Wolf K (2008) Tube travel: the role of proteases in individual and collective cancer cell invasion. Cancer Res 68:7247–9

242. Balzer EM, Tong Z, Paul CD, Hung W-C, Stroka KM, Boggs AE, Martin SS, Konstantopoulos K (2012) Physical confinement alters tumor cell adhesion and migration phenotypes. FASEB J 26:4045–56

243. Pathak A, Kumar S (2012) Independent regulation of tumor cell migration by matrix stiffness and confinement. Proc Natl Acad Sci 109:10334–9

244. Flesken-Nikitin A, Williams RM, Zipfel WR, Webb WW, Nikitin AY (2005) Use of multiphoton imaging for studying cell migration in the mouse. Methods Mol Biol 294:335–45

245. Zipfel WR, Williams RM, Webb WW (2003) Nonlinear magic: multiphoton microscopy in the biosciences. Nat Biotechnol 21:1369–77

246. Kraning-Rush CM, Carey SP, Califano JP, Reinhart-King CA (2012) Quantifying traction stresses in adherent cells. In: Asthagiri AR, Arkin A (eds) Methods Cell Biol, 110th ed. Elsevier Inc., pp 139–78

247. Friedl P (2004) Dynamic imaging of cellular interactions with extracellular matrix. Histochem Cell Biol 122:183–90

248. Etienne-Manneville S (2004) Actin and microtubules in cell motility: which one is in control? Traffic 5:470–7

249. Maller O, Hansen KC, Lyons TR, Acerbi I, Weaver VM, Prekeris R, Tan A-C, Schedin P (2013) Collagen architecture in pregnancy-induced protection from breast cancer. J Cell Sci 126:4108–20

250. Guiet R, Van Goethem E, Cougoule C, Balor S, Valette A, Al Saati T, Lowell CA, Le Cabec V, Maridonneau-Parini I (2011) The process of macrophage migration promotes matrix metalloproteinase-independent invasion by tumor cells. J Immunol 187:3806–14

251. Cox TR, Erler JT (2011) Remodeling and homeostasis of the extracellular matrix: implications for fibrotic diseases and cancer. Dis Model Mech 4:165–78

252. Palecek S, Loftus J, Ginsberg MH, Lauffenburger DA, Horwitz AF (1997) Integrin-ligand binding properties govern cell migration speed through cell-substratum adhesiveness. Nature 385:537–40

253. Zaman MH, Kamm RD, Matsudaira P, Lauffenburger DA (2005) Computational model for cell migration in three-dimensional matrices. Biophys J 89:1389–97

254. Berrier AL (2002) The integrin beta tail is required and sufficient to regulate adhesion signaling to Rac1. J Cell Sci 115:4285–91

255. Fischer RS, Gardel M, Ma X, Adelstein RS, Waterman CM (2009) Local cortical tension by myosin II guides 3D endothelial cell branching. Curr Biol 19:260–5

256. Morin TR, Ghassem-Zadeh SA, Lee J (2014) Traction force microscopy in rapidly moving cells reveals separate roles for ROCK and MLCK in the mechanics of retraction. Exp Cell Res 326:280–94

257. Vicente-Manzanares M, Koach MA, Whitmore L, Lamers ML, Horwitz AF (2008) Segregation and activation of myosin IIB creates a rear in migrating cells. J Cell Biol 183:543–54

258. Petersen OW, Lind Nielsen H, Gudjonsson T, Villadsen R, Rønnov-Jessen L, Bissell MJ (2001) The plasticity of human breast carcinoma cells is more than epithelial to mesenchymal conversion. Breast Cancer Res 3:213–7

259. Sahai E, Marshall CJ (2003) Differing modes of tumour cell invasion have distinct requirements for Rho/ROCK signalling and extracellular proteolysis. Nat Cell Biol 5:711–719

260. Stroka KM, Jiang H, Chen S-H, Tong Z, Wirtz D, Sun SX, Konstantopoulos K (2014) Water permeation drives tumor cell migration in confined microenvironments. Cell 157:611–23

261. Hawkins RJ, Piel M, Joanny JF, Prost J (2009) Pushing off the walls: a mechanism of cell motility in confinement. Phys Rev Lett 102:058103

262. Bissell MJ, Radisky D (2001) Putting tumours in context. Nat Rev Cancer 1:46–54

263. Marusyk A, Polyak K (2010) Tumor heterogeneity: causes and consequences. Biochim Biophys Acta 1805:105–17

264. Dong-Le Bourhis X, Berthois Y, Millot G, Degeorges A, Sylvi M, Martin P-M, Calvo F (1997) Effect of stromal and epithelial cells derived from normal and tumorous breast tissue on the proliferation of human breast cancer cell lines in co-culture. Int J Cancer 71:42–8

265. Guo X, Oshima H, Kitmura T, Taketo MM, Oshima M (2008) Stromal fibroblasts activated by tumor cells promote angiogenesis in mouse gastric cancer. J Biol Chem 283:19864–71

266. Jones JL, Shaw JA, Pringle JH, Walker RA (2003) Primary breast myoepithelial cells exert an invasion-suppressor effect on breast cancer cells via paracrine down-regulation of MMP expression in fibroblasts and tumour cells. J Pathol 201:562–72

267. Goswami S, Sahai E, Wyckoff JB, Cammer M, Cox D, Pixley FJ, Stanley ER, Segall JE, Condeelis JS (2005) Macrophages promote the invasion of breast carcinoma cells via a colony-stimulating factor-1/epidermal growth factor paracrine loop. Cancer Res 65:5278–5283

268. Gerlinger M, Rowan A, Horswell S, et al (2012) Intratumor heterogeneity and branched evolution revealed by multiregion sequencing. N Engl J Med 366:883–982

269. Weiss L (2000) Heterogeneity of cancer cell populations and metastasis. Cancer Metastasis Rev 19:345

270. Sabeh F, Ota I, Holmbeck K, et al (2004) Tumor cell traffic through the extracellular matrix is controlled by the membrane-anchored collagenase MT1-MMP. J Cell Biol 167:769–81

271. Friedl P, Locker J, Sahai E, Segall JE (2012) Classifying collective cancer cell invasion. Nat Cell Biol 14:777–83

272. Pampaloni F, Reynaud EG, Stelzer EHK (2007) The third dimension bridges the gap between cell culture and live tissue. Nat Rev Mol Cell Bio 8:839–45

273. Burdett E, Kasper FK, Mikos AG, Ludwig JA (2010) Engineering tumors: a tissue engineering perspective in cancer biology. Tissue Eng Part B Rev 16:351–9

274. Gumbiner BM (2005) Regulation of cadherin-mediated adhesion in morphogenesis. Nat Rev Mol Cell Bio 6:622–34

275. Lorenzo C, Frongia C, Jorand R, Fehrenbach J, Weiss P, Maandhui A, Gay G, Ducommun B, Lobjois V (2011) Live cell division dynamics monitoring in 3D large spheroid tumor models using light sheet microscopy. Cell Div 6:22

276. Pickl M, Ries CH (2009) Comparison of 3D and 2D tumor models reveals enhanced HER2 activation in 3D associated with an increased response to trastuzumab. Oncogene 28:461–8

277. Rezakhaniha R, Agianniotis A, Schrauwen J, Griffa A, Sage D, Bouten C, van de Vosse F, Unser M, Stergiopulos N (2012) Experimental investigation of

collagen waviness and orientation in the arterial adventitia using confocal laser scanning microscopy. Biomech Model Mechanobiol 11:461–73

278. Wolman SR (1986) Cytogenetic heterogeneity: its role in tumor evolution. Cancer Genet Cytogenet 19:129–40

279. Nowell PC (1976) The clonal evolution of tumor cell populations. Science 194:23–8

280. Aubele M, Mattis A, Zitzelsberger H, Walch A, Kremer M, Hutzler P, Höfler H, Werner M (1999) Intratumoral heterogeneity in breast carcinoma revealed by laser-microdissection and comparative genomic hybridization. Cancer Genet Cytogenet 110:94–102

281. Keller PJ, Lin AF, Arendt LM, et al (2010) Mapping the cellular and molecular heterogeneity of normal and malignant breast tissues and cultured cell lines. Breast Cancer Res 12:R87

282. Debnath J, Muthuswamy SK, Brugge JS (2003) Morphogenesis and oncogenesis of MCF-10A mammary epithelial acini grown in three-dimensional basement membrane cultures. Methods 30:256–68

283. Soule HD, Maloney TM, Wolman SR, Peterson WD, Brenz R, McGrath CM, Russo J, Pauley RJ, Jones RF, Brooks SC (1990) Isolation and characterization of a spontaneously immortalized human breast epithelial cell line, MCF-10. Cancer Res 50:6075–86

284. Santner S, Dawson P, Tait L, Soule H, Eliason J, Mohamed A, Wolman S, Heppner G, Miller F (2001) Malignant MCF10CA1 cell lines derived from premalignant human breast epithelial MCF10AT cells. Breast Cancer Res Treat 65:101–10

285. Ivascu A, Kubbies M (2007) Diversity of cell-mediated adhesions in breast cancer spheroids. Int J Oncol 31:1403–13

286. Foty RA, Steinberg MS (2004) Cadherin-mediated cell-cell adhesion and tissue segregation in relation to malignancy. Int J Dev Biol 48:397–409

287. Foty RA, Steinberg MS (2005) The differential adhesion hypothesis: a direct evaluation. Dev Biol 278:255–63

288. Vamvakidou AP, Mondrinos MJ, Petushi SP, Garcia FU, Lelkes PI, Tozeren A (2007) Heterogeneous breast tumoroids: an in vitro assay for investigating cellular heterogeneity and drug delivery. J Biomol Screen 12:13–20

289. Chanson L, Brown D, Garbe JC, Kuhn I, Stampfer MR, Bissell MJ, Brownfield D, LaBarge MA (2011) Self-organization is a dynamic and lineage-intrinsic property of mammary epithelial cells. Proc Natl Acad Sci USA 108:3264–9

290. Hirschhaeuser F, Menne H, Dittfeld C, West J, Mueller-Klieser W, Kunz-Schughart LA (2010) Multicellular tumor spheroids: an underestimated tool is catching up again. J Biotechnol 148:3–15

291. Sarrió D, Rodriguez-Pinilla SM, Hardisson D, Cano A, Moreno-Bueno G, Palacios J (2008) Epithelial-mesenchymal transition in breast cancer relates to the basal-like phenotype. Cancer Res 68:989–97

292. Wiercinska E, Naber HPH, Pardali E, van der Pluijm G, van Dam H, ten Dijke P (2011) The TGF-β/Smad pathway induces breast cancer cell invasion through the up-regulation of matrix metalloproteinase 2 and 9 in a spheroid invasion model system. Breast Cancer Res Treat 128:657–66

293. Debnath J, Mills KR, Collins NL, Reginato MJ, Muthuswamy SK, Brugge JS, Gudjonsson V (2002) The role of apoptosis in creating and maintaining luminal space within normal and oncogene-expressing mammary acini. Cell 111:29–40

294. Inaki M, Vishnu S, Cliffe A, Rørth P (2012) Effective guidance of collective migration based on differences in cell states. Proc Natl Acad Sci USA 109:2027–32

295. Khalil A, Friedl P (2010) Determinants of leader cells in collective cell migration. Integr Biol 2:568–74

296. Shieh AC, Rozansky HA, Hinz B, Swartz MA (2011) Tumor cell invasion is promoted by interstitial flow-induced matrix priming by stromal fibroblasts. Cancer Res 71:790–800

297. Friedl P, Maaser K, Klein CE, Niggemann B, Krohne G, Zänker KS (1997) Migration of highly aggressive MV3 melanoma cells in 3-dimensional collagen lattices results in local matrix reorganization and shedding of alpha2 and beta1 integrins and CD44. Cancer Res 57:2061–70

298. Gordon V, Valentine M, Gardel M, Andor-Ardo D, Dennison S, Bogdanov A, Weitz D, Deisboeck T (2003) Measuring the mechanical stress induced by an expanding multicellular tumor system: a case study. Exp Cell Res 289:58–66

299. De Smet F, Segura I, De Bock K, Hohensinner PJ, Carmeliet P (2009) Mechanisms of vessel branching: filopodia on endothelial tip cells lead the way. Arter Thromb Vasc Biol 29:639–49

300. Friedl P, Gilmour D (2009) Collective cell migration in morphogenesis, regeneration and cancer. Nat Rev Mol Cell Bio 10:445–57

301. Hu M, Yao J, Carroll DK, et al (2008) Regulation of in situ to invasive breast carcinoma transition. Cancer Cell 13:394–406

302. Brock A, Chang H, Huang S (2009) Non-genetic heterogeneity - a mutation-independent driving force for the somatic evolution of tumours. Nat Rev Genet 10:336–42

303. Yukinaga H, Shionyu C, Hirata E, Ui-Tei K, Nagashima T, Kondo S, Okada-Hatakeyama M, Naoki H, Matsuda M (2014) Fluctuation of Rac1 activity is associated with the phenotypic and transcriptional heterogeneity of glioma cells. J Cell Sci 127:1805–15

304. Liao D, Estévez-Salmerón L, Tlsty TD (2012) Generalized principles of stochasticity can be used to control dynamic heterogeneity. Phys Biol 9:065006

305. Singh DK, Ku C-J, Wichaidit C, Steininger RJ, Wu LF, Altschuler SJ (2010) Patterns of basal signaling heterogeneity can distinguish cellular populations with different drug sensitivities. Mol Syst Biol 6:369

306. Hughes L, Malone C, Chumsri S, Burger AM, McDonnell S (2008) Characterisation of breast cancer cell lines and establishment of a novel isogenic subclone to study migration, invasion and tumourigenicity. Clin Exp Metastasis 25:549–57

307. Fidler IJ, Kripke ML, Url S (1977) Metastasis results from preexisting variant cells within a malignant tumor. Science 197:893–5

308. Gulyani A, Vitriol E, Allen R, et al (2011) A biosensor generated via high-throughput screening quantifies cell edge Src dynamics. Nat Chem Biol 7:437–44

309. Meyer AS, Hughes-Alford SK, Kay JE, Castillo A, Wells A, Gertler FB, Lauffenburger DA (2012) 2D protrusion but not motility predicts growth factor-induced cancer cell migration in 3D collagen. J Cell Biol 197:721–9

310. Turner NC, Reis-Filho JS (2012) Genetic heterogeneity and cancer drug resistance. Lancet Oncol 13:e178–85

311. Roesch A, Fukunaga-Kalabis M, Schmidt EC, Zabierowski SE, Brafford PA, Vultur A, Basu D, Gimotty P, Vogt T, Herlyn M (2010) A temporarily distinct subpopulation of slow-cycling melanoma cells is required for continuous tumor growth. Cell 141:583–94

312. Chapman A, Fernandez del Ama L, Ferguson J, Kamarashev J, Wellbrock C, Hurlstone A (2014) Heterogeneous tumor subpopulations cooperate to drive invasion. Cell Rep 8:688–95

313. Bajikar SS, Fuchs C, Roller A, Theis FJ, Janes KA (2014) Parameterizing cell-to-cell regulatory heterogeneities via stochastic transcriptional profiles. Proc Natl Acad Sci U S A 111:E626–35

314. Spiller DG, Wood CD, Rand DA, White MRH (2010) Measurement of single-cell dynamics. Nature 465:736–45

315. Hughes AJ, Spelke DP, Xu Z, Kang C-C, Schaffer D V, Herr AE (2014) Single-cell western blotting. Nat Methods 11:749–55

316. Jiang T, Shi W, Natowicz R, Ononye SN, Wali VB, Kluger Y, Pusztai L, Hatzis C (2014) Statistical measures of transcriptional diversity capture genomic heterogeneity of cancer. BMC Genomics 15:876

317. Mierke CT, Frey B, Fellner M, Herrmann M, Fabry B (2011) Integrin α5β1 facilitates cancer cell invasion through enhanced contractile forces. J Cell Sci 124:369–83

318. Bajpai S, Mitchell MJ, King MR, Reinhart-King CA (2014) A microfluidic device to select for cells based on chemotactic phenotype. Technology 2:1–5

319. McDermott M, Eustace AJ, Busschots S, Breen L, Crown J, Clynes M, O'Donovan N, Stordal B (2014) In vitro development of chemotherapy and targeted therapy drug-resistant cancer cell lines: a practical guide with case studies. Front Oncol 4:40

320. Siegrist SE, Doe CQ (2007) Microtubule-induced cortical cell polarity. Genes Dev 21:483–96

321. Cho SY, Klemke RL (2002) Purification of pseudopodia from polarized cells reveals redistribution and activation of Rac through assembly of a CAS/Crk scaffold. J Cell Biol 156:725–36

322. Hsia DA, Mitra SK, Hauck CR, et al (2003) Differential regulation of cell motility and invasion by FAK. J Cell Biol 160:753–67

323. Borm B, Requardt RP, Herzog V, Kirfel G (2005) Membrane ruffles in cell migration: Indicators of inefficient lamellipodia adhesion and compartments of actin filament reorganization. Exp Cell Res 302:83–95

324. Mitra SK, Hanson DA, Schlaepfer DD (2005) Focal adhesion kinase: in command and control of cell motility. Nat Rev Mol Cell Biol 6:56–68

325. Gardel ML, Schneider IC, Aratyn-Schaus Y, Waterman CM (2010) Mechanical integration of actin and adhesion dynamics in cell migration. Annu Rev Cell Dev Biol 26:315–33

326. Raftopoulou M, Hall A (2004) Cell migration: Rho GTPases lead the way. Dev Biol 265:23–32

327. Beningo KA, Dembo M, Kaverina I, Small JV, Wang YL (2001) Nascent focal adhesions are responsible for the generation of strong propulsive forces in migrating fibroblasts. J Cell Biol 153:881–7

328. Shi H, Hugo W, Kong X, et al (2014) Acquired resistance and clonal evolution in melanoma during BRAF inhibitor therapy. Cancer Discov 4:80–93

329. Shackleton M, Quintana E, Fearon ER, Morrison SJ (2009) Heterogeneity in cancer: cancer stem cells versus clonal evolution. Cell 138:822–9

330. Burrell RA, Swanton C (2014) Tumour heterogeneity and the evolution of polyclonal drug resistance. Mol Oncol 8:1095–111

331. Kopfstein L, Christofori G (2006) Metastasis: cell-autonomous mechanisms versus contributions by the tumor microenvironment. Cell Mol Life Sci 63:449–68

332. Scott RW, Hooper S, Crighton D, et al (2010) LIM kinases are required for invasive path generation by tumor and tumor-associated stromal cells. J Cell Biol 191:169–85

333. Frantz C, Stewart KM, Weaver VM (2010) The extracellular matrix at a glance. J Cell Sci 123:4195–200

334. Williams CM, Engler AJ, Slone RD, Galante LL, Schwarzbauer JE (2008) Fibronectin expression modulates mammary epithelial cell proliferation during acinar differentiation. Cancer Res 68:3185–92

335. Plopper GE, Domanico SZ, Cirulli V, Kiosses WB, Quaranta V (1998) Migration of breast epithelial cells on laminin-5: differential role of integrins in normal and transformed cell types. Breast Cancer Res Treat

336. Streuli CH, Bailey N, Bissell MJ (1991) Control of mammary epithelial differentiation: basement membrane induces tissue-specific gene expression in

the absence of cell-cell interaction and morphological polarity. J Cell Biol 115:1383–95

337. Chaudhuri O, Koshy ST, Branco C, Shin J, Verbeke CS, Allison KH, Mooney DJ (2014) Extracellular matrix stiffness and composition jointly regulate the induction of malignant phenotypes in mammary epithelium. Nat Mater 13:970–8

338. Mori H, Lo AT, Inman JL, et al (2013) Transmembrane/cytoplasmic, rather than catalytic, domains of Mmp14 signal to MAPK activation and mammary branching morphogenesis via binding to integrin β1. Development 140:343–52

339. Shintani Y, Wheelock MJ, Johnson KR (2006) Phosphoinositide-3 Kinase–Rac1–c-Jun NH2-terminal Kinase signaling mediates collagen I–induced cell scattering and up-regulation of N-cadherin expression in mouse mammary epithelial cells. Mol Biol Cell 2963–75

340. Xu R, Boudreau A, Bissell MJ (2009) Tissue architecture and function: dynamic reciprocity via extra- and intra-cellular matrices. Cancer Metastasis Rev 28:167–76

341. Rooney N, Streuli CH (2011) How integrins control mammary epithelial differentiation: A possible role for the ILK-PINCH-Parvin complex. FEBS Lett 585:1663–72

342. Leight JL, Wozniak MA, Chen S, Lynch ML, Chen CS (2012) Matrix rigidity regulates a switch between TGF-β1-induced apoptosis and epithelial-mesenchymal transition. Mol Biol Cell 23:781–91

343. Wei SC, Fattet L, Tsai JH, et al (2015) Matrix stiffness drives epithelial–mesenchymal transition and tumour metastasis through a TWIST1–G3BP2 mechanotransduction pathway. Nat Cell Biol. doi: 10.1038/ncb3157

344. Zhang K, Corsa CA, Ponik SM, Prior JL, Piwnica-Worms D, Eliceiri KW, Keely PJ, Longmore GD (2013) The collagen receptor discoidin domain receptor 2 stabilizes SNAIL1 to facilitate breast cancer metastasis. Nat Cell Biol 15:677–87

345. Park J, Schwarzbauer JE (2014) Mammary epithelial cell interactions with fibronectin stimulate epithelial-mesenchymal transition. Oncogene 33:1649–57

346. Shintani Y, Maeda M, Chaika N, Johnson KR, Wheelock MJ (2008) Collagen I promotes epithelial-to-mesenchymal transition in lung cancer cells via transforming growth factor-β signaling. Am J Respir Cell Mol Biol 38:95–104

347. McGrail DJ, Mezencev R, Kieu QMN, McDonald JF, Dawson MR (2014) SNAIL-induced epithelial-to-mesenchymal transition produces concerted biophysical changes from altered cytoskeletal gene expression. FASEB J 29:1280–1289

348. Kim J-H, Asthagiri AR (2011) Matrix stiffening sensitizes epithelial cells to EGF and enables the loss of contact inhibition of proliferation. J Cell Sci 124:1280–7

349. Gudjonsson T, Rønnov-Jessen L, Villadsen R, Rank F, Bissell MJ, Petersen OW (2002) Normal and tumor-derived myoepithelial cells differ in their ability to interact with luminal breast epithelial cells for polarity and basement membrane deposition. J Cell Sci 115:39–50

350. O'Brien LE, Jou TS, Pollack AL, Zhang Q, Hansen SH, Yurchenco P, Mostov KE (2001) Rac1 orientates epithelial apical polarity through effects on basolateral laminin assembly. Nat Cell Biol 3:831–8

351. Godinho SA, Picone R, Burute M, Dagher R, Su Y, Leung CT, Polyak K, Brugge JS, Théry M, Pellman D (2014) Oncogene-like induction of cellular invasion from centrosome amplification. Nature 510:167–71

352. Barbolina M, Stack MS (2008) Membrane type 1-matrix metalloproteinase: substrate diversity in pericellular proteolysis. Semin Cell Dev Biol 19:24–33

353. Alcaraz J, Mori H, Ghajar CM, Brownfield D, Galgoczy R, Bissell MJ (2011) Collective epithelial cell invasion overcomes mechanical barriers of collagenous extracellular matrix by a narrow tube-like geometry and MMP14-dependent local softening. Integr Biol 3:1153–66

354. Hotary K, Allen E, Punturieri A, Yana I, Weiss SJ (2000) Regulation of cell invasion and morphogenesis in a three- dimensional type I collagen matrix by membrane-type matrix metalloproteinases 1, 2, and 3. J Cell Biol 149:1309–23

355. Lodillinsky C, Infante E, Guichard A, et al (2015) p63/MT1-MMP axis is required for in situ to invasive transition in basal-like breast cancer. Oncogene 1–14

356. Perentes JY, Kirkpatrick ND, Nagano S, Smith EY, Shaver CM, Sgroi D, Garkavtsev I, Munn LL, Jain RK, Boucher Y (2011) Cancer cell-associated MT1-MMP promotes blood vessel invasion and distant metastasis in triple-negative mammary tumors. Cancer Res 71:4527–38

357. Haas TL, Davis SJ, Madri JA (1998) Three-dimensional type I collagen lattices induce coordinate expression of matrix metalloproteinases MT1-MMP and MMP-2 in microvascular endothelial cells. J Biol Chem 273:3604–10

358. Sakai K, Nakamura T, Suzuki Y, Imizu T, Matsumoto K (2011) 3-D collagen-dependent cell surface expression of MT1-MMP and MMP-2 activation regardless of integrin β1 function and matrix stiffness. Biochem Bioph Res Co 412:98–103

359. Barbolina M V, Adley BP, Ariztia E V, Liu Y, Stack MS (2007) Microenvironmental regulation of membrane type 1 matrix metalloproteinase activity in ovarian carcinoma cells via collagen-induced EGR1 expression. J Biol Chem 282:4924–31

360. Zhang Z, Song T, Jin Y, Pan J, Zhang L, Wang L, Li P (2009) Epidermal growth factor receptor regulates MT1-MMP and MMP-2 synthesis in SiHa cells via both PI3-K/AKT and MAPK/ERK pathways. Int J Gynecol Cancer 19:998–1003

361. Zhang D, Brodt P (2003) Type 1 insulin-like growth factor regulates MT1-MMP synthesis and tumor invasion via PI 3-kinase/Akt signaling. Oncogene 22:974–82

362. Martinella-Catusse C, Polette M, Noel A, et al (2001) Down-regulation of MT1-MMP expression by the α3 chain of type IV collagen inhibits bronchial tumor cell line invasion. Lab Investig 81:167–75

363. Sudhakar YA, Verma RK, Pawar SC (2014) Type IV collagen α1-chain noncollagenous domain blocks MMP-2 activation both in-vitro and in-vivo. Sci Rep 4:2–10

364. Nyalendo C, Michaud M, Beaulieu E, Roghi C, Murphy G, Gingras D, Béliveau R (2007) Src-dependent phosphorylation of membrane type I matrix metalloproteinase on cytoplasmic tyrosine 573: Role in endothelial and tumor cell migration. J Biol Chem 282:15690–9

365. Gálvez BG, Matías-Román S, Yáñez-Mó M, Sánchez-Madrid F, Arroyo AG (2002) ECM regulates MT1-MMP localization with beta1 or alphavbeta3 integrins at distinct cell compartments modulating its internalization and activity on human endothelial cells. J Cell Biol 159:509–21

366. Hoshino D, Koshikawa N, Suzuki T, Quaranta V, Weaver AM, Seiki M, Ichikawa K (2012) Establishment and validation of computational model for MT1-MMP dependent ECM degradation and intervention strategies. PLoS Comput Biol 8:e1002479

367. Ng MR, Besser A, Danuser G, Brugge JS (2012) Substrate stiffness regulates cadherin-dependent collective migration through myosin-II contractility. J Cell Biol 199:545–63

368. Du J-Y, Chen M-C, Hsu T-C, Wang J-H, Brackenbury L, Lin T-H, Wu Y-Y, Yang Z, Streuli CH, Lee Y-J (2012) The RhoA-Rok-myosin II pathway is involved in extracellular matrix-mediated regulation of prolactin signaling in mammary epithelial cells. J Cell Physiol 227:1553–60

369. Akhtar N, Streuli CH (2006) Rac1 links integrin-mediated adhesion to the control of lactational differentiation in mammary epithelia. J Cell Biol 173:781–93

370. Lui C, Lee K, Nelson CM (2012) Matrix compliance and RhoA direct the differentiation of mammary progenitor cells. Biomech Model Mechanobiol 11:1241–9

371. Ahmed N, Riley C, Rice G, Quinn M (2005) Role of integrin receptors for fibronectin, collagen and laminin in the regulation of ovarian carcinoma functions in response to a matrix microenvironment. Clin Exp Metastasis 22:391–402

372. Delcommenne M, Streuli CH (1995) Control of integrin expression by extracellular matrix. J Biol Chem 270:26794–801

373. Petrie RJ, Gavara N, Chadwick RS, Yamada KM (2012) Nonpolarized signaling reveals two distinct modes of 3D cell migration. J Cell Biol 197:439–55

374. DeMali KA, Burridge K (2003) Coupling membrane protrusion and cell adhesion. J Cell Sci 116:2389–97

375. Moissoglu K, Schwartz MA (2006) Integrin signalling in directed cell migration. Biol Cell 98:547–55

376. Gilles C, Polette M, Zahm JM, Tournier JM, Volders L, Foidart JM, Birembaut P (1999) Vimentin contributes to human mammary epithelial cell migration. J Cell Sci 112:4615–25

377. Itoh Y, Seiki M (2004) MT1-MMP: an enzyme with multidimensional regulation. Trends Biochem Sci 29:285–9